Spectro-spatial architectures in rare-earth ion-doped crystals for wideband radiofrequency signal processing

Lothaire Ulrich

PSL UNIVERSITÉ PARIS

THÈSE DE DOCTORAT
DE L'UNIVERSITÉ PSL

Préparée à l'Institut Langevin, ESPCI

Architectures spectro-spatiales dans les cristaux dopés aux ions terre rare pour le traitement de signaux radiofréquence large bande

Spectro-spatial architectures in rare-earth ion-doped crystals for wideband radiofrequency signal processing

Soutenue par
Lothaire ULRICH
Le 14/12/2022

École doctorale n°564
Physique en Île-de-France

Spécialité
Optique
Interaction lumière-matière

Composition du jury :

Arnaud DERODE Professeur, Institut Langevin	*Président*
Lars RIPPE Associate Professor, Lund University	*Rapporteur*
Salvador SALES Professor, Universitat Politècnica de València	*Rapporteur*
Jean ETESSE Chargé de recherche, Institut de Physique de Nice	*Examinateur*
Diana SERRANO Chargée de recherche, Institut de Recherche de Chimie Paris	*Examinateur*
Julien DE ROSNY Directeur de recherche, Institut Langevin	*Directeur de thèse*

ESPCI PARIS | PSL

PhD thesis prepared in:

Thales Research & Technology
1 avenue Augustin Fresnel, 91767 Palaiseau Cedex, France

Institut Langevin
1 rue Jussieu, 75238 Paris Cedex 05, France

Remerciements

Les travaux synthétisés dans ce manuscrit n'auraient pas pu voir le jour sans la participation et le soutien de nombreuses personnes: quelques remerciements s'imposent.

Pour commencer, je voudrais adresser un énorme merci à toute mon équipe d'encadrement. J'ai eu la chance d'avoir pas moins de 5 personnes formidables pour s'occuper de moi, avec, malgré le nombre, une excellente synergie, et qui ont toutes indiscutablement enrichi mes années de thèse, chacune à sa manière.

Merci Julien pour avoir accepté la direction de ma thèse malgré un domaine d'expertise assez éloigné des terres rares. Merci pour toutes les discussions de traitement de signal, grâce à toi je crois avoir beaucoup mieux compris ce qu'était mon filtre.

Merci à Anne pour ta disponibilité et ta patience pour répondre à toutes mes questions sur le thulium, c'est toujours un grand plaisir d'échanger avec toi. Je ne peux pas m'empêcher de penser à l'une de nos premières discussions, où on se demandait «à partir de quand un petit délai devient positif». Ça m'a pris du temps mais je suis bien content d'avoir finalement trouvé la réponse.

Merci beaucoup à Loïc, pour toutes les discussions du soir, pour ton énorme culture scientifique, pour toujours chercher et trouver la solution quand ça ne marche pas, et tout ça dans l'humour et la bonne humeur. Tu ne peux pas t'empêcher de dérégler mes manips en entrant au labo, mais bon il paraît qu'on comprend mieux en faisant les réglages plusieurs fois !

Un grand merci également à Sacha, ç'a été sincérement un plaisir de travailler quotidiennement et d'échanger avec toi, que ce soit sur les terres rares ou sur tout sujet technique ou pas. Sans oublier les à-côtés, comme les séances d'escalade à la Troche ou les sessions musicales !

Finalement, un grand merci à toi Perrine. D'abord pour m'avoir fait confiance pour cette thèse, puis pour avoir été toujours à l'écoute pendant ces trois ans. Tu as toujours été d'excellent conseil, que ce soit scientifique ou humain. Merci pour tous les bons moments, tu as été une encadrante géniale !

I would like to thank warmly Lars Rippe, Salvador Sales, Arnaud Derode, Jean Etesse and Diana Serrano for accepting to be part of my PhD committee, for the time they have dedicated to review this thesis, and for the fruitful discussions that we had during the defense and beyond.

J'aimerais remercier Pascale Nouchi et Daniel Dolfi de m'avoir accueilli à TRT, d'abord pour un stage puis pour la thèse. Merci également à Christian Larat et Patrick Feneyrou de m'avoir encadré durant mon stage de fin d'étude, première expérience dans le monde de la recherche, et grâce à qui je suis maintenant convaincu de poursuivre dans cette voie.

Merci à tous les membres des laboratoires OTS et MNP pour les échanges toujours intéressants et conviviaux. Une mention spéciale à Vincent Crozatier, toujours disponible pour donner un coup de main, en particulier quand l'asservissement fait la grève.

Un grand merci à tous les doctorants sans qui l'ambiance serait bien différente, que ce soit pour la coinche ou la raclette (attention à la quiche au génépi !). Merci aux anciens: Delphin, Léa, Myriam, Simone, Benjamin, Guillaume, Jeremie, Vincent, Pierre, les Maxime, Inès, et à la relève: Bruno, Maxime, Tara, José, Mickael, Soizic, Alexandre, Clément, Guenole, Elsa. En particulier à Vincent, pour les blagues de qualité et les parties de badminton endiablées ; à Jérémie pour les conversations métaphysiques de tous poils ; à Pierre pour toutes les discussions et les bonnes tranches de rigolade dans le bureau, malgré la réunion weeb hebdomadaire non-autorisée par les autorités ; à Bruno, je crois qu'un grand destin musical nous attend ; et à Sylvain M, pas doctorant, mais ça n'empêche pas de rarement voir le fond du bol.

Merci aux amis de longue date, en particulier à Vincent, toujours disponible pour parler de cristaux autour d'un bon poulet croustillant au chinois municipal.

Merci à Jean, Edmond, Gabriel et Laurent pour tous les bons moments passés à la coloc de Massy 🎵

Un grand merci aux manzakin, qui m'ont accompagné par monts et par vaux autour de la Terre et qui ont bien changé ma vision du monde 🎶

Muchas gracias a mi muchachita por siempre confiar en mi, estoy muy ansioso por descubrir todas las aventuras que estamos a punto de vivir...

Finalement un grand merci à toute la famille pour tous ces moments magiques passés ensemble. Merci infiniment à papa et maman, merci pour vos conseils, votre soutien et votre confiance dans tous mes projets de vie, qui me poussent toujours en avant.

Ometepe style ✌

Contents

Introduction

The unique properties of rare-earth ions-doped crystals (REIC) make them unique candidates for a wide range of innovative technologies. Indeed, when inserted in a crystalline host, they combine long coherence times with a large inhomogeneous broadening. First applications have included optical memories [Lin et al., 1995], in which pages of data are stored under the shape of spectral features in the absorption profile of the material. More recently, the long coherence time of rare-earth ions has been exploited to develop quantum technologies, such as quantum memories, where the large bandwidths give access to high multiplexing of the information [Afzelius et al., 2009]. In the field of radio-frequency (RF) signal processing, REIC are also very promising materials, as they provide a very wide band of analysis at the RF scale. In this PhD thesis, we focus on the latter application.

More specifically, the subject of this thesis is the investigation of spectro-spatial architectures REIC for wideband RF signal processing. The first architecture of this kind, named "rainbow" architecture, was proposed at the end of the 90s for the function of wideband RF signal analysis [Galaup et al., 1998]. The rainbow spectrum analyzer, which is presented in detail in the first chapter of this thesis, has been the object of intense research. Among the first results, we can cite the PhD work of L. Ménager [Ménager, 2000]. Using thulium ions in a crystaline matrix as analog processors, the first experiment of the rainbow spectrum analyzer demonstrated a bandwidth of 35 MHz [Ménager et al., 2001]. Following studies progressively increased the bandwidth of analysis of two orders of magnitude up to a few GHz, with the work of in particular I. Lorgeré [Lorgeré et al., 2002] and V. Lavielle [Lavielle, 2004]. In the last report, a bandwidth above 20 GHz was demonstrated with a spectral resolution of 50 MHz, a time resolution below 100 μs, and a probability of intercept of 100 % [Berger et al., 2014], providing very promising performances for stringent civilian and defense applications. However, the analyzer was still limited by a dynamic range of 35 dB. Further studies performed by Y. Attal have predicted that the dynamic range of the analyzer could be increased by several orders of magnitude [Attal et al., 2016]. After these studies, the experimental dynamic range was indeed improved, but not yet to the level of the theoretical predictions. The dynamic range is the last aspect to improve for the rainbow spectrum analyzer to fully meet the requirement of most

stringent applications.

The present PhD work relies on all these studies performed during a time period of 20 years. In this thesis we address two different aspects related to the spectro-spatial architectures for RF processing. One of them is to investigate the potential of the spectro-spatial architecture for other RF processing functions. Namely, we will focus on the function of GHz-wide bandpass filter, which is a crucial component in our use case, as we will explain in the following. The other aspect is the direct continuity of the preceding works, with the objective to improve the dynamic range of the rainbow spectrum analyzer.

With these two different aspects to address, this thesis is presented as follows. In chapter I, we first introduce the motivations for RF spectrum analysis and RF filtering. We shown in particular the interest of rare-earth ions-doped crystals for those functions. We present then a rapid overview of the optical properties of rare-earth ions, and more specifically of the thulium-doped YAG crystal which is at the core of the experiments carried out in this thesis. Finally, we present a state of the art of the use of rare-earth ions in RF processing, and we explain in detail the principle of the rainbow RF spectrum analyzer.

Chapter II is dedicated to the demonstration of a RF filter inspired from the rainbow architecture, which we call the spectro-spatial RF filter. We first present the principle of the experiment. Then, we expose the experimental and theoretical studies that have been performed, with the objective to optimize the response of the filter in terms of amplitude and phase.

Chapter III is dedicated to the rainbow spectrum analyzer. It is divided into two subchapters III.A and III.B. In chapter III.A, we investigate the experimental limitations of the dynamic range of the analyzer. We first identify that an important obstacle is the temperature elevation inside the crystal caused by the optical excitation. We perform a parametrical study, in order to identify leverages allowing to overcome this limitation. In chapter III.B we develop an analytical model describing the spectral response, or apparatus function, of the analyzer. This model, which is an extension of the model of the spectro-spatial RF filter, allows to highlight various parameters of importance in order to optimize the response of the analyzer.

Finally, a general conlusion and perspectives to this manuscript and doctoral work are given in the last part.

Besides, to improve the readability of the text, we have moved in appendix the derivation of the models, in particular the model of the spectro-spatial RF filter and the model of the apparatus function of the rainbow spectrum analyzer, leaving only the final results in the main text.

Chapter I

Rare-earth ions for radio-frequency signal processing

In this first chapter, we present the current motivations and challenges in the field of wideband radio-frequency (RF) signal processing. Some RF functions can be addressed with light, and more specifically by using the optical properties of ions trapped in a host crystal. Among all types of RF signal processing, we focus especially on RF spectrum analysis and RF filtering, which are the two functions investigated during this PhD work. Then, we discuss optical properties of rare-eath ions-doped crystals (REIC) at low temperature. We present the main features of these ions, and more specifically of thulium as a dopant in a YAG crystal host. Finally, we will see that this type of materials can be used for a wide variety of RF signal processing functions. We will focus more specifically on RF spectrum analysis, investigated previously in our team, and RF filtering.

Contents

I.1 Wideband and high dynamic range RF signal processing

The motivation of the work carried out during this thesis is the wideband and high dynamic range detection and acquisition of RF signals, whose general principle is depicted in figure I.1. The usage of these functions spans from the detection and identification of radar emitters, like boats or planes, to the legal control of the different RF communication bands. Considering the exponential development of the communication networks (wifi, 4G, 5G...), the electromagnetic spectrum in the radio-frequency range becomes more and more dense (density of signals per frequency band) and broad (maximal reachable frequency). Concurrently, in the field of defense, the technology of emitters and receptors steadily improves, and stealth techniques such as frequency hopping are being used to minimize the probability of interception. To keep the pace with the increasing complexity of RF signals, the systems of detection must also evolve.

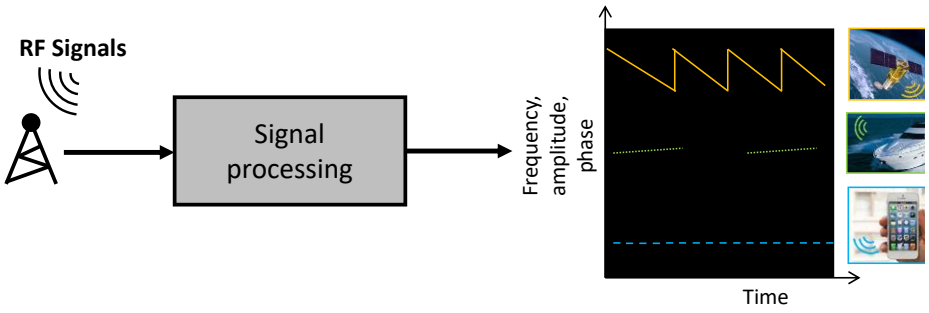

Figure I.1: General principle of signal surveillance – A signal processing function analyses the incoming RF signals in terms of frequency, amplitude and phase, in order to identify the emitters and acquire the signals.

Today, standard RF signal analysis techniques rely on full digital architectures. The electromagnetic environment is captured through an antenna, digitized by an analog-to-digital converter (ADC), and processed digitally via Fourier transform algorithms. Full digital RF processing is indeed particularly attractive for its unrivaled versatility: once the signal is recorded, any processing function can be applied. However, for the time being, this method suffers from two major drawbacks, particularly limiting in applications requiring wideband and high dynamic range analysis.

The first one lies in the performance of the conversion. Indeed, as illustrated in figure I.2, a compromise is to be made between the bandwidth and the dynamic range of an ADC. This limitation can stem in particular from the jitter of the sampling clock [Walden, 1994]. Currently, ADCs with a dynamic range above 60 dB are limited to a bandwidth of a few GHz, for example 5 GHz for the model AD9213 from Analog Devices, or the model ADC12DJ5200RF from Texas Instruments. As we observe in figure I.2, the performances of the converters steadily improve over the years. Indeed,

this topic is under constant investigation. We can cite the use of new materials, for example going from standard CMOS to superconducting technologies [Mukhanov et al., 2004]. Another solution to overcome their limited bandwidth, is to parallelize the ADCs in order cover the entire bandwidth [Gupta et al., 2007]. In this case, the system is more complex and allows to overcome the limited bandwidth.

The second major drawback of full digital systems is the huge data throughput. Indeed, digitizing a signal at 20 GHz, *i.e.* with at least 40 GS/s, with a dynamic range of 60 dB, is equivalent to the order of 400 gigabytes of data per second to process. Applying Fourier analysis on this amount of data requires huge processing power, which is not compatible with embedded and autonomous systems.

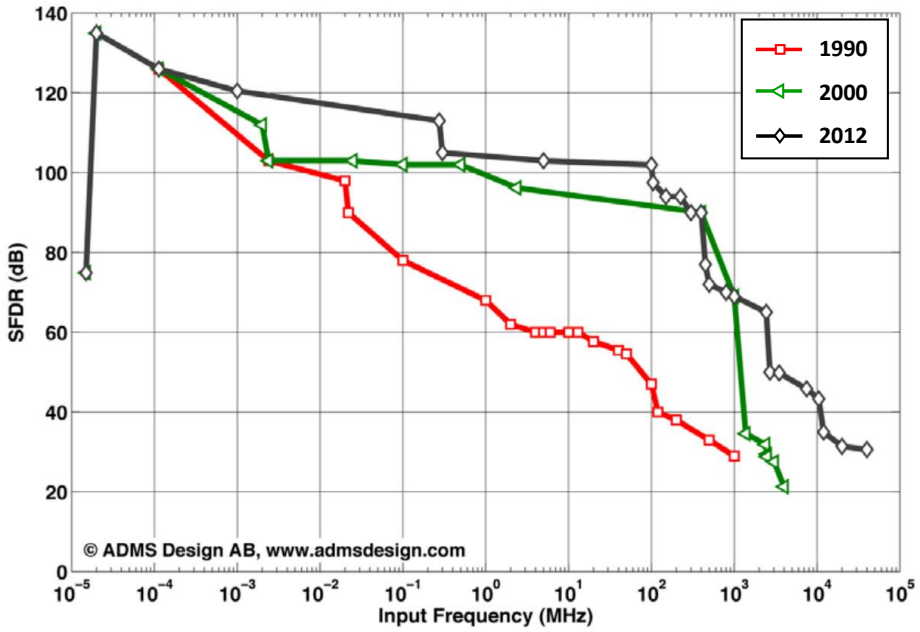

Figure I.2: Review of analog-to-digital converters, in terms of SFDR (Spurious-Free Dynamic Range) and input frequency, from [Jonsson, 2012]

One solution to address those two drawbacks simultaneously is to add an analog pre-processing stage. Indeed, at the cost of versatility, analog pre-processing allows to alleviate greatly the constraint on both the bandwidth of the ADC and the data throughput. Figure I.3 illustrates an example of architecture for frequency-selective digitization using an analog pre-processing stage, inspired from [Hogan et al., 2019]. We see that this architecture relies on a wideband spectrum analyzer and a GHz-wide tunable RF filter. Concurrently to the studies on the ADCs, this partly analog solution is also the object of thorough investigation, as presented in section I.1.1. This is the stand of the work presented in this thesis, where we investigate the two functions shown in figure I.3: wideband spectrum analysis and frequency-agile GHz-wide bandpass filtering.

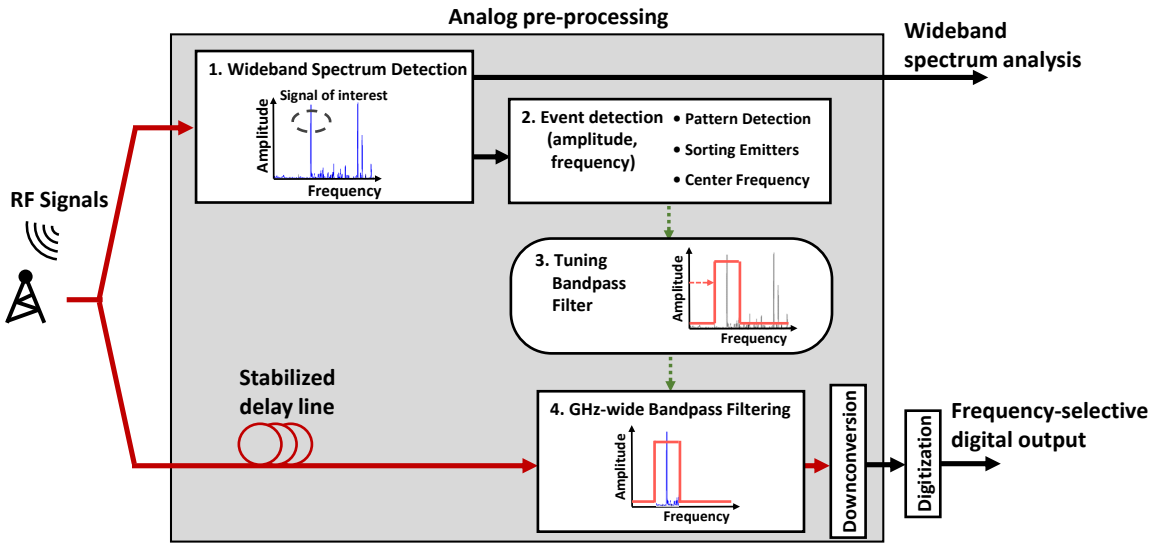

Figure I.3: Architecture for frequency selective digitization, using an analog pre-processing stage, inspired from [Hogan et al., 2019] – The incoming signal is split in two. The first part is sent in a wideband spectrum analyzer (1.), providing the amplitude and frequency of the signals over time. The spectra are fed to a fast event detection processor (2.), proceeding to pattern recognition and detecting the signals of interest. The spectra only represent a small amount of data compared to the full RF signals, which allows a fast treatment by this dedicated processor. When a signal is identified, the GHz-wide RF bandpass filter is tuned to match the target frequency (3.). The second part of the incoming signal, which was preserved in a delay line, is then filtered and digitized by the GHz-wide high dynamic range ADC. This architecture allows to reduce the constraint on the bandwidth of the ADC, and dramatically reduce the data thoughput since only the signals of interest are digitized. The frequency-selective digitization of even transient signals is made possible, while preserving a 100 % probability of interception over the complete instantaneous bandwidth using wideband spectrum analysis.

I.1.1 Spectrum analysis

In order to be competitive against the high versatility of digital processing, a self-standing RF spectrum analyzer must show high performances. The figures of merit for real-time wideband processing are in particular the instantaneous bandwidth, the dynamic range, and the spectral and time resolution. Table I.1 gives typical needs for these figures of merits in the field of surveillance in communication or radar.

Instantaneous bandwidth	Probability of interception	Spectral resolution	Time resolution	Dynamic range
$\geq$ 20 GHz	100 %	25 kHz to 100 MHz	10 μs to few ms	$\geq$ 60 dB

Table I.1: Typical needs for the principal figures of merits of spectrum analysis for surveillance in communication or radar. Exact values depend strongly on the application.

Historically, various technologies have been investigated for wideband spectrum analysis. We can cite for example the acousto-optic spectrum analyzers [Gurevich et al., 2004]. Using a piezoelectric transducer, an acoustic wave is generated inside a Bragg cell from the RF signal. The spatial wavelength of the acoustic wave depends on the RF frequency. A laser beam traveling through the crystal will be diffracted by the acoustic wave, with an angle of diffraction dependent on the RF frequency, which allows to retrieve the incoming RF spectrum. In this method, the bandwidth is limited to 1 to 2 GHz by the attenuation of the acoustic wave, which is not sufficient for actual wideband analysis requirements. Note that this technique is very interesting for space applications, and presently used in several missions, for its simplicity, low footprint and absence of moving parts [Korablev et al., 2018].

Other have focused on RF spectrum analysis using leaky wave antennas. Depending on the frequency of the RF signal, the antenna radiates in a different direction. Using a range of reception antennas, we can then access the frequency in real time. A very wide bandwidth of analysis of 60 GHz is shown in [King et al., 2021], but with a resolution currently limited to 1 GHz.

In the field of atomic physics, RF spectrum analysis has been performed using for example the quantum properties of NV centers in diamond [Magaletti et al., 2022]. Under magnetic field, the ground state of the NV center is separated into three hyperfine states $|0\rangle$, $|+1\rangle$ and $|-1\rangle$, whose frequency detuning is proportional to the magnetic field, and lies within the RF range. Under optical pumping, if the NV center was initially in state $|0\rangle$, then it emits strong photoluminescence. If it is intially in state $|\pm1\rangle$, then the photoluminescence is weak. The NV centers are initially prepared

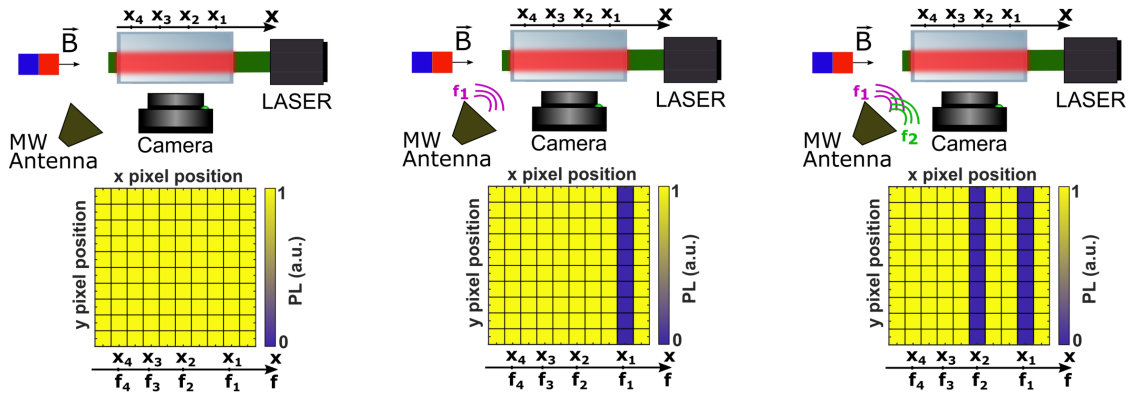

Figure I.4: Schematic of the experimental setup for the NV center-based spectral analysis, from [Magaletti et al., 2022] – MW antenna: microwave antenna, PL: photoluminescence, $\vec{B}$: magnetic field; Left: no RF signal is resonnant with the diamond, the photoluminescence is maximal. Center: one RF signal is resonnant with the diamond, which reduces the photoluminescence at one position. The correspondance position/RF frequency is given by the gradient of magnetic field. Right: several incoming RF signals are detected simultaneously.

in state $|0\rangle$. If an incoming RF signal matches the hyperfine detuning and excites the NV centers to a state $|\pm 1\rangle$, then the photoluminescence drops. This allows a RF-frequency selective measurement, where the frequency is determined by the applied magnetic field. As shown in figure I.4, if a gradient of magnetic field is applied, then each zone of the diamond is resonant with a different RF frequency, and we map the RF spectrum spatially in the crystal. The RF spectrum is then obtained with a simple image of the crystal. Promising results have been already demonstrated, with a bandwidth of analysis 25 GHz, a resolution of 50 MHz and a dynamic range of 40 dB.

Finally, RF spectrum analysis is also possible using the frequency-selective capacity of rare-earth ion-doped crystals (REIC) in the optical domain. Our team has extensively worked on the subject, and in particular demonstrated high performance in the so-called "rainbow" architecture [Berger et al., 2016]. We will describe this architecture in more detail in section I.3.2.

I.1.2 Filtering

As we illustrated in figure I.3, spectral analysis alone is not sufficient to acquire digitally the incoming RF signals. In order to digitize the signals of interest using a bandwidth-limited high dynamic range ADC, it is necessary to first filter them out.

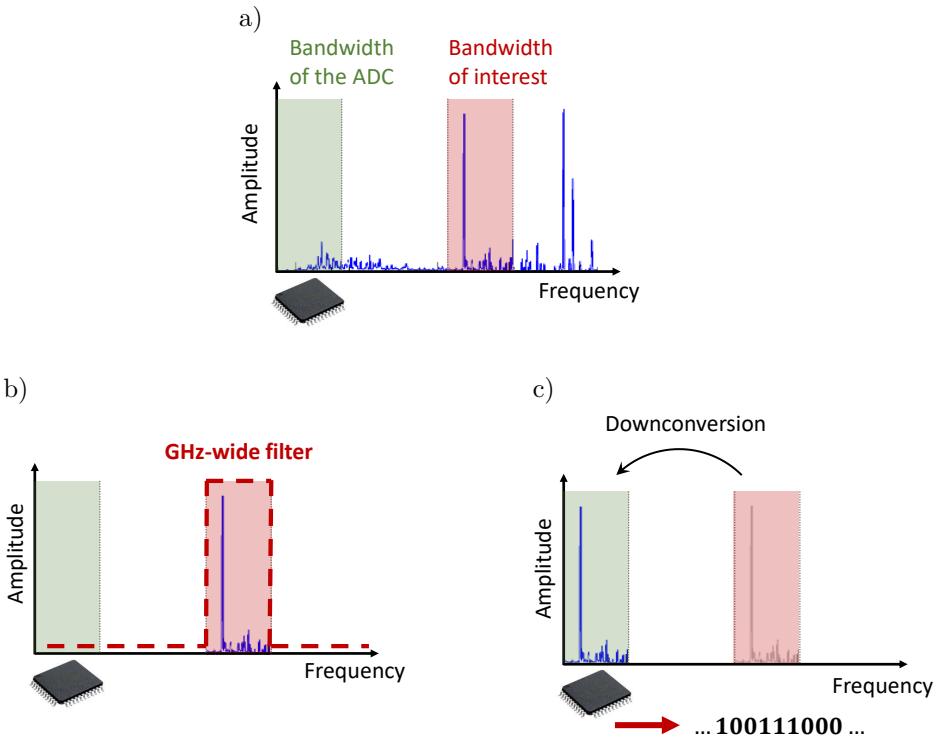

Figure I.5: Illustration of digitization of a high frequency signal using a high dynamic ADC with a bandwidth of a few GHz.

The typical operation to digitize a high frequency signal is illustrated in figure I.5. The band of interest is selected using a GHz-wide RF filter, downconverted to the band of the ADC, which can then convert the signal into digital data.

Many technologies have been investigated to propose RF signal filtering, from LC-type electronic circuit [Deevi and Rao, 2017] to MEMS devices [Fedder and Mukherjee, 2005]. Among the different solutions, photonic RF filters show particularly interesting properties for our applications. The principle of a photonic RF filter is to use the properties of optics to perform RF filtering. It generally relies on an optical filter, as depicted in figure I.6. The RF signal is transposed on an optical carrier using an intensity modulator, filtered in the optical domain, and downconverted back to the RF domain by mixing the filtered signal with a local oscillator on a photodiode. We present a state of the art of photonic RF filters in section II.1.

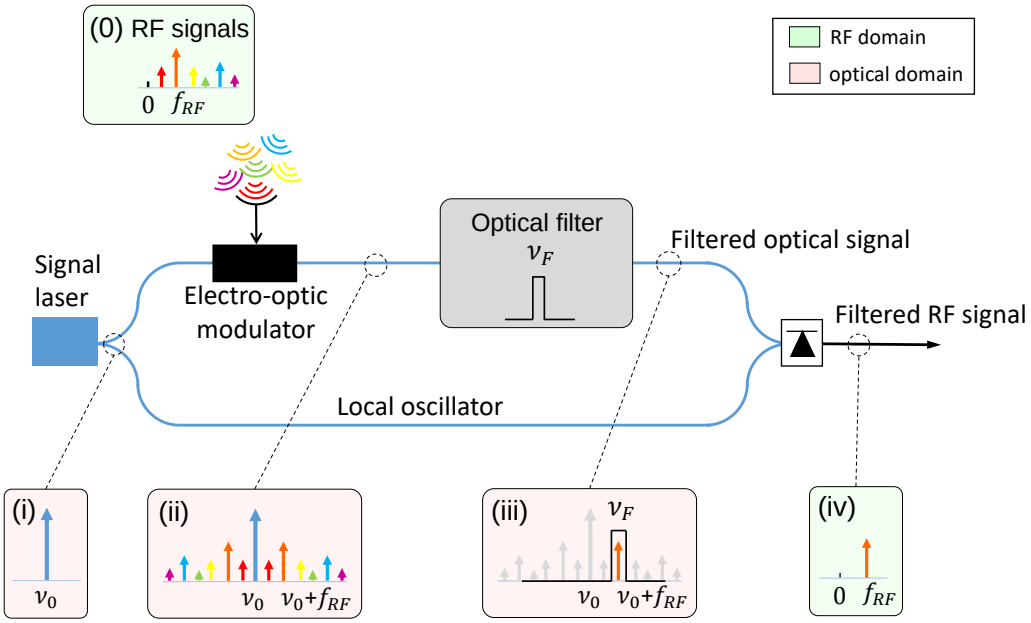

Figure I.6: Architecture of a photonic RF filter – The RF signals (0) are transposed on an optical carrier, the signal laser (i), via an intensity modulator. The optically carried RF signals (ii) are filtered optically (iii) and downconverted to RF range by mixing with a local oscillator on a photodiode (iv).

Photonic RF filters are very appealing in our applications for several reasons. First, they are generally very tunable at the RF scale. Indeed, the tens of GHz-wide RF domain is very narrow compared to optical frequencies. Second, it intrinsically includes a downconversion process, from optical domain to RF domain. If the frequency of the local oscillator can be tuned over a few tens of GHz, using for example a frequency shifter, it becomes possible to combine the signal-to-ADC downconversion (see figure I.5) with the optics-to-RF downconversion. Finally, we illustrated in figure I.3 the interest of delay lines. Carrying the RF signal on an optical frequency allows to take advantage of the technology of optical fibers, providing the high quality

delay lines needed in our use case (see figure I.3).

One of the objectives of this PhD work is to take advantage in our knowledge in REIC-based spectrum analysis to develop a REIC-based photonic RF filter. This utilization of REIC has never been reported before. Considering the remarkable characteristics of the spectrum analyzer and other processing functions reported in the litterature, we have reasons to believe that a REIC-based RF filter should reach very high performances. Besides, as shown in figure I.7, this could allow to mutualize the crystal and the equipment of the spectrum analyzer, to perform in one single environment the two analog functions from the digitization system shown in figure I.3.

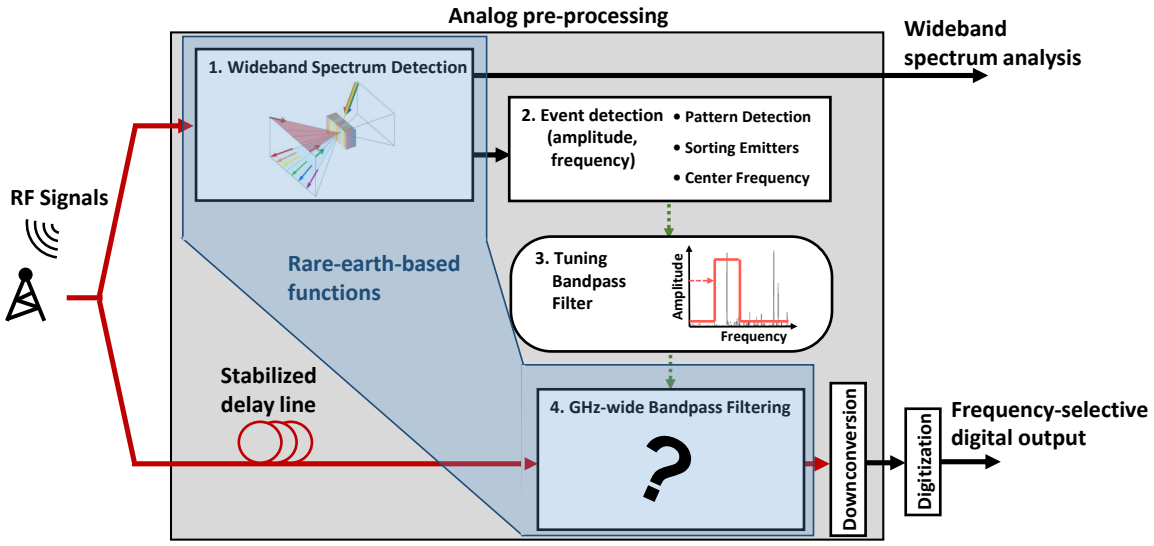

Figure I.7: Architecture for frequency selective digitization presented in figure I.3 – The blue shape shows the two analog components which could share the same crystal and experimental setup: spectrum analysis and RF filter.

I.2 Rare-earth ions and thulium-doped YAG crystals

As mentioned previously, the object of this thesis is to investigate RF processing functions using rare-earth ions-doped crystals (REIC). In this section, we present a brief overview of the unique properties of REIC, which make them particularly interesting candidates in our applications. After a presentation of the general properties of REIC, we will detail more specifically the Tm^{3+}:YAG crystal used in our experiments.

I.2.1 Overview of the rare-earth ions

Rare-earth elements are a family of 17 elements: the lanthanide series, comprised between lanthanum and lutetium, to which are generally added scandium and yttrium (see figure I.8). They were discovered between the late 18$^{\text{th}}$ and first half of 19$^{\text{th}}$ century in mineral oxides. The appelation of "rare" earth originates historically from the complexity of their extraction from the minerals. However, rare-earth elements are relatively abundant in the earth crust, between 100 and 1000 times more abundant than gold for example [Haynes et al., 2016].

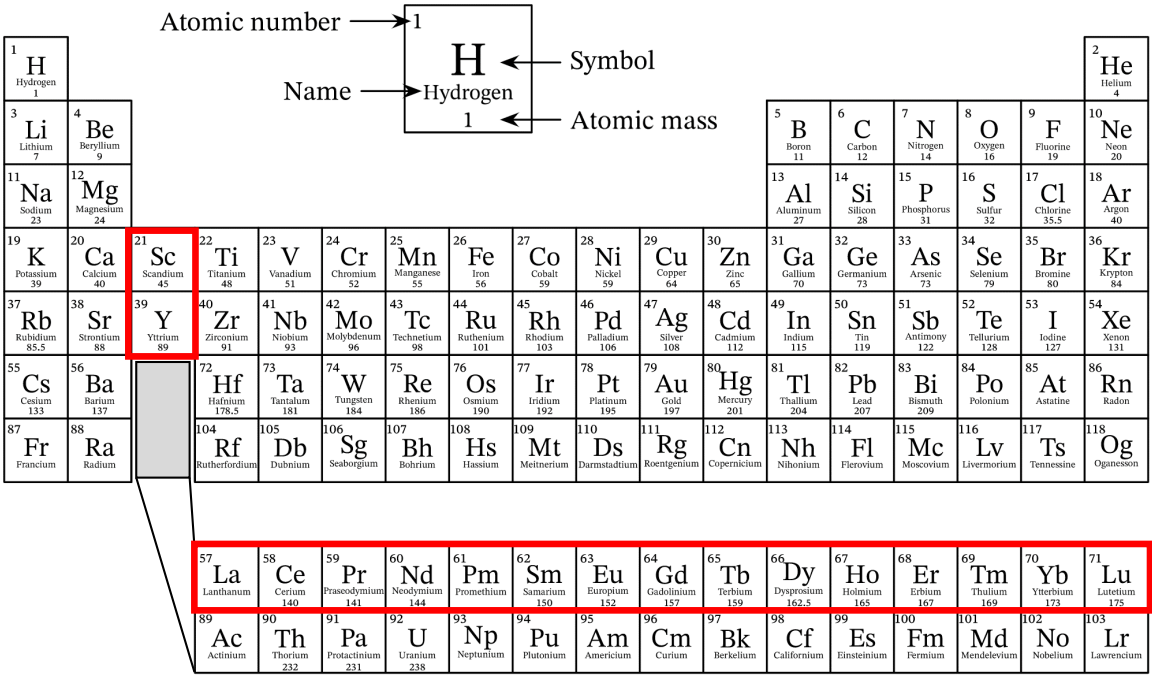

Figure I.8: Periodic table of the elements − Rare-earths are the elements between cerium and ytterbium.

Rare-earth ions are generally found in the oxidation state +III, which is often their only stable oxidation state. Except for scandium and ytterbium, in this state, their electronic structure is of the form:

$$(\text{core})^{46}5s^2 5p^6 4f^n \tag{I.1}$$

with $n = 0$ (lanthanum) to 14 (lutetium). The last energy levels are occupied by the $4f$ electrons. The energy levels of trivalent rare-earth ions are described in the Dieke diagram, historically reported in [Dieke, 1968] and extended in later studies, such as [Peijzel et al., 2005]. The transitions between the energy levels often correspond to optical transitions, in the visible or infrared range. Each ion exhibits transitions at different wavelength, which can prove more or less convenient in practice.

In REIC, the absorption line of an optical transition is characterized by two

features: the homogeneous and inhomogeneous linewidths (see figure I.9). The homogeneous linewidth corresponds to the absorption linewidth of a single ion. The frequency width at half maximum (FWHM) of the absorption is noted Γ_h. It is directly linked to the quantum coherence time of the transition, noted T_2, by the relation:

$$\Gamma_h = \frac{1}{\pi T_2}. \tag{I.2}$$

For an isolated ion in vacuum, T_2 is ultimately limited by the lifetime of the optical transition, noted T_1:

$$T_2 \leq 2T_1, \tag{I.3}$$

or, in other words,

$$\Gamma_h \geq \frac{1}{2T_1}. \tag{I.4}$$

The homogeneous linewidth of the transitions strongly depends on temperature. The wide interest in REIC is motivated by the fact that, at cryogenic temperature, the homogeneous linewidth of their optical transitions are exceptionally narrow. This unique property is granted by their electronic structure, with the fully occupied outer levels $5s$ and $5p$ acting as a protective shell for the $4f$ electrons (see expression I.1).

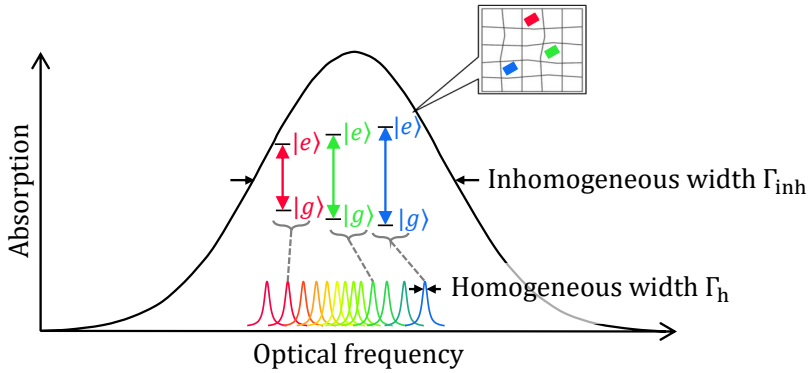

Figure I.9: Homogeneous and inhomogeneous broadening of an optical transition − The absorption linewidth of a single ion is called homogeneous linewidth. Due to inhomogeneities in the matrix, the resonnance frequency of each ion is slightly shifted. The linewidth of the collective broadened absorption is called inhomogeneous linewidth.

The inhomogeneous linewidth is a collective feature of the ions inside the matrix. Due to the defects and inhomogeneities of the matrix, each ion experiences a slightly different environment. As a result, the resonance of each ion is shifted, and the collective absorption is broadened. The FWHM of the inhomogeneous linewidth is noted Γ_{inh}.

Their properties of long coherence times and inhomogeneous broadening make REIC promising systems in various applcations. It includes in particular quantum technologies like quantum communications [Sangouard et al., 2008], where quantum

information is stored in the coherence of the transitions, and where a large inhomogeneous broadening could allow spectral multiplexing. More recent investigations have shown the interest of REIC in quantum computing, using individual rare-earth ions as qbits [Kinos et al., 2021]. In RF signal processing, the properties of homogeneous and inhomogeneous linewidths are also very interesting. Indeed, as detailed further in this thesis, we can inscribe processing functions in the absorption profile of the crystal. The inhomogeneous bandwidth is directly linked to the bandwidth of analysis, and the homogeneous bandwidth limits ultimately the spectral resolution of the processing.

The values of coherence time and inhomogeneous linewidth in a REIC depend on many parameters, in particular the couple rare-earth ion/matrix, the doping concentration, the temperature or the magnetic field strength and orientation. In thulium, optical coherence times from 1 to 400 μs have been reported, corresponding to homogeneous linewidths from 300 kHz to 8 kHz, with inhomogeneous linewidths from 3 to 300 GHz [Thiel et al., 2011]. A record optical coherence time of 4.4 ms has been reported in Er^{3+}:YSO, corresponding to an homogeneous linewidth below 100 Hz, and an inhomogeneous linewidth of 2.7 THz has been shown in a praseodymium-doped crystal [Thiel et al., 2011]. We see that REIC offer a wide variety of combinations, which can suit different applications.

I.2.2 Properties of thulium in a crystalline YAG matrix

Among all REICs, Tm^{3+}:YAG presents very promising properties for wideband RF signal processing, and has been used already for such applications [Merkel et al., 2014, Berger et al., 2016]. We also used this material throughout all this PhD work. In this section, we present the properties of Tm^{3+}:YAG crystals, justifying such interest for wideband RF signal processing.

Yttrium-aluminium garnet, or YAG, is a crystal whose unit cell is cubic with a side of 1.2 nm. Its chemical formula is $Y_3Al_5O_{12}$. The unit cell is shown in figure I.10a. It has a C_3 symetry around the [111] axis. When a YAG crystal is doped with thulium ions, the latter occupy the sites of the yttrium. This corresponds to one crystallographic sites with six different dipole orientations, represented in figure I.10b. In our experiments, we use a laser polarized along the [111] axis. This polarization is orthogonal to the dipoles 2, 4 and 6, and does not interact with them. The light interacts only with the ions of type 1, 3 and 5, which are all equivalent with respect to this excitation.

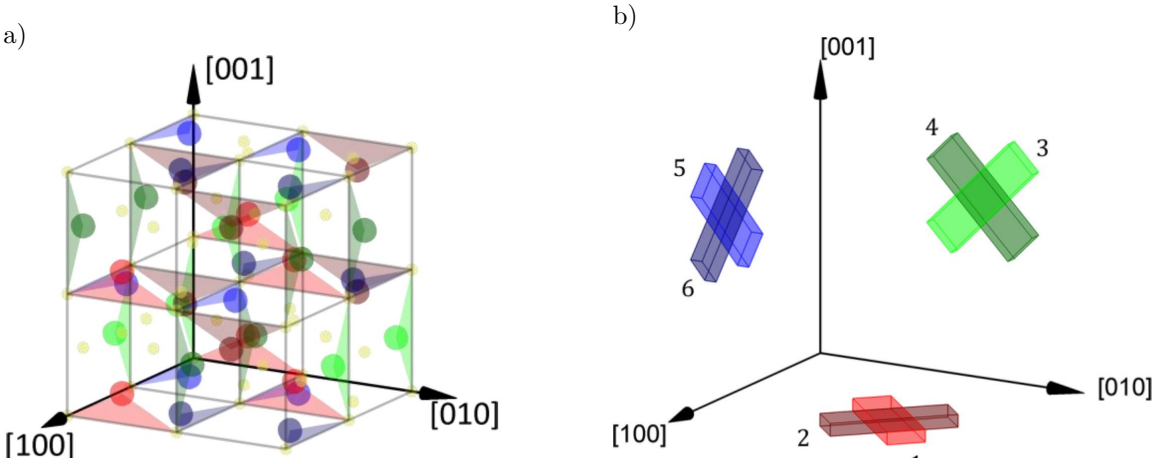

Figure I.10: a) Unit cell of a YAG crystal, from [Attal, 2017] – Yellow dots: Al ions; Red, green and blue dots (light and dark): Y ions. The colors corresponds to the six dipole orientations of figure b). The rectangles of width 1/2 and hight 1/8 help visualize the position of the Y ions. They are oriented along the axis [001] (red), [100] (green) and [010] (blue).

b) The Tm^{3+} ions occupy the sites of the yttrium. This corresponds to 6 different dipole orientations.

The first energy levels of the $4f$ electrons in thulium in YAG are shown in figure I.11. The optical transition is the $^3H_6$-$^3H_4$ transition at 793 nm. This wavelength is convenient in practice, as it gives access to high performance visible cameras, and is compatible with the telecom wavelength by frequency doubling. At a temperature of 3 K, the homogeneous linewidth of this transition lies around 10 kHz, for an inhomogeneous linewidth of 20 GHz. As mentioned before, in REIC-based RF processing, the inhomogeneous linewidth is linked to the instantaneous bandwidth of the processing, and the homogeneous bandwidth to the spectral resolution. We see that the properties of Tm^{3+}:YAG are well adapted for the needs of wideband RF signal processing recalled in table I.1.

In the following, we will call $^3H_6$ the ground state, noted $|g\rangle$, and $^3H_4$ the excited state, noted $|e\rangle$. From the $^3H_4$ level, the ions rapidly decay to $^3F_4$ via $^3H_5$, with a characteristic time of the order of 600 μs [Basiev et al., 1996]. With a 10 ns lifetime, the $^3H_5$ is very short-lived, and will be neglected in the following. Under the action of the crystal field, each level is split into Stark manifolds (not shown in figure I.11). The difference between two Stark levels is of the order of a few THz. A complete measurement of the energy levels of the first manifolds in Tm^{3+}:YAG is reported in [Gruber et al., 1989]. Within a Stark manifold, the levels of higher energy rapidly decay to the level of lowest energy in typically 1 μs, through non-radiative processes. For this reason, we will only consider the lowest level of each manifold here.

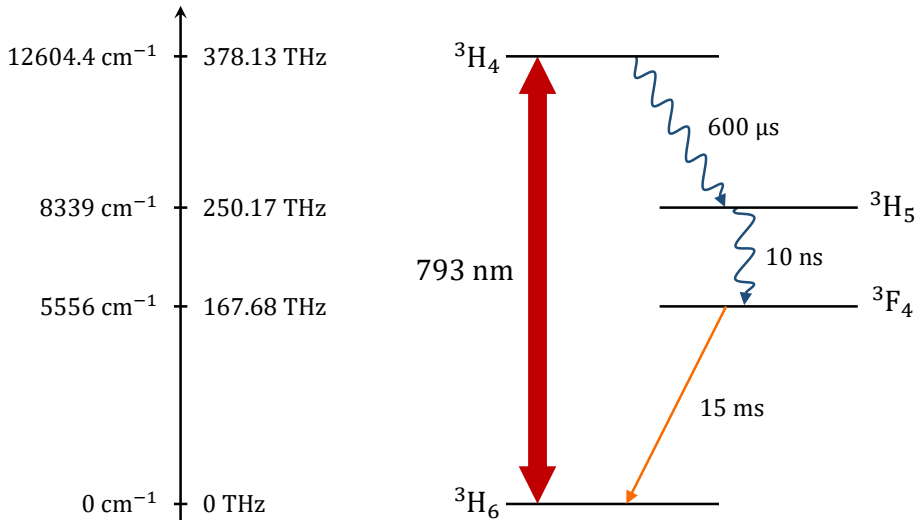

Figure I.11: Lowest energy levels of the $4f$ electrons in thulium and typical lifetimes at 3 K – red large arrow: optical transition used in the experiments, blue wavy arrow: non-radiative decay (emission of phonon), orange straight arrow: radiative decay (emission of photon).

The $^3F_4$ level has a rather long lifetime, noted T_m, of the order of 15 ms [Basiev et al., 1996]. This state is called metastable state, noted $|m\rangle$. The existence of a metastable state, along with the inhomogeneous broadening of the transition described in figure I.9, gives access to a crucial property called Spectral Hole Burning (SHB), described in figure I.12. If a laser narrower than Γ_h is applied on the crystal, only the corresponding class of ions is excited, and decays to the metastable state. Before eventually decaying to the ground state, the ions are stored in the metastable state for a characteristic time T_m. During this time, they cannot absorb light. This depopulation of the ground state results in a hole in the absorption profile. The lifetime of the hole equals the lifetime of the metastable level T_m. This SHB property is available at each point in the crystal. So, using SHB, we can shape the absorption

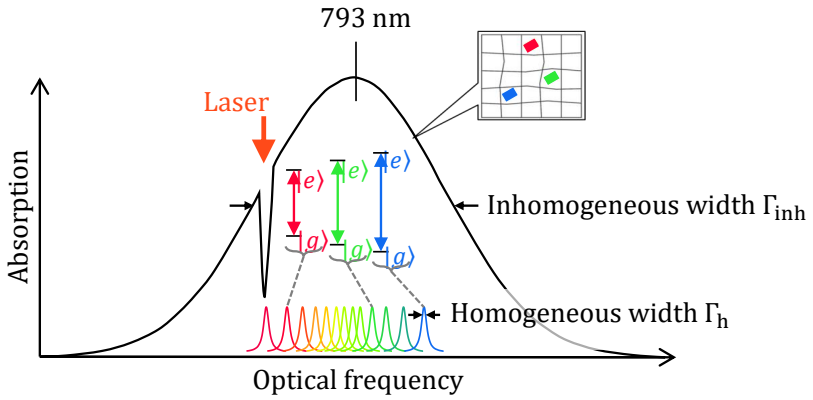

Figure I.12: Illustration of Spectral Hole Burning (SHB) – Shining a laser on the crystal depopulates the corresponding class of ions, which is stored in the metastable level. A transparency window appears in the absorption profile, called a spectral hole.

of the crystal with respect to both frequency and position. As we will see later, this is crucial in our experiments, where we program both spectral and spatial (spectro-spatial) absorption gratings in the crystal.

In the configuration presented above, the lifetime of a spectral feature inscribed in the absorption of the crystal is $T_m \simeq 15$ ms. In some cases, it is interesting to reach longer storage of the populations, in order to maintain the features for a longer time in the absorption profile. This can be achieved by adding a magnetic field on the crystal. As depicted in figure I.13, under magnetic field, due to the nuclear spin 1/2 of thulium, the excited and ground states split into two Zeeman levels. The branching ratio between the Zeeman levels of $|e\rangle$ and $|g\rangle$ depends on the orientation of the magnetic field. It was shown in [Louchet, 2008] that, if the magnetic field is oriented along the [111] axis, then the non spin-conservative transitions $|g_1\rangle$-$|e_2\rangle$ and $|g_2\rangle$-$|e_1\rangle$ are strongly forbidden. In practice we will use this [111] orientation, which simplifies greatly the system of levels. Besides, the dipole orientations 1, 3 and 5 (see I.10), which are equivalent with respect to the laser field polarized along [111], are also equivalent with respect to the [111] permanent magnetic field. As a result, the Zeeman splitting is equal for the three sites. The Zeeman splittings Δ_g and Δ_e are proportional to the magnetic field B, with the gyromagnetic ratios:

$$\Delta_g = \gamma^{(g)} B, \qquad \Delta_e = \gamma^{(e)} B \tag{I.5}$$

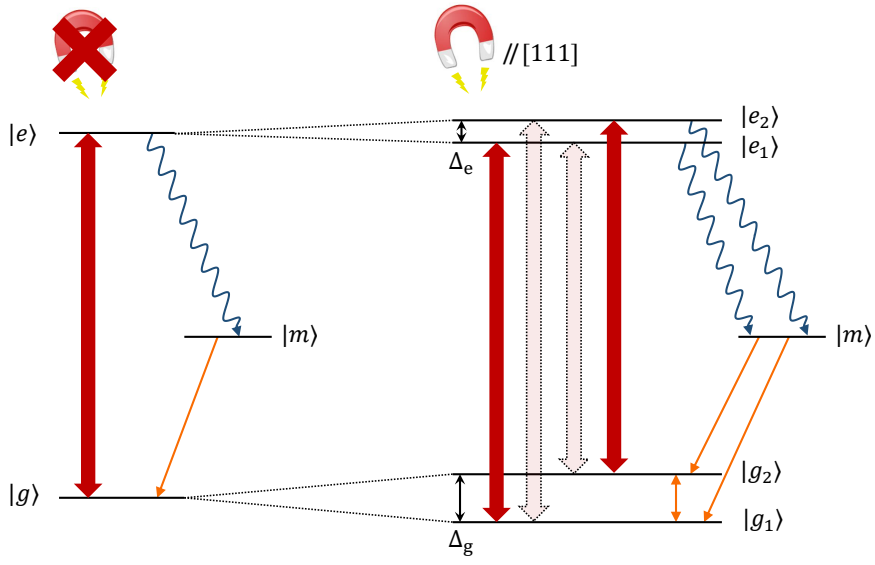

Figure I.13: Zeeman splitting of the ground and excited states under a permanent magnetic field – Blue wavy arrow: non-radiative decay, orange straight arrow: radiative decay, red arrow: authorized optical transition, light red dotted arrow: forbidden optical transition. If the magnetic field is oriented along the crystaline direction [111], then the cross-spin optical transitions $|g_1\rangle$-$|e_2\rangle$ and $|g_2\rangle$-$|e_1\rangle$ are forbidden.

The gyromagnetic ratio in the case of a magnetic field oriented along [111] was measured in [Louchet, 2008]:

$$\gamma^{(g)}_{[111]} = 329 \text{ MHz/T}, \qquad \gamma^{(e)}_{[111]} = 67 \text{ MHz/T} \tag{I.6}$$

When the experiments presented in this thesis feature a magnetic field, the latter will always be implicitly oriented along direction [111].

In figure I.14, we depict the simplified energy levels of Tm^{3+}:YAG under a [111] magnetic field. In this example, we excite an ion from $|g_2\rangle$ to $|e_2\rangle$. The ions decay non-radiatively to the metastable state $|m\rangle$ with a characteristic time $T_1 = 685$ μs. Then, they decay back to the two ground states with a characteristic time $T_m = 24$ ms, with a proportion of 2/3 to the original spin state, and 1/3 to the opposite spin state.

Without pumping, the population in the ground state Zeeman levels return to thermal equilibrium with a characteristic time noted T_g. Chapter III.A is dedicated to the measure of T_g under various experimental conditions. As we will see, between 3 and 5 K, T_g can vary from 0.2 to 20 s. We see that $T_g \gg T_m$. So, with magnetic field, the shelving state in play for the SHB processes changes from the metastable state to the ground state hyperfine structure. In figure I.14, after some excitation cycles, $|g_2\rangle$ is fully depopulated and all ions are stored in $|g_1\rangle$. This way, we burn a hole in the absorption profile at the frequency $|g_2\rangle$-$|e_2\rangle$. Note that we simultaneously

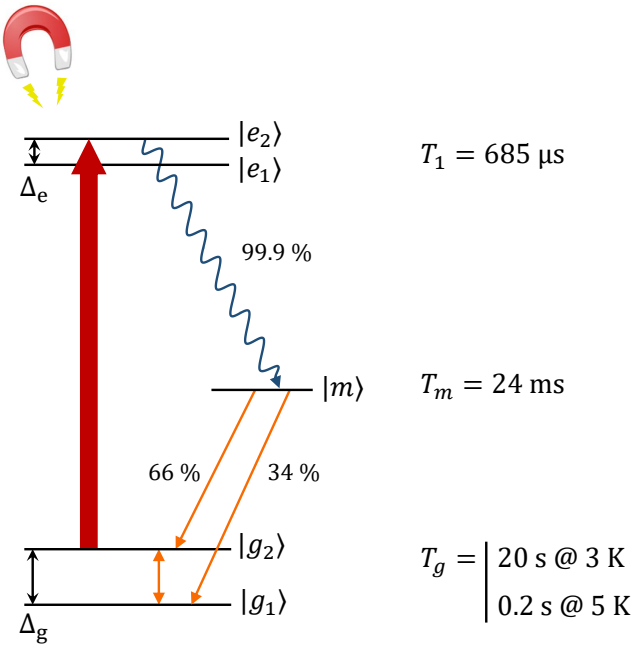

Figure I.14: Simplified energy levels of Tm^{3+}:YAG under [111] magnetic field and decay processes – We took here the example of an excitation $|g_2\rangle$-$|e_2\rangle$. The decay processes are identical for an excitation $|g_1\rangle$-$|e_1\rangle$. The decay rates between the different levels in our setup were measured in [Attal, 2017].

increase the absorption at the frequency $|g_1\rangle$-$|e_1\rangle$, which creates so-called antiholes in the absorption profile. This is discussed in more detail in section II.3.1 or in [Linget et al., 2015].

In this thesis, we will work either without magnetic fied, with the levels depicted in figure I.11, or with a magnetic field oriented along the [111] crystalline axis, with the levels depicted in figure I.14.

I.3 Previous works on rare-earth-based RF signal processing

In this section, we present a state of the art of the use of REIC for RF signal processing. We will then present the architecture and principle of the "rainbow" spectrum analyzer.

I.3.1 General state of the art (all processing functions)

As mentioned in the previous sections, REIC, and in particular Tm:$^{3+}$:YAG, show very promising properties for high dynamic range and wideband RF signal processing. Various RF processing functions have already been demonstrated using REIC.

Many architectures rely on the so-called three-pulse photon echo mechanism: if two laser pulses are sent on the crystal, with a time delay inferior to T_2, then the

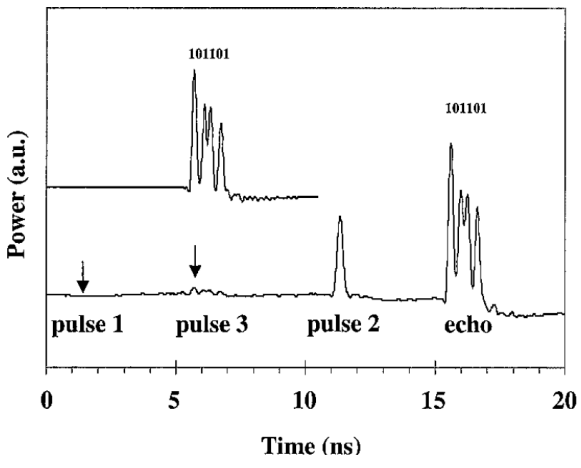

Figure I.15: Demonstration of true-time delay using a Tm^{3+}:YAG crystal, from [Tian et al., 2001] – Programming pulses 1 and 2 are sent periodically on the crystal to maintain the function of time delay (note that pulse 1 is not seen by the photodetector in the proposed setup; its instant of arrival is marked by an arrow). At any moment, the signal pulse 3 carrying the information, materialized here by a series of bits, can be sent on the crystal (upper line). An echo is observed, reproducing the features of the signal pulse. The delay between echo and pulse 3 is equal to the delay between pulses 1 and 2.

function of time delay is imprinted in the absorption profile of the crystal, under the form of a spectral grating. If a signal pulse travels then through the crystal, an echo of this pulse will be emitted after a delay equal to the programming delay.

A straightforward RF processing function achievable using this phenomena is the function of true-time delay, reported for example in [Tian et al., 2001], and described in figure I.15. The large inhomogeneous linewidth of the REIC allows to dispose from a large processing bandwidth, and consequently high output data rate, possibly exceeding 10 Gbit/s. Instead of pairs of monochromatic pulses, the absorption of the crystal can also be shaped using pairs of chirped pulses [Reibel et al., 2004]. More generally, using a pair of chirped pulses is conceptually equivalent but provides more flexibility in the features imprinted in the absorption.

Complex functions have been demonstrated using pairs of chirped pulses, such as time reversal of RF signals [Linget et al., 2013]. In this architecture, described in figure I.16, the programming (engraving) pulses are two symmetrical linearly chirped pulses. This configuration allows to write a different delay for each frequency contained in the chirp. The crystal behaves then as a dispersive filter. The input pulse 3 is also chirped, and modulated in intensity with the RF signal. With the relation frequency/delay written by the engraving beams (the echo of frequency ν_4 is more delayed than the echo of frequency ν_1), the amplitude of the overall echo is time-reversed with respect to the input. Recent works have demonstrated very promising

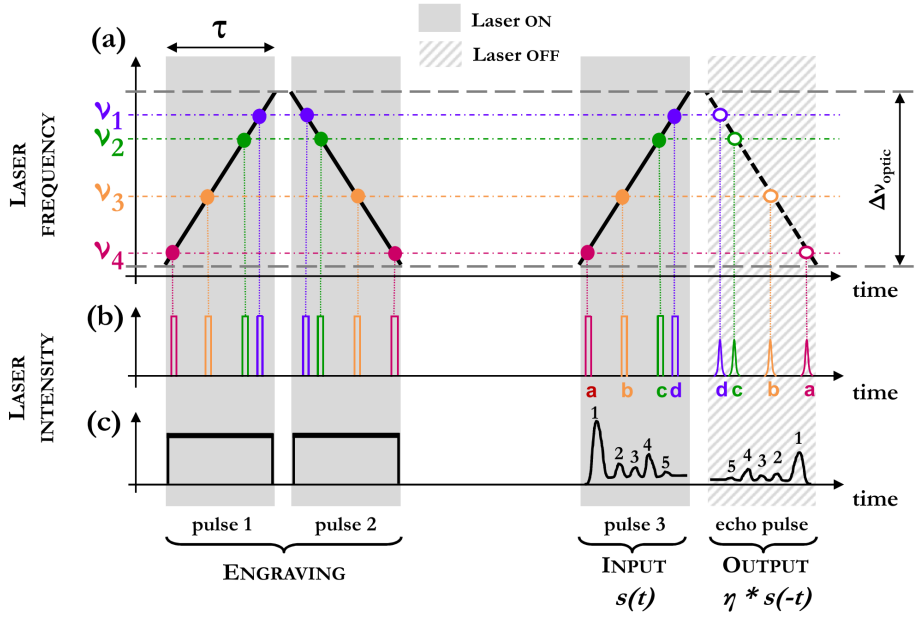

Figure I.16: Principle of time reversal of RF signals, from [Linget et al., 2013] – The two symmetrical linearly chirped engraving pulses inscribe a frequency-dependent time-delay. The input pulse is also chirped, and modulated in intensity with the RF signal. With the relation frequency vs delay, the amplitude of the echo is time-reversed with respect to the input, and can be captured by a photodetector.

results in terms of product time×bandwidth, with processing of signals of duration > 10 μs and potentially GHz bandwidth [Louchet-Chauvet, 2018]. Other functions have been demonstrated using linearly chirped pulses, like time-frequency conversion [Crozatier et al., 2004] or time correlation [Schlottau and Wagner, 2004]. In all those applications, the unique properties of REIC allow to possibly reach very high values of time×bandwidth product.

We remind that, in this thesis, we focus in particular on the functions of RF spectrum analysis and RF filtering. In the field of RF spectrum analysis, two main architectures are currently investigated using REIC. The photographic architecture is conceptually the most simple, and does not rely on photon echo like the aforementioned studies. The principle, illustrated in figure I.17, consists in imprinting the RF spectrum in the absorption profile of the REIC via SHB, then read it with a chirped laser. The signal laser is sent continuously on the crystal, constantly reshaping the absorption profile. By repeatedly chirping the read-out laser, a probability of interception of the signals of 100 % can be achieved thanks to the "memory" of the atoms. High performances have been demonstrated in a Tm^{3+}:YAG crystal by S2 Corporation [Merkel et al., 2014], with a spectral resolution below the MHz, an instantaneous bandwidth of analysis of 20 GHz, and a Spurious Free Dynamic Range (SFDR) above 60 dB. The weakness of this architecture is the time resolution, ultimately limited by the lifetime of the storage state. Besides, a tradeoff is to be made between spectral and time resolution, since increasing the spectral resolution requires to slow down the read-out chirp.

The second architecture of wideband RF spectrum analysis using REIC is called the "rainbow" architecture. The REIC is programmed to act as a ultra high resolution diffraction grating, allowing separate spatially the different components of the RF spectrum. We detail the principle of the rainbow spectrum analyzer in section I.3.2.

Contrarily to REIC-based RF spectrum analysis, which has been already studied in the past years, REIC-based RF filtering is a completely new field of investigation. Optical filtering for medical imaging has been reported in [Kinos et al., 2016] using spectral holes in a Pr^{3+}:YSO crystal. A transparency window is burnt in the absorption profile at the target frequency, in order to filter an incoming signal. However, because some residual transmission always occurs outside of the spectral hole, the dynamic range would be limited to around 15 dB using our crystals, which is not sufficient for RF filtering. In the chapter II of this thesis, we present the first demonstration of high dynamic range RF filtering using REIC.

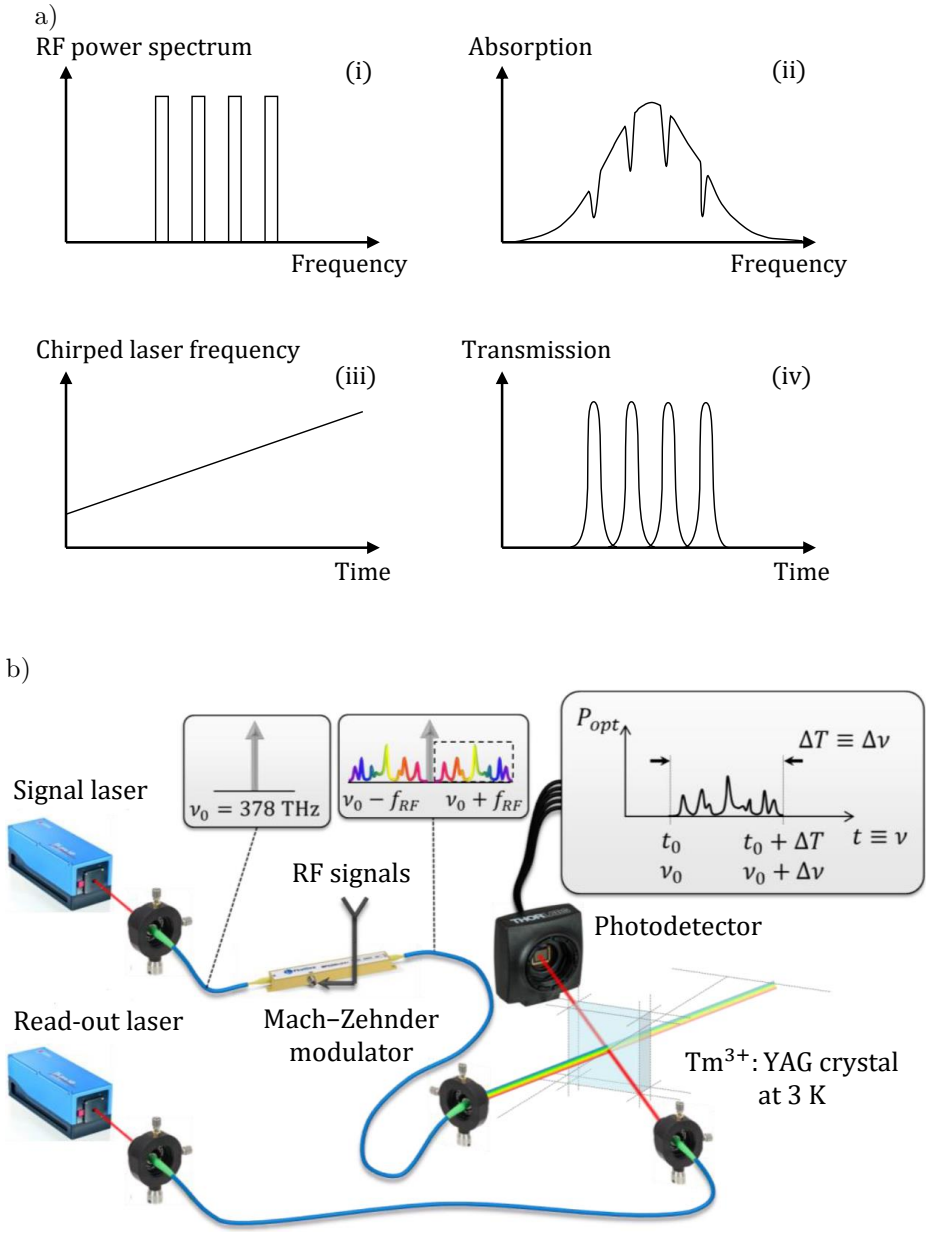

Figure I.17: a) Principle of the photographic SHB spectrum analyzer, from [Le Gouët et al., 2007] – The RF spectrum (i) is imprinted in the absorption profile of the REIC via SHB (ii). A read-out laser is chirped over the inhomogeneous bandwidth (iii), and the RF spectrum is retrieved by measuring the transmission over time (iv).

b) Illustration of the implementation of the photographic SHB spectrum analyzer reported in [Merkel et al., 2014], from [Attal, 2017] – A signal laser is modulated in intensity with the incoming RF signals. Its center frequency is set on the edge of the inhomogeneous line, so that only one sideband is imprinted in the REIC absorption profile via SHB. A read-out laser shines the same volume in the crystal as the signal laser and is chirped over the absorption profile to retrieve the RF spectrum.

I.3.2 Rainbow spectrum analyzer

As mentioned before, the core of this thesis is to study the spectro-spatial architectures, inspired from the rainbow spectrum analyzer developed previously in the team. Using the unique properties of REIC, this architecture was investigated to develop a RF spectrum analyzer. In this section we present the rainbow spectrum analyzer. Its performances are reported in [Berger et al., 2016], which is the starting point of this thesis.

The principle of the rainbow spectrum analyzer is shown in figure I.18. The incoming RF signals are captured through an antenna. They are upconverted via an intensity modulator on a monochromatic laser, called the signal laser, and sent on the REIC. As we will describe in the following, the crystal is beforehand programmed to diffract the different spectral components of the incoming signal in specific directions. We acquire the diffracted beams with a camera, and make the correspondance between pixel and frequency to retrieve the RF spectrum.

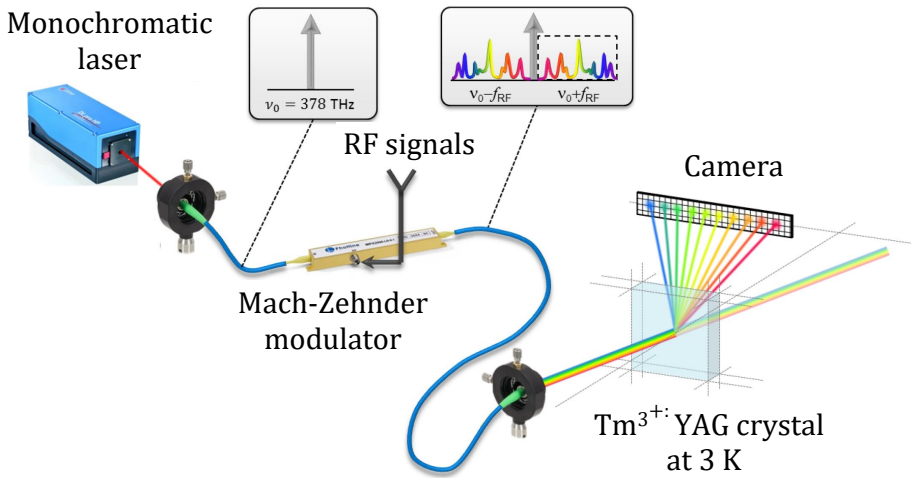

Figure I.18: Principle of the rainbow spectrum analyzer – The ensemble programming the diffraction gratings is not shown here.

The crystal is programmed using a second laser, called the programming laser. As depicted in figure I.19, the laser is split into two beams, which are mixed in free space in the crystal with an angle θ. The superposition of the beams results in interference fringes. At the points of constructive interference, the light burns a hole in the absorption profile of the crystal, specifically at the frequency of the programming laser. At the points of destructive interference, no SHB occurs and the crystal remains absorbant. As a result, the interference fringes are converted into a transmission grating by SHB. Note that the diffraction grating obtained with this technique is frequency-selective: the grating can only be seen by an incoming signal with the exact same frequency than the programming laser. The spectral resolution of this

grating is ultimately limited by the homogeneous linewidth, which corresponds to the narrowest spectral feature than can be imprinted in the absorption profile. In our case $\Gamma_h \simeq 10$ kHz. This spectral resolution is incomparably better than the diffraction limit of a standard grating. Let us derive a quick order of magnitude. The resolution of a grating made of N equispaced infinitely thin slits, around a frequency ν, is given by ν/N. In our experiment, the gratings are engraved over the order of 5 mm (size of the beams), with fringes spaced by around 5 μm (see chapter III.B), so the grating is made of $N \sim 10^3$ fringes. The optical frequency is $\nu \sim 300$ THz. So, the spectral resolution of an equivalent diffraction-limited grating made of slits is of the order of 300 MHz, almost 5 order of magnitude above our frequency-selective grating.

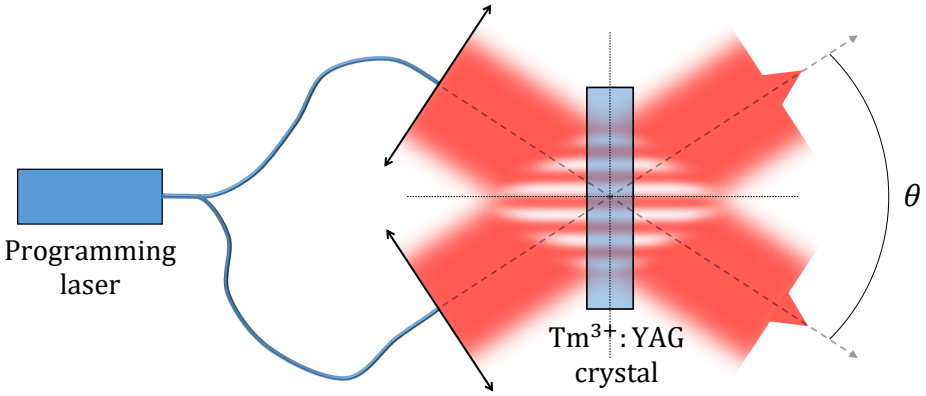

Figure I.19: Programming a spatial grating – The programming is split in two and mixed in the crystal with an angle. The interference fringes are converted into a transmission grating in the crystal via SHB.

As we will see in chapter II, the angle of diffraction is equal to the angle between the programming beams. As an example, in order to diffract two frequencies in two different directions, we start by setting the programming laser to the first frequency, with the corresponding angle between the beams, and we imprint the first grating. Then, we change the frequency and angle an imprint the second grating. It is important to note that both grating coexist simultaneously in the crystal. Indeed, they are made of two different and independent classes of ions.

In the rainbow spectrum analyzer, instead of only two gratings, we program a continuum of gratings. For this, as illustrated in figure I.20, we chirp the programming laser frequency, and we sweep synchronously the angle of one programming beam. This way, we associate bijectively one diffraction angle to one frequency, and detecting the position on the camera becomes equivalent to detect the frequency of the input.

Once the grating is written, it only survives during the lifetime of the storage state. Without magnetic field, this is the metastable lifetime $T_m \simeq 15$ ms. With

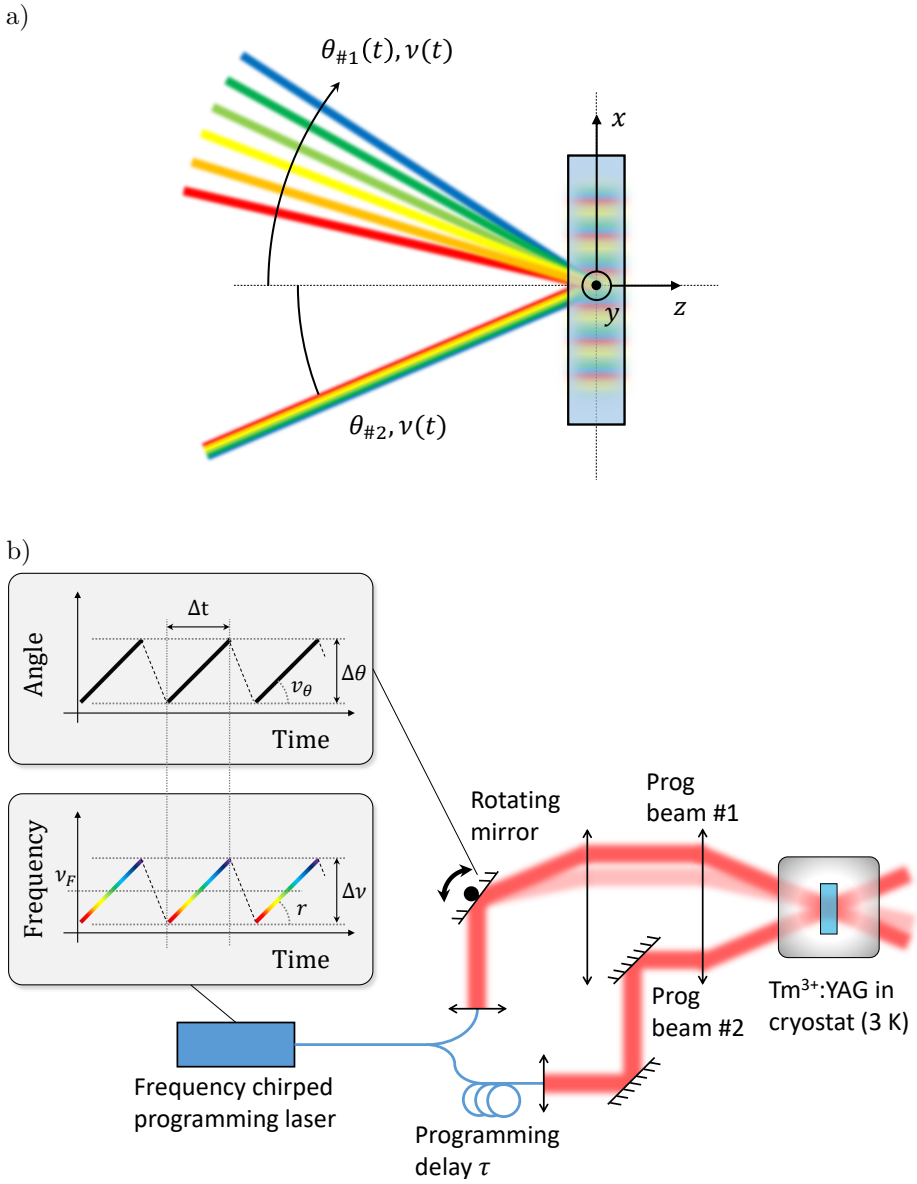

Figure I.20: a) Programming a continuum of spatial gratings – The programming laser is chirped over the desired frequency range. One beam is fixed, and the other one is swept angularly, synchronously with the frequency chirp.

b) Schematic of the programming stage – The angular sweep is performed by a rotating mirror located in focal plane equivalent to the crystal.

magnetic field, this is the spin lifetime T_g of the order of 1 s. However we want the diffractive function to be present at all time inside the crystal, to be able to detect incoming signals continuously. For this, we refresh the grating by sending periodically the programming chirps, reaching a steady-state. In order to perform simultaneously the programming and read-out, the beams are disposed in different planes, in a contrapropageant rectangle configuration (see figure I.21).

Note that, as depicted in figure I.20b, a delay τ can be added to the fixed pro-

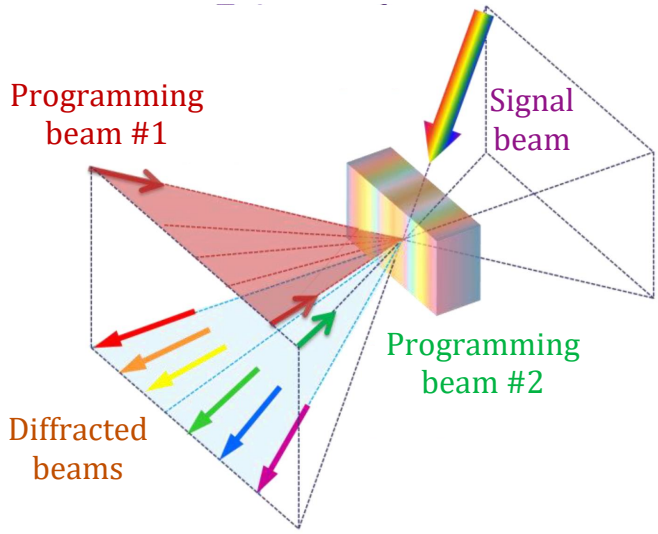

Figure I.21: Spatial configuration of the programming beams, the signal beam carrying the RF signals, and the diffracted beams

gramming beam. We will see in chapters II and III.B that the programming delay is actually necessary to obtain good performances. It is interesting to note that, with a delay, the two programming beams reach the crystal at different times, so light interference does not occur anymore. However, the two beams still interfere through the processes of atomic excitation. This phenomenon is driven by the coherence time of the excited transition T_2. If $\tau > T_2$, then the two fields E_1 and E_2 act separately, and the ions are senstitive to $|E_1|^2 + |E_2|^2$. In this case no interference occur, and we do not obtain any grating. If $\tau < T_2$, then the two fields act as one, and the ions are effectively sensitive to $|E_1 + E_2|^2$. In this case we observe interferences, even if the beams do not interfere directly with one another. The spectral counterpart of a time delay τ is a sine function of period $1/\tau$. So, if the programming delay is > 0, then we imprint not only a spatial grating, but also a spectral grating. At each point of the crystal, the absorption versus the resonance frequency of the ions is modulated. In a nutshell, the angle between the programming beams creates a spatial grating, and the time delay creates a spectral grating. In our case, where we combine both, we obtain a spectro-spatial grating.

I.4 Conclusion

In this introductive chapter we have presented the need for RF signal processing. We have discussed the limitations of full-digital processing, and emphasized the interest of an analog pre-processing stage to alleviate the digital processing, and especially using photonic tools. We have presented some analog technologies in the field of spectrum analysis and signal filtering. Then, we have described the main properties of rare-earth ions, and more particularly of Tm^{3+}:YAG. Finally, we have shown various RF

signal processing architectures based on REIC. We have presented in more detail the previous works of our team in the realization of a spectrum analyzer based on the rainbow architecture using REIC.

Chapter II is dedicated to the study of a RF filter, based on a spectro-spatial architecture inspired from the rainbow spectrum analyzer, that we call the spectro-spatial RF filter. We will present an experimental and theoretical study, in order to optimize the performances of this novel experiment. The spectro-spatial RF filter also provides a new approach of the rainbow spectrum analyzer, which will help the understanding of the latter.

Chapter III is dedicated to the study of the rainbow spectrum analyzer. First, we investigate the phenomenon limiting the diffraction efficiency in the setup, and in particular thermal effects inside the crystal. Second, we will present a novel analytical model describing the frequency response of the spectrum analyzer, in order to determine the importance of several experimental parameters.

Chapter II

Spectro-spatial RF filter

In this chapter we discuss the implementation of a radio frequency filter using a Tm^{3+}:YAG crystal, using the spectro-spatial architecture inspired from the rainbow spectrum analyzer described in section I.3.2. We make use of the Spectral Hole Burning properties and the long optical coherence time of the rare-earth ions to "program" a spectro-spatial grating in the crystal. This grating allows to diffract spatially the desired frequencies and filter them out from the input signal. We will study the characteristics of the spectro-spatial RF filter in terms of rejection, shape of the filter, and frequency agility, using an experimental implementaion and an analytical model.

In the first section we introduce briefly the field of photonic RF filters, and present the issues at stake. In section two, we depict the architecture of the spectro-spatial filter and its experimental implementation. We describe how we create an optical filter in the crystal, and how we make an RF filter from this optical filter. In the third section, we present a parametrical study aiming to determine the relevant parameters ruling the filter shape. We show the best performances we could reach with the current setup. In section four, we develop an analytical model describing the filter response, relying on the optical Bloch equations and the wave equation. We use this model to discuss the importance of various parameters, in particular the role of causality in the filter response. In the last section, we finally investigate the phase response of the filter, comparing experiment and model.

II.1 Introduction: photonic RF filters

In section I.1.2 we have shown the importance of GHz-wide RF filters in the field of radar or communication surveillance. In particular, we have presented the interest of photonic RF filters for these applications. Indeed, they generally exhibit a very high frequency tunability at the RF scale, include an intrinsic optical downconversion stage adaptable for RF downconversion, and are compatible with low loss optical fiber delay lines. For these reasons, photonic RF filters are currently a dynamic field of investigation. In this section, we present a short state of the art of photonics RF filters. A more complete review was reported recently in [Yao and Capmany, 2022].

Photonic RF filters are often either notch filters of bandpass filters. Notch filters, such as [Xue et al., 2008], can be used in RF signal processing to block parasitic or jammer signals. In this work, we focus more specifically on bandpass filters, for the case of use presented in section I.9. Depending on the application, different features will be required from a bandpass filter. These features include in particular the rectangle shape of the filter, given by the width of the passing band, the steepness of the sides and the rejection, as illustrated in figure II.1. The rejection at a given frequency from the edge of the filter is defined as the difference, in dB, between the transmission level within the passing band, and the transmission level at this frequency. In this chapter, we will use two figures of merit to quantify the rectangular shape of the filters:

- The global rejection, given in dB. We define this quantity as the rejection between the passing band and the noise floor.
- The steepness of the sides. We also quantify this feature in dB, by measuring the rejection at 50 MHz from the edge of the passing band.

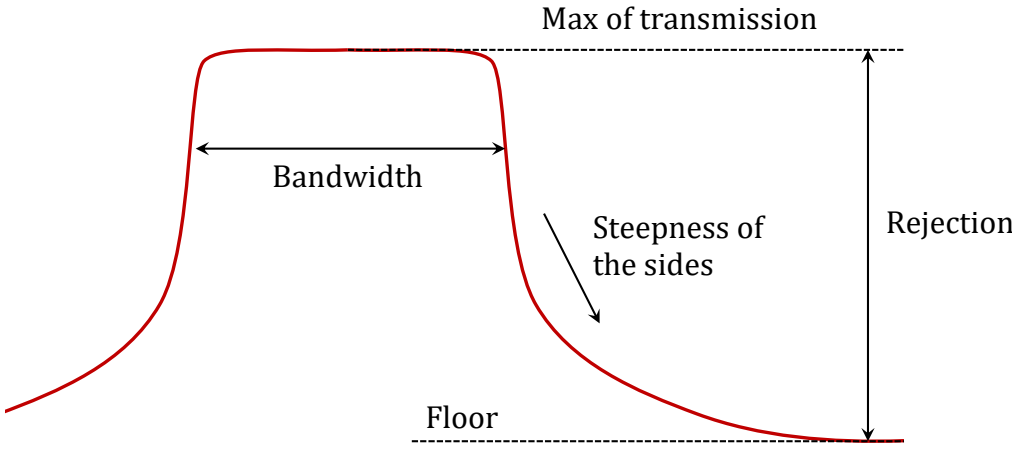

Figure II.1: Features of a filter – The rectangle shape is defined by the bandwidth, the steepness of the sides and the rejection.

As presented in section I.1.2, this work is dedicated to the study of GHz-wide filters, namely between 100 MHz and 10 GHz, which is the bandwidth of the high dynamic range ADCs that we wish to address.

To our knowledge, the higher global rejection ever reported for a photonic RF filter is the Brillouin scattering-based filter reported in [Li et al., 2017], with a rejection of 80 dB. However, this filter has a fixed bandwidth of 7.7 MHz, which is too small for our applications. Unfortunately, we observe from the litterature that the rejection and steepness generally degrade when the bandwidth increases (see table II.1). The rejection of filters larger than 1 GHz is generally lower than 45 dB. Besides, filters with tunable bandwidth generally present a less optimal shape, closer to a trapezoid than to a rectangle. Indeed, the tunability of a filter generally requires some complexity in the architecture, which is often made at the expense of the steepness.

	Reference	Global rejection [dB]	Rejection at 50 MHz from the edge [dB]	Bandwidth [GHz]
Fixed BW	[Li et al., 2017]	80	50	0.008
	[Preussler et al., 2016]	50	35	0.2
	[Ghelfi et al., 2019]	45	40	1
Tunable BW	[Matsko et al., 2012]	75	2	0.65-0.85
	[Savchenkov et al., 2009]	70	2	0.25-1
	[Norberg et al., 2011]	32	< 2	1.9-5.4
	[Guzzon et al., 2010]	40	< 2	3-7.4

Table II.1: Comparison between photonic RF filters reported in the literature − The references are sorted by bandwidth. Filters with bandwidth > 1 GHz are currently limited to 45 dB of rejection. Besides the bandwidth tunability is generally achieved at the expense of the steepness of the sides.

In this chapter, we present the spectro-spatial RF filter that was investigated during this PhD work. In section II.2 we describe the architecture of the filter. We present then in sections II.3, resp. II.4, the experimental, resp. theoretical study which were performed to understand the behaviour of the filter and optimize its performances. Whereas the amplitude response of the filter discussed in this section is essential to define the performance of the filter, its phase is also an important feature. In section II.5 we discuss the phase response of the filter.

II.2 Architecture of the spectro-spatial filter

II.2.1 Overall architecture

In this section we present the architecture of the filter and the experimental setup. It is largely inspired from the rainbow spectrum analyzer reported in [Ménager et al., 2001], or more recently in [Berger et al., 2016].

The core of the setup consists in a thulium doped YAG crystal maintained at 3 K in a closed-cycle cryostat. The crystal is "programmed" (more explanations in section II.2.2) to diffract spatially a selected range of optical frequencies only, which results in an optical band-pass filter on the diffracted beam. Our RF filter takes advantage of this optical filtering, as depicted in figure II.2: the RF input signal is captured by an antenna and transposed onto an optical carrier via a fibered lithium niobate electro-optic intensity modulator. The light is then collimated into free space to enter the crystal. The selected frequency range is diffracted by the crystal, which filters out this band from the transmitted beam. The diffracted beam is then coupled back to an optical fiber and mixed with the carrier used as a local oscillator (LO). The RF beat note is acquired using a photodiode ET-4000F from EOT with a > 12.5 GHz

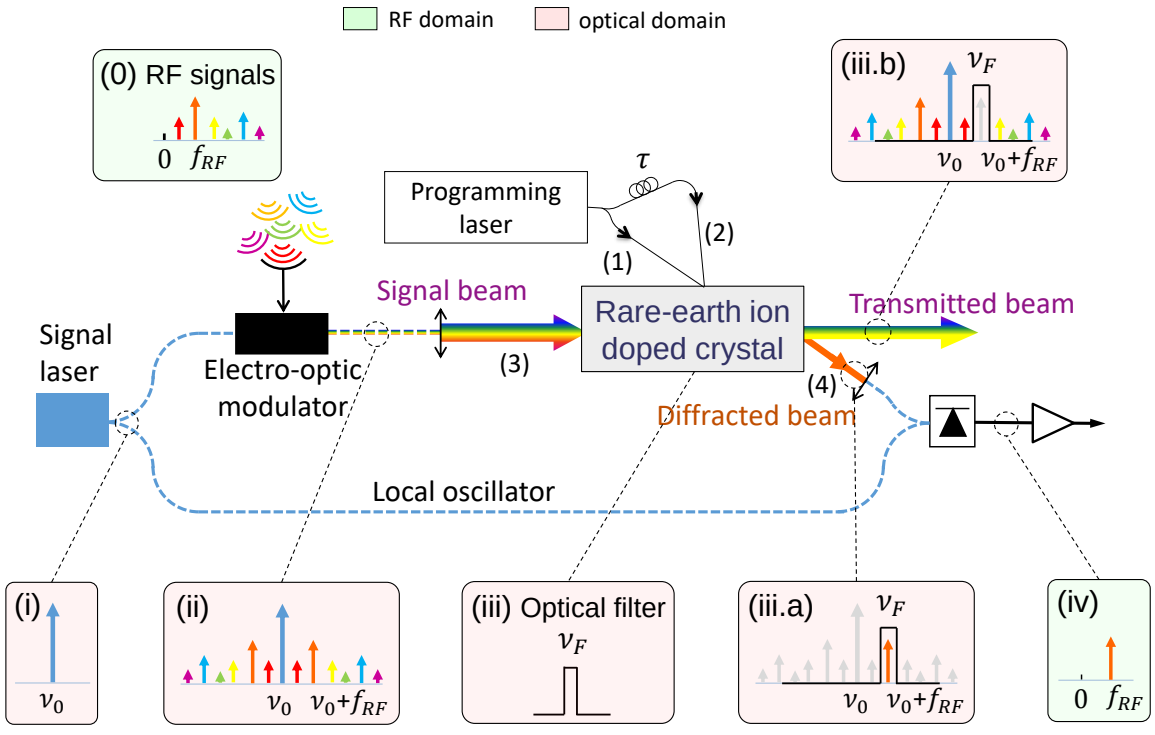

Figure II.2: Principle of the spectro-spatial filter – the RF signals are up-converted to optical frequency via an electro-optic intensity modulator, filtered in the optical domain by the crystal, and demodulated back to RF range by mixing the diffracted beam with a local oscillator on a photodiode. The fibered part is depicted by dashed line and the free space propagation around the crystal by colored arrows.

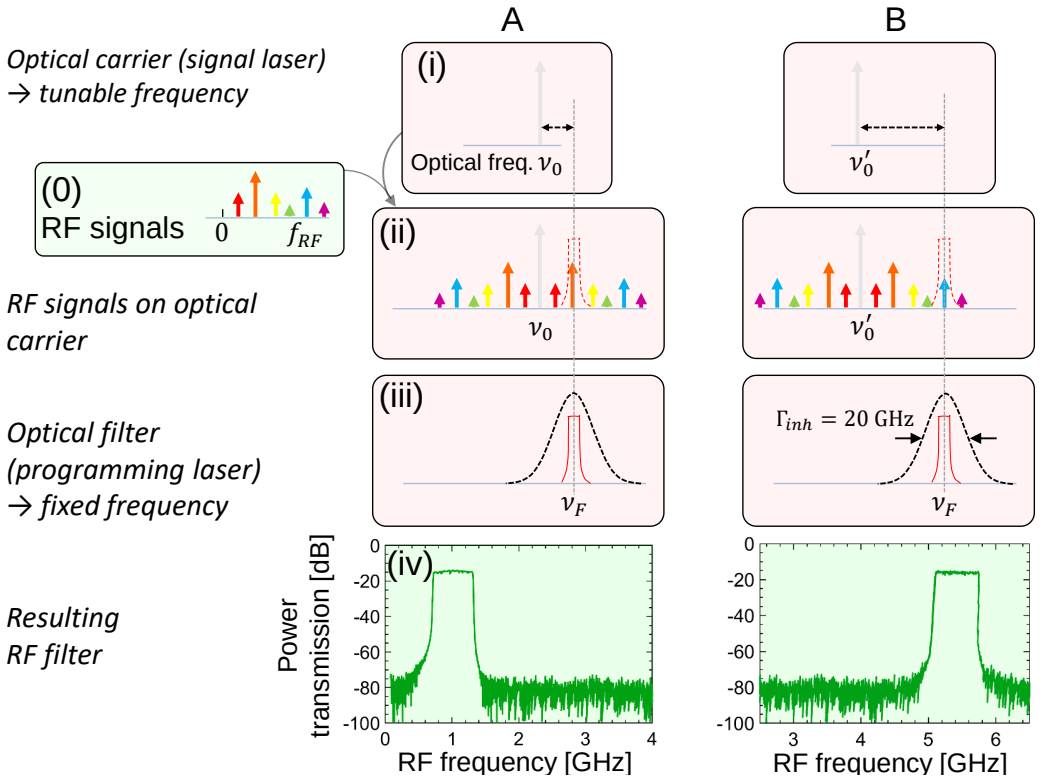

Figure II.3: Tuning the RF filter – the optical filter center frequency ν_F is kept constant at all time. In case A the optical laser frequency is set to ν_0 so that the orange frequency is filtered by the optical filter. If we wish to filter the blue frequency in case B, we shift the optical carrier frequency to ν_0' so that the blue frequency matches the optical filter.

bandwidth, which is finally amplified using a 36 dB electrical amplifier.

The tunability of an RF filter is a very important feature. As described in figure II.3, the center frequency of the RF filter is given by the detuning between the signal laser and the optical filter. The optical filter center frequency ν_F is kept constant at all times. In order to shift the band to be filtered, the signal laser is tuned so that the desired frequency matches the optical filter frequency. The tunability speed of our RF filter is given by the tunability of the signal laser. A tunability speed up to 1 GHz in a few μs has been reached [Kervella et al., 2014] using a commercial laser similar to the one we used. In our experiment, the signal laser slowly drifts with respect to the optical filter frequency at a rate of 10 MHz/s, due to thermal instability, limiting the tuning accuracy of our RF filter. However, a simple locking system of the detuning between the signal and programming laser would allow to cancel this residual drift. The signal laser does not limit the RF filter's tuning range, since it can be tuned over typically 5 THz. In our experiment, the tuning range is first limited by the photodiode to around 20 GHz.

The first difference between the spectro-spatial RF filter and the rainbow spectrum analyzer described in section I.3.2 is that, in the first case, the frequencies are diffracted in a single direction, whereas in the second, the diffraction direction is

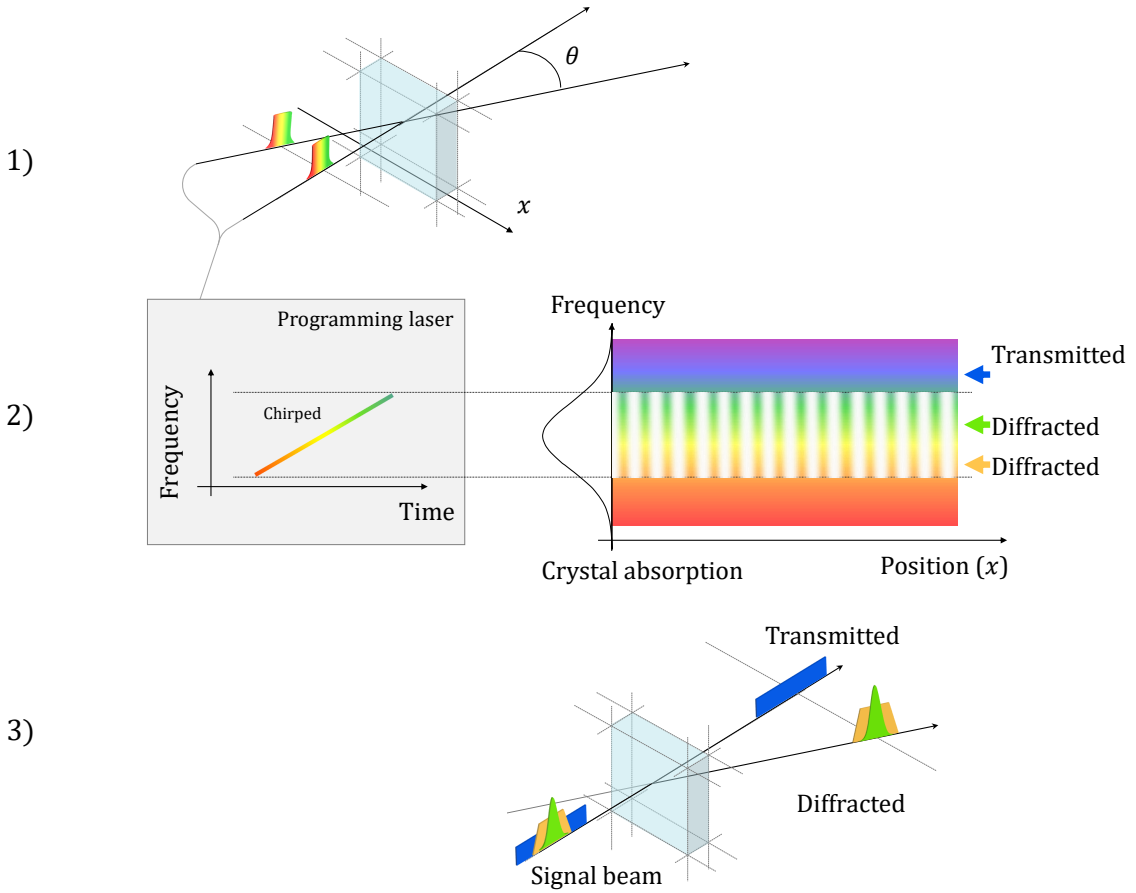

Figure II.4: Programming the optical filter – 1) The programming laser is chirped over the wanted frequency band. It is split in two beams and mixed in the crystal with an angle. 2) The two programming beams make interference fringes along the transverse x axis. The constructive fringes are converted into transmission fringes at the corresponding frequencies by Spectral Hole Burning. 3) Only the frequencies from the signal beam corresponding to the programming chirp (*e.g.* the green and orange signals) experience a spatial grating and are diffracted. The others frequencies (here the blue signal) are transmitted.

spreadout to be imaged on a camera. The second difference is the detection: in the rainbow analyzer, the spatially diffracted optical beams are detected with a camera ; for the filter, we collect and demodulate the single diffracted beam with a photodiode, which provides the complete RF signal (phase and amplitude) with a high signal over noise ratio.

II.2.2 Programming a spectro-spatial grating

The programming stage is described in figure II.4. It relies on the Spectral Hole Burning (SHB) of the crystal, in order to engrave diffraction gratings. The geometry is inspired from traditional frequency-selective holography, described for example in [Shen and Kachru, 1997], but using pairs of linear frequency chirped pulses, such as in [Reibel et al., 2002].

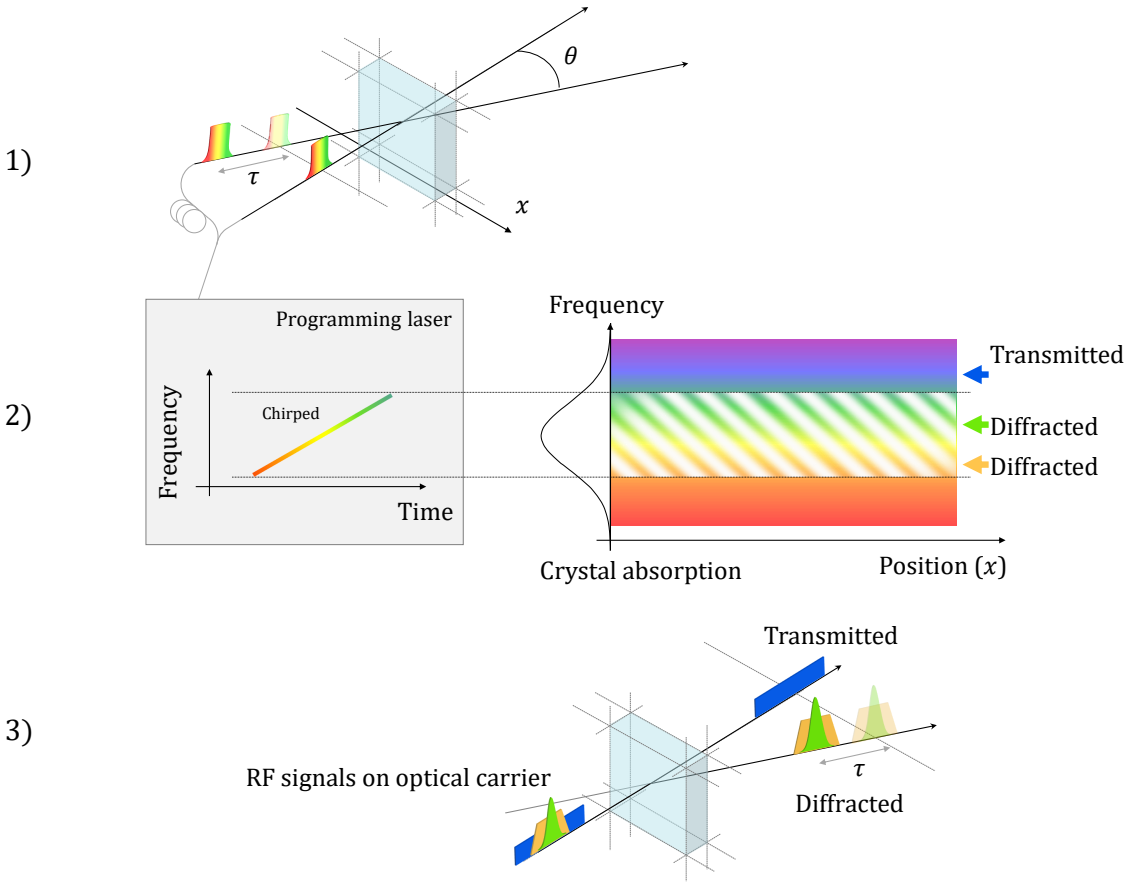

Figure II.5: Programming the optical filter with a programming delay – 1) A delay is added between the programming beams compared to figure II.4. 2) This changes the spatial grating into a spectro-spatial grating. 3) This results in a delay in the diffracted beam with respect to the signal beam.

We make use of a second laser, called the programming laser. We set the programming laser frequency at the center of the 20 GHz inhomogeneous width of the Tm^{3+} optical transition, and we chirp its frequency over the desired filter bandwidth $\Delta\nu$. The programming beam is split into two arms, which are mixed in the crystal with a fixed angle. This creates a spatial interference pattern of illumination in the crystal. Where the spatial intereference is constructive, a hole is burnt in the absorption of the crystal at the specific frequency through Spectral Hole Burning. Where the interference is destructive, the crystal remains opaque. We obtain a periodic modulation of the absorption profile along the perpendicular direction of the beams.

We can then shine the signal beam on the crystal. Only the spectral components of the signal beam within $\Delta\nu$ experience the spatial absorption gratings and are thus diffracted into a different direction: the desired frequencies are spatially filtered out from the signal beam. The other frequencies are simply transmitted, and discarded. Note that the gratings corresponding to each frequency coexist spatially at the same place in the crystal, but they are all independent since they involve different classes of ions.

This principle, described in figure II.4, results indeed in an optical filter. Nevertheless, as we will see in the following sections II.3 and II.4, this will result in a poor quality filter. In order to obtain a good square filter response, it is necessary to add a delay between the two programming beams. If the delay is shorter than the coherence time of the optical transition, the spatial grating from figure II.4 becomes a spectro-spatial grating in figure II.5. This is a so-called photon echo configuration [Lorgeré et al., 2002]: the spectral part of the spectro-spatial grating is equivalent to a time delay. The diffracted beam is now diffracted not only in space, but also in time. It is delayed by the same amount than the programming delay.

A detailed analytical model of the spectro-spatial filter will be presented in section II.4. It will allow to understand the interest of spectro-spatial gratings, compared to only spatial gratings, to obtain the best shape for the spectro-spatial filter. For now, we present a simplified model explaining the principle of spectro-spatial diffraction, and in particular the role of causality.

The variables used in this simple model are depicted in figure II.6.

We describe the crystal as a photorefractive film whose transmission is proportional to the intensity of the light. In this simple model, we consider that the frequency ν of the beams is constant. The programming beams are $E_1(\vec{r},t) = E_0 \exp\left(i\vec{k_1}\cdot\vec{r} - 2i\pi\nu t\right)$ and $E_2(\vec{r},t) = E_0 \exp\left(i\vec{k_2}\cdot\vec{r} - 2i\pi\nu(t-\tau)\right)$. E_2 is delayed by τ with respect to E_1 and propagates along a different direction given by its wavevector $\vec{k_2}$. The optical transmission of the layer is then given by:

$$
\begin{aligned}
H_{\text{opt}}(\vec{r},t) &\propto |E_1+E_2|^2 && \text{(II.1)}\\
&= |E_1|^2 + |E_2|^2 + E_1E_2^* + E_1^*E_2 && \text{(II.2)}\\
&= 2E_0^2 + 2E_0\cos\left((\vec{k_2}-\vec{k_1})\cdot\vec{r} + 2\pi\nu\tau\right) && \text{(II.3)}\\
&= 2E_0^2 + E_0\exp\left(-i(\vec{k_2}-\vec{k_1})\cdot\vec{r} - 2i\pi\nu\tau\right) + E_0\exp\left(i(\vec{k_2}-\vec{k_1})\cdot\vec{r} + 2i\pi\nu\tau\right) && \text{(II.4)}
\end{aligned}
$$

Equation II.3 depicts the spectro-spatial grating. It has a space period $\vec{k}_g = 2\pi/|\vec{k_2}-\vec{k_1}|$ in direction $\vec{k_2}-\vec{k_1}$ (corresponding to direction x in figure II.4 and II.5), and a spectral period $1/\tau$. Let us consider a signal beam with the same frequency than the programming beams: $E_3(\vec{r},t) = E_0\exp\left(i\vec{k_3}\cdot\vec{r} - 2i\pi\nu t\right)$. The output beam is then given by $E_4 = E_3 \times H_{\text{opt}}$. We obtain three contributions:

$$
\begin{aligned}
E_4(\vec{r},t) \propto\ & E_0^3\exp\left(i\vec{k_3}\cdot\vec{r} - 2i\pi\nu t\right)\\
&+ E_0^3\exp\left(i\left[\vec{k_3}-(\vec{k_2}-\vec{k_1})\right]\cdot\vec{r} - 2i\pi\nu(t+\tau)\right)\\
&+ E_0^3\exp\left(i\left[\vec{k_3}+(\vec{k_2}-\vec{k_1})\right]\cdot\vec{r} - 2i\pi\nu(t-\tau)\right) \qquad \text{(II.5)}
\end{aligned}
$$

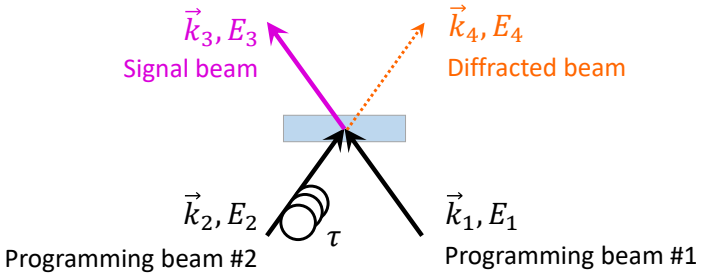

Figure II.6: Illustration of the variables used in the present model (section II.2.2).

The three contributions propagate in different directions, so we can experimentally separate them. We define the orders of diffraction respectively $+1$, 0, -1 by the contribution experiencing a delay respectively $> 0, = 0, < 0$. The first term of equation II.5 is the diffraction of order 0, it is not deviated nor delayed. We cannot observe it in practice since it is overlapped spatially with the transmitted beam. Considering that $\tau > 0$, the second term is the diffraction of order -1, which experiences a negative delay. A negative delay means that it should leave the crystal before the input, which is forbidden by causality. The only contribution that we can use in practice is the third one. It is the diffraction of order $+1$, diffracted in space by the vector $\vec{k}_2 - \vec{k}_1$ and in time by a delay τ. In the following, the "diffracted beam" will refer to this $+1$ order of diffraction allowed by causality.

This simple model provides a first understanding of the phenomenon involved. In reality however, the repartition between orders $+1$ and -1 is not as binary as this simple description suggests. There actually exists a transition zone around $\tau = 0$ where the diffracted power progressively shifts from order $+1$ to order -1. This will be discussed in section II.4, where we develop a more detailed model describing the filter and the crystal response.

We must keep in mind that while time diffraction is constrained to positive delays by causality, spatial diffraction is also constrained by the phase matching condition, which states, as shown above, that $\vec{k}_4 = \vec{k}_3 \pm (\vec{k}_2 - \vec{k}_1)$ [Mossberg, 1982]. The conservation of energy during the diffraction ensures that $\left|\vec{k}_4\right| = \left|\vec{k}_3\right|$. Note that here the signal beam can only be diffracted if it has the same frequency than the programming beams, so $\left|\vec{k}_3\right| = \left|\vec{k}_1\right| = \left|\vec{k}_2\right|$.

Let us consider the simple geometry described in figure II.7 where $\vec{k}_3 = \vec{k}_1$. In case a), beam #2 is delayed by τ with respect to beam #1. As discussed in the previous paragraph, $\vec{k}_4 = \vec{k}_3 + (\vec{k}_2 - \vec{k}_1)$. In our case we obtain $\vec{k}_4 = \vec{k}_2$ so $\left|\vec{k}_4\right| = \left|\vec{k}_2\right| = \left|\vec{k}_3\right|$: the phase matching condition is respected and the diffraction is allowed. In case b) we have switched the delay: now beam #1 is delayed with respect to beam #2. This is equivalent to take $\tau < 0$ in all previous equations. The discussion of the previous paragraph is then reversed and the $+1$ diffraction order is now the second contribution

from equation II.5. We obtain $\vec{k}_4 = \vec{k}_3 - (\vec{k}_2 - \vec{k}_1) = 2\vec{k}_3 - \vec{k}_2$ so $\left|\vec{k}_4\right| \neq \left|\vec{k}_3\right|$. In this case no diffraction can occur because order -1 violates causality, and order $+1$ violates the phase matching condition: both are forbidden.

In the experiments we will always work in configurations similar to a) where the phase matching condition is respected, so that the diffracted beam (order $+1$) can exist.

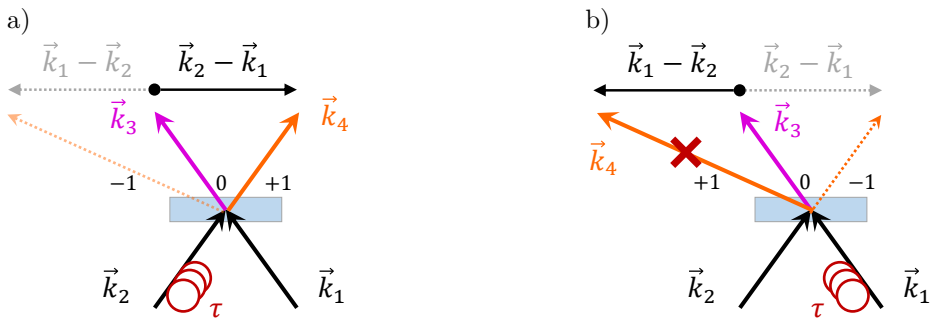

Figure II.7: Illustration of causality and phase matching condition – a) Beam #2 is delayed, so the wave-vector of diffraction $+1$ is $\vec{k}_4 = \vec{k}_3 + (\vec{k}_2 - \vec{k}_1)$. $\left|\vec{k}_4\right| = \left|\vec{k}_3\right|$ so this diffraction is allowed. b) Beam #1 is delayed, so the wave-vector of diffraction $+1$ is $\vec{k}_4 = \vec{k}_3 - (\vec{k}_2 - \vec{k}_1)$. $\left|\vec{k}_4\right| \neq \left|\vec{k}_3\right|$ so this diffraction is not allowed. Dashed arrows show the -1 diffraction order forbidden by causality.

II.2.3 Experimental details

This section is dedicated to provide supplementary experimental details, in order to provide a better view of the experimental setup.

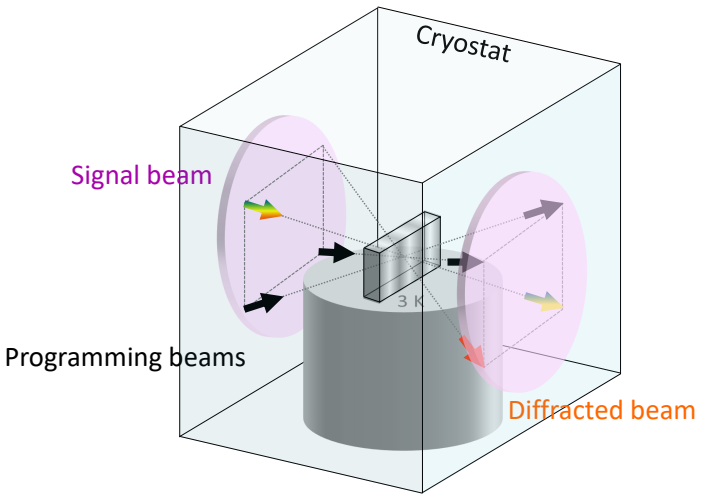

Figure II.8: Geometry of the crystal and the beams in the cryostat – The programming and signal beams enter the cold chamber through an optical lens, and form a rectangle configuration with the diffracted beam.

Figure II.8 depicts the geometry of the beams and the crystal. The Tm^{3+}:YAG crystal is attached to a 3 K cold finger in the cold chamber of a closed-cycle cryostat. Two lenses on opposite sides of the cold chamber provide optical access to the cristal. The two programming beams enter the crystal from two different directions. The signal beam is propagating outside the plane formed by the programming beams, so that the diffracted beam does not overlap with any of the three other beams: the four beams form a rectangle configuration.

The crystal is 3 mm thick, 5 mm tall and 7 mm large. The doping concentration of the Tm^{3+} ions is 0.5 % atomic, resulting in an optical depth $\alpha L = 2$ for the ${}^3H_6 - {}^3H_4$ transition centered at 793.37 nm in vacuum. The optical depth $\alpha L = 1.8$ was found to maximize the diffraction efficiency [Linget et al., 2015]. It is given by a tradeoff, since a thick crystal means a thick grating which diffracts more light, but also means more absorption.

The programming and signal beams enter the crystal in free space with a 0.65 mm $1/e^2$-radius gaussian shape. The horizontal angle between the programming beams is 40 mrad, and the vertical angle between the programming beams and the signal beam is 10 mrad. A magnetic field of 10 to 70 mT can be applied on the sample using a permanent magnet resting on top of the chamber.

From an applicative point of view, the RF filter is required to work continuously, meaning that the spectro-spatial grating must be present at all time in the crystal, in order to filter the signal beam continuously. The lifetime of the grating depends on the shelving state in which the ions are stored. The atomic structure of the thulium ions is recalled in I.11. Without magnetic field, the shelving state is the metastable state ${}^3F_4$, with a lifetime of 15 ms [Basiev et al., 1996]. With a magnetic field, a

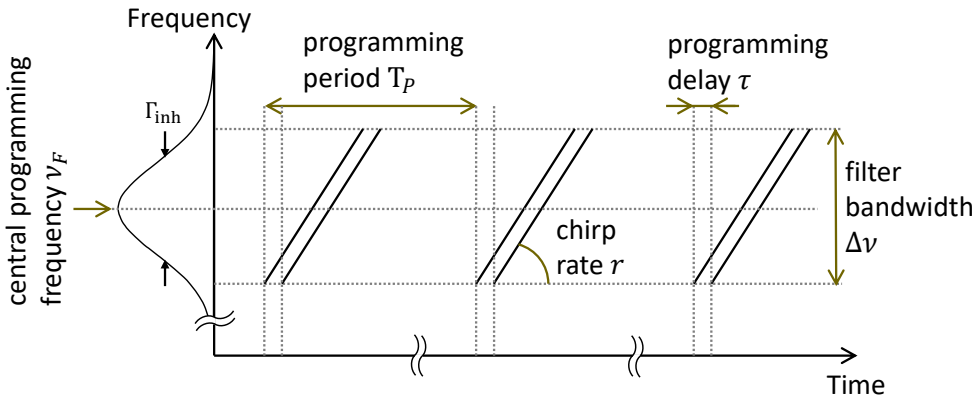

Figure II.9: Chronogram of the programming beams – The two programming beams, separated by a delay τ, are repeated periodically to maintain the spectro-spatial grating in a steady-state. T_P is set to 5 ms, and ν_F is set roughly to the center of the inhomogeneous width. We will vary the other parameters in the following studies.

much longer lifetime can be reached by storing the ions in a ground state Zeeman level. In this case the lifetime is highly dependent on the temperature, and can range from 2 to 20 seconds between 3 and 4 K. A study about the spin lifetime is presented in chapter III.A. In both cases, due to this finite lifetime, it is necessary to send periodically the programming beams in the crystal, in order to refresh the grating and reach a steady state. Figure II.9 presents a chronogram of the programming beams. In our experiment, the programming period is set to $T_P = 5$ ms.

The programming laser is a DFB at 1586 nm. Its frequency is chirped over the desired bandwidth by electrical current modulation. The electrical signal is pre-corrected with the laser response. The reproducibility of the chirp is controlled via a feedback loop, described schematically in figure II.10a. We did not make any major improvement of this feedback loop since its first report in [Kervella et al., 2014].

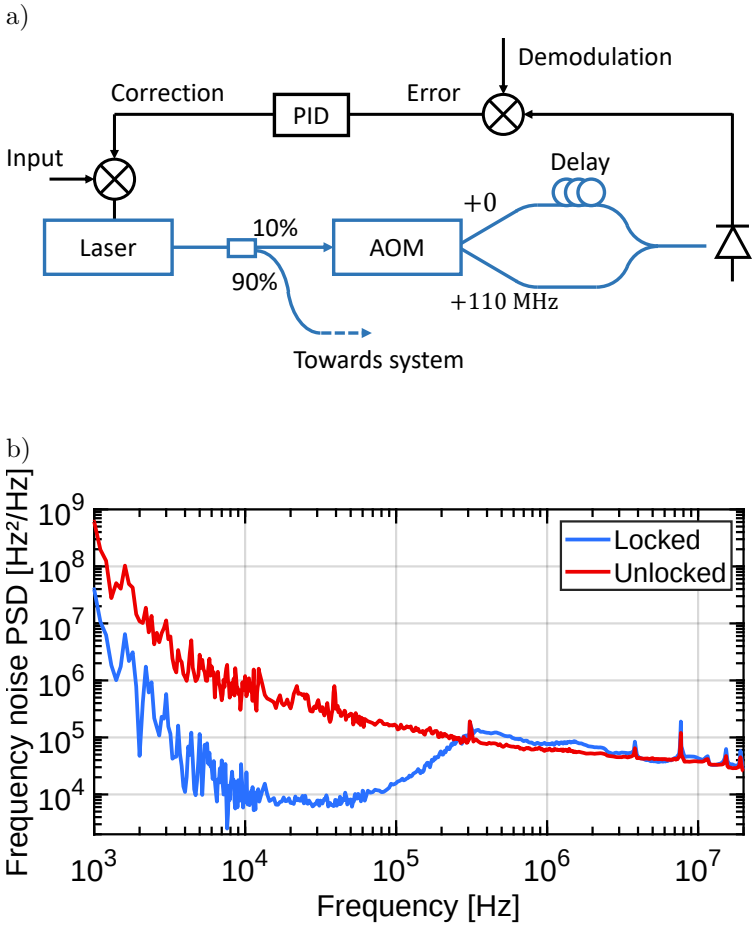

Figure II.10: a) Feedback loop on the programming chirp frequency, based on an imbalanced Mach-Zehnder interferometer – AOM: acousto-optic modulator.

b) Frequency noise of the programming laser with and without feedback loop – The blue curve corresponds to the laser locked to a constant frequency.

10 % of the optical power is used for the frequency lock. It goes through an acousto-optic modulator (AOM) which produces two beams detuned by 110 MHz. These two beams are mixed on a photodiode to measure the instantaneous laser frequency variations. The signal is then demodulated to obtain the error signal, which goes through a PID block before correcting the input signal. The frequency noise of the laser, locked and unlocked, is shown in figure II.10b. With the feedback loop, the instantaneous frequency of the laser varies randomly within 5 MHz around the linear frequency setpoint. The lower limit of the filter's bandwidth is ultimately given by the homogeneous width, but it is limited in practice to 50 MHz due to experimental noises, such as this frequency noise of the programming laser.

II.2.4 Power balance and diffraction efficiency

In this section, we present a power budget of the spectro-spatial RF filter, in order to identify parameters ruling the transmission level of the filter. The complete derivation is presented in appendix A.1. Considering that the RF input voltage is low compared to the modulator RF half-wave voltage V_π, the RF transmission can be written:

$$\frac{P_{\text{out}}}{P_{\text{in}}} \propto P_0^2 \left(\frac{\pi}{V_\pi}\right)^2 Z_{\text{MZM}}\ \eta_{\text{diff}}\ \mathcal{R}_L^2 G R \tag{II.6}$$

where P_0 is the signal beam optical power, Z_{MZM} is the input impedance of the intensity modulator, η_{diff} is the diffraction efficiency of the crystal, $\mathcal{R}_L$ is the photodiode responsivity, G is the post-photodiode amplification and R is the resistive load of the receiver. In our setup $P_0 = 10$ mW, $V_\pi = 1.4$ V, $\mathcal{R}_L = 0.4$ A/W and $G = 36$ dB.

Among all the parameters of equation II.6, the diffraction efficiency η_{diff} is most crucial. Indeed, it is much smaller in practice than expected theoretically.

A model describing the diffraction efficiency was developped in [Linget et al., 2015]. In the case of "large angle" between the two programming beams, defined as angles above 11 mrad, an upper bound to the diffraction efficiency of 11.6% was predicted. In such conditions, a diffraction efficiency of 6.3 % with a 5 MHz-wide grating was demonstrated experimentally [Linget et al., 2015].

Our experiment is similar to this previous demonstration, except for the programming bandwidth which is much larger, between 100 MHz and 20 GHz. We could only reach a diffraction efficiency of 2 % with a bandwidth of 100 MHz, and 0.5% with a bandwidth of 20 GHz. The diffraction efficiency decreases dramatically with the programming bandwidth. It is critical in our experiments, where we adress very large bandwidths. The object of chapter III.A is to investigate this issue, in order to

increase the diffraction efficiency.

II.3 Optimizing the filter shape

In the previous section we have described the architecture of the RF filter, and presented the mode of operation allowing to run the experiment. We will now identify through an experimental study the different parameters ruling the features depicted in figure II.1. The features of interest are the global rejection, given by the maximum of transmission and the noise floor, and the shape of the sides. This parametrical study provides physical understanding of the experiment, and will allow to optimize the filter shape.

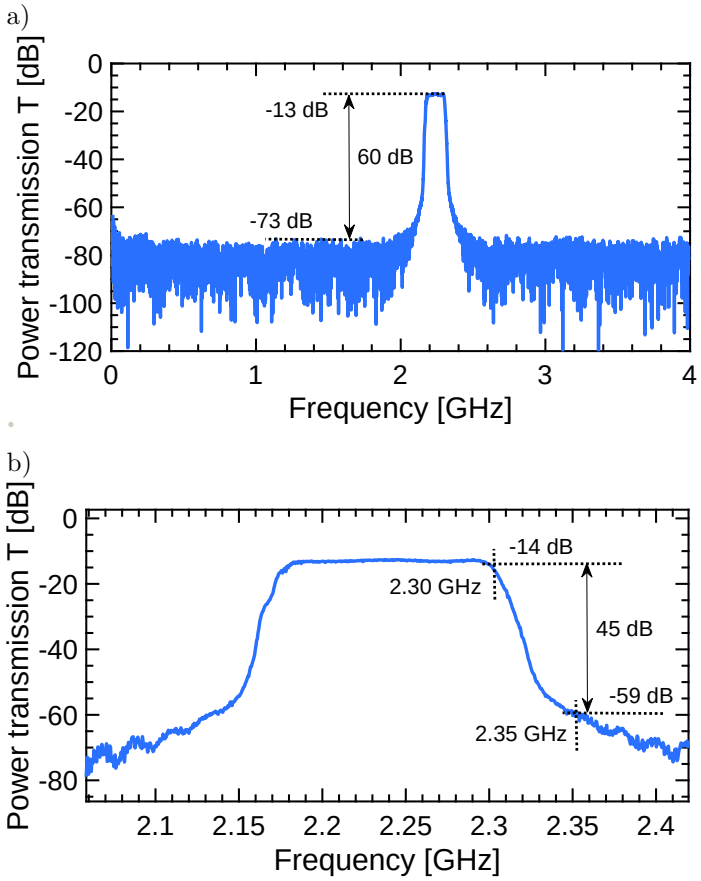

Figure II.11: a) Power transmission T of a 100 MHz wide filter in the best experimental conditions given by our study, providing a remarkable global rejection of 60 dB.
b) Close-up on the filter − the sides are very steep with a 45 dB rejection at 50 MHz from the edge of the filter.

All the experimental curves presented in this chapter are acquired using a Vector Network Analyzer (VNA). This equipment sends a monochromatic RF signal in the input of the system, in our case the electro-optic modulator (see figure II.2). It measures the output signal, here after the photodiode and the electrical amplifier,

specifically at the input frequency, and provides the amplitude ratio and phase difference between input and output. The input frequency is swept slowly over the desired range, with a rate below the kHz. We obtain the transfer function of our system with respect to frequency.

Figure II.11 shows the typical amplitude response of the filter when meeting the optimal conditions given by the study presented in the following. We reach a global rejection of 60 dB, and very steep sides with a rejection of 45 dB at 50 MHz from the edge of the filter. These results are at the state of the art in the field of GHz-wide photonic RF filters (see table II.1).

II.3.1 Magnetic field

Adding a magnetic field dramatically changes the behaviour of the ions. This can be used to improve greatly the diffraction efficiency of the spectro-spatial grating. We will quickly recall the principle, for more detail refer to [Linget et al., 2015]. As described in figure II.12, adding a magnetic field splits both the ground and excited state into two Zeeman levels. Without magnetic field, the storage level allowing to depopulate the ground state is the metastable state, with a 15 ms lifetime. With magnetic field, the storage state is the ground state Zeeman level, with a lifetime ranging from 2 to 20 s (see chapter III.A), much longer than the metastable state. As presented in section I.2.2, if the magnetic field is applied along the [111] axis of the crystal, then all ions are magnetically equivalent and experience the same splitting. Nevertheless, the Zeeman splitting is different for the ground and excited state. The gyromagnetic ratio have been measured [Louchet, 2008] and amount to $\gamma^{(g)} = 329$ MHz/T for the ground state, and $\gamma^{(e)} = 67$ MHz/T for the excited state. In the experiment, the magnetic field is created by a permanent magnet resting on the cold chamber. We can vary the magnetic field by moving the magnet closer or further from the crystal.

At rest, the ions are equally distributed between the ground state Zeeman levels g_1 and g_2. We note Δ_{ge} the splitting difference between ground and excited state under a given magnetic field. It was shown in [Louchet, 2008] that, if the magnetic field is oriented along the [111] axis, then the cross transitions g_1-e_2 and g_2-e_1 are forbidden. As depicted in figure II.13a, due to this splitting difference, there are now two classes of ions resonant with a given laser fequency ν_L: one where the g_1-e_1 transition is resonant (1), and one where the g_2-e_2 is resonnant (2). In class (1), the ions are pumped into the g_2 level, so we create an excess of ions available for the g_2-e_2 transition. The frequency of this transition is $\nu_L - \Delta_{ge}$: we have increased the absorption at this frequency. Similarly in class (2), the ions are pumped into the g_1 level, resulting in an excess of ions available for the g_1-e_1 transition of frequency $\nu_L + \Delta_{ge}$, and the absorption at this frequency is increased.

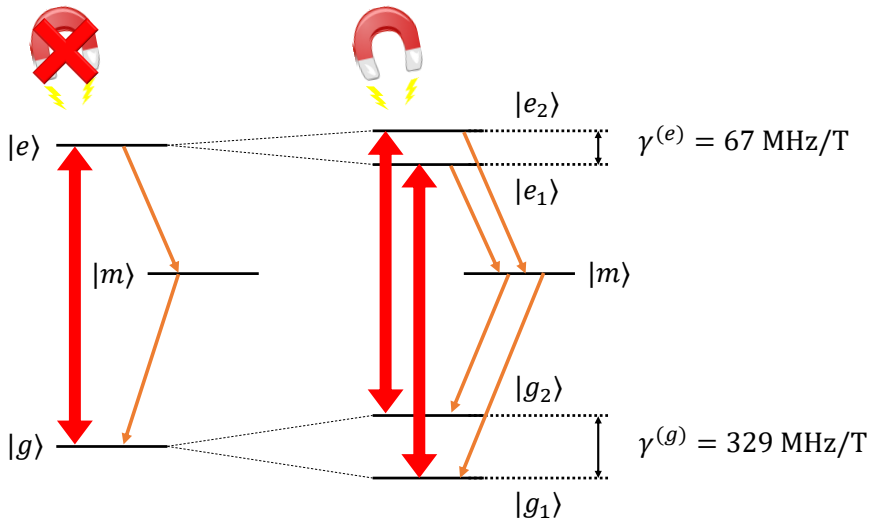

Figure II.12: Simplified energy levels of Tm^{3+} in YAG with and without magnetic field – The Zeeman splitting depends on the magnetic field, with a ratio of $\gamma^{(g)} = 329$ MHz/T for the ground state, and $\gamma^{(e)} = 67$ MHz/T for the excited state.

In a nutshell, with a magnetic field, burning a hole in the absorption profile at frequency ν_L results in two antiholes at frequencies $\nu_L - \Delta_{ge}$ and $\nu_L + \Delta_{ge}$. A typical hole-antihole profile is shown figure II.13b. For more detailed SHB spectroscopy of a Tm^{3+}:YAG crystal under magnetic field, refer to [Attal, 2017] section III.2.3. Note that, in this Λ-scheme with magnetic field, all ions are always in a $^3H_6$ level. So the number of ions optically active for the $^3H_6$-$^3H_4$ transition is conserved, and the mean absorption is constant. In other words, the sum of the areas of the antiholes equals the area of the hole.

We can use this behaviour to increase the constrast of the grating. As mentioned in section II.2, the grating we enscribe in the absorption profile is a sine function of period $1/\tau$. Under magnetic field we can then separate three contributions: the grating corresponding to the hole, and two "antigratings" corresponding to the two antiholes. If the antigratings contribute constructively to the main grating, its contrast is doubled. If they contribute destructively, they cancel out and the resulting contrast falls to zero. We describe this idea in figure II.14a and II.14b. We demonstrate the phenomenon experimentally in figure II.14c. The programming delay is $\tau = 45$ ns, corresponding to a spectral grating of period $1/\tau = 22$ MHz. In the orange curve we apply a magnetic field $B = 42$ mT, resulting in $\Delta_{ge} = (\gamma^{(g)} - \gamma^{(e)}) \times B = 11$ MHz. Here $\Delta_{ge} = 1/(2\tau)$ so the antigratings are constructive with the grating and the transmission level in the passing band is high. In the purple curve we apply a field $B = 84$ mT, resulting in $\Delta_{ge} = 22$ MHz $= 1/\tau$. The antigratings are destructive with the grating and the rejection is lowered by almost 20 dB.

Figure II.15 shows a 1 GHz-wide filter centered at 1 GHz, with or without magnetic field, and with low and high optical programming power. We choose a delay

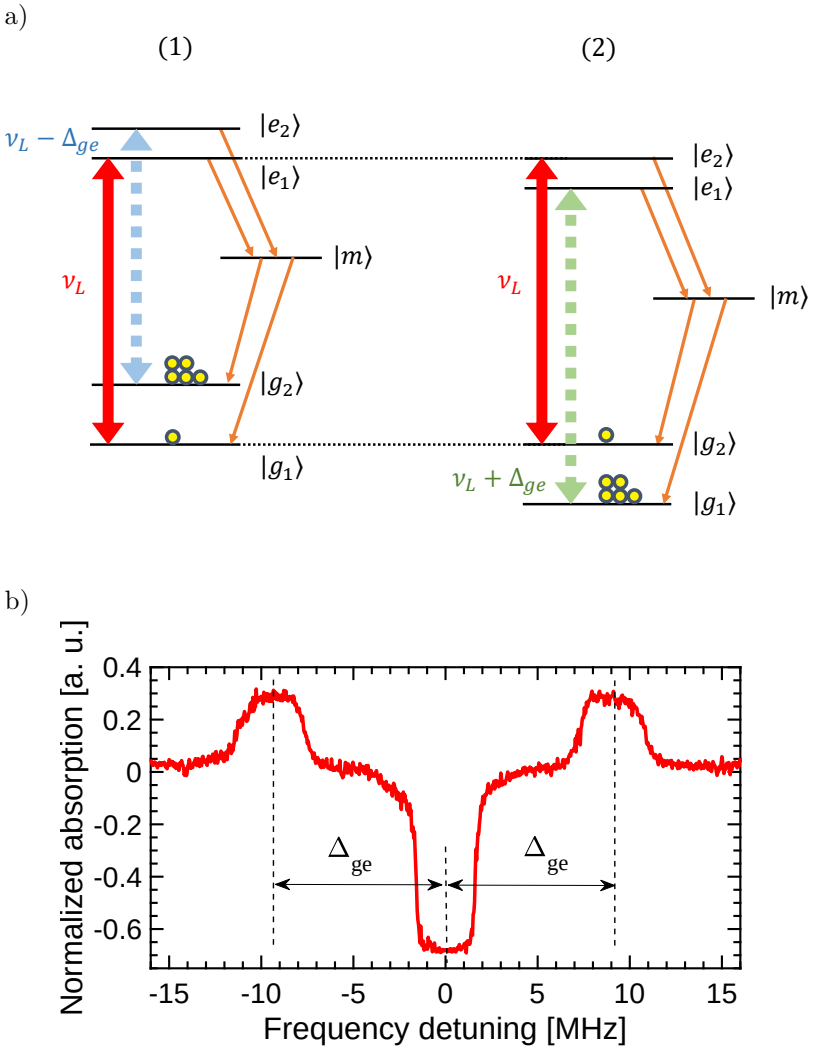

Figure II.13: a) Resonance of the two classes of ions at the same frequency – The excitation at ν_L (red arrow) pumps the ions (yellow circles) from class (1) [resp. class (2)] from $|g_1\rangle$ to $|g_2\rangle$ [resp. $|g_2\rangle$ to $|g_1\rangle$], increasing the absorption of the complementary transition at $\nu_L - \Delta_{ge}$ (blue arrow) [resp. $\nu_L + \Delta_{ge}$ (green arrow)].

b) SHB spectroscopy of the crystal under magnetic field – We plot the difference between absorption after excitation and absorption baseline. The excitation is a square centered around frequency ν_L. Antiholes appear around $\nu_L - \Delta_{ge}$ and $\nu_L + \Delta_{ge}$. The sum of the areas of the two antiholes equals the area of the hole.

of 23 ns with an adapted magnetic field of 83 mT. The magnetic field increases dramatically the transmission of the filter, by enhancing the contrast of the grating and the diffraction efficiency. At a low optical power of 12 mW peak per programming beam, adding a magnetic field increases the transmission by 30 dB (light red and light blue curves). With magnetic field, increasing the optical programming power to 110 mW peak per programming beam does not increase the transmission of the filter: the diffracted power is already maximal at 12 mW peak per programming beam. On the contrary, without magnetic field, increasing the power to 110 mW peak per programming beam dramatically improves the transmission: more optical power is

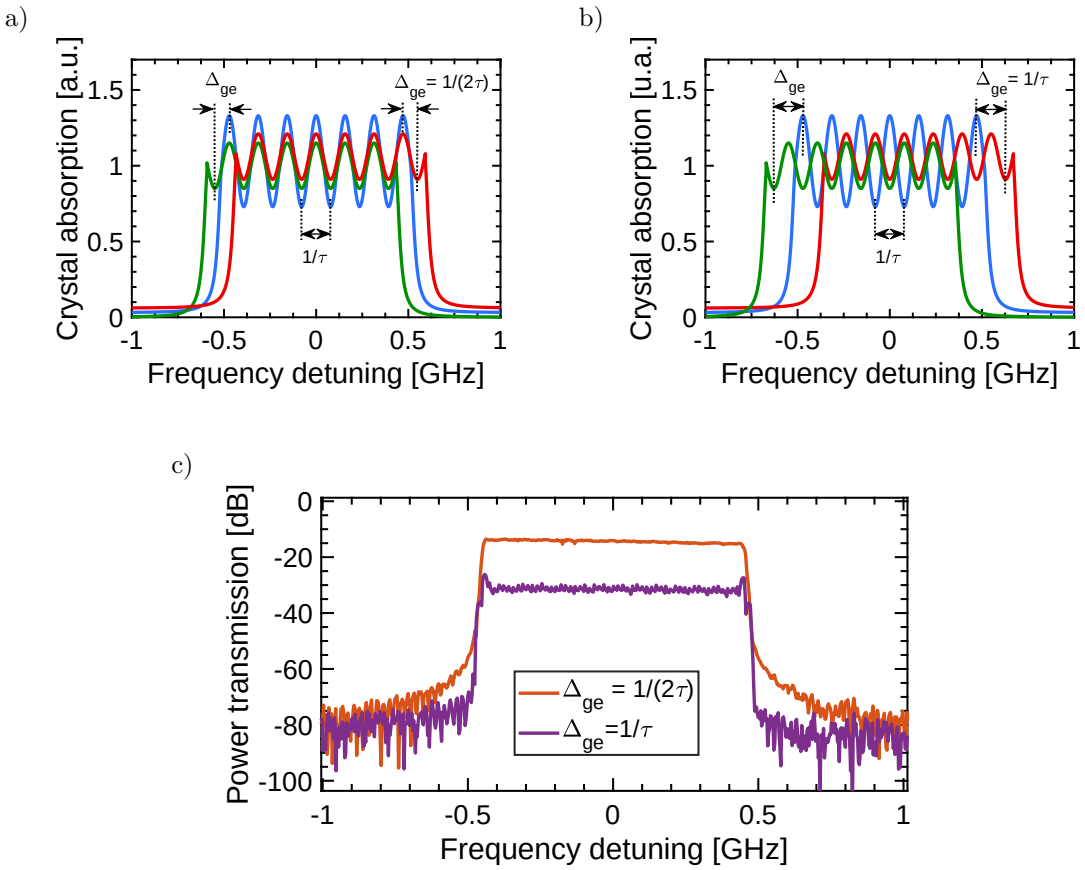

Figure II.14: a) Illustration of the grating (blue) and the antigratings (red and green) – The common period of the grating and the antigratings is $1/\tau$ (not to scale in the figure). When $\Delta_{ge} = 1/(2\tau)$, the antigratings are in phase with the grating. They sum up constructively to produce an overall grating with a doubled contrast. We moved slightly vertically the green and red curves to distinguish them; they have actually the same level.

b) When $\Delta_{ge} = 1/\tau$, the antigratings are in opposition with the grating. They sum up destructively and reduce the contrast to zero.

c) Power transmission of the filter in cases a) and b) – When $\Delta_{ge} = 1/(2\tau)$ (a), the contrast of the grating is high, so the diffraction is strong. When $\Delta_{ge} = 1/\tau$ (b), the contrast of the grating is low, so the diffraction is weak.

required to reach maximal diffraction. This is due to the much shorter lifetime of the storage state in this configuration, which requires to pump the ions at a higher rate, with more optical power. We could not experimentally reach the maximal contrast without magnetic field, as our programming laser was unable to deliver sufficient optical power.

We expect the maximal grating without magnetic field to be at most half of the maximal grating with magnetic field, for the reasons mentioned above. It could be even less due to non linear phenomena occuring at high optical power, such as instantaneous diffusion, as detailed in section III.A.

We observe that, going from 12 to 110 mW with magnetic field makes the sides go

up, degrading the steepness of the filter. Indeed, as discussed later on in section II.3.4, the sides of the filter are caused in this case by the phase noise of the programming laser. In the passing band, the contrast of the grating already is at its maximum with 12 mW. So, when we increase the optical power, the contribution of the noise on the sides goes up, whereas the passing band is already maximal.

We observe small periodic dips on the top of the curves under magnetic field. They are caused by the periodic pumping cycle of the cryostation, inducing vibrations in the whole setup, occuring periodically during the sweep of the VNA. We note also that the lines without magnetic field are much thicker. We believe that this is due to the much shorter lifetime of the storage state in this case, inducing a drop in the grating contrast between each programming repetition. We observe this drop by stroboscopy with the sweep of the VNA.

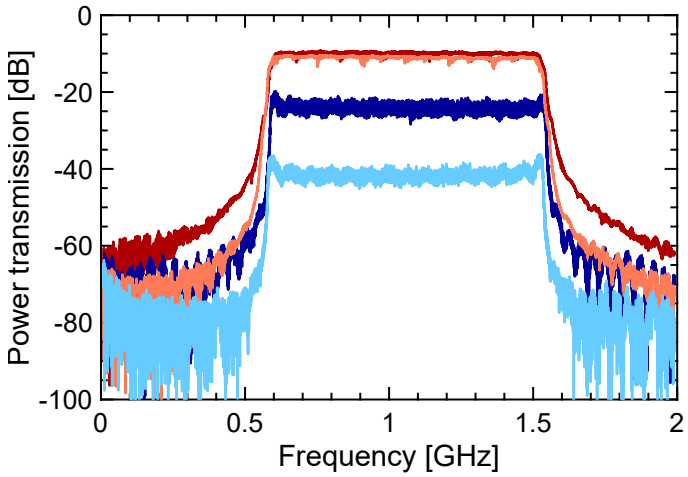

Figure II.15: Influence of the magnetic field – red curves: with magnetic field, blue curves: without magnetic field, dark curve: with high optical programming power (110 mW peak per programming beam), light curves: with low optical programming power (12 mW peak per programming beam).

As the magnetic field increases, the antiholes move further away from the hole. In this case we can observe the two anti gratings outflanking the main grating on the sides, creating "shoulders" as shown in figure II.16. With a 80 mT field, it is clearly visible in the filter side. The edge of the filter and the shoulder are separated by $\Delta_{ge} = (\gamma^{(g)} - \gamma^{(e)}) \times B$. As the magnetic field decreases, the shoulder progressively disappears inside the filter side. For $B \leq 50$ mT, or $\Delta_{ge} < 13$ MHz, or $\tau > 38$ ns, it almost completely overlaps with the side of the filter. The antigratings do not degrade anymore the shape of the filter sides. It was measured that the Zeeman level lifetime is constant above 10 mT [Louchet-Chauvet, 2019] (and up to 500 mT [Veissier et al., 2016]). So in principle we could decrease the magnetic field up to 10 mT without degrading the properties of the filter.

To conclude, adding a magnetic field between 10 mT and 50 mT greatly improves the filter behaviour, if the programming delay is matched according to $\Delta_{ge} = 1/(2\tau)$.

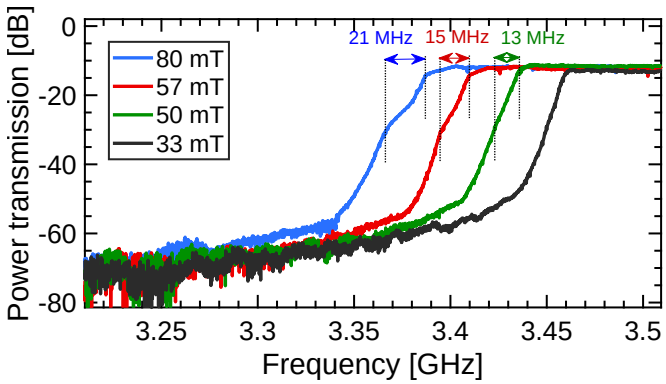

Figure II.16: Edge of the filter under different magnetic fields – We adapt the programming delay for each magnetic field. The separation between the shoulder and the edge matches the expected value of $\Delta_{ge} = (\gamma^{(g)} - \gamma^{(e)}) \times B$ for each magnetic field. The antigrating progressively overlaps with the grating as Δ_{ge} decreases, i.e. as the programming delay increases. In this figure, we have moved each curves horizontally for readability.

The condition $\Delta_{ge} = 1/(2\tau)$ certifies the grating and the antigratings sum up constructively, increasing the maximal contrast by a factor 2. Besides, as shown in figure II.15, applying a magnetic field is particularly attractive in a low power configuration, since it enables a 30 dB gain on the filter maximal transmission. Indeed, since the spin lifetime is much lower than the metastable lifetime, we reach the maximal diffraction with much less optical power. Finally, the condition 10 mT $\leq B \leq$ 50 mT ensures that the field is sufficient to obtain long spin lifetimes, but not strong enough for the antigratings to outflank the filter sides and degrade their shape.

II.3.2 Intensity noise of the signal laser

We saw in the previous section that we can increase the diffraction efficiency by adding a magnetic field, which increases the maximum of transmission in the passing band. In order to enhance the rejection, an alternative is to decrease the noise floor. We show here that the noise floor is limited by the relative intensity noise (RIN) of the signal laser.

Figure II.17b exhibits the noise floor level in the different configurations from figure II.17a. The green curve is obtained by switching off the diffracted beam and the local oscillator. It displays the noise brought by the RF reception chain, i.e. photodiode, amplifier and VNA. The detection of only the local oscillator by the photodiode significantly increases the noise floor (red curve). This curve is essentially an RIN measurement of the signal laser. Adding the diffracted beam, which is the normal configuration of the spectro-spatial filter, does not increase further the noise floor (blue curve). We conclude that the major contribution of the noise floor in our setup is the GHz-range RIN of the local oscillator. This contribution increases the noise floor by at least 20 dB up to 12 GHz, decreasing by the same amount the

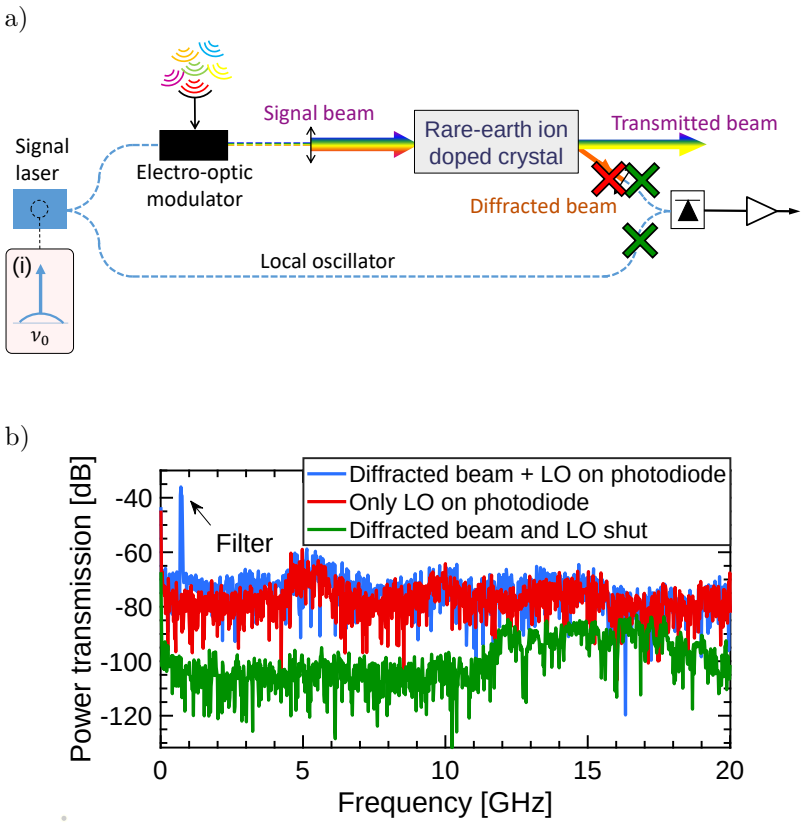

Figure II.17: a) Influence of the RIN of the programming laser – We switch off the diffracted beam and/or the local oscillator. Switching off a link is depicted by a cross, with colors corresponding to the curves in b).
b) VNA measurement with or without diffracted beam and local oscillator.

rejection.

Several techniques already exist to reduce the RIN in lasers. Among them, laser linewidth narrowing has been demonstrated using spectral hole burning in rare-earth ions doped crystals [Thiel et al., 2014b]. The principle is for the laser to cross the crystal, and to self-filter via the spectral hole it creates. This method could be interesting given our similar setup.

II.3.3 Programming delay

In the previous sections we have focused on the rejection of the filter. We have identified how an adapted magnetic field can increase the top of the filter, and how the signal laser intensity noise limits the noise floor. We will now focus on the sides of the filter, and see how we can get closer to a square shape. In this section we investigate the influence of the programming delay (see figure II.5) on the shape of the filter. We perform this study without a magnetic field. Indeed, otherwise we would need to adapt the magnetic field for each delay according to $\Delta_{ge} = 1/(2\tau)$,

which is not feasible for very short delays. Besides, removing the magnetic field allows to get rid of the antigratings, which changes the shape of the filter on the sides as discussed in the previous section.

The delay τ between the two programming beams is a key parameter ruling the shape of the filter. Figure II.18 shows the behaviour of a 100 MHz-wide filter when varying the programming delay. We observe in figure II.18a that with short delays, we parasitely excite ions outside the filter bandwidth: we dramatically degrade the filter rejection up to 35 dB at a few hundreds of MHz from the edge, and the filter top shape is altered. When increasing the delay from 0.1 ns to 48.2 ns, the sides of

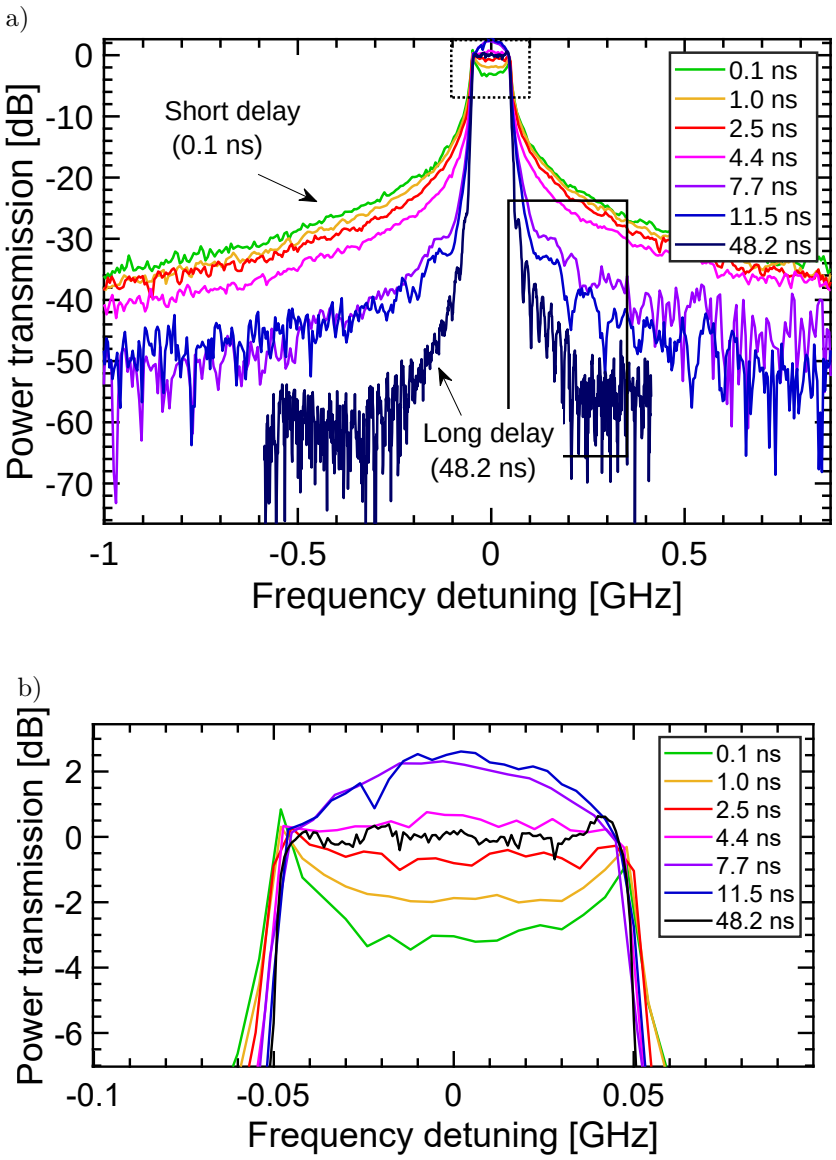

Figure II.18: a) Power transmission for different programming delays – The power transmission is normalized to 0 dB.

b) Close-up on the dashed line square from A (top of the filter).

the filter become progressively steeper. We see in figure II.18b that, in parallel, the filter's top goes from a convex to a concave shape before finally reaching a flat shape.

The physical origin of those peculiar behaviours at short delays is discussed with more detail in section II.4. It is related to causality, which forbids some part of the diffraction at low delay. This results in a diffraction distorted in time, and spectrally broadened.

Note that, fortunately, the two mechanisms that we identified to influence the filter shape – the antigratings outflanking the filter under magnetic field (section II.3.1), and the diffraction delay competing with causality (section II.3.3) – both go in the same direction: increasing the programming delay improves the filter shape.

II.3.4 Phase noise of the programming laser

We observe experimentally that for delays longer than 48 ns, the steepness of the sides does not increase anymore with the programming delay (data not shown). We conclude that, above this delay, another phenomenon limits the shape of the sides.

In figure II.18a we observe oscillations in the tails of the filter for $\tau = 11.5$ and 48.2 ns. Figure II.19a is a close-up on these oscillations (full line squared area from figure II.18a). The period of the oscillations is $1/\tau$, reminiscent of the phase noise of a laser filtered by an interferometer [Tkach and Chraplyvy, 1986]. This suggests that, at large delay, the steepness of the sides is limited by the phase noise of one of the lasers.

In our experiment, two lasers interact with the crystal: the programming laser and the signal laser. Each one travels through its own interferometer. We can identify the laser in cause by identifying the interferometer.

The interferometer of the signal beam is the one that demodulates the diffracted beam with the local oscillator (see figure II.2). The delay of this interferometer is its own physical delay, plus the programming delay τ experienced by the diffracted beam. We verify experimentally in figure II.19b that the period of the oscillations does not depend on the delay of this interferometer.

So, the oscillations are given by the intereferometer of the programming beam, and not of the signal beam. We conclude that the phase noise of the programming beam is limiting the steepness of the sides at large programming delay. As we will see in section II.4.5, this is in accordance with our analytical model of the spectro-spatial filter.

So, in practice, a delay of 48 ns, i.e. 10 m of optical fiber, provides the best achievable shape given our current setup. This delay results in the remarkable rejection of 45 dB at 50 MHz from the edge.

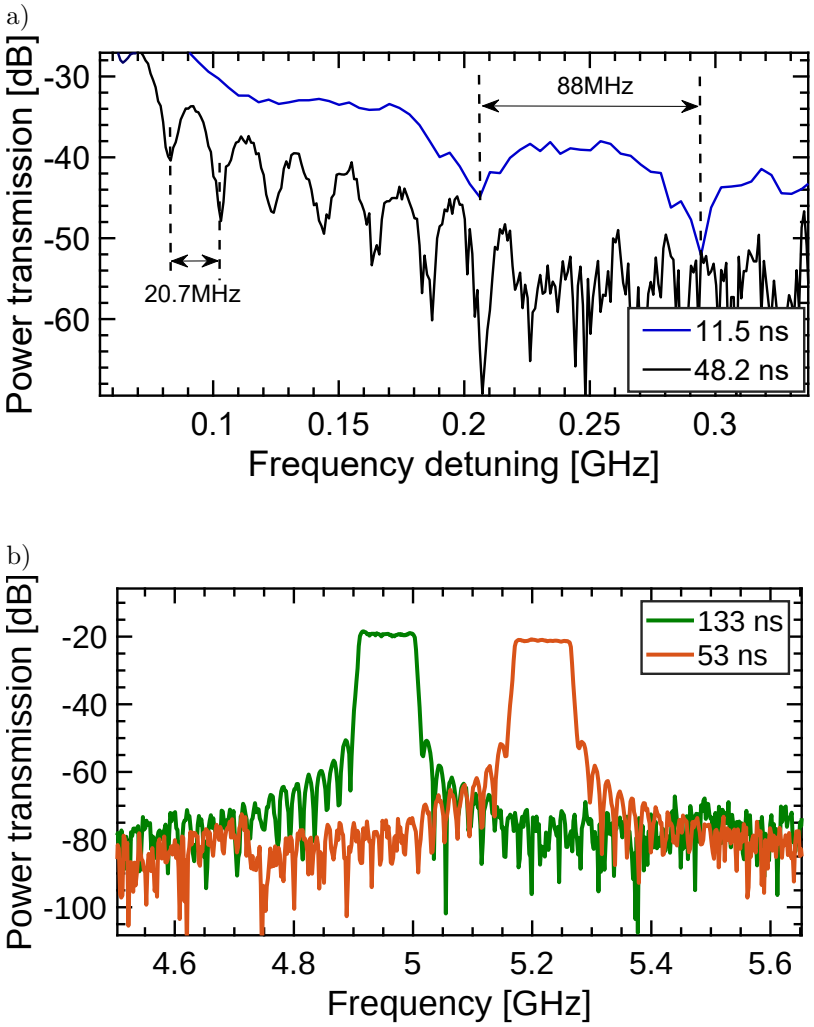

Figure II.19: a) Influence of the programming delay τ – This figure is a close-up on the tail of the 11.5 ns and 48.2 ns filters from figure II.18a (full line square). The period of the oscillations is $1/\tau$.

b) Influence of the demodulation delay – the period of the oscillations in the tails is not changed, even when increasing the demodulation delay by more than a factor 2. We changed the center frequency between the two experimental acquisitions for readibility.

II.3.5 Conclusion of the experimental study

We have identified the different parameters ruling the filter shape and rejection. Figure II.1 depicted the features of interest of an RF filter. In figure II.20 we emphasize the different parts of the same curve, and associate the parameter ruling each region.

We identified the diffraction efficiency as a critical parameter to increase the rejection. We have seen that adding a correct magnetic field increases largely the diffraction efficiency.

The noise floor is given by the RIN of the signal laser, directly captured by the

photodiode via the local oscillator. This RIN also directly limits the global rejection of the filter.

The sides of the filter are first given by the programming delay. More details on the underlying phenomenon are given in next section. If we increase the programming delay, thus making the sides steeper, we ultimately get limited by the phase noise of the programming laser, which engraves gratings outside the desired frequency band. Antigratings caused by the magnetic field can also degrade a bit the filter shape by adding small shoulders close to the edge of the filter.

In conclusion, in order to enhance the filter rejection and steepness, we must work to improve the diffraction efficiency, reduce the signal laser intensity noise, and the programming laser phase noise.

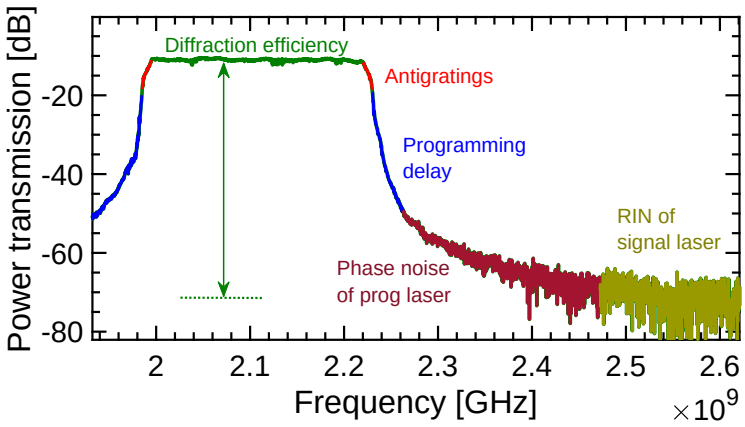

Figure II.20: Identification of the different regions of an spectro-spatial RF filter, and the parameters in cause.

II.4 Analytical model

To get more insight on the filter shape and to understand the influence of different parameters mentioned above, we developed a theoretical semiclassical approach using the Optical Bloch Equations and the wave equation. We derive the transfer function of the filter under the hypothesis of optically thin crystal and short excitations compared to the excited state lifetime T_1.

Note that the hypothesis of short excitation compared to the excited state lifetime is valid, although the excitation chirp typically lasts 2 ms $\gg T_1 = 685$ μs. Indeed, the chirp only interacts with an ion over its homogeneous linewidth $\Gamma_h = 10$ kHz. So, even with a chirp as slow as 100 MHz in 2 ms, the interaction time actually is 2 ms/100 MHz$\times$10 kHz $= 20$ μs $\ll T_1$.

The complete demonstration of the model is presented in appendix A.2. We find that the spectro-spatial filter is a convolution filter: in frequency domain, the output

is the product of the input with a transfer function H. The transfer function of the spectro-spatial RF filter is given by:

$$H(\nu') \propto \left[\left(|\tilde{A}_1|^2 e^{2i\pi\nu\tau}\right) \otimes \mathcal{L}_h \otimes \mathcal{L}_h \otimes \tilde{Y}\right](\nu) \tag{II.7}$$

where ν is the RF frequency, $\nu' = \nu + (\nu_F - \nu_0)$ with ν_F is the central optical frequency of the filter, and ν_0 the signal laser frequency, $\tilde{f}$ the Fourier transform of f, $\mathcal{L}_h$ the lorentzian homogeneous lineshape of the optical transition ${}^3\mathrm{H}_6 - {}^3\mathrm{H}_4$ of Tm^{3+}, Y the Heaviside function, and τ is the programming delay. $\otimes$ stands for the convolution product.

A_1 is the complex amplitude of the electric field of the first programming beam $E_1(t) = A_1(t)e^{i(\vec{k}_1\cdot\vec{r}-\omega t)}$. We remind the reader that the second programming beam is a replica of the first pulse, delayed by τ and propagating along the wavevector $\vec{k}_2$. As described in section II.2, we program the crystal using a chirp. So we will consider an excitation with the form $A_1(t) = e^{2i\pi r t^2/2} \times \mathrm{rect}(t)$, where r is the chirp rate, and rect() is a rectangle function delimiting the start and the end of the chirp in time. A_1 can also include phase or intensity laser noise, but we will not consider any noise here, except in section II.4.5.

Equation II.7 provides an intuitive understanding of the filter response. The response is given first by the programming excitation $|\tilde{A}_1|^2 e^{2i\pi\nu\tau}$. This excitation is the power spectral density of the programming beam amplitude, multiplied by a complex exponential. The exponential expresses the diffraction delay, or equivalently the spectral grating, result of the coherent application of the two delayed beams. The excitation is convoluted twice by the homogeneous linewidth $\mathcal{L}_h$ – once for the programming step, once for the read-out – and convoluted by the Heaviside function Y expressing causality. The power transmission of the filter is given by $T = |H|^2$.

In figure II.21 we compare the model with experimental measurements. We plot in dashed line the experimental curves from figure II.18 for three delays: 2.5 ns, 11.5 ns and 48.2 ns. We plot in full line the analytical model in the corresponding conditions. We can compare the overall shape between experiment and model in figure II.21a. We focus on the passing band on the top of the filter in figure II.21b. The model is in excellent agreement with the experimental curves, despite a weak discrepancy on the wings of the filter for lower delays, for example 2.5 ns. To perfectly match the wings for small delays, the model should be fed with a delay approximately 1 ns larger than the experimental delay. The passing band is perfectly described, even regarding the small oscillations observed at 48.2 ns.

Note that, as mentioned in section II.3.4, the oscillations on the wings are caused by the phase noise of the programming laser. They do not appear here as we have

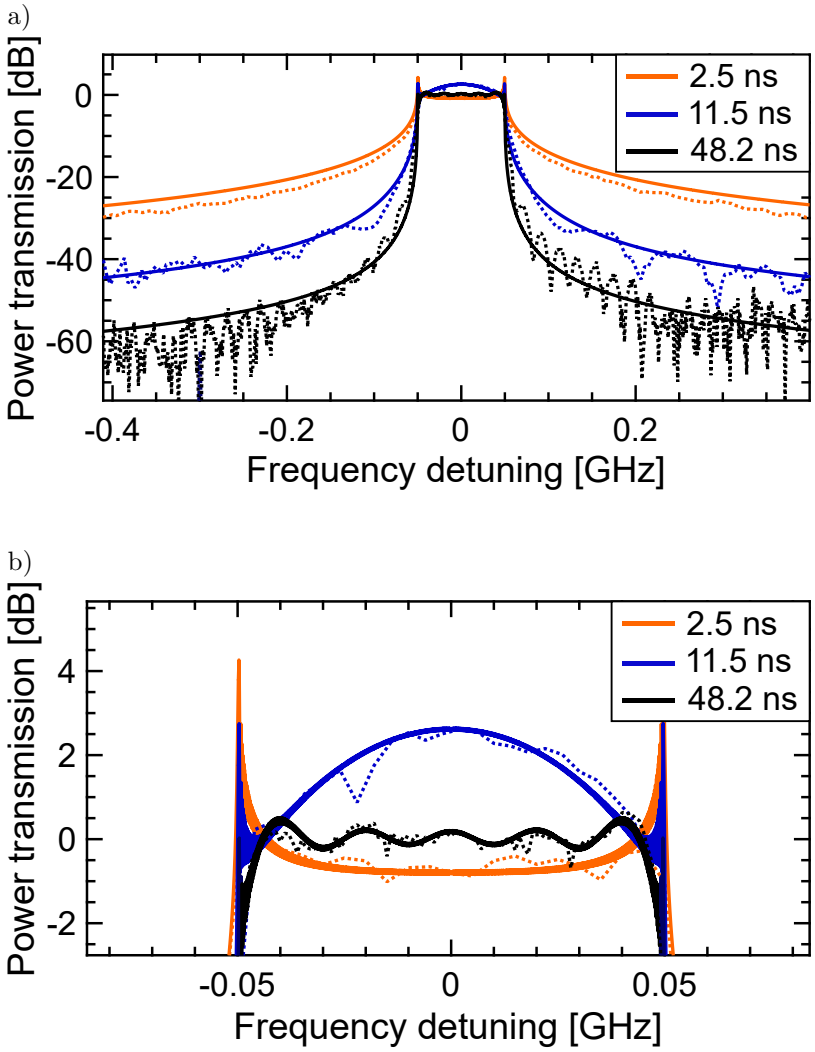

Figure II.21: a) Experimental (full line) and theoretical (dashed line) normalized power transmission T for three curves from figure II.18: 2.3 ns (orange), 11.4 ns (blue), 48.3 ns (black);
b) Close-up on the top of the curves from a).

not included any laser phase noise in the model yet. This point will be discussed in section II.4.4.

The agreement between the model and the experiment is very convincing, so we consider that we can use the analytical model to physically understand different aspects of the behaviour of the filter.

II.4.1 Impulse response

In section II.3.3 we have observed experimentally a dramatic broadening of the filter, in the case of short programming delays. In this section we will use our analytical

model to understand this peculiar behaviour. In order to get more insight on the effect of the programming delay τ, we start from equation II.7. The programming excitation $|\tilde{A}_1|^2 e^{2i\pi\nu\tau}$ is made of two parts:

- $\tilde{A}_1$ is a chirp in our case, with a bandwidth > 10 MHz , typically of the order of several GHz.
- $e^{2i\pi\nu\tau}$ describes the spectral grating, result of the coherent excitation by the two delayed pulses. We work with delays typically < 100 ns, so the spectral period is $1/\tau > 10$ MHz.

The 10 kHz homogeneous linewidth of the optical transition is much narrower than these two features, so we can actually neglect the convolution by the lorentzian lineshapes $\mathcal{L}_h$ in II.7. We obtain:

$$H(\nu') \propto \left[\left(|\tilde{A}_1|^2 e^{2i\pi\nu\tau}\right) \otimes \tilde{Y}\right](\nu) \tag{II.8}$$

The impulse response, characteristic from a filter, is defined as $h = F^{-1}[H]$, where F is the Fourier transform operator. We obtain:

$$\boxed{h(t) \propto F^{-1}\left[|\tilde{A}_1|^2\right](t-\tau) \times Y(t)} \tag{II.9}$$

We see in equation II.9 that the response of the filter is ruled by the function $F^{-1}\left[|\tilde{A}_1|^2\right]$. This formula is very general and applies to any shape of programming pulses. We can apply it to our specific case, where we program the filter using chirps of bandwidth $\Delta\nu$: the power spectral density $|\tilde{A}_1|^2$ of the programming field is essentially a square of width $\Delta\nu$, and $F^{-1}\left[|\tilde{A}_1|^2\right]$ is cardinal sine of width $1/\Delta\nu$. So, in our case, the impulse response is a cardinal sine function, delayed by τ, and truncated at $t = 0$ by the Heaviside function. We can distinguish two cases, depicted in figure II.22:

- If τ is shorter than the duration of $F^{-1}\left[|\tilde{A}_1|^2\right]$, *i.e.* $\tau \ll 1/\Delta\nu$ in our case, then the Heaviside function Y truncates it from $t = 0$. The causality only gives access to the part of $F^{-1}\left[|\tilde{A}_1|^2\right]$ contained in positive times. This truncation results in the spectral broadening observed in figure II.18.
- When τ exceeds the duration of $F^{-1}\left[|\tilde{A}_1|^2\right]$, *i.e.* $\tau \gg 1/\Delta\nu$ in our case, its domain is fully contained in the positive times. We can then discard Y, and equation II.8 becomes:

$$H(\nu') \propto |\tilde{A}_1|^2(\nu) \times e^{2i\pi\nu\tau} \tag{II.10}$$

The transmission is then given by the power spectral density of the programming field $|\tilde{A}_1|^2$, delayed by τ.

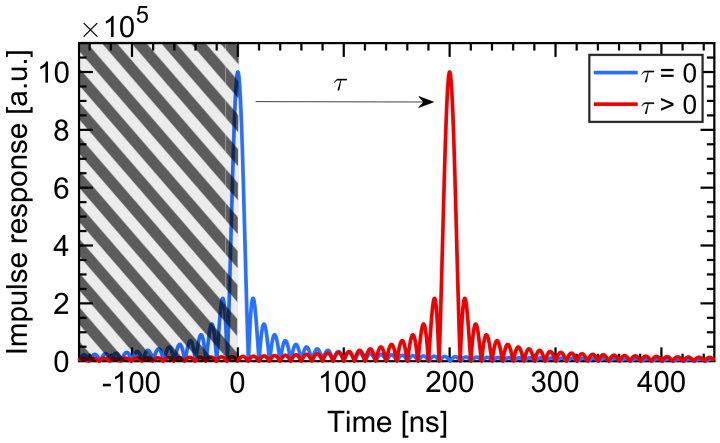

Figure II.22: Impulse response of a 100 MHz filter – $F^{-1}\left[|\tilde{A}_1|^2\right]$ is a cardinal sine of width 1/100 MHz = 10 ns. Only the part of this function contained in positive time contributes to the impulse response. The truncation at $t = 0$ results in the spectral broadening of the shape of the filter for short delays.

This phenomena can be understood physically as follows: because of the dynamics of the system, in particular its spectral response, the output of an impulse input is not an impulse, but is broadened in time. If the output is not delayed with respect to the input, some part of the output is then supposed to exit the system before the input. This uncausal part is physically forbidden. The output is then truncated, and its spectral counterpart, the filter response, is broadened.

In our case, thanks to the long coherence time of the optical transition, we can impose a delay to the output with respect to the input (see figure II.5). If this delay is longer than the duration of the impulse response, then the latter is entirely contained in positive time. It is not truncated, and the shape of the filter is not limited by causality anymore: the amplitude of the transmission is only given by $|\tilde{A}_1|^2$. For long delays, we are then limited by the quality of the programming pulse A_1, and in particular by the programming laser phase noise, as mentioned in section II.3.4.

In our case A_1 is a chirp, so $|\tilde{A}_1|^2$ is close to a square, whose width is the chirp bandwidth. So $F^{-1}\left[|\tilde{A}_1|^2\right]$ is a cardinal sine function, as we can see in figure II.22, and its characteristic duration is the inverse of the filter bandwidth.

Note that this relation between impulse response and output delay is not specific to the spectro-spatial filter. We can mention for example the Bragg gratings, where the output delay is given by the length of the grating. It was shown, for example in [Shekar et al., 2021], that as the length of a Bragg grating increases, the filter amplitude, given by the reflectivity, increases. The longer the grating, the steeper and more efficient the filter. It is rather intuitive in a Bragg grating, since as the

length increases, the light crosses more oscillations of the refractive index and is more filtered.

II.4.2 Programming delay

As we saw experimentally in figure II.18, the programming delay τ impacts both steepness of the sides of the filter, and the flatness of the its top. The analytical model allows to observe these phenomena more precisely.

Figure II.23 depicts the influence of the programing delay. Figure II.23a shows the filter's top when varying this delay. As the delay increases, oscillations appear on the top. Their amplitude progressively decrease, until the top becomes flat. In fig-

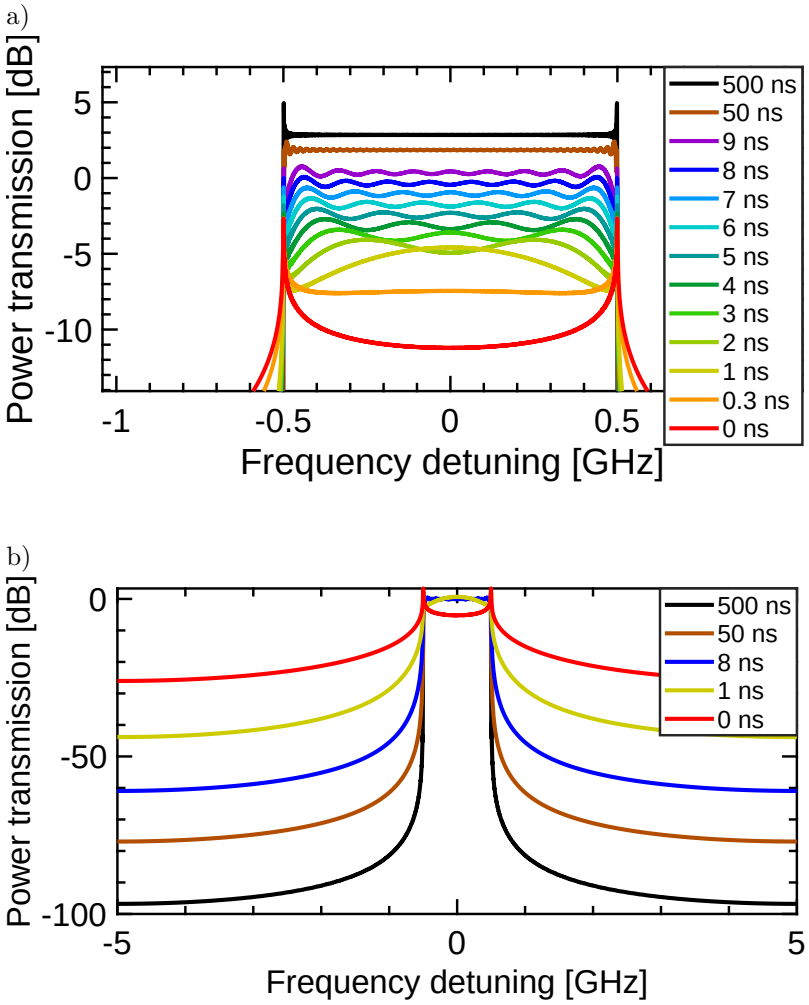

Figure II.23: a) Top of 1 GHz filters for different programming delays – For readability, in this figure only, the level of each curve has been changed to separate the curves vertically. As the delay increases, oscillations appear and their amplitude decrease, until the top of the filter becomes completely flat.

b) Overall shape for five curves from a) – Here the level of the curves is not modified.

ure II.23b we plot the overall shape of five filters from the upper figure for comparison. As mentioned before, as the delay increases, the filter's sides become steeper.

In the case of the 1 GHz filter from figure II.23, a 50 ns delay provides a satisfactory shape, with a deviation on the top of the filter below 1 dB and a rejection of 45 dB at 50 MHz from the edge.

II.4.3 Filter bandwidth

In the previous section we saw that a 50 ns programming delay provides a satisfactory shape for a 1 GHz filter. However, this value depends on the filter bandwidth. As depicted in figure II.24, the shape of the filter is actually given by the product [programming delay × filter bandwidth]. From figure II.24a to II.24b to II.24c we successively increase the bandwidth by a factor 10, while decreasing the delay by a factor 10. We observe that the shape of the the filter is unchanged, except for the filter bandwidth that is increased. Figure II.24c is slightly different due of numerical errors, because the delays are close to the numerical time step.

This behaviour is actually expected from the impulse function $F^{-1}\left[|\tilde{A}_1|^2\right]$ derived in section II.4.1. The duration of the cardinal sine impulse function is directly given by 1/bandwidth. So the shorter the bandwidth, the longer the impulse response, and longer delay is required to shift it entirely in positive time domain.

In practice, this property implies that, in order to work with a range of different bandwidths, it is necessary to use a programming delay providing a satisfactory shape for the smallest bandwidth.

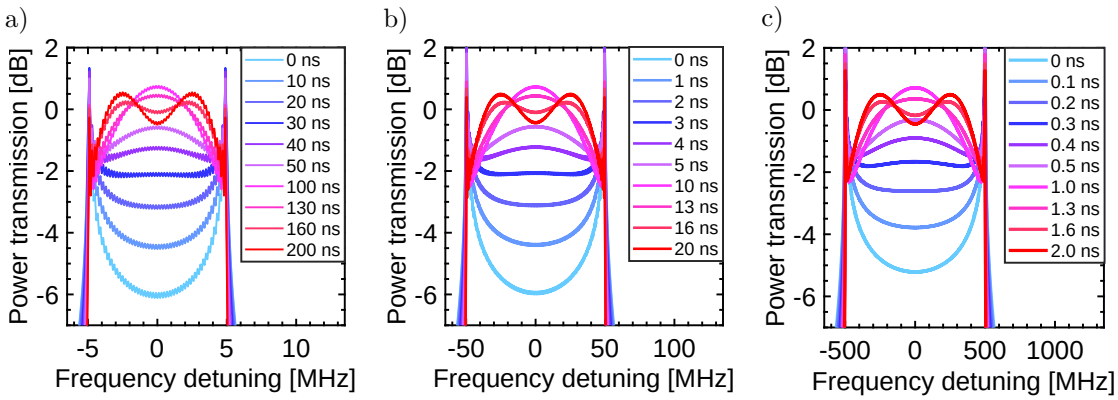

Figure II.24: Shape of the filter given by the product bandwidth × delay – In b) we have increased the bandwidth by a factor 10 and decreased the delay by a factor 10 with respect to a). Same operation for c) with respect to b). We observe qualitatively that the shape is identical in the three situations, except for the horizontal dilatation given by the filter bandwidth.

II.4.4 Time shape of the programming pulse

From the previous discussions, for exemple equation II.8, we see that the programming pulse A_1 only intervenes through its power spectral density $|\tilde{A}_1|^2$. In our experiment, a chirp is used to write the spectro-spatial grating. However, any excitation with the same power spectral density $|\tilde{A}_1|^2$ would result in the same transfer function.

We chose to program the crystal using chirps, because of the versatility of this method: we can choose precisely the frequency bands, pulse duration, etc. Interestingly, for a given bandwidth, the duration of the chirp, or equivalently the chirp rate, does not influence the filter shape. As illustrated in figure II.25, those parameters only influence the level of the filter, but not its shape. Indeed, in the hypothesis of low optical power, a slower chirp means more optical power deposited for each class of ion, so a higher grating contrast and higher diffraction.

The level of the filter is actually given by the mean optical power. The result would be identical by increasing the programming optical power or the repetition rate. Note however that this is only true at low optical power. Indeed, the model is derived in a perturbative regime, without saturation. In practice the level does not increase since we already reach the maximal contrast, as seen previously in figure II.15.

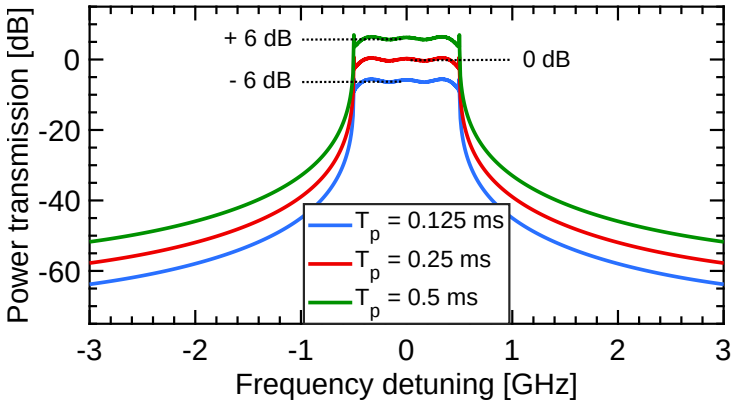

Figure II.25: Influence of the programming chirp duration T_p – At constant bandwidth, T_p, or in an equivalent manner the chirp rate, does not change the filter shape, but only the level. If the pulse duration is doubled, each class of ions receives twice as much optical power. The transfer function H is then doubled, so the power transmission $|H|^2$ is multiplied by a factor 4, hence the 6 dB increase.

II.4.5 Phase noise of the programming laser

Finally, we include the programming phase noise in the model. We now write $A_1(t) = e^{2i\pi rt^2/2} \times \mathrm{rect}(t) \times e^{i\phi(t)}$.

According to its specifications, the linewidth of our programming laser is of the order 500 kHz. In first intent, the phase noise of a laser can be approximated by a random phase walk, which results in a lorentzian spectrum. So, we take $\phi(t)$ as a random phase walk, resulting in a lorentzian laser lineshape of 500 kHz. In figure II.26a we compare the model, including the programming phase noise, with the experimental 48 ns curve from figure II.18. The period of the oscillations on the tails is perfectly reproduced, and the amplitude is similar.

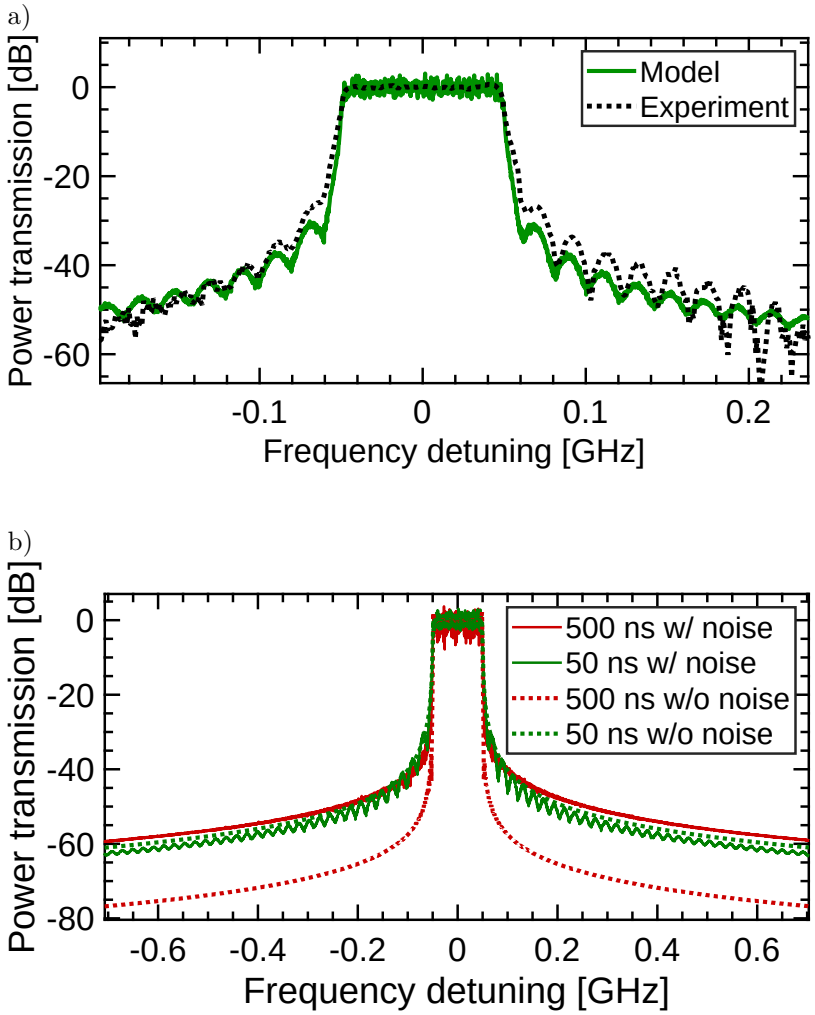

Figure II.26: a) Comparison between experiment and model with phase noise
b) Influence of the programming phase noise at long programming delays – When the delay is long enough, the phase noise becomes the parameter limiting the rejection.

Note that, in the analytical model presented in appendix A.2, we suppose that the programming beams are strictly identical at each repetition. Between two programming steps, the grating fades away slightly according to its lifetime, and we refresh exactly the same grating. The grating at steady state is then only the programmed spectrum, weighted by the lifetime and the repetition rate. Now if the laser contains phase noise, then each repetition is somehow different, and the dynamics of

overwriting an already existing grating must be taken into account. We did not investigate more on this topic, and the curves with phase noise presented in figure II.26 are simply averaged over 10 repetitions.

Nevertheless we obtain interesting results. Figure II.26b depicts the influence of the programming phase noise for long programming delays. In dotted line we show the modeled filter response without phase noise. With a 500 ns delay (red), we obtain a rejection on the tails almost 20 dB higher than with 50 ns (green). With phase noise the behaviour is completely different. The rejection does not change much with or without phase noise for a 50 ns delay. However, for 500 ns, the rejection is dramatically degraded, and the level of the tails is increased up to the 50 ns curve. This figure is in agreement with the fact that we could not experimentally observe any improvement of the filter shape by increasing the delay above 50 ns.

II.5 Phase response

II.5.1 Validation of the model

Up to now, we only presented the amplitude response of the spectro-spatial filter. However, the phase transmission is also a critical feature. Indeed, if the delay experienced by each frequency is not controlled, then the relative phase between different signals is lost. This is prohibitive in many applications where part of the information is encoded in phase.

In order to preserve the phase information of a multifrequency signal, a true time delay is necessary, meaning that all frequencies experience the same delay. This is equivalent to a linear phase versus the frequency. Indeed, a constant delay changes formally $e^{2i\pi\nu t}$ in $e^{2i\pi\nu(t-\tau)}$, so the added phase is linear in ν as $-2\pi\nu\tau$. In other words, the ideal transfer function is a linear dephasing within the passing band, and 0 otherwise. It reads formally:

$$H(\nu) = \begin{cases} e^{-2i\pi\nu\tau}, & \text{in the passing band} \\ 0, & \text{otherwise.} \end{cases} \tag{II.11}$$

Figure II.27 shows the complete Bode diagram of a spectro-spatial RF filter. The power transmission, called gain here to comply with the litterature, is shown in figure II.27a, and the phase transmission in figure II.27b. We compare the experimental measurement with the analytical model. Besides the very good agreement in the amplitude response, as discussed previously, we also obtain a remarkable agreement in the phase response. Note that, in order to obtain the correct phase response, we must substract a constant slope to the experimental curve. We believe that the VNA was miscalibrated during the acquisition, adding a constant delay, *i.e.* a linear phase

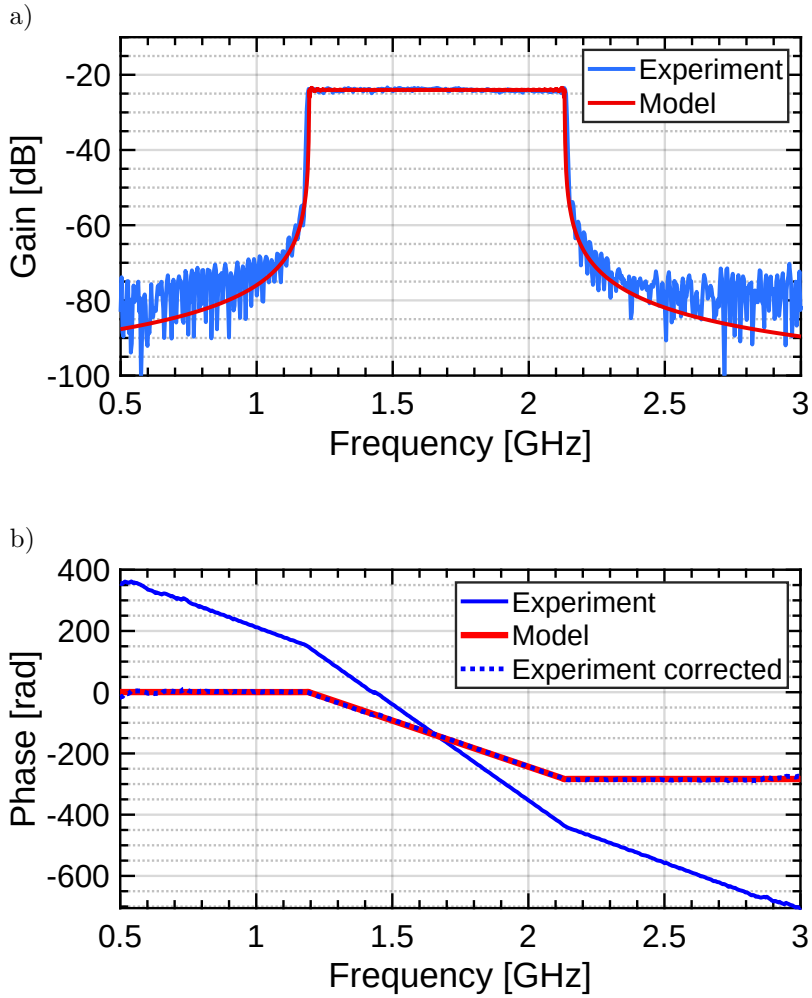

Figure II.27: Bode diagram of the spectro-spatial RF filter – a) Gain response. The curves were taken before optimization, hence the lower rejection.
b) Phase response. To match the model, we must substract a linear phase baseline, probably caused by a miscalibration of the measurement apparatus.

baseline.

II.5.2 Linear phase response and true-time delay

We can now plot the phase response for different delays, as we did for the amplitude response in the previous section. Figure II.28 displays the phase response given by the analytical model for a 1 GHz filter, corresponding to the amplitude responses from figure II.23b. We know from the litterature that the output beam is a photon echo, which is supposed to experience a true-time delay equal to the programming delay τ. In terms of phase, this is equivalent to a dephasing $-2\pi\nu\tau$. In figure II.28, dashed arrows depict those $-2\pi\nu\tau$ lines beside each curve for comparison.

We observe that for long delays, above 8 ns here, the phase response is almost

perfectly linear, and with the expected $-2\pi\tau$ slope. At $\tau = 1$ ns, the phase response is no longer linear in the passing band. The $\tau = 0$ ns curve is best seen in figure II.29a, and its slope is indeed non zero within the passing band.

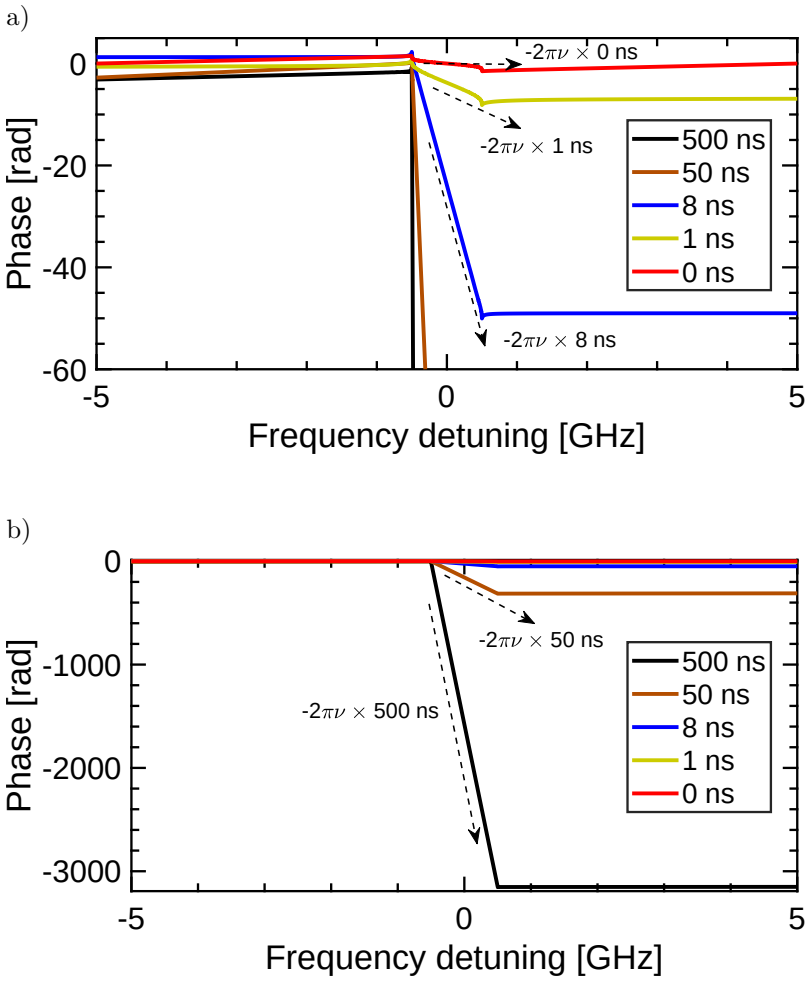

Figure II.28: Phase response corresponding to the amplitude responses from figure II.23b. We show the short delays in a), and zoom out on the long delays in b). The dashed arrows depict the $-2\pi\nu\tau$ lines, to be compared with the phase curves. The 0 ns curve is best seen in figure II.29a.

True-time delay is an essential component in many RF systems, such as phased array antenna [Ng et al., 1991, Wickham et al., 1995, Dolfi et al., 1991] or some filtering architectures [Toughlian et al., 1994, Coppinger et al., 1996]. In this frame, true-time delay by photon echo is a very promising technique, which has been largely investigated [Merkel and Babbitt, 1996, Tian et al., 2001, Reibel et al., 2002]. The present discussion demonstrates an interesting limit to the true-time delay by photon echo at short delay: a photon echo cannot produce a true time delay if the delay is too short.

Indeed, as the programming delay τ tends to zero, the delay of the photon echo does not tend to zero. Instead, it converges to a given non-zero dephasing. This limit is the filter phase response at $\tau = 0$, shown in figure II.28a or II.29a. This zero delay response is not linear within the passing band: the output signal is distorted and we no longer have a true time delay.

We observe from figure II.28 that, for a 1 GHz filter, the phase response seems linear within the passing band for $\tau > 10$ ns. So, if the incoming beam is entirely contained within $\Delta\nu$, then the photon echo actually experiences a true-time delay for $\tau > 10$ ns.

As discussed in section II.4.4, the transfer function is defined by the product [programming bandwidth $\times$ programming delay]. So the previous condition can easily be generalized to any programming bandwidth $\Delta\nu$. We find that, if the input beam is entirely contained within $\Delta\nu$, then the photon echo actually experiences a true-time delay if the following condition is typically fulfilled:

$$\tau > \frac{10}{\Delta\nu}. \tag{II.12}$$

Note that this condition is not very constraining in practice, since one is usually interested in large delays. Indeed, rare earth ions are precisely used for the long coherence times of their transition at low temperature, giving access to long delays.

II.5.3 Minimum phase response

From the point of view of the filter theory, a important quantity defining a filter is its minimum phase response. This concept is very well explained in [Lenz et al., 1998]. The well-known Kramers-Krönig relations state that the real and imaginary part of any causal complex function are directly linked. In terms of amplitude and phase, it can be shown that a given amplitude response defines a minimum phase response. The phase versus frequency of any causal (physical) system necessarily decreases faster than the minimum phase response.

It can be shown that the minimum phase response is directly related to the changes in amplitude response [Lenz et al., 1998]. In particular, a constant amplitude response implies a linear minimum phase response. Formally, the minimum phase response is given by the Hilbert transform of $\ln|H(\nu)|$ [Lenz et al., 1998, Kop et al., 1997]. Note that, whereas the minimum phase response is an important characteristic of a physical system, most of the time we do not wish to reach this minimum. Indeed, as mentioned before, one usually seeks a linear phase response, which is not especially the case for the minimum phase response [Madsen and Zhao, 1999].

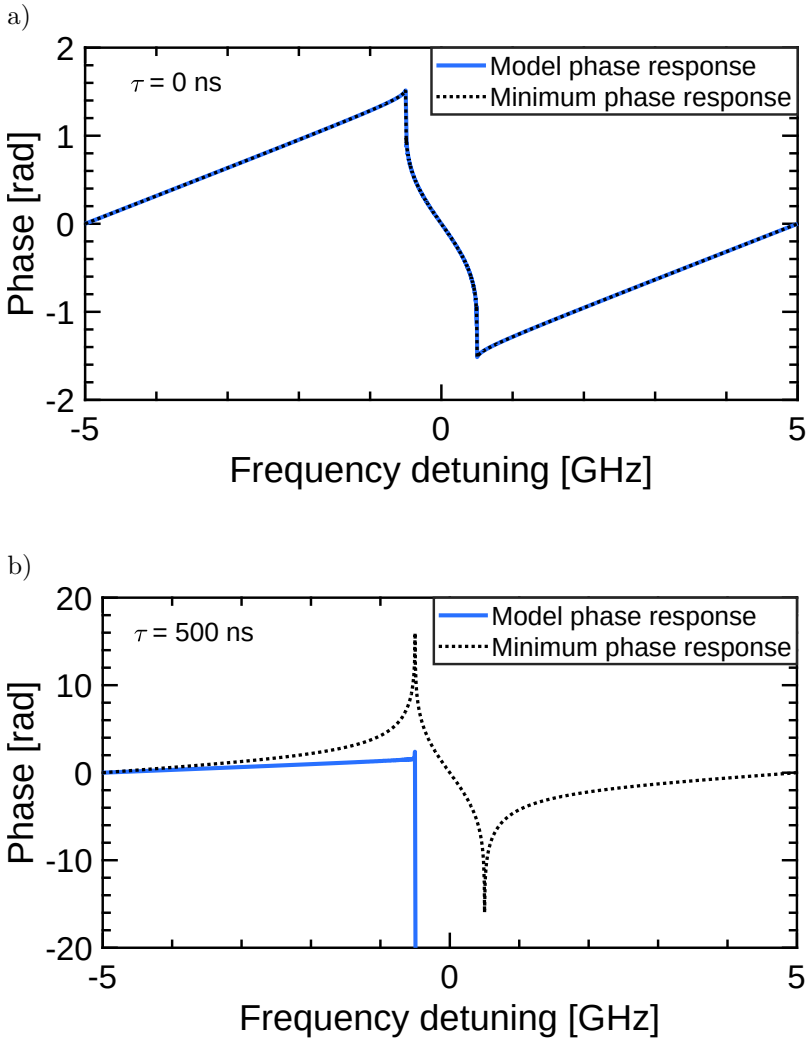

Figure II.29: Comparison between the phase response (full blue line) and the minimum phase response given by the amplitude response (dashed black line) for $\tau = 0$ and 500 ns.
a) At $\tau = 0$ ns, the phase response is equal to the minimum phase response.
b) At $\tau = 500$ ns, the phase response is very different from the minimum phase response. Due to the vertical scale, we only see the top of the phase response, which equals to roughly -3000 rad at 5 GHz. See figure II.28b for the complete curve.

In figure II.29 we compare the spectro-spatial filter phase response provided by our model with the minimum phase response, for a bandwidth of 1 GHz. The minimum phase response is derived as the Hilbert transform of $\ln|H(\nu)|$, where $|H(\nu)|$ is shown squared in figure II.23b.

At $\tau = 0$, as shown in figure II.29a, the filter response predicted by the analytical model is strictly identical to the theoretical minimum phase response. We understand this property by the fact that, at $\tau = 0$, the output phase response is only limited by causality, instead of other physical phenomenon. As such, the phase response is minimal in the sense of causality. When τ increases, the minimum phase response

changes. We show in figure II.29b the phase response for $\tau = 500$ ns. The amplitude response becomes steeper (see figure II.23b), so the minimum phase response becomes sharper. In this case, causality does not limit the phase response anymore, so it is not equal to the minimum phase response anymore. The phase response is then given by the photon echo phenomenon, which predicts a true delay and the linear phase response observed in figure II.28b.

II.6 Conclusion

In this chapter we have presented the spectro-spatial RF filter. We have demonstrated its high capabilities, placing the spectro-spatial RF filter at the state of the art of GHz range photonic RF filters (see table II.1). It reaches a global rejection of 60 dB, 15 dB higher than the state of the art of the filters of this kind. Its shape can be customized over a 20 GHz band, and, despite this wide tunability, the spectro-spatial RF filter has very steep sides with a rejection of 45 dB at 50 MHz from the edge, contrarily to other filters from the litterature. Finally, the presented filter can be tuned very quickly at any RF frequency.

In this chapter, we presented an experimental study and an analytical model, allowing to have a deep understanding of the physics of the system. The properties are remarkably well described by the model. We emphasized the critical and intrinsic role of causality. We identified other critical parameters ruling the rejection and the shape of the filter, such as the programming laser phase noise, the signal laser intensity noise, or the magnetic field.

We have determined that the performances are currently limited by the laser noises. In order to improve the filter shape, the next step is to improve the programming laser phase noise and the signal laser intensity noise. Although more difficult to handle, the diffraction efficiency is also a crucial parameter to enhance the rejection of the filter. The latter will be the object of chapter III.A.

Nevertheless, despite the remarkable reported performances, the large size and power consumption of the experiment, in particular due to the closed-cycle cryogenics, does not allow its integration in a portable autonomous device. The spectro-spatial RF filter will most probably not be used as a standalone system. However, the study discussed in this chapter presents at least two major interests.

First, the spectro-spatial RF filter would be highly interesting when combined with another system using REIC, such as a rainbow spectrum analyzer [Berger et al., 2016, Merkel et al., 2014]. Mutualizing the equipment – crystal, cryostat, lasers – would upgrade the rainbow spectrum analyzer with a very high quality RF filter with almost no additional cost, size, weight and power consumption, and compatible

with a down-converting stage or/and a stabilized delay line.

Second, the experiment we discussed in this chapter is also a simpler version of the rainbow spectrum analyzer. As such, it is of great help in understanding the complex behaviour of the spectrum analyzer. The study of the latter will be the object of the next chapter III. In particular in part III.B, we will rely on results from this chapter II to discuss the effect causality and Doppler effect in the rainbow spectrum analyzer.

Chapter III

Rainbow spectrum analyzer

Chapter III is dedicated to the rainbow spectrum analyzer. Spectrum analysis is indeed the major application of the spectro-spatial architecture initiated by Laboratoire Aimé Cotton and developed by Thales Research & Technology. Indeed, whereas the spectro-spatial RF filter is very recent work, the first experiment of rainbow spectrum analysis was reported more than 20 years ago in 2001 [Lorgeré et al., 2001]. However, many questions are still to be investigated.

We remind that the architecture of the rainbow spectrum analyzer is described in the introduction, in section I.3.2. It is not detailed in the present chapter. This chapter is divided into two subchapters, focusing on two very different aspects of the rainbow spectrum analyzer.

Despite the high dynamic range demonstrated in the rainbow spectrum analyzer, theoretical studies predict that it could reach even higher values [Attal et al., 2016]. Indeed, the experiment is currently limited by the diffraction efficiency, especially, when the programming bandwidth becomes large. Less diffracted power signifies less collected signal, and less dynamic range. Chapter III.A is devoted to a study of the relation between the programming bandwidth and the dynamic range of the spectrum analyzer.

In chapter III.B, we focus on the spectral response, or apparatus function, of the rainbow spectrum analyzer. This spectral response is crucial in the performances of the analyzer, as it defines its spectral resolution and dynamic range. We present an analytical model, based on the model of the spectro-spatial RF filter, describing the apparatus function of the rainbow spectrum analyzer. We use this model to precise our understanding of the physical processes at stake, in order to determine the effect of various experimental parameters.

Chapter III.A

SHB spectroscopy of a Tm^{3+}:YAG crystal under optical pumping

In this chapter III.A, we investigate phenomena limiting the dynamic range of the rainbow spectrum analyzer. The dynamic range of the analyzer is directly proportional to the diffraction efficiency. Unfortunately, we observe in practice that, in the spectro-spatial architectures, increasing the programming bandwidth results in a dramatical drop of the diffraction efficiency. A previous study on the diffraction efficiency in spectral gratings was reported in [Linget et al., 2015]. In this paper, a diffraction efficiency of 6.3 % was demonstrated over a 5 MHz grating. With a 100 MHz grating, we only obtain experimentally an efficiency of 2 %. In the rainbow spectrum analyzer, where we program the crystal over 20 GHz, the diffraction efficiency drops below 0.5 %. We see that this phenomenon causes a decrease of more than 10 dB of the diffraction efficiency, so of the dynamic range of the analyzer. The objective of the present chapter is to understand this effect, and propose solutions to preserve a high diffraction efficiency even with large programming bandwidths.

In section III.A.1, we will explain this multifactorial process. We will see that at large programming bandwidth, a temperature elevation in the crystal causes a drop of the lifetime of the programmed features. This effect magnifies the phenomenon of Instantaneous Spectral Diffusion, resulting in a drop of the diffraction efficiency. In section III.A.2, we describe our experimental methodology. We access the temperature inside the crystal by SHB spectroscopy, measuring the lifetime of spectral holes. We present finally in section III.A.3 the results obtained during this study.

Contents

III.A.1 Temperature and Instantaneous Spectral Diffusion

In this first section, we analyze the causes of this efficiency drop. First, we explain how the resonnance frequency of each ions randomly jumps when optical excitation is applied, a phenomenon known as Instantaneous Spectral Diffusion (ISD). We show how the effect of ISD is magnified when the spin lifetime T_g is low, which blurs the diffraction grating, and ultimately degrades the diffraction efficiency.

III.A.1.1 Instantaneous Spectral Diffusion

Inside the crystal matrix, in spite of the shielding by outer electron orbitals, the rare-earth ions weakly interact with each other. The Instantaneous Spectral Diffusion designates the fact that, when one ion goes from one energy level to another, its interaction with the surrounding ions varies, which slightly changes the energy levels of the latters. As a consequence, the resonance frequency of the surrounding ions jumps. Besides, the frequency jump is different for each ion. Indeed, the ion-ion interaction is *a priori* anisotropic, and strongly depends on the distance between the ions, which are randomly located inside the matrix.

The consequence of ISD on a spectral feature is described in figure III.A.1. We take the example of a narrow hole burnt in the absorption profile. Using a strong laser beam, we excite ions in another part of the spectrum. Given the spatial distribution of the ions inside the crystals, some of these ions are sufficiently close spatially to ions from the narrow hole to interact with them. The parameter of importance here is the spatial proximity of the ions, not their proximity in the spectrum. The excited ions cycle through different energy levels, which modifies their interaction with the ions from the narrow hole. Consequently, the resonnance of the ions from the narrow hole jumps to other frequencies, close but different from the original one. Because of the random spatial distribution of the ions inside the crystal, causing a random distribution of the interactions between the excited ions and the ions from the narrow hole, the frequency jump of each ion is different. As a result, the hole is blured: it becomes broader and more shallow. In the case of a grating, similarly to a simple hole, the ISD blurs the absorption pattern, which reduces the contrast.

ISD is a dynamical process, linked to the amount of ions which are displaced to other levels [Thiel et al., 2014a]. It can be described as a broadening of the effective homogeneous linewidth. In case of a two levels system, the broadening reads as

$$\Gamma_{\mathrm{h}}^{\mathrm{eff}} = \Gamma_{\mathrm{h}} + \beta n_e \tag{III.A.1}$$

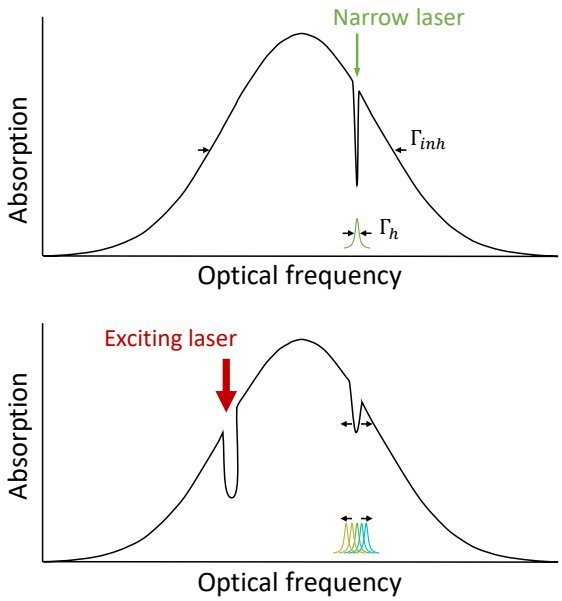

Figure III.A.1: Illustration of the effect of Instantaneous Spectral Diffusion on a spectral feature (from [Attal, 2017]) – We take the example of a narrow hole. We excite ions in another part of the spectrum with a strong laser. Given the spatial distribution of the ions inside the crystals, some of these ions are sufficiently close spatially to ions from the narrow hole to interact with them, although they are far spectrally. The excitation modifies this interaction, and the resonnance frequency of the ions from the narrow hole jumps. Because of the random spatial distribution of the ions inside the crystal, the resonance frequency of each ion jumps from a different amount. As a result, the hole is blured: it becomes broader and more shallow.

where Γ_h is the homogeneous width at rest, $\Gamma_\mathrm{h}^\mathrm{eff}$ is the effective homogeneous width after excitation, and n_e is the density of ions excited by the laser. The coefficient β is expressed in Hz.cm^3. It describes the broadening of the homogeneous width per density unit of ions being displaced to the excited state. In an optical pumping scheme where the ions are successively transferred to different states, ISD can originate from any of the population transfers. A β coefficient is therefore given for all pairs i, j of levels involved in the population transfer. The broadening then reads as

$$\Gamma_\mathrm{h}^\mathrm{eff} = \Gamma_\mathrm{h} + \sum_{i,j} \beta_{ij} n_{ij} \tag{III.A.2}$$

In the case of Tm:YAG, we consider 4 possible population transfers. The corresponding values for beta are given in table III.A.1.

In rare-earth ions-doped crystals, ISD is generally explained by dipole-dipole interaction between the ions, for example in ruby [Taylor and Hessler, 1974], Tb^{3+}:$LiYF_4$ [Liu et al., 1987], Eu^{3+}:Y_2O_3 [Huang et al., 1989], or Er^{3+}:YSO [Dajczgewand et al., 2015]. However, in Tm^{3+}:YAG, the ion-ion interaction causing ISD is still unknown. It was shown that neither the electric nor magnetic dipole interaction could quantitatively explain the measurements [Attal, 2017].

Transition	ISD coefficient β [Hz.cm^3]
$\|g\rangle \leftrightarrow \|e\rangle$	5.24 10^{-13} Hz.cm^3
$\|g\rangle \leftrightarrow \|m\rangle$	1.36 10^{-13} Hz.cm^3
$\|m\rangle \leftrightarrow \|e\rangle$	1.30 10^{-12} Hz.cm^3
$\|g_1\rangle \leftrightarrow \|g_2\rangle$	$< 9\ 10^{-14}$ Hz.cm^3

Table III.A.1: ISD coefficients β measured in [Attal, 2017] in our 0.5 %-doped Tm^{3+}:YAG crystal – $|g\rangle$, $|m\rangle$ and $|e\rangle$ respectively correspond to the $^3H_6$, $^3F_4$ and $^3H_4$ levels of the thulium without magnetic field. $|g_1\rangle$ and $|g_2\rangle$ correspond to the Zeeman sublevels of $^3H_6$ under magnetic field. See figure I.14 for the energy levels.

ISD is usually a weak phenomenon, but becomes noticeable when many ions are excited. It is a major issue in our experiments of spectral analysis because we address a large number of ions. In the spectrum analyzer, we even excite the whole inhomogeneous bandwidth. In this case, every single ion in the crystal cycles through different states and contributes to ISD. The diffraction efficiency is intrinsically limited by the bluring effect of ISD, which degrades the contrast of the diffraction grating.

It is possible to reduce the impact of ISD. A first option is to decrease the doping concentration [Thiel et al., 2014a]. Indeed, at low concentration, the distance between ions is large, so they interact weakly and the ISD is small. However, a low concentration requires to increase the thickness of the crystal to keep the total absorption constant. This implies geometrical constraints in the spectro-spatial architectures, where all beams reach the crystal with different angles.

Another option is to increase the storage lifetime. As mentioned before, in practice, we use a magnetic field to improve the diffraction. The storage state is then the Zeeman level, whose lifetime is noted T_g (see figure II.12). We remind the reader that we work under steady state, repeating the programming double chirp periodically, with period T_P, to maintain the grating in the crystal. The critical role of the storage time T_g in the effect of ISD can be understood intuitively considering two limit cases:

- $T_g \ll T_P$: Between two programming steps, the grating decays to zero. At each repetition, all ions must be pumped again to form the grating. At each repetition, every excited ion cycles through the various energy levels, so ISD is maximal.

- $T_g \gg T_P$: We first send a first double chirp. The engraved spectrum is close to the excitation spectrum, but blurred by ISD due to this first excitation. Nevertheless, many ions are already in the correct state. We send a second double chirp. Only the ions which did not end in the correct state after the first step are now excited. This represents a smaller portion of the ions, so the ISD is much

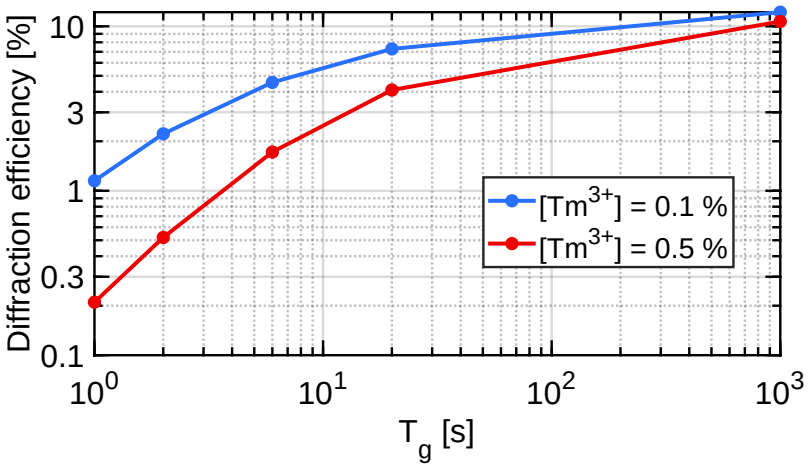

Figure III.A.2: Simulated diffraction efficiency versus T_g for two concentration of Tm^{3+} ions with an excitation over 20 GHz – As the storage time decreases, the impact of ISD increases, so the diffraction efficiency decreases. Decreasing the Tm^{3+} concentration, hence the impact of ISD, by a factor 5, greatly enhances the diffraction efficiency, especially at low T_g. For comparison, as we will see in the following sections, T_g = 20 s at rest, and decreases between 1 and 2 s under typical optical excitation, corresponding to a loss of a factor more than ten on the diffraction efficiency.

smaller. At each repetition, as we get closer to the excitation spectrum, the ISD is reduced. We iteratively converge towards the exact excitation spectrum. The effect of ISD is progressively mitigated.

Figure III.A.2 is a simulation. It is given by the model developed by Y. Attal, reported in [Attal et al., 2016] or in chapter II from [Attal, 2017]. This model allows to derives the diffraction efficiency at steady state for a wide variety of configurations, and includes in particular the ISD. This simulation shows that the diffraction efficiency logarithmically increases with T_g. The red curve corresponds to our crystal, with a Tm^{3+} concentration of 0.5 %. In blue, we decrease the concentration, so the ISD, by a factor 5. We observe that for very long T_g of 10^3 s, the two curves are close: the ISD has little impact on the diffraction efficiency. For T_g = 1 s on the contrary, the effect of ISD is strong and we obtain a factor 5 between the two concentrations.

With this preliminary study, we see that a long storage time is highly desirable in order to reach large diffraction efficiencies, since it reduces the effect of ISD. It is particularly important to keep the storage times long when working with large doping concentrations.

III.A.1.2 Temperature dependence of the spin lifetime

In our spectrum analyzer scheme, the storage time is given by the spin lifetime, *i.e.* the characteristic time after which the two Zeeman sublevels of the ground state return to thermal equilibrium. The thermal equilibrium is given by the Boltzmann

distribution, which gives, considering the MHz spin transition and a temperature of 3 K, an equal population between the two spin states. T_g corresponds to the time for the contrast of our spectro-spatial grating to decay to zero, since it is intrinsically an out-of-equilibrium repartition of the ions between their spin levels. Previous works have determined that the relaxation between the two Zeeman states is caused by spin-lattice interaction [Abragam and Bleaney, 2012]. In other words, T_g is limited by spin-lattice relaxations.

The lower the temperature, the smaller the energy of the phonons in the lattice. At low temperature, and considering the energy levels of the thulium ions in YAG, three types of spin-lattice interaction can induce spin relaxation: the direct process, the Orbach process and the Raman process. In this section, we present briefly these processes. The discussion is intentionally expeditious, as more details can be found in the litterature, such as [Abragam and Bleaney, 2012]. An illustration of the three processes are given in figure III.A.3.

The direct process (III.A.3a) is a single phonon process. A phonon whose energy matches the Zeeman splitting is absorbed by the ion, which changes its spin state.

The Orbach process (III.A.3b) describes a resonant two phonon process, involving an auxiliary higher energy level. The auxiliary level is generally a crystal field level. The ion moves up from one Zeeman level to the auxiliary higher energy level with a first phonon, and moves down to the other Zeeman level with a second phonon. The energy difference between the two phonons must correspond to the Zeeman splitting.

Finally, the Raman process (III.A.3c) describes a non-resonant two phonon process. It is similar to the Orbach process, except that the auxiliary level is a virtual out-of-resonnance level. The ion interacts with a phonon of any frequency, and emits

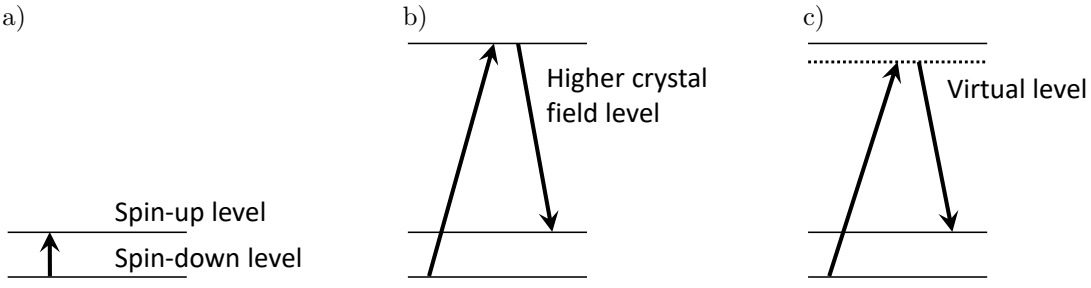

Figure III.A.3: Illustration of the different spin relaxation process – We take the example of an ion in spin-down relaxing to spin-up.
a) Direct process: a single phonon is absorbed, whose energy equals the Zeeman splitting.
b) Orbach process: the ion absorbs two higher energy phonons, and transits through a higher level. The energy difference between the phonons must match the Zeeman splitting.
c) Raman process: Similar to Orbach process, but the transition level is a virtual level.

another phonon. Again, the energy difference between the two phonons must correspond to the Zeeman splitting.

It has been shown in [Veissier et al., 2016] that, in Tm^{3+}:YAG crystals cooled at 3 to 5 K, the two phonon resonant Orbach process is dominant. With the Orbach process, the spin lifetime varies as:

$$T_g \propto \exp\left(\frac{\Delta}{k_B T}\right) \tag{III.A.3}$$

where Δ is the energy difference between the spin states and the auxiliary level.

Interestingly, we can compare the phonon density to the crystal field levels: according to Bose-Einstein theory, the spectral density of phonon population reads:

$$n(\omega) \propto \frac{\omega^2}{\exp\left(\frac{\hbar\omega}{k_B T}\right) - 1}. \tag{III.A.4}$$

Figure III.A.4 depicts the phonon density at 3 K and 4 K. In our experiments, we

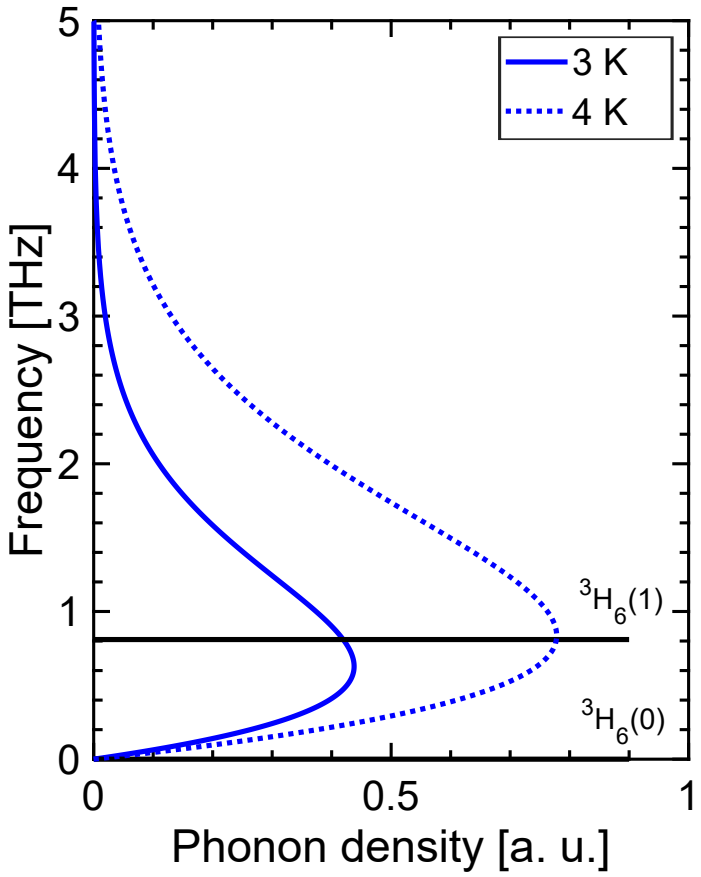

Figure III.A.4: Phonon density at 3 K and 4 K, and first two levels of the $^3H_6$ multiplet of thulium, $^3H_6(0)$ and $^3H_6(1)$. The following level $^3H_6(2)$ has an energy of 6.5 THz.

apply a magnetic field of a few tens of mT, resulting in a Zeeman splitting below 10 MHz. Considering the vertical scale, the Zeeman sublevels are not distinguishable in the figure. Given the low phonon density in this frequency range, we qualitatively expect a weak direct process. The energy of the crystal field levels of Tm^{3+}:YAG were measured in [Gruber et al., 1989]. We display the ground state $^3H_6(0)$ at 0 Hz, and the first excited crystal field level $^3H_6(1)$, which has an energy of 0.81 THz. The next level $^3H_6(2)$ has an energy of 6.5 THz and is out of the graph. At those temperatures, we observe that the phonon density is almost maximal around the $^3H_6(1)$ crystal field level. Therefore, we can expect the resonant two phonon Orbach process to be strong in this temperature range. This qualitative analysis is in agreement with the observations from [Veissier et al., 2016], showing a dominant Orbach process.

As a conclusion, the presence of the $^3H_6(1)$ level at the maximum of the phonon density at our temperatures implies a strong Orbach relaxation process, so T_g rapidly decreases with the temperature. So, limiting the temperature inside the excited region, *i.e.* within the spectro-spatial grating, is critical to increase the spin lifetime T_g, allowing to increase the diffraction efficiency.

III.A.2 Experimental setup

We have identified in the previous section that increasing the spin lifetime T_g is an interesting option to cancel the ISD and increase the diffraction efficiency. We now present the experimental setup allowing to measure T_g in conditions similar to that of our rainbow spectrum analyzer.

Figure III.A.5 depicts the principle of the setup. We have four optical fiber inputs, allowing to access different configurations. The two free space paths can be moved to explore differents regions inside the crystal.

The probe laser is the laser performing the spin lifetime measurement. We use here a DL100 Toptica laser. Its frequency is constant over time, within the inhomogeneous linewidth. It goes through a double path acousto-optic modulator, allowing to create the probe sequence described in the chronogram III.A.7.

The role of the excitation laser is to mimic the programming laser from the rainbow spectrum analyzer. It is a DL Pro Toptica laser amplified by two semiconductor optical amplifiers (SOA). We chirp its frequency with a triangle modulation across 10 GHz within the inhomogeneous linewidth of the crystal, with a repetition rate of 1 kHz. Its power can be tuned from 0 to 20 mW. As illustrated in figure III.A.6, the probe is spectrally separated from the excitation. If not, the probe sequence would be immediately erased by the excitation.

Figure III.A.5 presents a situation where we excite and probe the crystal at the same spot. For example, this is the configuration of figures III.A.12b and III.A.14.

The setup also allows to move the excitation separately from the probe, by connecting the excitation to one of the two fiber inputs at the bottom. This is the case of figures III.A.12a and III.A.13, where we probe different spots while the excitation is kept at the center.

The signal is acquired with a photodiode. It is protected from the strong excitation laser with a rotating mirror. During the short acquisition of the probe signal, we shut off the excitation laser and point the mirror towards the photodiode.

The chronogram of the probe sequence is presented in figure III.A.7. After turning on the magnetic field, we burn a hole in the absorption profile. We choose to burn a hole over a small band of 3 MHz. Burning a hole over a small band, rather than a single frequency, allows in particular to reduce the effect of laser instability during the hole burning step. Then, we wait for the hole to decay during a given waiting time. We finally read-out the spectral feature by chirping the laser over 40 MHz and measuring its transmission via the photodiode.

In order to obtain the spin lifetime T_g, we repeat the probe sequence while varying the waiting time, and we measure the decay of the hole. Typical transmission profiles for different waiting times are shown in figure III.A.8a. We observe the hole-antiholes profile discussed in section II.4.1. The amplitude of the hole progressively decreases to zero. Note that we substract here the baseline, in order plot only the difference to equilibrium.

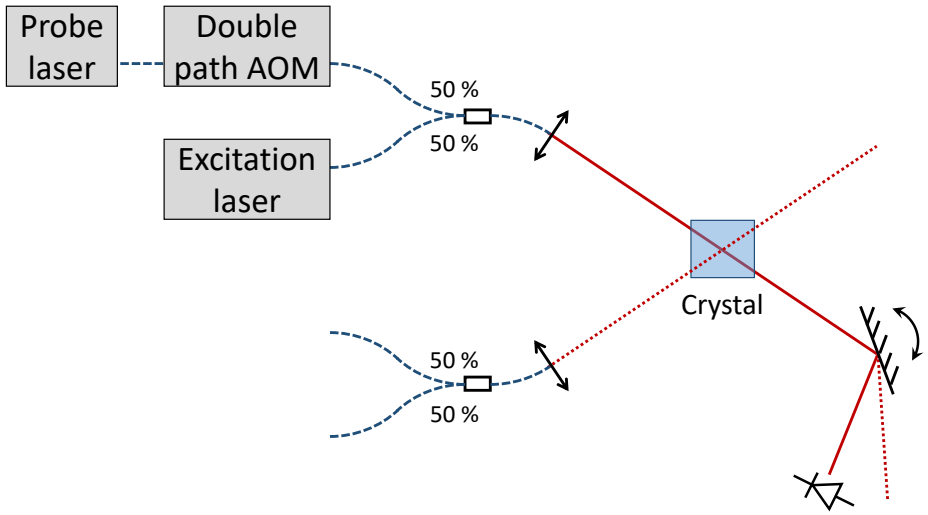

Figure III.A.5: Illustration of the spin lifetime measurement setup – Optical fibers are shown in blue dashed line, and free space paths in red line. Both free space paths can be moved spatially to explore the crystal. We show here the case where we excite and probe at the same spot. The probe laser is modulated by an acousto-optic modulator (AOM) and mixed with the excitation through a 50/50 coupler. They are collimated in free space (black arrow) and cross the crystal. The signal is acquired through a photodiode, protected from the strong excitation beam with a rotating mirror.

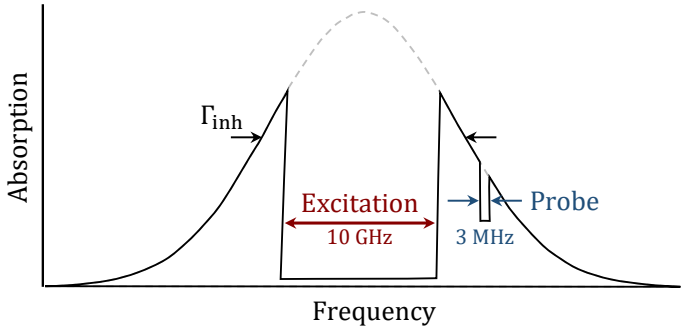

Figure III.A.6: Illustration of the frequency range of the excitation and the probe with respect to the inhomogeneous linewidth of the crystal − We excite over 10 GHz within the inhomogeneous width. The probe hole is burnt over 3 MHz on the side of the inhomogeneous linewidth.

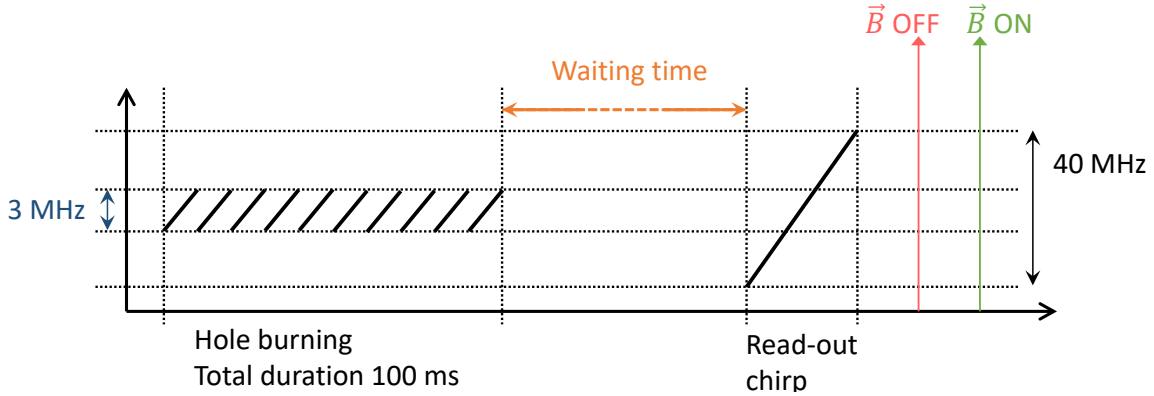

Figure III.A.7: Chronogram of the probe sequence − A hole is burnt in the absorption profile by repeating a chirp over a small bandwidth of 3 MHz. After a given waiting time, we scan the laser across 40 MHz to read-out the transmission profile around the hole. Then we switch the magnetic field off and on to reset the ions between the two spin states.

The area of the hole is proportional to the number of displaced ions. So the decay of the area also follows the exponential decay with time constant T_g. We plot in figure III.A.8b the area of the hole for many waiting times. We finally obtain T_g by fitting the experimental curve with a function of the form $A\exp(-t/T_g)+B$. The B coefficient accounts for the misestimation of the transmission baseline due to the measurement noise.

Not all measurements presented in section III.A.3 invole the excitation laser. When they do, the excitation laser is always on. We only switch it off briefly during the read-out (see chronogram III.A.7) to avoid blinding the photodiode.

As we can see, measuring T_g in a given configuration requires to repeat the probe sequence from chronogram III.A.7 a few tens of times with different waiting times. Besides, between each repetition, we must wait for the hole to vanish completely, to

ensure that we rewrite the exact same hole. In our experiments, T_g can exceed 20 s, which means that the crystal returns to equilibrium in roughly two minutes. As a consequence, the measurement a of single value of T_g can easily take more than one hour.

As depicted in figure III.A.7, in order to accelerate the measurement, we switch the magnetic field off and on after the probe. When the two Zeeman levels merge, the spins mix up. When we split them again, they become equally populated.

In practice, we create the magnetic field with a permanent magnet lying on the cold chamber. We use an electrical motor to move the magnet up and down, thus switching the magnetic field off and on. Nevertheless, one measurement still takes up to 20 minutes for long T_g.

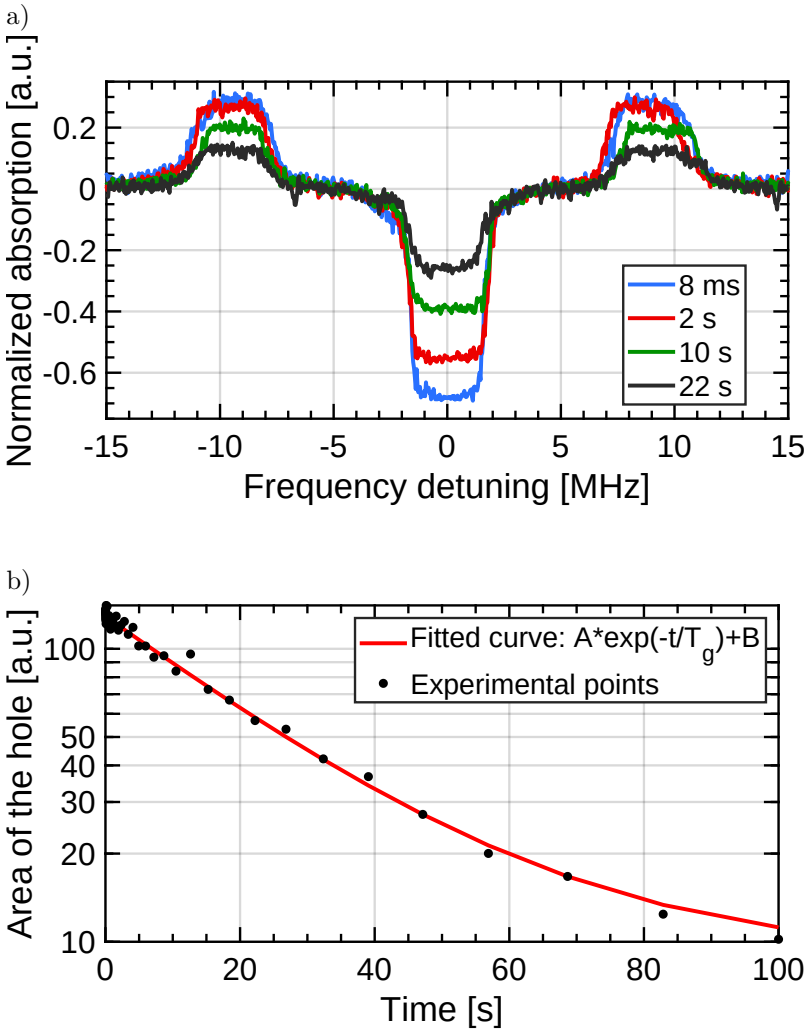

Figure III.A.8: a) Example of decay of the hole and antiholes with the waiting time.
b) Fit of the decay curve to obtain T_g – We measure the area of the hole when increasing the waiting time. We obtain T_g by fitting the curve by a function of the form $A\exp(-t/T_g) + B$.

III.A.3 Results

In this section, we present the results of the experimental study. We measure the influence of different parameters on the spin lifetime T_g. Our objective is to determine if T_g can be increased without major changes in the setup, which would allow to improve greatly the diffraction efficiency.

III.A.3.1 Validation of the experiment

In order to confirm the validity of the experiment, we begin with a characterization of T_g versus the temperature of the crystal. Our crystal is placed in a vacuum chamber, and cooled by contact with the gold-coated cold finger of the cryostat. A clamp is screwed to the cold finger to press the crystal against the cold finger. We measure the spin lifetime without excitation laser when varying the temperature setpoint of the cryostat. The results are given in figure III.A.9 for a magnetic field of 12 mT. We obtain a lifetime $T_g = 23$ s at 2.9 K. This is the minimal temperature achievable by our cryostat. T_g drops dramatically as the temperature increases, to 1.5 s at 4 K and to 0.25 s at 5 K.

We compare our results with other studies in figure III.A.9. We show in black triangle previous measurements reported by our group [Attal, 2017] for a magnetic field of 10 mT. The lifetimes found then were a factor 10 below ours. We suspect that, at that time, the contact with the cold finger was poor, and that the crystal was less protected from outter radiation. This results in a crystal actually hotter than the cryostat sensors, moving artificially the curve to the left.

The green triangles show data reported in [Louchet-Chauvet, 2019] for a magnetic

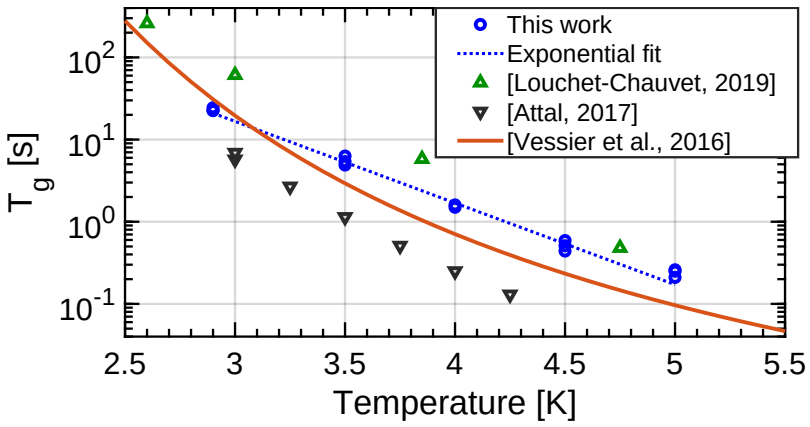

Figure III.A.9: Validation of the experiment – We compare our results (blue circles) with previous measurements from [Attal, 2017] and [Louchet-Chauvet, 2019], and with the model from [Veissier et al., 2016]. The dashed line shows the exponential fit of our results given in equation III.A.5. The magnetic field is 12 mT for all curves, except [Attal, 2017] which is at 10 mT.

field of 12 mT. This study is performed on a crystal equivalent to ours, but placed in a helium bath. This type of cryostat should provide a better thermalization than our closed-cycle cryostat, hence less uncertainty on the crystal temperature, and more reliable measurement.

Finally, we also report a model developed in [Veissier et al., 2016]. This model describes the temperature and magnetic field dependence of T_g through direct and Orbach relaxation processes. We observe a small discrepancy above 4 K between this model and the data from the present study, where the model predicts values a factor two below the experiment. Note that 12 mT is on the lower edge of magnetic field that the model claims to describe, so this model may not be perfectly accurate for this value. Nevertheless, the model provides a good order of magnitude of the experimental behaviour.

From figure III.A.9 we can fit an exponential relation between T_g and T for our crystal. We obtain

$$T_g = b \exp(-aT) \tag{III.A.5}$$

with $a = 2.29$ K^{-1} and $b = 1.60\ 10^4$ s. We will use this relation to convert lifetime to temperature in the following, when temperature behaviour is more relevant than the lifetime behaviour.

We observe in figure III.A.10 that the decay of T_g with the temperature does not depend on the magnetic field, in this range of field and temperature. This behaviour is predicted by the model from [Veissier et al., 2016] mentioned above, as we can see in figure III.A.10. It is expected from the fact that the dominant decay process is the Orbach process, which depends on the energy difference with the crystal field auxiliary level, not between the Zeeman levels themselves.

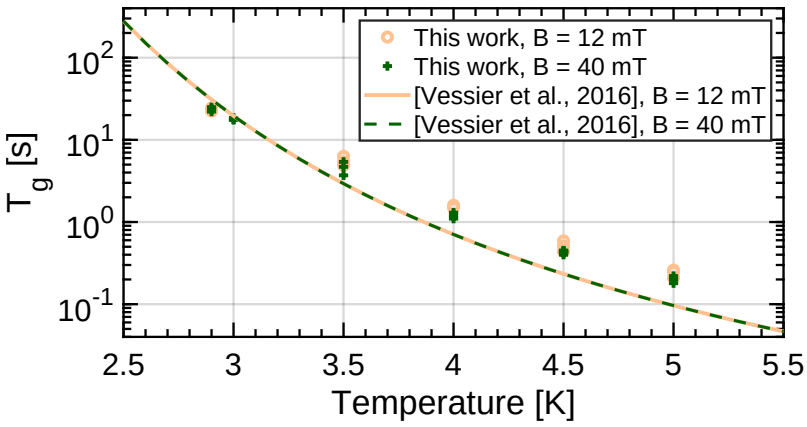

Figure III.A.10: Influence of the magnetic field – In this range, the magnetic field does not cause any visible change in the spin lifetime. This is well predicted by the model from [Veissier et al., 2016], whose two curves are superimposed.

III.A.3.2 Programming optical power

We now get closer to the experimental conditions of the rainbow spectrum analyzer by adding a excitation beam, reproducing the programming beam of the rainbow spectrum analyzer. We excite the center of the crystal with an amplified DFB laser. Its frequency is chirped over 10 GHz, at the middle of the inhomogeneous linewidth of the thulium (see figure III.A.6). We can vary the mean power reaching the crystal from 0 to 20 mW.

We plot in figure III.A.11 the lifetime versus the mean optical power of the programming beam. We measure between 3 and 5 times each experimental point. The error bars depict the extremal values obtained in each configuration. We proceed the same way in all following experimental curves.

With only 0.5 mW, we already reduce T_g from 23 seconds at rest to 15 seconds. At 20 mW, which is a typical power in our experiments, it drops to 1 second. In terms of temperature, according to equation III.A.5, $T_g = 1$ s correponds to a temperature of 4.2 K. This is a rise of 1.3 K compared to the crystal temperature without excitation. The cooling power of the cryostat is of the order of 100 mW, which should allow to absorb the heat load. This temperature increase observed experimentally despite a sufficient cooling power hints that the heat is trapped inside the crystal, due to a high thermal resistance between the points of excitation and the cold finger.

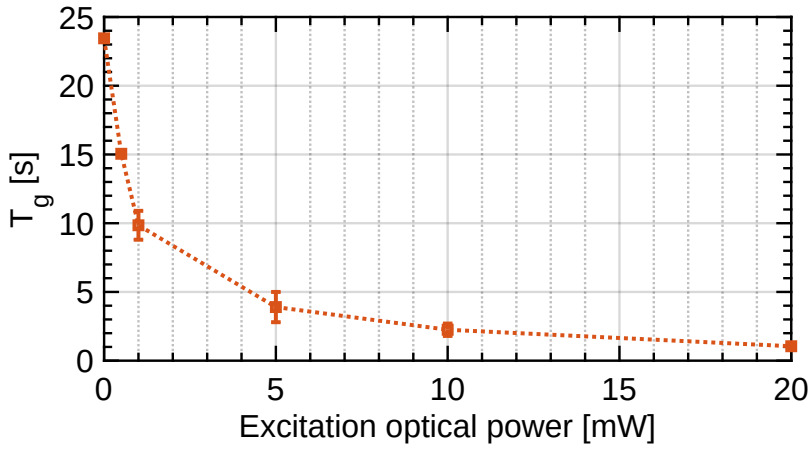

Figure III.A.11: T_g versus optical power of the excitation – The excitation mimics the programming laser from the rainbow spectrum analyzer. It is chirped over 10 GHz centered on the inhomogeneous linewidth of the crystal.

As mentioned previously, the objective of this study is to reduce the drop of T_g at high optical power. Canceling the thermal effects would allow to enhance T_g under a 20 mW excitation from 1 s to more than 20 s, as it is at rest. As shown in figure III.A.2, the diffraction efficiency would then increase by a factor 10.

III.A.3.3 Heat diffusion model

We have seen in section III.A.1.2 that the drop of T_g is related to the temperature increase caused by the wideband excitation. So the thermalization of the crystal should improve directly T_g.

We first study the heat diffusion inside the crystal, in order to determine where the heat accumulation occurs. We realize a first measurement by placing the exciting beam at the center of the crystal. We perform T_g measurements at different vertical positions. An illustration is given by figure III.A.12a. The results are given in figure III.A.13a.

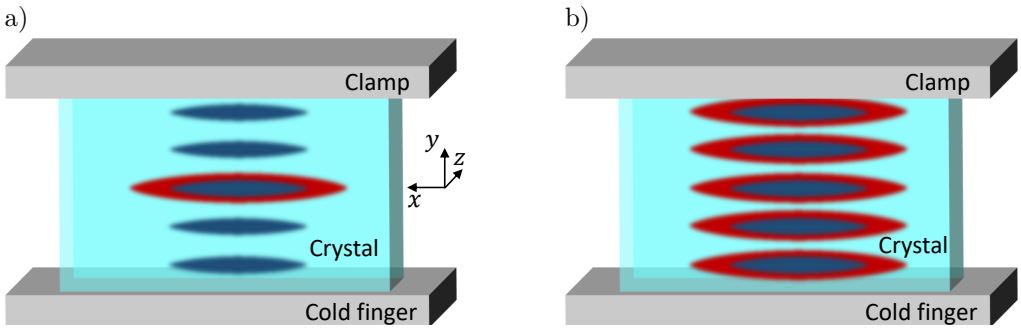

Figure III.A.12: Illustration of heat diffusion measurements – Red dots: excitation, blue dots: probe beam. Drawing a) refers to figure III.A.13. We keep the excitation at the center of the crystal, while taking measurements along the vertical axis. Drawing b) refers to figure III.A.14. We move the excitation along the vertical axis and, for each position, we take a measurement at the exact same spot.

In figure III.A.13a we plot T_g in the crystal along the vertical axis, while the excitation is in the center of the crystal. The crystal is cooled by the cold finger on the bottom, and by an aluminium clamp on the top, which is screwed to the cold finger and holds the sample. In figure III.A.13b we plot the temperature profile (red dotted line) inside the crystal, deduced from figure III.A.13a using equation III.A.5. We observe that T is a 0.05 K lower on the crystal−cold finger interface than on the crystal−clamp interface. Indeed the heat transfer is less efficient through the clamp, since the heat must travel across the clamp and the screws before being evacuated by the cold finger. However we note that the thermal dissipation via the clamp is not so low, in spite of the small surface of contact on the screw head and in the screw thread.

This measurement also allows to infer thermal coefficients of the crystal. Here, we present a simple heat diffusion model. We make the hypothesis that the programming laser heats the crystal uniformely along directions x and z, and that the vacuum inside the cold chamber prevents any conductive dissipation from the side faces of the crystal. This way, heat diffusion is only 1D along the y-axis.

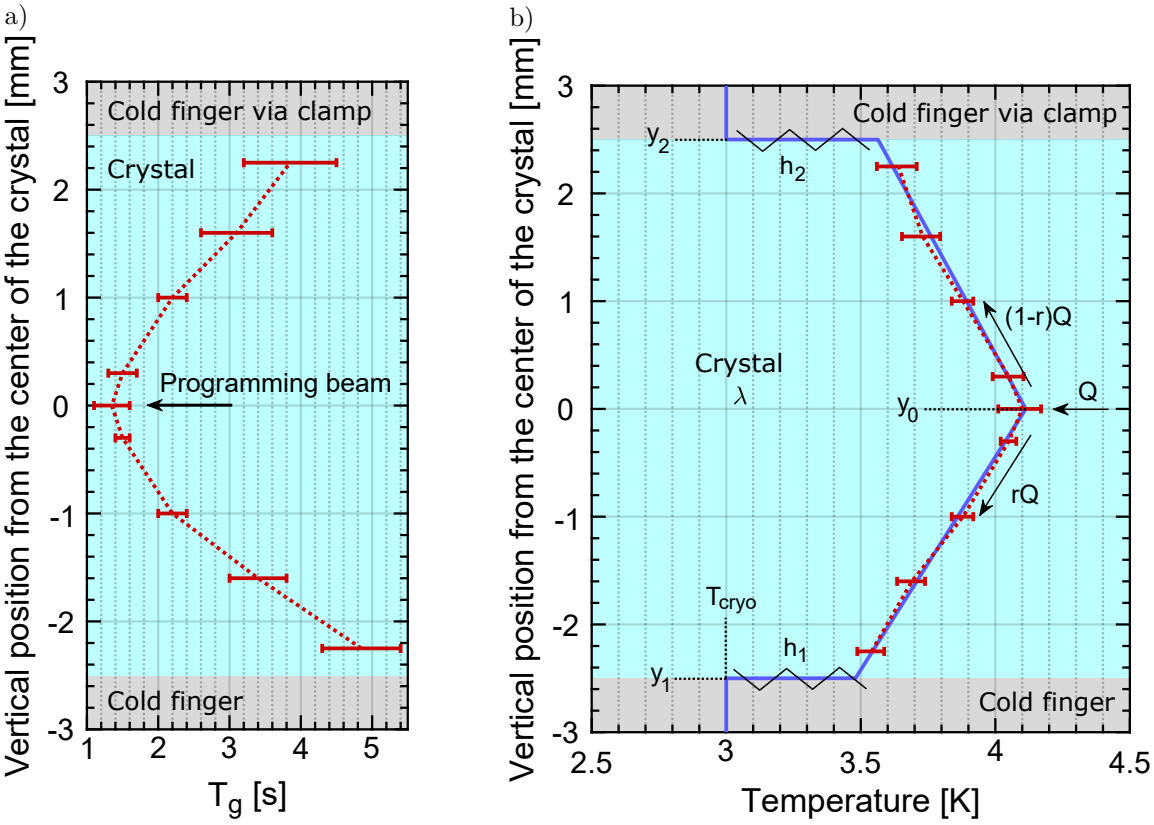

Figure III.A.13: a) Evolution of T_g along the vertical axis of the crystal with a constant excitation at the center of the crystal.

b) Temperature profile deduced from a), and heat diffusion model – Red dashed line: temperature profile deduced from a), using equation III.A.5; Black annotations: variables used in the heat diffusion model; Blue line: Fit of the heat diffusion model to the experiment with variables λ, h_1 and h_2.

Note that the hypothesis of uniform heating in the (x, z) plane is rather strong. In reality, the beam radius at $1/e^2$ along x is 1.3 mm, while the crystal is 5 mm-wide, so the beam only occupies roughly 2/3 of the crystal width. Moreover, the probe beam is not infinitely thin in the y direction. It is gaussian with a diameter of approximately 0.5 mm. However, the model gives a first approximation of the numerical values, as well as tendencies for the influence of the various parameters.

We show in black in figure III.A.13b the variables used in this heat diffusion model. The laser is equivalent to a heat source Q applied at $y = y_0$. Some fraction rQ is evacuated towards the cold finger, some fraction $(1 - r)Q$ towards the clamp, with $r \in [0, 1]$.

At steady state, assuming purely conductive heat transfer processes, the heat

equation in the upper and lower part of the crystal read:

$$\begin{cases} -\lambda \dfrac{\mathrm{d}T}{\mathrm{d}y}(y) = -\dfrac{rQ}{S}, & y \leq y_0 \\ -\lambda \dfrac{\mathrm{d}T}{\mathrm{d}y}(y) = \dfrac{(1-r)Q}{S}, & y \geq y_0 \end{cases} \tag{III.A.6}$$

where λ is the thermal conductivity of the crystal, and S the surface of the interfaces. We can define the interface thermal conductances h_1 for the cold finger interface at position y_1, and h_2 for the clamp interface at position y_2. The boundary conditions are:

$$\begin{cases} T(y_1) = T_{\text{cryo}} + \dfrac{rQ}{Sh_1} \\ T(y_2) = T_{\text{cryo}} + \dfrac{(1-r)Q}{Sh_2} \end{cases} \tag{III.A.7}$$

where T_{cryo} stands for the cold head temperature, which is given experimentally by the sensors from the cryostat. From equations III.A.6 and III.A.7 we obtain the temperature profile:

$$\boxed{\begin{cases} T(y) = \dfrac{rQ}{\lambda S}(y - y_1) + T_{\text{cryo}} + \dfrac{rQ}{Sh_1}, & y \leq y_0 \\ T(y) = -\dfrac{(1-r)Q}{\lambda S}(y - y_2) + T_{\text{cryo}} + \dfrac{(1-r)Q}{Sh_2}, & y \geq y_0. \end{cases}} \tag{III.A.8}$$

We finally invoke the temperature continuity at $y = y_0$ to obtain r. We find from equation III.A.8:

$$\frac{rQ}{\lambda S}(y_0 - y_1) + T_{\text{cryo}} + \frac{rQ}{Sh_1} = -\frac{(1-r)Q}{\lambda S}(y_0 - y_2) + T_{\text{cryo}} + \frac{(1-r)Q}{Sh_2} \tag{III.A.9}$$

T_{cryo} and Q/S cancel out. We rewrite equation III.A.9:

$$\frac{r}{\lambda}(y_0 - y_1) + \frac{r}{h_1} - \frac{r}{\lambda}(y_0 - y_2) + \frac{r}{h_1} = -\frac{1}{\lambda}(y_0 - y_2) + \frac{1}{h_2} \tag{III.A.10}$$

We obtain finally:

$$\boxed{r = \frac{\dfrac{1}{\lambda}(y_2 - y_0) + \dfrac{1}{h_2}}{\dfrac{1}{\lambda}(y_2 - y_1) + \dfrac{1}{h_2} + \dfrac{1}{h_1}}} \tag{III.A.11}$$

The fraction of heat passing through one side or the other is given, on the one hand, by the distances to the interfaces, and, on the other hand, by the relative thermal resistance of the two interfaces. The importance of diffusion versus interfaces is

given by the ratio between $\Delta y/\lambda$ and $1/h_{1,2}$.

We estimate the numerical values of the experimental parameters. The crystal is 5 mm tall, and the excitation is at its center, so we take $y_1 = -2.5$ mm, $y_2 = +2.5$ mm and $y_0 = 0$. The surface of the crystal on each thermal contact interface is $S = 90$ mm^2. At rest, the temperature measured by the cryostat is 2.9 K. However, due the heat load brought by the programming beam, the temperature is a bit higher, and we measure $T_{\text{cryo}} = 3$ K.

The mean incoming programming power is 20 mW. We measure experimentally that 90 % of this power is absorbed by the crystal. However, not all the absorbed power contributes to heating. Indeed, the decay channels from the excited state to the ground state can be either radiative, emitting photons which do not heat the crystal, or non-radiative, emitting phonons and heating the crystal. The preponderance of radiative or non-radiative channels is described in [Caird et al., 1975].

In our case, we excite the $^3\text{H}_6$–$^3\text{H}_4$ transition of energy $\Delta E_{\text{tot}} = 378$ THz. From the excited state $^3\text{H}_4$, the ions decay essentially to the metastable state $^3\text{F}_4$ via the intermediate state $^3\text{H}_5$. These transitions are non-radiative: they emit phonons which contribute to the heat. The total phonon energy emited via this non-radiative channel is the difference between $^3\text{H}_4$ and $^3\text{F}_4$, $\Delta E_{\text{nr}} = 211$ THz. From $^3\text{F}_4$, the electrons then decay to the ground state $^3\text{H}_6$ via a radiative transition, which does not heat the crystal. We can then estimate the heat load as $Q = 20 \times 0.9 \times 211/378 = 10$ mW. Refer to figure I.11 for the energy structure of the thulium.

The unknown parameters, which we wish to obtain, are the thermal conductivity of the crystal λ, and the interface thermal conductances h_1 and h_2. In order to determine these parameters, we fit the temperature measurement from figure III.A.13 with the heat diffusion model, given by equations III.A.8 and III.A.11. The experimental temperature profile is indeed close to the model, which predicts two linear parts from the excitation point towards both edges, so fitting the experiment seems valid. The fit is shown in blue line in figure III.A.13b. We obtain the following quantities:

$$\lambda = 0.24 \text{ W.m}^{-1}\text{.K}^{-1}$$

$$h_1 = 125 \text{ W.m}^{-2}\text{.K}^{-1}$$

$$h_2 = 93 \text{ W.m}^{-2}\text{.K}^{-1}$$

Thermal conductance at the interfaces in cryostats has been widely investigated by the cryogenics community. Values of thermal conductance versus temperature are reported for example in [Jeong and Park, 2015] for different interfaces at cryogenic temperature. Values between 200 and 700 W.m^{-2}.K^{-1} are reported at 3 K for copper-copper interface, with indium or Apiezon-N grease thermal joint. The conductances

h_1 and h_2 of the interfaces, although within the same order of magnitude, are several times lower. We discuss this point in the following section III.A.3.5.

We could not find any measurement of thermal conductivity in Tm^{3+}:YAG at cryogenic temperature in the litterature. Thermal conductivities of pure YAG crystals around 20 $W.m^{-1}.K^{-1}$ are reported in [Slack and Oliver, 1971]. Besides, studies on other materials, like [Liu et al., 2011] or [Benbachir et al., 1985], indicate that a dopant can decrease by several times the thermal conductivity of the host. So, despite the lack of data, we can estimate our value to be within the right order of magnitude.

The values of bulk conductivity and interface conductance are a bit low compared to the litterature. This might be due to the hypothesis of uniform heating in the (x, z)-plane.

Nevertheless, from a pratical point of view, we can conclude from figure III.A.13b that, the heat diffusion in the bulk on the one hand, and the thermal resistance of the interfaces on the other hand, seem to contribute equally to the temperature elevation of the crystal.

We remind the reader that the objective is to increase T_g, hence to decrease the temperature, at the point $y = y_0$. Equation III.A.8 explicits the two mechanisms increasing the temperature at $y = y_0$. We want to cancel thoses two terms:

1) $\frac{rQ}{\lambda S}(y_0 - y_1)$ accounts for the heat diffusion in the bulk. We cannot easily improve the crystal conductivity λ. However, since $0 \leq r \leq 1$, this term tends to 0 when $y_0 \to y_1$. we should be able to decrease this contribution by moving the excitation closer to the interface.

2) $\frac{rQ}{Sh_1}$ is the contribution of the interface. We can decrease this term by increasing the thermal conductance at the interface h_1.

With these two conditions 1) $y_0 \to y_1$ and 2) $h_1 \to +\infty$, equation III.A.8 simply becomes $T(y_0) = T_{\text{cryo}}$. This is the optimal situation where the temperature and T_g are only limited by the cryostat. We discuss the conditions 1) and 2) in the two following sections.

III.A.3.4 Position of the excitation

We first try to cancel the contribution of heat diffusion in the bulk of the crystal. As mentioned before, a simple option for this is to move the excitation closer to the cold finger. Formally, $\frac{rQ}{\lambda S}(y_0 - y_1)$ accounts for the impact of thermal conductivity in III.A.8, which tends to zero when y_0 tends to y_1. Figure III.A.14a depicts a network of curves, showing the evolution of the temperature profile inside the crystal predicted

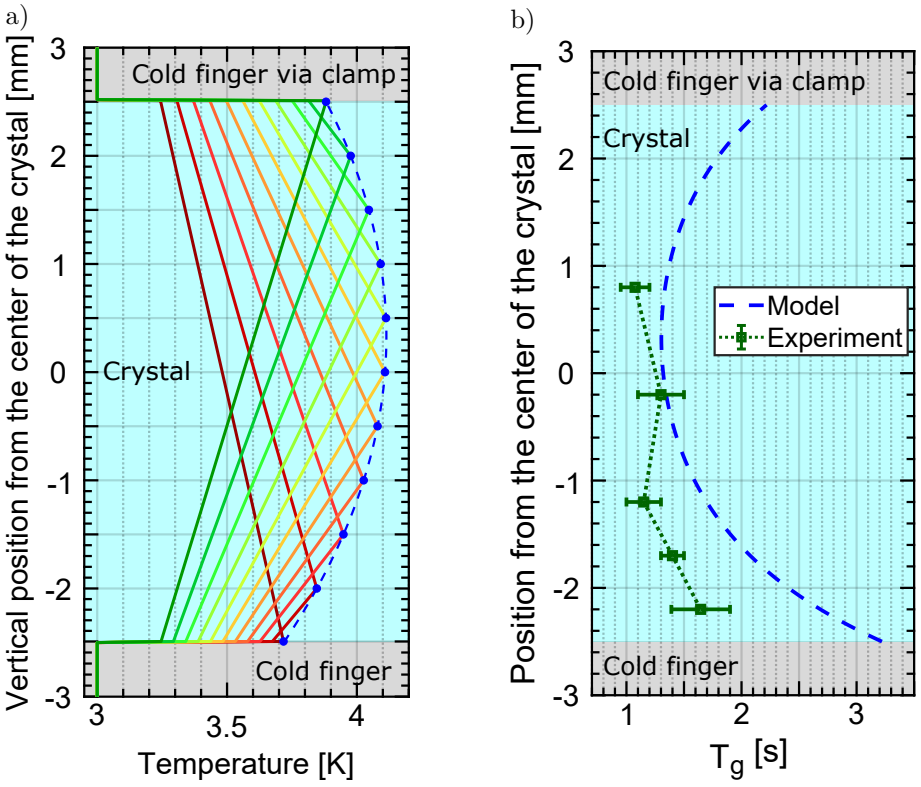

Figure III.A.14: a) Temperature profile given by the heat diffusion model when varying the position of the excitation y_0. For each curve we focus on the temperature at the excitation point, represented in blue dots and dashed line.

b) Lifetime T_g at the point of excitation when the excitation is moved along the vertical axis of the crystal – blue: theoretical profile deduced from the blue curve from a) and equation III.A.5, green: experiment.

by the heat diffusion model, when y_0 is moved along the height of the crystal. The temperature at the excitation point is indeed lower when the excitation is closer to the interfaces.

We perform the measurement illustrated in figure III.A.12b. We move the excitation spot vertically along the crystal, and we probe T_g at the same spot. The results are given in figure III.A.14b. We plot in green the experimental curve, and in blue the behaviour predicted by the heat diffusion model. We see that the experiment does not follow exactly the expected profile. Instead of increasing from 1.5 s in the center to 3.5 s by the cold finger, T_g remains rather constant along the crystal.

In order to understand this unexpectedly flat profile, complementary measurements should be performed. The first step would be to measure the complete temperature profile inside the crystal for each position of the excitation, to obtain the experimental counterpart of figure III.A.14b. Then we should be able to confirm, or not, if the heat diffusion model correctly describes the experimental temperature profile in this case. If not, it may give some hints on what additional phenomena

should be taken into account.

III.A.3.5 Thermal interfaces with the crystal

We now discuss the possibility to improve the thermal conductance at the interfaces in order to reduce the temperature at the excitation point. The main leverage at our disposal here is the pressure applied on the crystal. It has been demonstrated that the thermal conductance at an interface increases linearly with the pressure between the materials [Tariq and Asif, 2016]. So increasing the pressure over the crystal seems indeed an interesting solution.

In our case we have two interfaces, with conductances h_1 and h_2 determined in the previous section III.A.3.3. Increasing the pressure should improve simultaneously the two interfaces. To get some order of magnitude, figure III.A.15 show T and T_g at the excitation spot, when multiplying h_1 and h_2 by a common factor. This figure is a prediction from the heat diffusion model, with all parameters other than h_1 and h_2 kept equal to figure III.A.11. If we improve the conductances by a factor 10, we decrease the temperature at the center from 4.1 K to 3.6 K (black curve), which corresponds to increasing T_g from 1.5 s to 4 s (red curve). According to figure III.A.2, this results in an enhancement of the diffraction efficiency from 0.3 to 1.5 %, which is already an interesting factor 5.

Note that $T(y_0)$ converges to a limit value when h_1 and h_2 tend to infinity. The limit value is derived from equations III.A.8 and III.A.11. This value gives the maximal T_g that we can expect by improving the thermal interfaces.

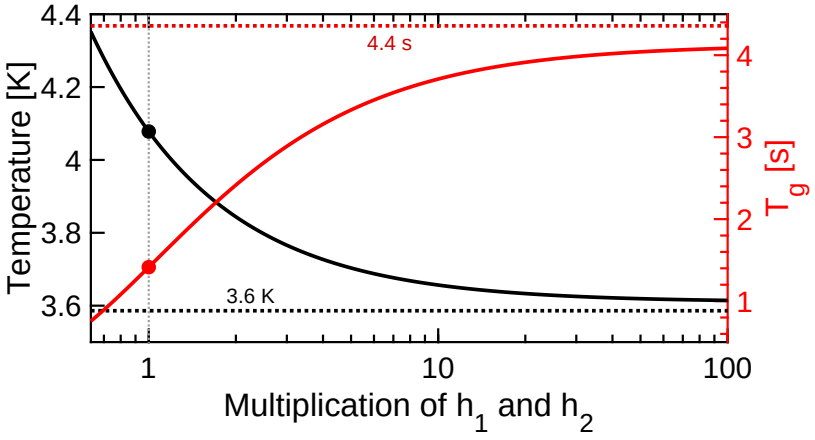

Figure III.A.15: Evolution of T (black) and T_g (red) when h_1 and h_2 are multiplied by a common factor – The curves converge to asymptotes shown in dashed lines.

Figure III.A.17 shows T_g when increasing the pressure applied over the crystal. The programming beam is identical as before, chirped over 10 GHz at the center

of the thulium inhomogeneous linewidth, with 20 mW of mean optical power. As mentioned in previous section III.A.3.3, the crystal is pressed on the cold finger using a clamp, itself screwed to the cold finger. The clamping is depicted schematically in figure III.A.16. The pression is increased by increasing the torque applied on the screws.

In figure III.A.17, P_{ref} refers to our reference pressure, which was applied for all the measurements of this thesis, except in this section where we vary the pressure. In particular, the estimation of h_1 and h_2 in section III.A.3.3 was made under this pressure P_{ref}. It is actually close to the maximal pressure that we can apply without breaking the screws, with our smallest crystal of 90 mm^2. That is why we only show pressure below this point.

P_{ref} corresponds to a torque of 100 N.cm applied on four M2.5 screws. It is difficult to estimate the resulting force or pressure, since it largely depends on empirical parameters, in particular the cleanliness of the screw threads. Considering the torque applied at room temperature and the differential contraction of the materials at cryogenic temperature, we estimate this value at a few tens of MPa.

The red curve depicts the behaviour of a crystal with a surface $S = 90$ mm^2. This is the reference crystal of this chapter: all curves have been taken with this crystal, except in the present figure III.A.17. Due to practical limitations, we could only take one point between 0 and P_{ref}.

We observe that, instead of increasing linearly as we expected from figure III.A.15, T_g seems to saturate. We conclude that here, increasing the pressure does not increase h_1 and h_2. The clamping is depicted schematically in figure III.A.16a. For the 90 mm^2, the clamp is larger than the crystal. We deem possible that, when screwing stronger, the clamp actually bends over the crystal instead of pressing uniformely. This would result in a decrease of h_2, which may explain that T_g does not increase as much as expected.

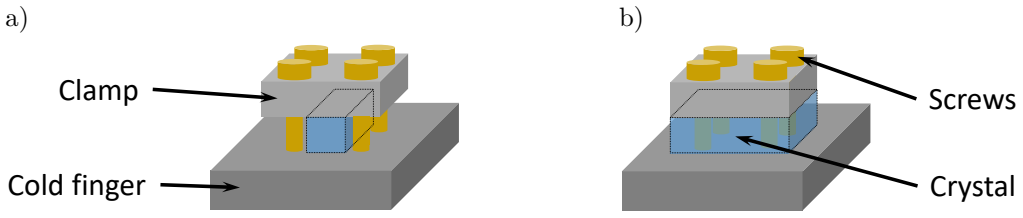

Figure III.A.16: Schematic of the clamping of the crystals – a) 90 mm^2 crystal, b) 235 mm^2 crystal.

We repeat the experiment with a larger crystal of 235 mm^2. As depicted in figure III.A.16b, now the clamp has the same size than the crystal, so it should not bend.

The result is shown in blue in figure III.A.17. Although we cannot explore high pressure to not break the screws, T_g seems more linear, in accordance with figure III.A.15.

The results presented here are only first hints on the behaviour of T_g versus the pressure applied on the crystal. More measurements are necessary in order to conclude. It should be useful to acquire more points between 0 and P_{ref} to observe with more detail the saturation with the 90 mm^2 crystal. We may also try to change the clamping setup to allow higher pressure.

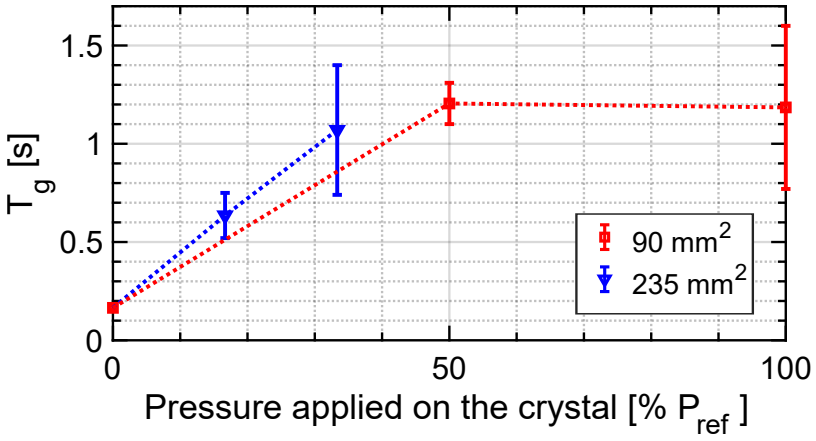

Figure III.A.17: T_g versus pressure applied on the crystal, for two sizes of crystal.

Beside the pressure, we also attempted to improve the thermal contact by changing the thermal joint at the interface with out-of-the-shelf materials. The cold finger is initially coated with a thin layer of gold. We added either a supplementary film of gold, or cryogenic thermal grease. We could not observe any improvement of the diffraction efficiency. This suggests that, from a material point of view, the original gold coating is not limiting heat dissipation.

In conclusion, although it should be theoretically possible to increase T_g by pressing the crystal stronger, it does not seem possible without reworking the setup. In particular, the clamp should be reworked to allow more pressure, and to prevent any bending.

III.A.4 Conclusion

In this chapter, we have seen that canceling the drop of T_g observed under wideband excitation could increase the diffraction efficiency by a factor ten. We have presented preliminary results of SHB spectroscopy of Tm^{3+}:YAG, allowing to measure spin lifetime under optical excitation in various configurations.

We have identified the thermal mechanisms responsible for the decrease of T_g with the excitation optical power. In our setup, heat diffusion inside the crystal on the one hand, and thermal conductance at the interface on the other hand, have similar contributions to the temperature elevation at the excitation point. We presented first attempts to reduce those two contributions. We identified leverages of improvement, by moving the excitation spot closer to the cold finger, and pressing the crystal stronger. However, for the time being, we could not obtain a notable increase of T_g.

Despite unexpected experimental behaviour, the proposed approach seems theoretically promising to us. Complementary measurements should be performed in order to confirm the results presented here. In particular, it would be interesting to perform more complete temperature measurements inside the crystal in the different configurations. This would allow to confirm that the leverages identified are relevant, and can effectively be used to increase the diffraction efficiency.

Chapter III.B

Apparatus function of the rainbow spectrum analyzer

The apparatus function of a spectrum analyzer is defined as its frequency response to a monochromatic input. It is a crucial property, as it defines in particular the resolution of the analyzer, and the multi-signal dynamic range, that is how much will a strong signal contaminate the whole band. We remind that the principle of the rainbow spectrum analyzer is to write an ensemble of transmission gratings in the crystal, by sweeping synchronously the frequency and the angle between the programming beams. The detailed description is given in section I.3.2.

Two analytical models of the apparatus function of the analyzer have been developed in the past. However, based on the study of the spectro-spatial RF filter carried out during this thesis, we suspect that these two models may overlook some physical phenomenon. In this chapter III.B, we establish a novel model of the apparatus function of the rainbow spectrum analyzer, by extending the model of the spectro-spatial RF filter. Our objectives are to obtain an intuitive understanding of the physical phenomena ruling the apparatus function, and to determine the importance of several parameters in our experimental setup.

In the first section, we introduce an heuristic approach of the physical processes at stake in the rainbow spectrum analyzer, and we present the two analytical models which have been developed in the past, showing their limitations. In section two, we expose our novel analytical model describing the apparatus function of the rainbow spectrum analyzer. In the third section, we use our model to identify and explain intuitively the phenomenon ruling the apparatus function. For this, we apply the model to intentionally exaggerated parameters, in order to magnify the different effects. Note that this implies broad and distorted apparatus functions, which do not represent the true experiment. This is the object of section four, in which we apply the model to our true experimental conditions, to determine the importance in practice of the effects identified previously.

III.B.1 Introduction

In this first section, we introduce the problematic. First, we present an intuitive approach of the model, in order to ease the comprehension of the whole chapter. Then we present the two models of apparatus function of the rainbow spectrum analyzer that have been developed in the past.

III.B.1.1 First approach of the model

In this subsection, we present an intuitive interpretation of how the gratings are written inside the crystal. The interpretation discussed here is not detailed nor justified. Its role is simply to provide a first approach of the analytical model discussed in detail in the rest of the chapter.

In all the chapter, we will consider 7 mm-wide crystal. We will consider that the programming and signal beams are gaussian, with a radius at $1/e^2$ of 1.5 mm. The angle between the two programming beams varies between 0 and 320 mrad. These values are the values of our experiment. The configuration and the geometry of the crystal are recalled in figure III.B.1.

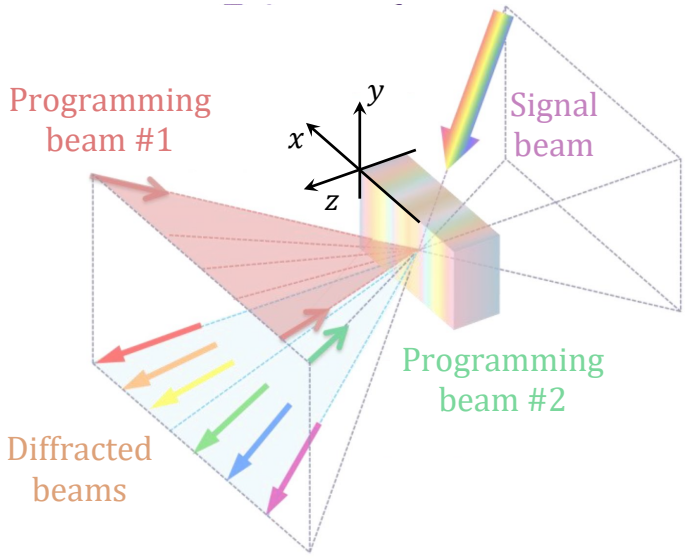

Figure III.B.1: Geometry of the crystal– The beams propagate around direction z. The transverse position x will be the variable of interest in all this chapter. The diffraction grating is indeed a function of x. The Fourier conjugate of variable x is the diffraction angle θ.

As explained in the introductive section I.3.2, we program the spectro-spatial grating by sweeping in frequency and in angle the programming beams. This creates an ensemble of independent spatial gratings, each one corresponding to a class of ions. The phase relation between each spatial grating gives the spectral component

of the overall grating. However, each spatial grating can be treated independently. Let us consider one specific frequency, as illustrated in figure III.B.2.

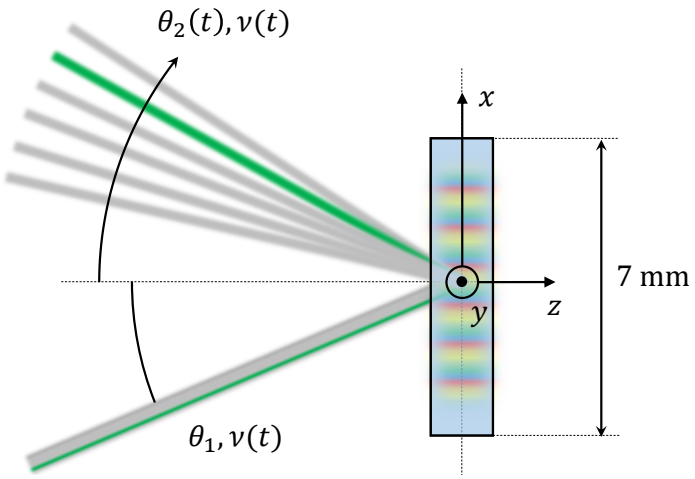

Figure III.B.2: Programming the gratings – This figure corresponds to figure I.20a from the introduction. The laser frequency ν is chirped, and one of the two beams is swept angularly. Each frequency from the chirp writes its own grating along direction x, and all gratings coexist simultaneously in the crystal. In figure III.B.3 we consider the grating corresponding to one frequency, for example here the green frequency.

We illustrate in figure III.B.3 the transmission profile that we can intuitively expect from the grating. The transmission grating is created by the interference fringes between the two programming beams. The interference is a sinusoidal function, so we also expect the grating to be sinusoidal. If the incoming beams were infinitely wide, we would obtain a sinusoidal grating along the width of the crystal. In all this chapter, we will note $K(x, \nu)$ the transmission of the grating if the beams were infinitely wide along x. This function describes the transmission along the transverse dimension x of the grating made of the ions of resonnance frequency ν. This function is obtained formally from our analytical model, and will be presented in detail in this chapter.

In reality, the two programming beams and the signal beam are not infinite along x. They have a gaussian shape, noted $G(x)$, considered identical for the three beams. The grating is only effective where the three beams overlap: the intereference only occurs where the programming beams overlap, and the resulting grating is only effective where it overlaps with the signal beam. The superposition corresponds to a gaussian envelope given by $G(x)^3$. In the following, the word "grating" will always refer to this effective grating, given by $G^3 \times K$.

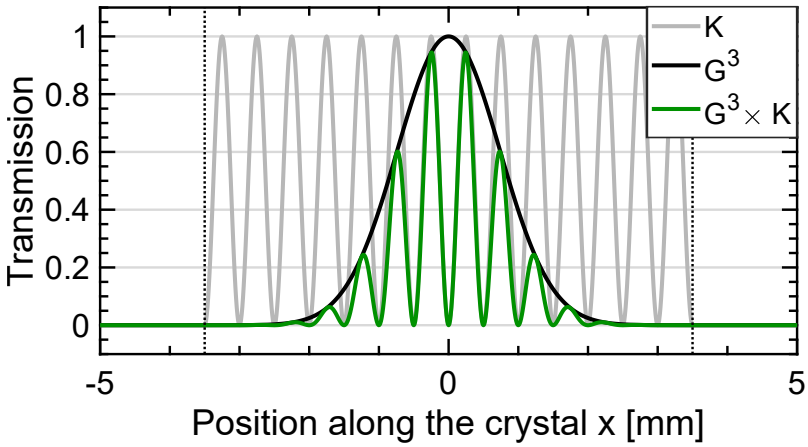

Figure III.B.3: Illustration of the spatial grating for one frequency among the chirp bandwidth – If the three beams were infinitely wide, we would expect a sinusoidal grating over the crystal (white background). This is represented by the function K. In reality, the beams have a gaussian shape, noted $G(x)$. The superposition of the three beams limits spatially the grating to an envelope G^3, so the effective grating is given by $G^3 \times K$. Note that the spatial frequency of the grating has been decreased for readability; it is typically 100 times higher in reality (see section III.B.3.3). The crystal size and the gaussian are to scale.

The representation that we just presented is an intuitive representation of the spatial components of the spectro-spatial grating. As we will see in this chapter, in the ideal case, this interpretation is indeed correct. However, in some situations, the function K can become distorted: both the amplitude and the spatial frequency of the grating can vary along the crystal. We remind that, in the rainbow spectrum analyzer, we detect a frequency by detecting the diffracted beam on a camera in far field. We understand that, if the grating is distorted, then the spatial diffraction is less sharp, which broadens the apparatus function of the analyzer. Our objective is to obtain a function K as close to a sine as possible, so that the diffraction is only limited by the gaussian shape of the beams.

The diffracted field in near field is proportional to the transmission of the grating. In the Fraunhofer diffraction regime, the spatial profile of the beam in far field is then obtained by spatial Fourier transform of the spatial profile of the beam in near field. The apparatus function, which is a function of the frequency, is finally deduced from the shape of the diffracted beam in far field along, function of the angle θ, with the angle/frequency correspondance given by the programming beams.

In this chapter, we present an analytical model describing the grating and the diffraction, in order to obtain the apparatus function of the spectrum analyzer. We will first identify and discuss the phenomena causing the distortion of the amplitude and spatial frequency of K. Then, we will determine their influence in experimental conditions.

III.B.1.2 Previous works

Two previous studies have already proposed models of the apparatus function of the rainbow spectrum analyzer. However, in the light of the work performed on the RF filter, we suspect that their hypothesis may lead to overlook some physical phenomenon. The aim of the present work is to develop a novel analytical model of the apparatus function with weaker hypothesis, and to obtain a better description of the rainbow spectrum analyzer. Simultaneously, we want to take advantage of a more detailed model to gain a better understanding of the physical phenomena occuring in the experiment.

A model of the apparatus function is presented in [Lavielle, 2004]. The derivation is performed in the hypothesis of infinitely long programming delay τ. Similarly to the RF filter discussed in section II.4.2, at long programming delay, causality can be discarded. In this case, equations are greatly simplified, and we can obtain an easy analytical formula. However, one of our objectives is to study the influence of causality on the apparatus function. Indeed, we demonstrated in section II.13 the crucial influence of the programming delay on the spectro-spatial RF filter. We want our model to determine if the programming delay is also an important parameter in the spectrum analyzer. If it is, we will determine the minimal delay resulting in a satisfactory shape.

The other model describing the apparatus function is discussed in [Lorgeré et al., 2002]. This time, the model claims to include causality, and to apply also to short programming delays. Although the paper does not provide an interpretation in terms of diffracted field, the work discussed in the present chapter allows to understand the implication of the formula in terms of near field of the diffracted field. The analysis is presented in appendix A.5. We find that, according to this paper, the diffracted field in the crystal can be described as an oscillating function contained in a truncated gaussian envelope. As illustrated in figure III.B.4a, without programming delay, the truncature happens in the middle of the crystal. When the delay is increased, the place of the truncature moves towards the side of the crystal, as depicted in figure III.B.4b. We show in figure III.B.4c that the half gaussian in near field results in a wide apparatus function with lorentzian shape. As the delay increases and the envelope of the near field becomes gaussian, the far field, and so the apparatus function, achieve a sharper gaussian shape.

This model was used to choose a suitable programming delay in our current experiment. However, we suspect that it may not describe the general case. Indeed, as we will see in this chapter, the truncature illustrated in figure III.B.4 is a consequence

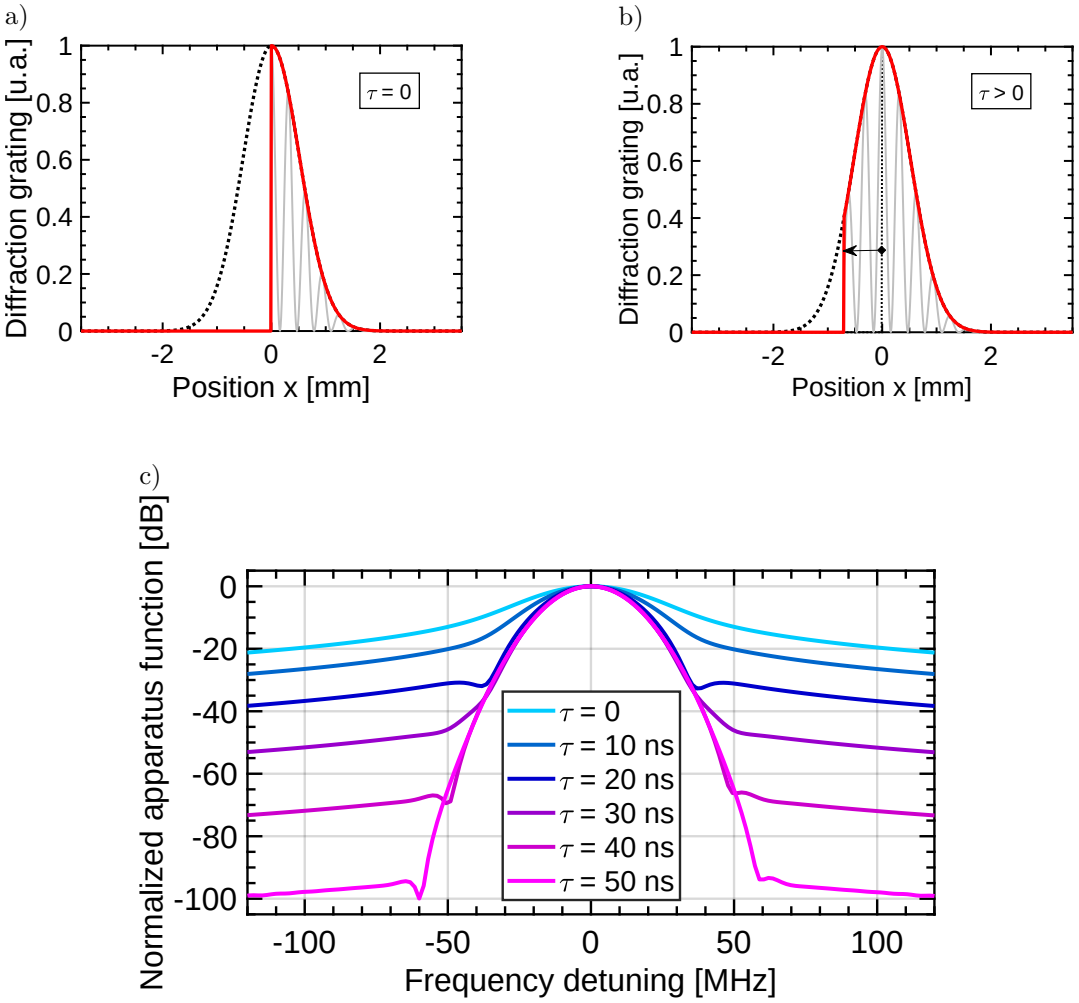

Figure III.B.4: a) Illustration of the model from [Lorgeré et al., 2002] – Black dots: superposition of the three beams G^3, grey: transmission of the diffraction grating $G^3 \times K$ (spatial frequency not to scale), red: amplitude of the transmission of the diffraction grating. According to this model, if $\tau = 0$, the gaussian amplitude of the transmission of the grating is truncated at $x = 0$.

b) When τ increases, the place of the truncature is moved to the left and the grating becomes more and more gaussian.

c) Apparatus function according to the model from [Lorgeré et al., 2002] for $\tau = 0$ to 50 ns. The plot is given for a programming chirp of $\Delta\nu = 20$GHz in $\Delta t = 2$ ms, and an angular sweep of $\Delta\theta = 320$ mrad in the same duration. The diameter of the beams at half intensity is 1.5 mm.

of causality. Besides, our works on the spectro-spatial RF filter from chapter II revealed that the effect of causality is not discontinuous, but ruled by the cardinal sine impulse response discussed in section II.4.1. For this reason, we suspect that some processes linked to causality may have been overlooked in the model presented in the paper, resulting in the discontinuous truncature. The study presented in this chapter will provide a physical understanding of the physical phenomenon occuring

in the spectrum analyzer, allowing to determine if some can be neglected.

In section III.B.2, we present a novel analytical model of the apparatus function, more general and with weaker hypothesis than the two aforementioned models. In section III.B.3 we will run our model with parameters intentionally more extreme than in the experiment. Although the resulting apparatus functions are artificially broad and distorted, and do not represent the real experiment, this will allow to highlight different consequences of causality. Our objective is in particular, based on the works performed on the spectro-spatial RF filter of chapter II, to understand more clearly the effect of causality in the rainbow spectrum analyzer. Finally, in section III.B.4, we will then apply the model to the real set of parameters. We will determine if the programming delay has indeed some influence on the apparatus function in the current experimental setup as predicted by [Lorgeré et al., 2002], and, if it does, quantify its effect.

III.B.2 Analytical model of the apparatus function

In this section, we present the analytical model that we developed, describing the apparatus function of the rainbow spectrum analyzer.

III.B.2.1 Diffracted field

The model of the rainbow spectrum analyzer is an extension of the model for the spectro-spatial RF filter discussed in section II.4. In the filter, we did not consider any spatial dimension. Indeed, the response of the filter only depends on the frequency, and not on the spatial shape of the diffracted beam. In the spectrum analyzer on the contrary, we perform a correspondance between angle of diffraction and frequency of the signal. So the diffraction must be spatially as sharp as possible, in order to distinguish close frequencies. The sharpness of the diffraction, or in other words the apparatus function, gives the resolution of the spectrum analyzer.

The complete derivation of the model is given in appendix A.3. We obtain first the diffracted field in near field, *i.e.* right at the output of the crystal:

$$\tilde{\mathcal{A}}_4(x, \nu + \nu_F) \propto G(x)^3 \times K(x, \nu) \times e^{2i\pi\tau v_\theta x/\lambda}. \tag{III.B.1}$$

As in section III.B.1.1, G depicts the gaussian shape of the beams, supposed identical for the two programming beams and the signal beam. G^3 accounts for the superposition of the two programming beams and the signal beam. $K(x, \nu)$

describes the transmission of the diffraction grating along x, for the class of ions of frequency ν, in the case where the beams are infinitely wide along x. As we will see in section III.B.3, $K(x,\nu)$ is an oscillating function of the variable x, whose amplitude and spatial frequency can vary along the crystal. Note that K was depicted as a sine function in section III.B.1. The derivation of appendix A.3 is performed in complex notation, so K is now described by an oscillating complex exponential. With $\otimes_\nu$ the convolution product of variable ν, K is defined as:

$$K(x,\nu) = \mathcal{L}_h \otimes_\nu \mathcal{L}_h \otimes_\nu \tilde{Y} \otimes_\nu \left[\tilde{A}_1^*(\nu)\tilde{A}_1(\nu - v_\theta x/\lambda)e^{2i\pi(\nu - v_\theta x/\lambda)\tau}\right]. \tag{III.B.2}$$

K can also be written equivalently in terms of Fourier transforms:

$$K(x,\nu) = F_t\left[e^{-2\Gamma t}Y(t)F_t^{-1}\left[\tilde{A}_1^*(\nu)\tilde{A}_1(\nu - v_\theta x/\lambda)\right](t-\tau)\right](\nu). \tag{III.B.3}$$

The notations are as follows:

- F_x (resp. F_t) accounts for the Fourier transform along position x (resp. time t) whose conjugate variable is the angle θ (resp. the frequency ν).
- ν is the frequency of the monochromatic signal beam. We remind that diffraction is a linear phenomenon in frequency, so that if the input is monochromatic at frequency ν, then the diffracted signal is necessarily monochromatic also at frequency ν.
- θ on the contrary can be any angle. Indeed, the objective the derivation is to quantify how a monochromatic signal at frequency ν is spread out in space.
- Γ is the homogeneous linewidth,
- Y the Heaviside causality function,
- v_θ the radial velocity of the rotating mirror,
- λ the center wavelength,
- τ the programming delay,
- ν_F the center frequency of the programming chirp.
- A_1 is again the amplitude of programming beam #1, which accounts for the programming chirp and eventually laser noise.

As mentioned in section III.B.1.1, the diffracted field in far field is given by the spatial Fourier transform of the field in near field:

$$\tilde{\mathcal{A}}_4(\theta',\nu') \propto \tilde{G} \otimes_\theta \tilde{G} \otimes_\theta \tilde{G} \otimes_\theta \tilde{K}(\theta,\nu), \tag{III.B.4}$$

where we noted $\theta' = \theta + v_\theta \tau$ and $\nu' = \nu + \nu_F$. $\otimes_\theta$ accounts the convolution product of variable θ, and $\tilde{G}$ and $\tilde{K}$ for the spatial Fourier transforms of G and K.

Note that, in equation III.B.4, $\tilde{\mathcal{A}}_4$ is a function of θ' and ν' instead of θ and ν. ν' accounts for the fact that the selected RF frequency depends on the detuning between programming and signal laser. The idea is identical to the spectro-spatial RF filter (see figure II.3).

We understand θ' as a slight Doppler shift caused by the rotating mirror. It can be neglected in practice: typically, in our experiment, $v_\theta \sim 100$ mrad/ms, and $\tau < 100$ ns, so $v_\theta \tau < 10$ μrad. On the other hand, θ can range from 0 to 300 mrad. So in the end, given our angular scale, $\theta' \simeq \theta$.

We point out the fact that the Doppler effect appears under two different contributions. The first one is this global shift, which is negligible as we just explained. On the contrary, the second one is crucial and intrinsically defines the shape of the apparatus function. It accounts for an inhomogeneous grating along the x-axis. This effect is the object of section III.B.3.

III.B.2.2 Apparatus function

The apparatus function is defined as the response of the spectrum analyzer to a monochromatic signal. The resolution of the spectrum analyzer is given by the width of the apparatus function. As depicted in figure III.B.5, if the apparatus function is too wide, close signals cannot be distinguished. The response should be as sharp as possible to improve the resolution of the setup.

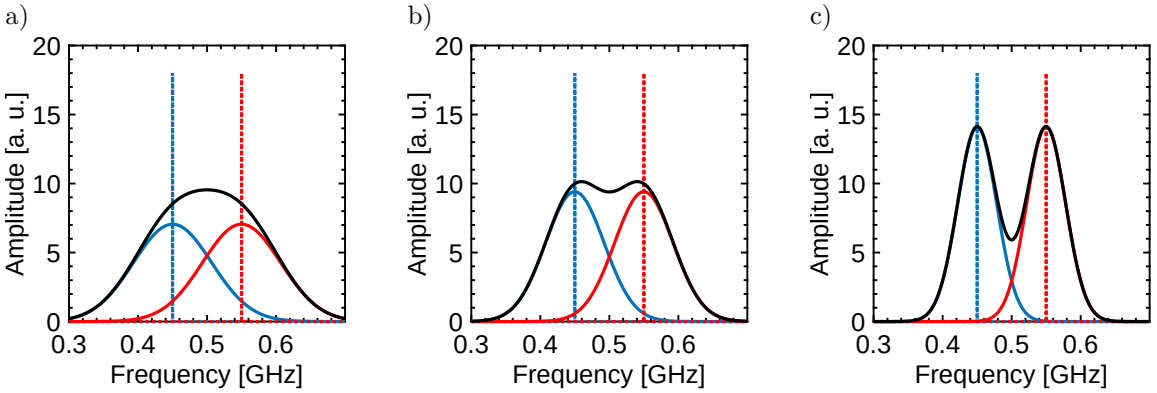

Figure III.B.5: Illustration of the resolution of the spectrum analyzer – We show in dotted line two monochromatic input signals (blue and red), and in full line the response of the spectrum analyzer of each one. When both arrive simultaneously, the signals sum up (black line). If the apparatus function is too wide, then the two signals are not distinguishable. If the apparatus function is sharp, we can distinguish the two signals.

In the previous section, we have derived the diffracted field in far field, as a

function of θ and ν. We now convert the diffracted field into an apparatus function, with a bijective correspondance between the diffraction angle θ and an equivalent frequency ν_θ. The correspondance is given by the synchronized sweeps in angle and frequency of programming beam #1 (see figure I.20). In our experiment, the chirps in angle and frequency are both linear, so θ and ν_θ are linked by a linear relation: $\nu_\theta = \frac{\Delta\nu}{\Delta\theta}\theta = \frac{r}{v_\theta}\theta$.

We note $\mathcal{S}(\nu_\theta, \nu)$ the apparatus function of the spectrum analyzer. This function depends on two frequencies ν_θ and ν. ν is the frequency of the monochromatic input signal. An input signal of frequency ν is diffracted mainly in a given direction θ_0, associated to a frequency ν_{θ_0}. If the correspondance is properly achieved, then $\nu_{\theta_0} = \nu$. However, the diffracted beam diverges angularly to some extent. The function $\nu_\theta \mapsto \mathcal{S}(\nu_\theta, \nu)$ describes how the angular dispersion of the diffracted field is wrongly understood as a frequency dispersion by the system.

The fact that the apparatus function $\mathcal{S}$ depends on both ν_θ and ν suggests that the function $\nu_\theta \mapsto \mathcal{S}(\nu_\theta, \nu)$ may be different for each signal frequency ν. In practice we see that it is qualitatively identical within the programmed frequency band, as depicted in figure III.B.6. To simplify the discussion and avoid confusion, we will now consider only the apparatus function at the center of the programmed frequency band, that is, with the previous notations, $\nu = \nu_F$. This way, we can write only $\mathcal{S}(\nu_\theta)$. We must keep in mind that ν_θ is not a true frequency. It is an "equivalent" frequency deduced by the spectrum analyzer from the angle/frequency correspondance. Ideally, $\mathcal{S}(\nu_\theta)$ should be a Dirac function at $\nu_\theta = \nu$.

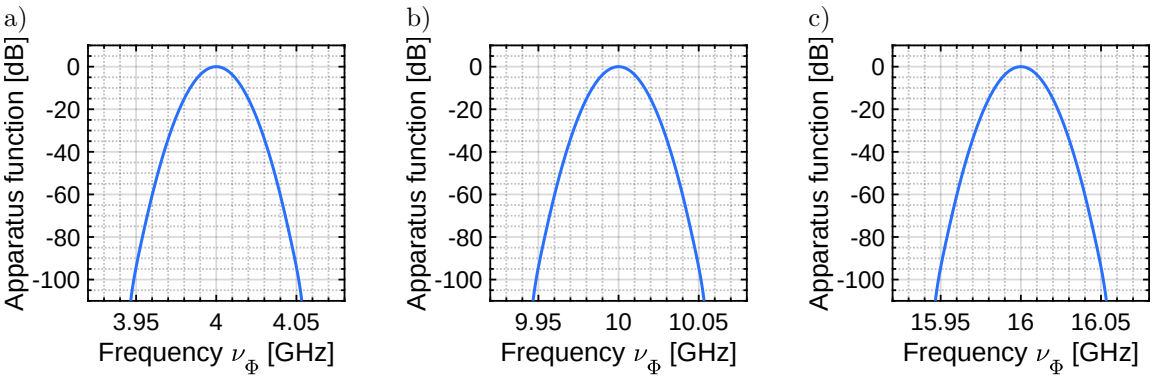

Figure III.B.6: Example of apparatus function for three different input frequencies $\nu = 4$ (a), 10 (b) or 16 (c) GHz – The curves are plotted for a chirp of $\Delta\nu = 20$ GHz in $\Delta t = 2$ ms, an angular chirp of $\Delta\theta = 320$ mrad of the same duration Δt, and a programming delay $\tau = 50$ ns. The curves are identical for the different frequencies. In the following, for simplicity, we will only consider the center frequency of the programming bandwidth ν_F. In terms of RF equivalent frequency ν_θ, it corresponds to $\nu_{\theta_0} = \Delta\nu/2$. Here, this is equivalent to consider that all curves are equal to figure b), which has $\nu_{\theta_0} = 10$ GHz.

III.B.3 Interpretation of the model

In the previous section, we have derived an analytical model describing the apparatus function of the spectrum analyzer. We now exploit this model to obtain a physical interpretation of the phenomenon occuring in the spectrum analyzer. The present section is not intended to describe the real experiment, but to understand some of the physical processes happening. For this, we run the model with parameters intentionally far from the reality, in order to exacerbate the effect of causality.

In this section, we discuss the relation between causality and Doppler effect in the spectrum analyzer. We see how a Doppler shift can change dramatically the apparatus function. We discuss these phenomenon by studying the diffracted field in near field, right after the crystal, where we can give an intuitive understanding. We obtain the diffracted field in far field by spatial Fourier transform, and finally the apparatus function by associating angles to frequencies.

As mentioned before, for simplicity, we only consider the response at ν_F, the center of the frequency range. We write $K(x) = K(x, \nu_F)$ and $\tilde{\mathcal{A}}_4(x) = \tilde{\mathcal{A}}_4(x, \nu_F)$. With these notations, the diffracted field in near field is given by $\tilde{\mathcal{A}}_4(x) = G(x)^3 \times K(x)$.

We recall the principle of the programming beams in the spectrum analyzer in figure III.B.5, highlighting the places of importance to understand the effect of Doppler

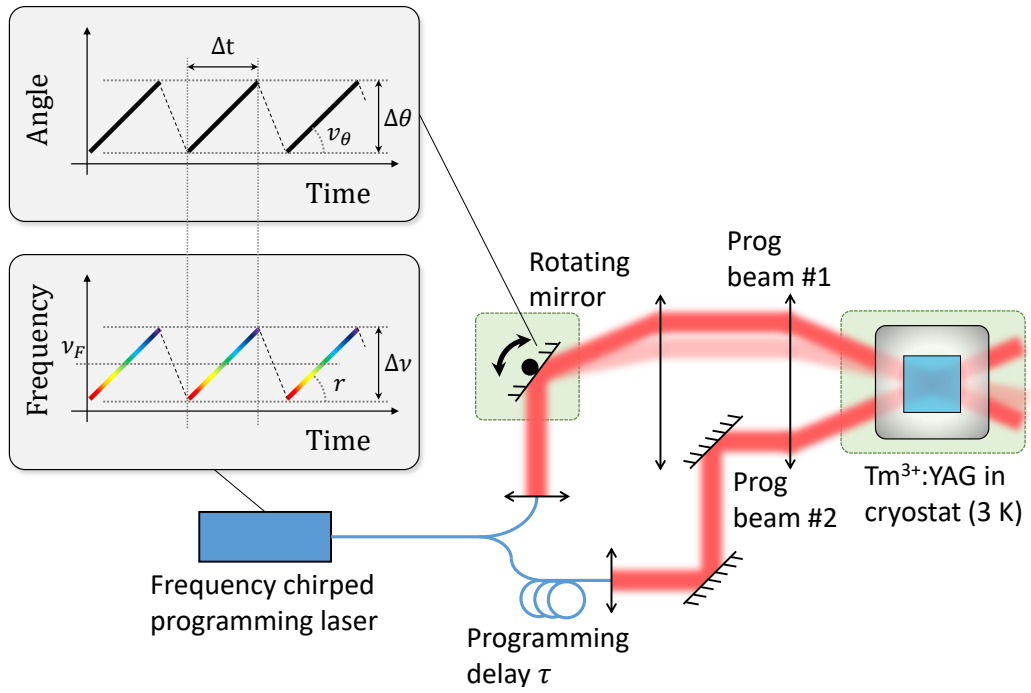

Figure III.B.7: Schematical architecture of the spectrum analyzer – The frequency chirp of the laser and the angular sweep of th emirror are synchronized. Programming beam #1 is the moving beam and programming beam #2 is the delayed beam. In figure III.B.9, we will detail the effect of Doppler shift on the rotating mirror and in the crystal (green squares).

shift. Those places are the rotating mirror and the crystal. In the following, we detail the influence of Doppler effect at those two spots.

III.B.3.1 Amplitude of the grating

In figure III.B.8, we plot in blue line the square modulus of the function K along the crystal. We remind that K describes the transmission of the diffraction grating when the three incident beams are infinitely wide along x. In a real situation with finite beams, the transmission of the grating, so also the diffracted field, is given by the product $K \times G^3$. Note that, as illustrated in section III.B.1.1, K is an oscillating function: here we show the amplitude of K, which is the envelope of this oscillation.

a)

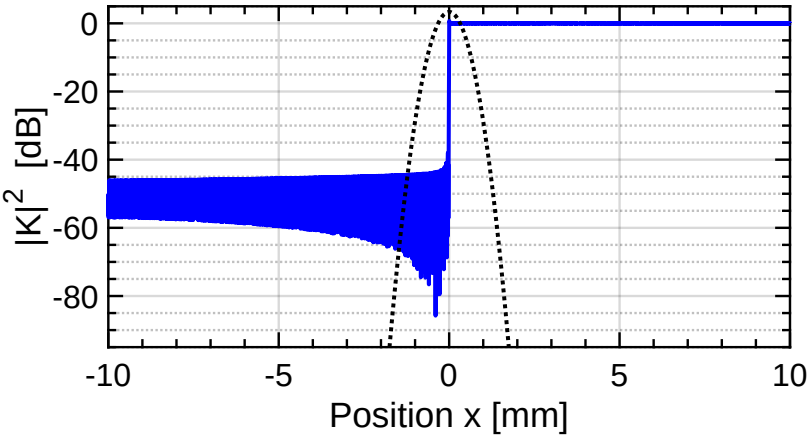

b)

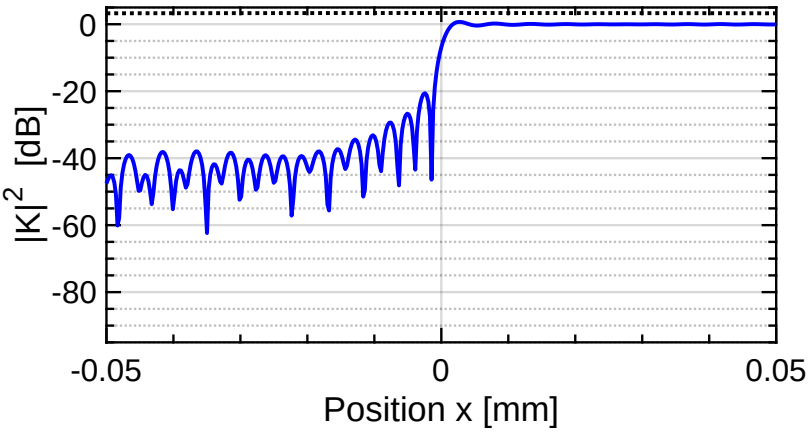

Figure III.B.8: $|K|^2$ versus x (blue line) – a) We remind that K describes the diffraction grating if the programming and signal beams were infinitely wide. We plot in dashed line $|G^3|^2$, which describes the superposition between the programming and signal beams. The diffracted power is $\tilde{\mathcal{A}}_4 \propto |G^3 \times K|^2$. $|K|^2$ is plotted for $\Delta\nu = 10$ GHz, $\Delta t = 1$ μs, $\Delta\theta = 320$ mrad, $\tau = 0$.

b) Close-up on the transition zone at $x = 0$.

Figure III.B.8b shows two different regions: in the region $x > 0$, the amplitude of K is almost constant. In the region $x < 0$, $|K|^2$ dramatically drops to less than -40 dB, and decreases slowly. This behaviour is similar to the model from [Lorgeré et al., 2002], illustrated in figure III.B.4, except that the transmission does not fall exactly to zero for $x < 0$. Note that figure III.B.8 is plotted in logarithmic scale, whereas figure III.B.4 was plotted in linear scale as it falls to zero. The main difference between the two models is the transition $x = 0$. As shown in figure III.B.8b, in our model, instead of a perfect truncature at $x = 0$, we observe a progressive transition. The shape of the transition is rather complex, with strong oscillations in zone $x < 0$, and small oscillations in the zone $x > 0$, which gradually disappear. As we will see in section III.B.4, this progressive transition around $x = 0$ changes radically the conclusions of our model compared to [Lorgeré et al., 2002], when applied to our experimental parameters.

Figure III.B.8 can be explained by the Doppler effect as depicted in figure III.B.9. A Doppler shift occurs when the programming beam #1 reflects on the rotating mirror. As illustrated in figure III.B.9a, the mirror rotates around its center. In the center of the mirror, no Doppler shift occurs (zone 2). The beam has a spatial extent and also reflects on the sides of the mirror. In this illustration, the mirror rotates counter-clockwise. As a result, in zone 1, the reflexion spot moves in the same direction than the light, which experiences a positive Doppler shift. Inversely, in zone 3, the light experiences a negative Doppler shift. As a result, after the rotating mirror, the frequency of the chirp is not homogeneous along the x axis. According to equation III.B.2, the shift is given by $-v_\theta x/\lambda$. With the parameters of figure III.B.8, this corresponds to 400 MHz at 1 mm from the center.

The Doppler shift is very small compared to the 400 THz optical frequency. However, it can have important consequences on the diffraction grating. Indeed, as depicted in figure III.B.9b, this shift can be large compared to the frequency difference with programming beam #2. We remind that programming beam #2 is delayed, with a programming delay τ (see figure III.B.7). The two beams originally experience the same frequency chirp, since they originate from the same laser. In zone 2, there is no Doppler shift, so the effective delay τ_{eff} between the chirps is exactly the programming delay τ. In zone 1 where $x < 0$, as we saw before, beam #1 is blue-shifted by the quantity $-v_\theta x/\lambda$. As a consequence, the delay between the chirps is artificially reduced. In zone 3 where $x > 0$, it is the contrary and $\tau_{\text{eff}} > \tau$. With r the chirp rate, the effective delay reads $\tau_{\text{eff}} = \tau + v_\theta x/(\lambda r) < \tau$. In the configuration of figure III.B.8, this corresponds to an addition of 40 ns at 1 mm from the center. As a consequence we obtain a linear distribution of effective delay along the x-axis.

Note that, beside the change of effective delay, the Doppler shift also implies that the chirps of beams #1 and #2 do not correspond exactly anymore. So the effective programmed bandwidth is also reduced on the sides of the crystal.

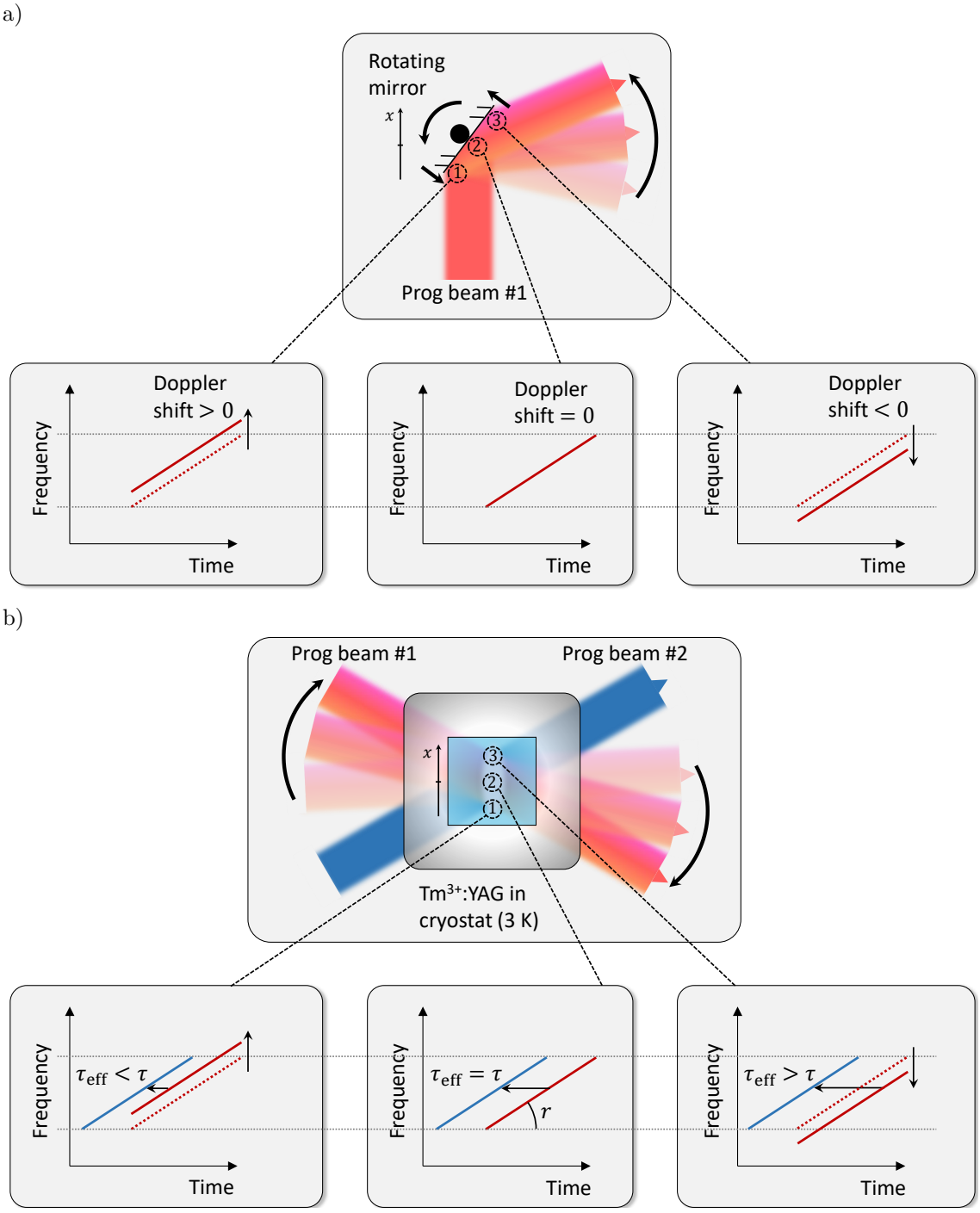

Figure III.B.9: a) Influence of Doppler effect on the rotating mirror – In the inserts: dotted line = frequency chirp before the mirror, full line = frequency chirp after the mirror. In zone 1, the beam is blue-shifted by the velocity of the mirror. In zone 2 it is not shifted. In zone 3 it is red shifted. The Doppler shift is equal to $-v_\theta x/\lambda$.

b) Influence of Doppler effect in the crystal – Programming beam #2 (in blue here) is a replica of beam #1, but immobile and delayed by τ. In zone 1, the blue shift of beam #1 is equivalent to a delay $v_\theta x/(\lambda r)$. So the effective delay between the beams is $\tau_{\text{eff}} = \tau + v_\theta x/(\lambda r) < \tau$. In zone 2, $\tau_{\text{eff}} = \tau$, and in zone 3, $\tau_{\text{eff}} > \tau$. This results in an inhomogeneous delay along the x-axis.

The transition at $x = 0$ in figure III.B.8 can be interpreted using the spectro-spatial RF filter. Indeed, this provides an intuitive understanding in terms of effective delay and causality. We consider that at each position x is written a spectro-spatial filter, each one with a slightly different excitation due to the Doppler shift. The spatial shape of the diffracted field along x is given by the transmission of all these adjacent filters.

We plot in figure III.B.10 the filter transmission for $\tau = -0.5$ to 0.5 ns, for a 10 GHz filter like in figure III.B.8. Note that this curve is similar to figure II.23, but with negative delays. We remind that we only consider the center frequency of the filter. We see that the transmission of the grating is reduced by more than 30 dB between 0.5 and -0.5 ns. With $\tau_{\text{eff}} = v_\theta x/(\lambda r)$, this is equivalent to go from -0.012 mm to 0.012 mm. This is in agreement with figure III.B.8b, where the diffraction indeed decreases by more than 30 dB between those two points.

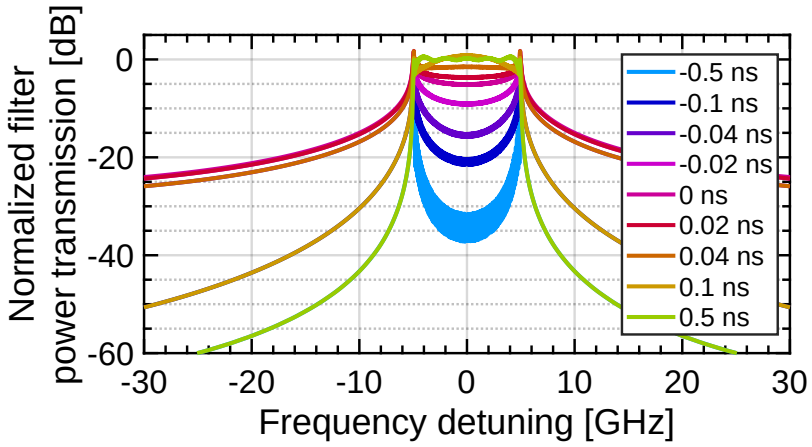

Figure III.B.10: Normalized power transmission of the spectro-spatial RF filter for positive and negative programming delays – From -0.5 to 0.02 ns, all the curves are superimposed outside the passing band.

So, this simple interpretation in terms of spectro-spatial RF filter, considering an effective delay varying along the crystal, explains correctly the drop of amplitude around $\tau_{\text{eff}} = 0$. For $x > 0$, the Doppler shift results in a positive effective delay, so diffraction is allowed by causality. For $x < 0$, the Doppler shift implies a negative effective delay. The diffraction becomes non-causal and is strongly forbidden.

Note that the transmission is not rigourously null at negative delay. Indeed, as depicted in figure II.22 showing the impulse response of the spectro-spatial RF filter, the intensity of the diffraction is given by the inverse Fourier transform of the impulse response truncated from $t = 0$. Since in our case the impulse response is essentially a cardinal sine function, its support is infinite. So the integral, although very small for negative delays, is never null. Besides, the oscillations for $x < 0$ in figure III.B.8b are a consequence of the oscillations of the cardinal sine impulse reponse.

Finally, we remark that the horizontal scale of the function K (figure II.24) depends on the parameters. It depends in particular on v_θ: if the angular speed of the mirror is decreased, then the Doppler shift is weaker on the sides of the mirror, and K is stretched out proportionnaly. It also depends on the bandwidth $\Delta\nu$: we saw in figure II.24 that the shape of the spectro-spatial filter is given by the product bandwidth $\times$ delay. For example, in figure III.B.8, $x = 1$ mm corresponds to $\tau_{\text{eff}} = v_\theta x/(\lambda r) = 40$ ns. If $\Delta\nu$ is divided by ten from 10 GHz to 1 GHz, then this point becomes equivalent to multiplying by ten τ_{eff} to 400 ns, so K is contracted.

III.B.3.2 Effect of the programming delay on the amplitude

As we saw in the previous section III.B.3.2, the position x along the crystal is equivalent to an effective delay $\tau_{\text{eff}} = \tau + v_\theta x/(\lambda r)$. In figure III.B.8, $\tau = 0$, so the transition between $\tau_{\text{eff}} < 0$ and $\tau_{\text{eff}} > 0$ occurs at $x = 0$. As shown in figure III.B.11a, if τ is increased, then this position is displaced to the left of the crystal ($x < 0$). We see in figure III.B.11b that, in this case, the step progressively disappears from the gaussian shape of the diffracted beam.

As depicted in figure III.B.11c, this effect has a dramatic influence on the shape of the diffracted field in far fied $F_x[G^3 \times K]$. At small delay, a large part of the gaussian shape in near field is truncated. In far field, this translates into a plateau, limiting the rejection of the spectrum analyzer. As the programming delay increases, the plateau decreases, and the shape of the diffracted field in far field becomes progressively closer a gaussian, increasing the rejection of the analyzer.

Note that, in this example, the plateau is dramatically decreased by 100 dB from $\tau = 0$ to 100 ns. In practice, the effect may be less important. Indeed, as explained before, it is caused by the Doppler effect, and is all the more notable when the Doppler effet is strong. For this figure we considered fast angular sweeps of $v_\theta = 32\ 10^4$ rad/s. In practice, v_θ is slower by a factor 2000, which reduces proportionally the Doppler effect. The behaviour of the apparatus function with the experimental parameters is discussed in section III.B.4.

a)

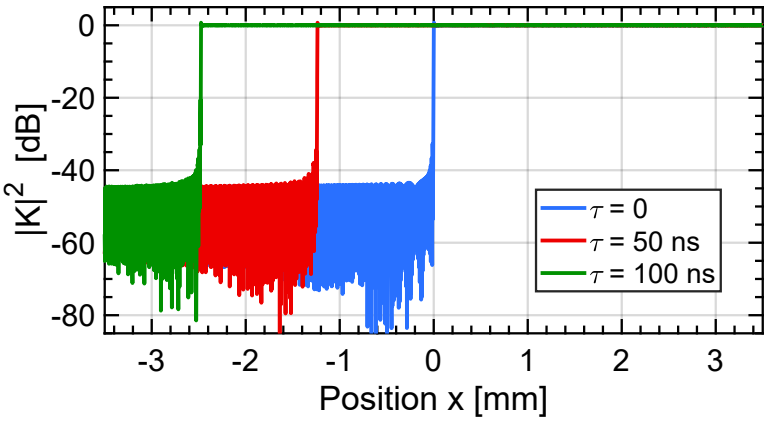

b)

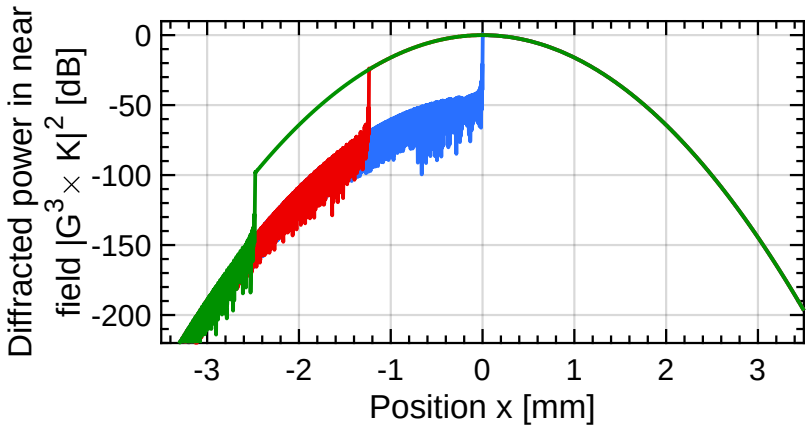

c)

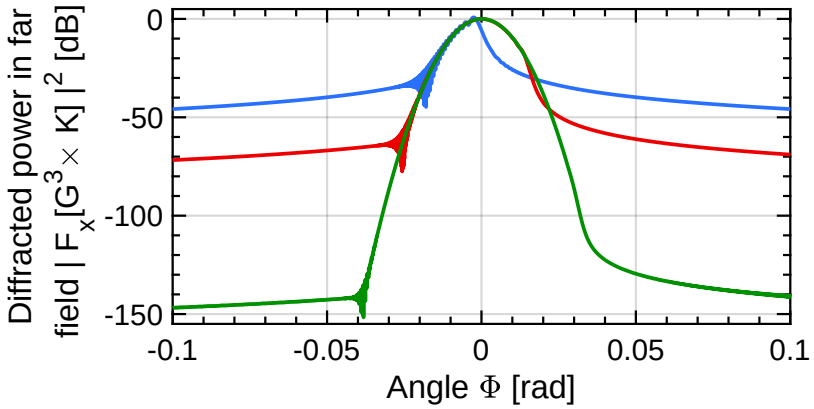

Figure III.B.11: Influence of the programming delay on the diffraction. In this figure, the parameters of the chirps are $\Delta\nu = 10$ GHz, $\Delta t = 1$ μs, $\Delta\theta = 320$ mrad, and $\tau = 0$ (blue curve), 50 ns (red curve) or 100 ns (green curve). As τ increases, the function K is displaced to the side of the crystal. The truncature progressively disappears from the gaussian shape of the diffracted field in near field. As a result, the shape of diffracted beam in far field also becomes closer to a gaussian and the plateau observed at small delay decreases, which increases the rejection of the spectrum analyzer.

III.B.3.3 Spatial frequency of the grating

In the previous section, we have seen how a long programming delay can move the transition $\tau_{\text{eff}} = 0$ outside the crystal. For large programming delays, the amplitude of the transmission of the grating becomes flat, which cancels the plateau observed in far field. The shape of the diffracted beam in far field becomes fully gaussian, resulting in a higher rejection for the spectrum analyzer. In this section, we will see that the Doppler effect also has an influence in the region $\tau_{\text{eff}} > 0$. Indeed, even if the amplitude of the grating is flat along the crystal, its spatial frequency is not necessarily constant. The Doppler effect creates a variation of the frequency of the grating along the crystal, which broadens the apparatus function.

In all the present section, we take $\Delta\nu = 10$ GHz and $\Delta\theta = 320$ mrad. We vary Δt to 1, 2 and 4 μs, which changes v_θ to 32, 16 and 8×10^4 rad/s. Note that this also changes the chirp rate r, but we saw in section II.24 that r only modifies the amplitude of the response, and not its shape. Since we only discuss the shape of the response here, we normalize the amplitude of the apparatus function to 0 dB. We take $\tau = 141$ ns, so that, for $\Delta t = 1$ ns, the transition $\tau_{\text{eff}} = 0$ is right on the edge of the crystal, at $x = -3.5$ mm (see figure III.B.11a). With this value, τ is long enough to avoid the transition $\tau_{\text{eff}} = 0$ in the three cases.

First of all, let us derive quickly the grating's spatial frequency f_x that we expect in our case. The configuration of the wave-vectors is recalled figure III.B.12. The wave-vector of the grating is $\vec{k}_g = 2\pi f_x \hat{x}$. We identified in equation II.3 that $\vec{k}_g = \pm(\vec{k}_2 - \vec{k}_1)$. With θ the angle between $\vec{k}_2$ and $\vec{k}_1$, or $\vec{k}_3$ and $\vec{k}_4$, we find by simple trigonometry that $|\vec{k}_g| = 2\sin(\theta/2)|\vec{k}_4|$. As mentioned before, we focus here on the spatial grating corresponding to the central frequency of the chirp. So, with the angle/frequency correspondance, we expect the diffraction to occur at the center of the angular sweep, at $\theta = \Delta\theta/2$. This corresponds to $\theta = 320/2 = 160$ mrad. So, with $2\pi/|\vec{k}_4| = \lambda = 793$ nm, we obtain $f_x = 2\sin(\theta/2)|\vec{k}_4|/(2\pi) = 0.2\ \mu\text{m}^{-1}$.

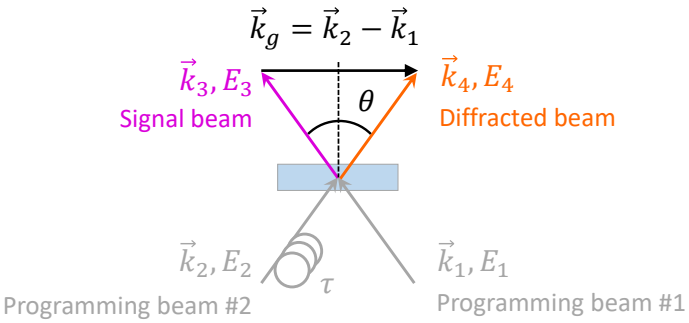

Figure III.B.12: Illustration of the wave-vectors configuration

In figure III.B.13a, we plot the spatial frequency of the diffraction grating along the crystal, given by the frequency of the function K. First, we observe that the

frequency is not constant along the crystal. We understand that this inhomogeneous frequency can result in a broadening of the diffraction: on the left of the crystal ($x < 0$), the frequency is lower, so the diffracted beam is less deviated by the grating. On the right, on the contrary, the diffracted field is more deviated by the grating. As a consequence, the angle of diffraction varies along the crystal, and the diffracted beam in far field is broadened. Second, we observe that, at the center of the crystal, where no Doppler shift occurs, the frequency of the grating is equal to the expected frequency of 0.2 μm^{-1} derived previously. This observation hints that the Doppler effect is again at the origin of this effect. Figure III.B.13b depicts the normalized apparatus function in the configuration. We observe that, indeed, when the angular sweep becomes faster the apparatus function becomes broader.

a)

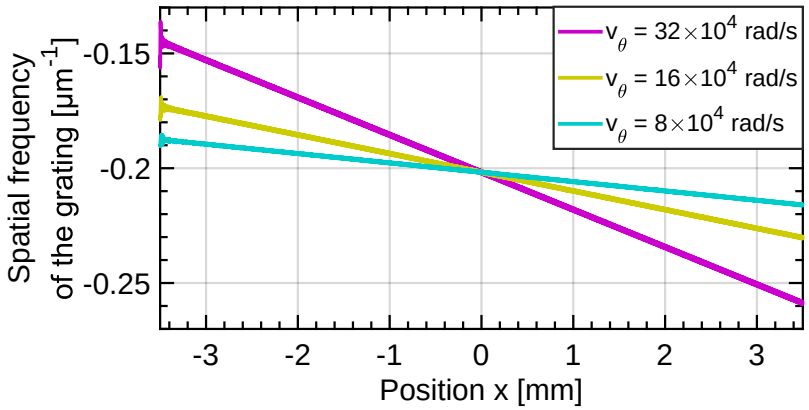

b)

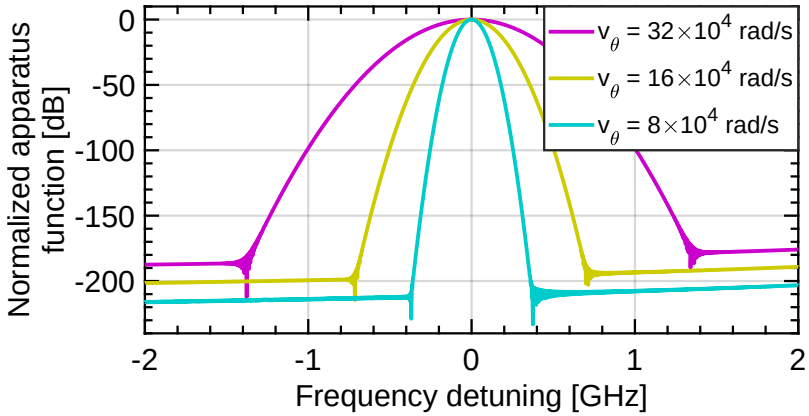

Figure III.B.13: a) Spatial frequency of the grating K along the crystal, for $\Delta\nu = 10$ GHz and $\Delta\theta = 320$ mrad. We vary Δt to 1, 2 and 4 μs, or equivalently v_θ to 32, 16 and 8×10^4 rad/s.

b) Apparatus function normalized to 0 dB. Different frequencies means different angles of diffraction. So the stronger the gradient of frequency, the broader the diffraction.

Similarly to previous section III.B.3.1, we interpret this behaviour in terms of spectro-spatial filter, which provides a more intuitive understanding. We consider that we write a spectro-spatial filter at each position of the crystal, with variations in the programming beams caused by the Doppler effect. In the previous section, we saw that the amplitude of the grating along the crystal can be described correctly by considering that each filter experiences an effective delay. We want to know if this interpretation is also sufficient to describe the frequency of the grating.

In figure III.B.14, we plot the frequency of a fictive grating made of spectro-spatial filters at each position x, with delays varying as $\tau_{\text{eff}} = \tau + v_\theta x/(\lambda r)$. We see that the frequency is constant: the description in terms of effective delay is not sufficient to describe the change of frequency along the crystal.

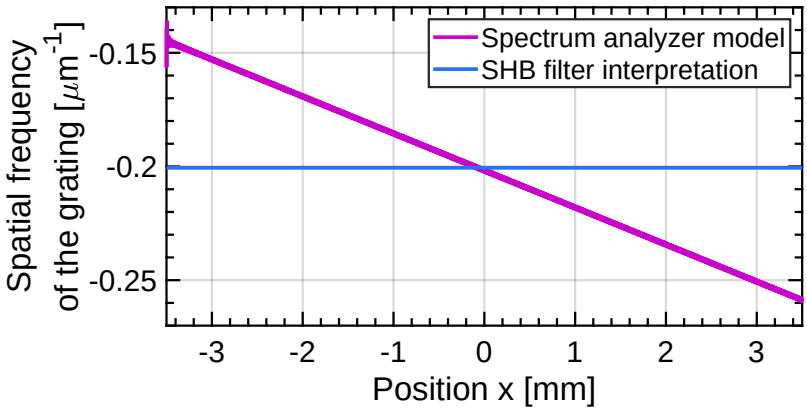

Figure III.B.14: Spatial frequency of a fictive grating made of spectro-spatial filters at each position x, with delays varying as $\tau_{\text{eff}} = \tau + v_\theta x/(\lambda r)$. We take the parameters from the curve $v_\theta = 32$ rad/s from figure III.B.13a. The frequency of the fictive grating, and does not match the model: the interpretation in terms of effective delay is not sufficient to explain the variation of frequency.

We must also take into account that, due to the Doppler effect, one chirp slides in frequency with respect to the other along the crystal. In figure III.B.9b we explained how the Doppler shift of beam #1 induces a variation of the effective delay with respect to beam #2. We illustrate in figure III.B.15 how the Doppler effect also causes the programmed band to shrink along the crystal. We remind that we consider the central frequency ν_F of the programming bandwidth, shown in green line in the figure. In zone 2 there is no Doppler shift, so ν_F is effectively at the center of the bandwidth. In zone 1, the Doppler shift is positive, so the red chirp moves up. As a consequence, the bandwidth is reduced upwards and ν_F is no longer the center of the filter. Relatively to this new filter, the green line is now in the lower frequency range, at half the Doppler shift from the center. Inversely, in zone 3, the Doppler shift is negative, so the green line is in the higher frequency range of the chirp. From the point a view of the filter, the frequency of interest is moving with respect to the filter's center frequency. Instead of considering frequency ν_F, this is equivalent to consider an equivalent frequency at half the Doppler shift from the center $\nu_{\text{eff}} = \nu_F + v_\theta x/(2\lambda)$.

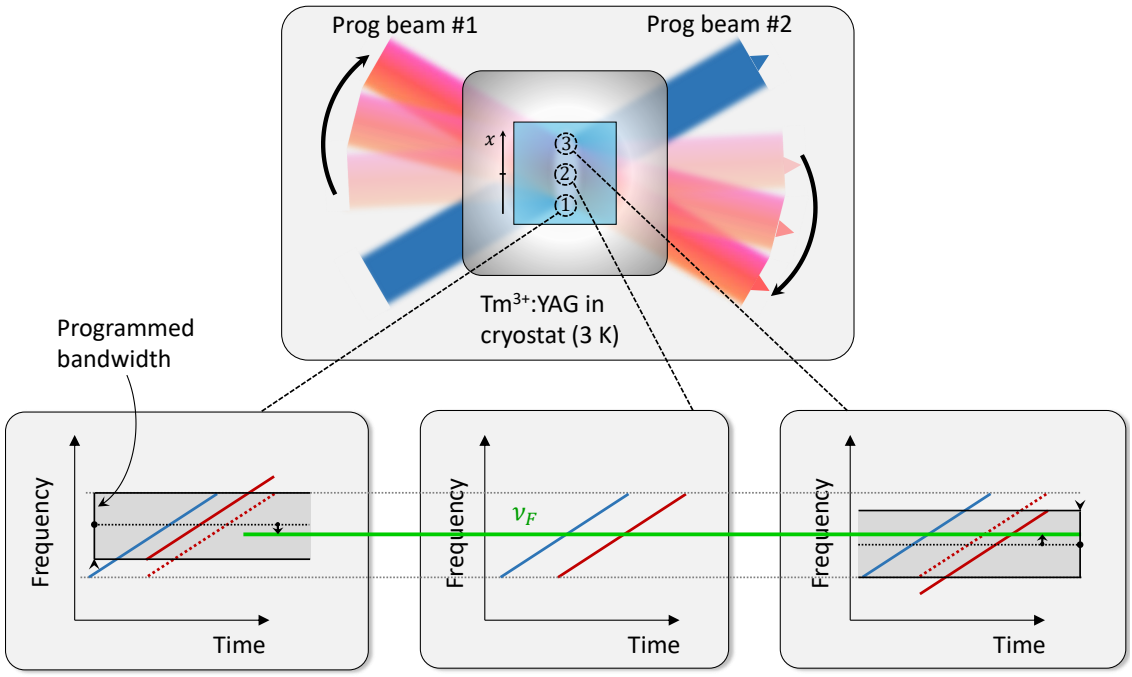

Figure III.B.15: Illustration of the change of frequency of interest along the crystal – We consider the apparatus function at $\nu = \nu_F$. In zone 2 where no Doppler shift occurs, ν_F is effectively the center of the programmed band. In zone 1, beam #1 is blue-shifted, so the bottom frequencies of beam #2 do not correspond to beam #1 anymore. The low frequencies are not programmed anymore: the bandwidth shrinks, and ν_F is no longer the center of the programmed band. The opposite happens in zone 3. The important phenomenon to understand the quadratic phase is the detuning of ν_F with respect to the center of the filter along the crystal.

In figure III.B.16, we plot the spatial frequency of a fictive grating made of individual spectro-spatial filters at each position x, when varying the delay as $\tau_{\text{eff}} = \tau + v_\theta x/(\lambda r)$, and changing the frequency of interest as $\nu_{\text{eff}} = \nu_F + v_\theta x/(2\lambda)$. We keep the same parameters as in the rest of the present section, with $v_\theta = 32$ rad/s. We also plot the corresponding curve from figure III.B.13a for comparison. The frequency of the fictive grating is effectively linear. The two curves are superimposed, which confirms that the intuitive interpretation in terms of effective delay and effective frequency is correct.

To understand how this results in a linear frequency of the grating along the crystal, we must go back to section II.5.2, which discusses the phase of the spectro-spatial filter. We showed that the phase of the filter reads $\phi = -2\pi\nu\tau$. By injecting the expressions of τ_{eff} and ν_{eff}, $\phi(x)$ reveals a second order polynome, with a quadratic term given by $-2\pi(v_\theta x)^2/(2\lambda^2 r)$. So the spatial frequency, defined as $f_x = \frac{1}{2\pi}\frac{\partial\phi}{\partial x}$, displays indeed a linear term with the negative slope $\delta f_{\text{lin}} = v_\theta^2/(\lambda^2 r)$. Let us compare this formula to figure III.B.13a. We find graphically a slope of respectively 4.1, 8.1 and 16.1 ± 0.3 $\mu\text{m}^{-1}/\text{m}$ for $v_\theta = 4$, 8, 16 $\times 10^4$ μs. The formula provides $\delta f_{\text{lin}} = 4.1$, 8.1, 16.3 $\mu\text{m}^{-1}/\text{m}$, so it is in agreement with the model.

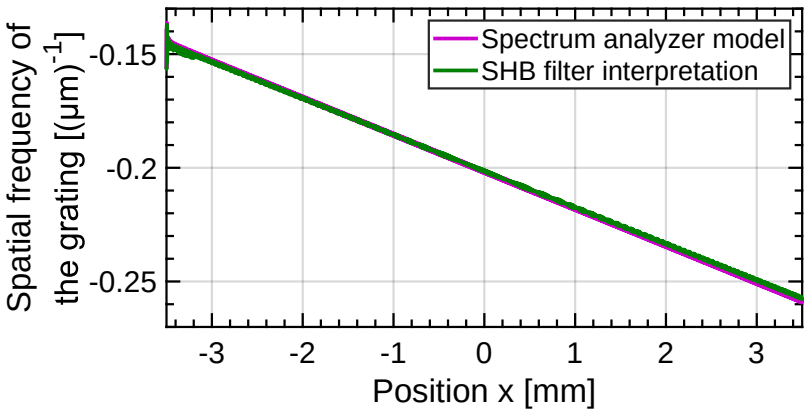

Figure III.B.16: Spatial frequency of a fictive grating made of spectro-spatial filters at each position x, with delays varying as $\tau_{\text{eff}} = \tau + v_\theta x/(\lambda r)$, and frequency of interest varying as $\nu_{\text{eff}} = \nu_F + v_\theta x/(2\lambda)$. Unlike figure III.B.14, the frequency of the fictive grating corresponds well to the spectrum analyzer model. The interpretation in terms of both effective delay and effective frequency is correct.

As a conclusion, we see that, even if the amplitude of the function K is constant over the crystal and the shape of the diffracted beam is gaussian, the apparatus function can still be very broad. Indeed, in inhomogeneous frequency of the grating over the crystal can disperse the diffraction, and broaden the diffracted beam.

The Doppler effect links the temporal phase of the diffraction and the spatial phase of the grating. The Doppler shift of diffracted beam #1 is equivalent to both a delay and a frequency detuning with respect to beam #2. As a result, the spatial frequency of the grating is not constant along the crystal: each point of the crystal diffracts the incoming beam in a slightly different direction, which broadens the apparatus function.

III.B.4 Application of the model to the experiment

In this section, we conclude our study on the apparatus function of the rainbow spectrum analyzer by applying our analytical model to the experimental conditions. We aim to obtain a simple expression of the apparatus function of the spectrum analyzer, and determine the contributions which are relevant in practice. Our parameters are $\Delta t = 2$ ms, $\Delta\nu = 20$ GHz, $\Delta\theta = 320$ mrad, and a crystal width of $\Delta x = 7$ mm.

Let us start from equation III.B.1. First of all, we saw at the end of section III.B.2.1 that, in our conditions, $\theta' \simeq \theta$. This equivalent to neglect the term

$e^{2i\pi\tau v_\theta x/\lambda}$ in equation III.B.1. We obtain simply:

$$\tilde{\mathcal{A}}_4(x,\nu') \propto G(x)^3 \times K(x,\nu) \tag{III.B.5}$$

With the help of the analysis presented section III.B.3, we will now simplify the function K in this expression, by evaluating first its phase, then its amplitude. We write $\tilde{\mathcal{A}}_4$ in polar notation by noting $\phi(x,\nu)$ the argument of $K(x,\nu)$:

$$\tilde{\mathcal{A}}_4(x,\nu') \propto G(x)^3 \ |K(x,\nu)| \times e^{i\phi(x,\nu)} \tag{III.B.6}$$

Let us compare the broadening brought respectively by the phase and the amplitude of $\tilde{\mathcal{A}}_4$. As demonstrated in section III.B.3.3, the contribution of the phase term $e^{i\phi(x,\nu)}$ is a spatial frequency chirp, with the chirp rate $\delta f_{\text{lin}} = \frac{v_\theta^2}{\lambda^2 r} = \frac{\Delta\theta^2}{\lambda^2 \Delta t \Delta\nu}$. Over the width of the crystal, this corresponds to a chirp width of $\delta f_{\text{lin}} \Delta x$. As can be deduced directly from the discussion of figure III.B.12, we can then write this width in terms of diffracton angle with the relation $\theta = \lambda f_x$. For readability, we can convert it in terms of equivalent RF frequency ν_θ by multiplying by $\frac{\Delta\nu}{\Delta\theta}$. We obtain that the broadening brought by the spatial frequency chirp is $\frac{\Delta\theta\Delta x}{\lambda\Delta t}$, equal in our case to 1 MHz.

Let us evaluate the width of the amplitude part $G^3\,|K|$. We saw in section III.B.3.2 that the narrowest shape in far field is obtained when τ is large enough so that $|K|$ is equal to 1 all over the crystal. In this case, the amplitude of the grating is simply given by G^3. We note w the radius at $1/e^2$ of one beam, *i.e.* of the gaussian function G. The diffracted profile in far field, given by spatial Fourier transform of G^3, is then a gaussian function of the variable θ, with a radius at $1/e^2$ of $\frac{\lambda\sqrt{3}}{\pi w}$. In terms of equivalent RF frequency, this corresponds to a full width at $1/e^2$ of $\frac{2\lambda\sqrt{3}\Delta\nu}{\pi w \Delta\theta}$, equal in our case to 36 MHz.

We see that, in our experiment, the width of the frequency chirp is reasonably smaller than the width of the amplitude contribution, even in the narrowest case where $|K| = 1$. As a result, we can consider that the shape of the apparatus function is only determined by the amplitude of the grating along the crystal: the spectro-spatial frequency of the grating can be considered constant. This frequency is found by noting that each position x expriences a spectral grating, whose period is given by the effective delay $\tau_{\text{eff}} = \tau + \frac{v_\theta x}{\lambda r}$. We obtain the following expression:

$$\tilde{\mathcal{A}}_4(x,\nu') \propto G(x)^3 \ |K(x,\nu)| \times e^{-2i\pi\nu(\tau+\frac{v_\theta x}{\lambda r})} \tag{III.B.7}$$

Now that we have simplified the phase of K, let us evaluate its amplitude $|K|$. We have shown in section III.B.3.2 that the amplitude of K is equivalent to the amplitude of a fictive grating, made of spectro-spatial filters at each position x, with

delays varying as $\tau_{\text{eff}} = \tau + \frac{x v_\theta}{\lambda r} = \tau + \frac{x \Delta\theta}{\lambda \Delta\nu}$. We reverse the formula: $x = (\tau - \tau_{\text{eff}}) \frac{\lambda \Delta\nu}{\Delta\theta}$.

As seen in section II.4.1, the characteristic scale over which the delay has an influence on the filter response is the width of the cardinal sine impulse response, given by $1/\Delta\nu$. In the spectrum analyzer, this characteristic delay corresponds to a characteristic distance, through the Doppler effect and the effective delay. This characteristic scale is found by injecting $\tau_{\text{eff}} = \tau - 1/\Delta\nu$ in the above forumla, giving $\frac{1}{\Delta\nu} \frac{\lambda\Delta\nu}{\Delta\theta} = \frac{\lambda}{\Delta\theta}$. This is the characteristic distance of the variations of the amplitude of K along the crystal, in particular in the transition between positive and negative delay. In our case, we obtain a characteristic scale of 2 μm.

This value must be compared to the other contributions of the amplitude of the grating, in our case the gaussian superposition of the three beams, given by G^3. In our experiment, the width of G^3 is $\frac{w}{\sqrt{3}} \simeq 1$ mm. Since the characteristic scale of variations of $|K|$ is much smaller than the width of the gaussian, the fine variations of $|K|$ can be neglected. In other words, given the 1 mm-width of the grating, the truncature made by K, which occurs over 2 μm, can be considered infinitely quick: $|K|$ can be taken as a simple Heaviside function. The position of the truncature is the position where the effective delay $\tau_{\text{eff}} = \tau + \frac{x\Delta\theta}{\lambda\Delta\nu}$ equals to zero. We finally obtain:

$$\boxed{\tilde{\mathcal{A}}_4(x, \nu') \propto G(x)^3 \; Y\left(\tau + \frac{v_\theta x}{\lambda r}\right) e^{-2i\pi\nu(\tau + \frac{v_\theta x}{\lambda r})}} \tag{III.B.8}$$

To summarize the previous analysis, if the following conditions are met:

– the width of the spatial frequency chirp along the crystal is negligible before the width of the diffracted profile, *i.e.*:

$$\frac{\Delta\theta \Delta x}{\lambda \Delta t} \ll \frac{2\lambda\sqrt{3}\Delta\nu}{\pi w \Delta\theta} \tag{III.B.9}$$

– the variations of $|K|$ are fast before the gaussian shape of the grating, *i.e.*:

$$\frac{\lambda}{\Delta\theta} \ll \frac{w}{\sqrt{3}} \tag{III.B.10}$$

then the diffracted field can be described in a simple way by equation III.B.8. Note that these conditions do not depend on the delay.

Although the analysis discussed above is rather qualitative, equation III.B.8 can also be demonstrated formally: we prove in appendix A.4 that applying the model to a programming chirp without time limits, simply written $e^{i\pi r t^2}$, results in the same expression. Indeed, removing the time limits of the chirp is equivalent to neglect the fine effects of causality, since the cardinal sine impulse response described in

figure II.22 becomes infinitely narrow.

With equation III.B.8, the response in far field then reads:

$$\tilde{\mathcal{A}}_4(\theta,\nu') = \int \tilde{\mathcal{A}}_4(x,\nu') e^{2i\pi\frac{\theta x}{\lambda}} \mathrm{d}x \tag{III.B.11}$$

$$\propto \int G(x)^3 Y\left(\tau + \frac{v_\theta x}{\lambda r}\right) e^{2i\pi\frac{x}{\lambda}\left(\theta - \frac{v_\theta \nu}{r}\right)} \mathrm{d}x \; e^{-2i\pi\nu\tau} \tag{III.B.12}$$

$$\propto \int_{-x_\tau}^{+\infty} G(x)^3 e^{2i\pi\frac{x}{\lambda}\left(\theta - \frac{v_\theta \nu}{r}\right)} \mathrm{d}x \; e^{-2i\pi\nu\tau} \tag{III.B.13}$$

where x_τ describes the position of the truncature of the grating, defined as:

$$x_\tau = \tau\lambda\frac{r}{v_\theta} = \tau\lambda\frac{\Delta\nu}{\Delta\theta} \tag{III.B.14}$$

In order to write the apparatus function $\mathcal{S}(\nu_\theta,\nu)$, we replace θ using the angle-frequency correspondance: $\nu_\theta = \frac{r}{v_\theta}\theta = \frac{\Delta\nu}{\Delta\theta}\theta$. The apparatus function is then given by the square modulus of the diffracted field in far field. We obtain:

$$\mathcal{S}(\nu_\theta,\nu') \propto \left|\int_{-x_\tau}^{+\infty} G(x)^3 e^{\frac{2i\pi x}{\lambda}\frac{\Delta\theta}{\Delta\nu}(\nu_\theta-\nu)} \mathrm{d}x\right|^2 \tag{III.B.15}$$

Note that, as shown in appendix A.5, this final expression is consistent with the apparatus function claimed in [Lorgeré et al., 2002].

We showed in figure III.B.6 that the apparatus function does not depend on the read-out optical frequency ν. So, we can simplify further the expression by discarding the dependance on ν. Writing $\mathcal{S}(\nu_\theta) = \mathcal{S}(\nu_\theta, \nu = 0)$, we find:

$$\mathcal{S}(\nu_\theta) \propto \left|\int_{-x_\tau}^{+\infty} G(x)^3 e^{\frac{2i\pi x}{\lambda}\frac{\Delta\theta}{\Delta\nu}\nu_\theta} \mathrm{d}x\right|^2 \tag{III.B.16}$$

Finally, we must consider the fact that the integral of equation III.B.16 goes to infinity. In fact, the interaction between the beams only occurs inside the crystal, so G^3, which describes this interaction, is null outside the range $[-\Delta x/2, \Delta x/2]$. As a result, the upper bound of the integral is limited to $\Delta x/2$. The lower bound depends of x_τ: if $x_\tau \geq \Delta x/2$, that is if τ is large enough to move the transition $K = 0$ to $K = 1$ outside the crystal, then we integrate over the whole width, starting from $-\Delta x/2$. On the contrary, if $x_\tau < \Delta x/2$, then the first part of the grating is cropped, and the integral starts from $-x_\tau$. We obtain a simple final expression for the apparatus function of the rainbow spectrum analyzer:

$$\boxed{\mathcal{S}(\nu_\theta) \propto \left|\int_{-\min(x_\tau, \frac{\Delta x}{2})}^{\frac{\Delta x}{2}} G(x)^3 e^{\frac{2i\pi x}{\lambda}\frac{\Delta\theta}{\Delta\nu}\nu_\theta} \mathrm{d}x\right|^2} \tag{III.B.17}$$

a)

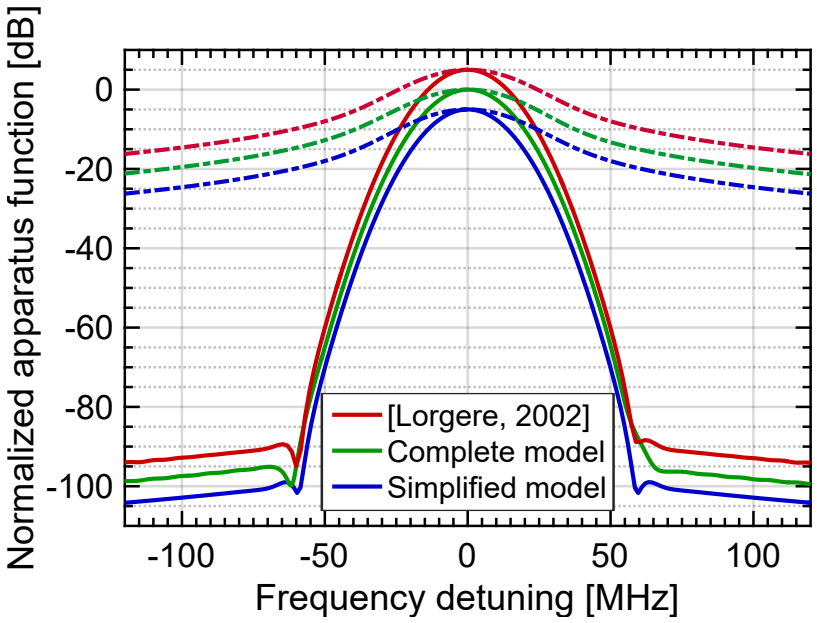

b)

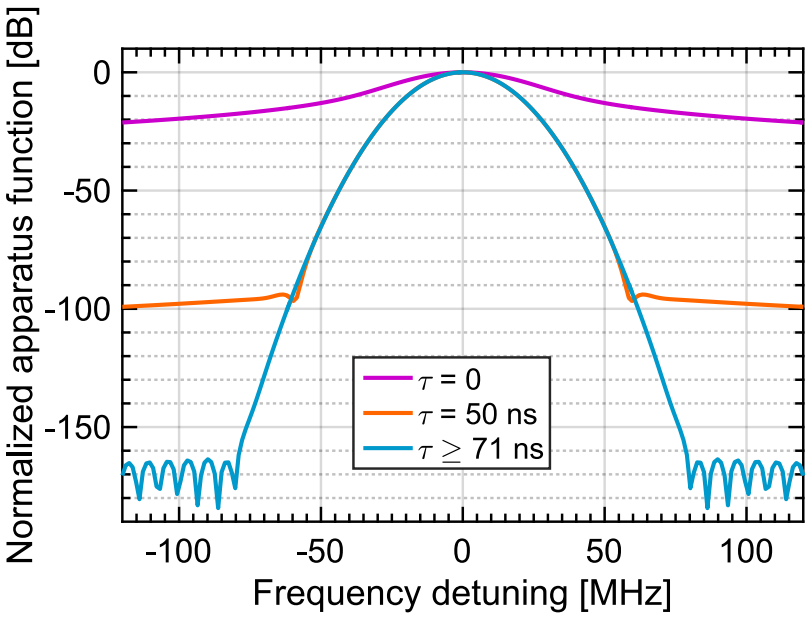

Figure III.B.17: a) Comparison between the three models in the conditions of the experiment – The model from [Lorgeré et al., 2002] (red) and the model from this thesis, in its complete (green) and simplified (blue) version, are plotted with the experimental parameters of $\Delta\nu = 20$ GHz, $\Delta\theta = 320$ mrad, $\Delta t = 2$ ms, and $\tau = 0$ (dashed line) or $\tau = 50$ ns (solid line). The red and blue curves were moved vertically by respectively +5 dB and −5 dB for readability. We see that, exept for small details due to numerical approximation, in these conditions, the three models are in perfect agreement.

b) Apparatus function for $\tau = 0$, 50 and > 71 ns – Given our experimental conditions, above 71 ns, increasing the programming delay does not improve the apparatus function. In this case, the rejection far from the signal is limited by a plateau to 160 dB. Note that this is not limiting in practice, as the level of noise is much higher.

We confirm graphically in figure III.B.17a that the model from this thesis, in both its exhaustive version (equation III.B.4) and simplified version (equation III.B.17), and the model from [Lorgeré et al., 2002] all provide the same results in the conditions of our experiment. This confirms that the analysis presented before and the resulting simple expression of equation III.B.17 are valid in our case.

One of the conlusions one can draw from our model is that, as explained above, above a certain point, increasing the programming delay τ does not improve anymore the apparatus function. Indeed, if $x_\tau \geq \Delta x/2$, then the transition of K is moved outside the crystal, and K becomes constant to 1 all over the crystal. With the definition $x_\tau = \tau\lambda\frac{\Delta\nu}{\Delta\theta}$ given in equation III.B.14, this limit value is $\tau_{\text{lim}} = \frac{\Delta x}{2\lambda}\frac{\Delta\theta}{\Delta\nu}$. In our experimental conditions, we obtain $\tau_{\text{lim}} = 71$ ns. Above this delay, the apparatus function becomes geometry-limited by the size of the crystal and the beams to the shape shown in figure III.B.17b.

We originally intended to compare the models to experimental data. However, due to a failure of our cryostat, we could not proceed to the experimental validation yet. We can compare the model to measurements taken previously with the experiment. We show the comparison in figure III.B.18. The gaussian shape of the diffracted beam is well described by the model. However, we only have access to data with long delays of 50 ns, which does not allow to observe the distortion predicted at short delay. Experimental data at short delay is necessary to confirm the models.

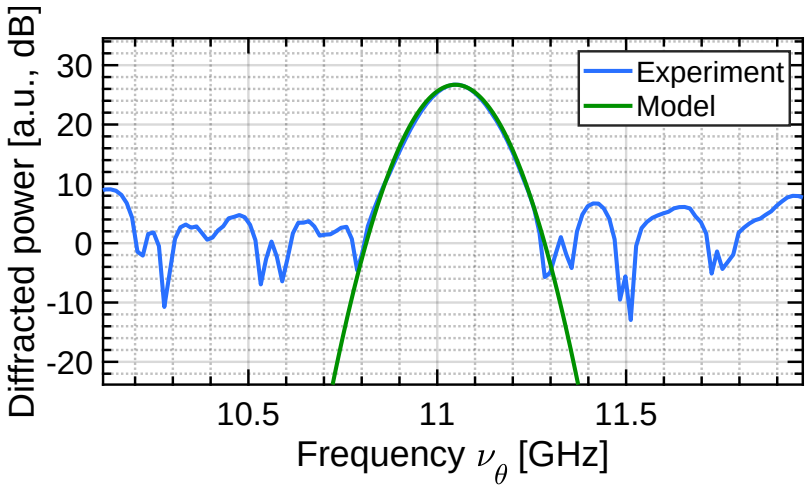

Figure III.B.18: Comparison between model and experiment – The parameters of the experiment are $\Delta\nu = 20$ GHz, $\Delta\theta = 320$ mrad, $\Delta t = 2$ ms and $\tau = 50$ ns.

III.B.5 Conclusion

In this chapter, we have developed an analytical model describing the rainbow spectrum analyzer. This model is an extension of the model for the spectro-spatial RF filter developed in chapter II, and provides the apparatus function of the spectrum analyzer. By considering that we write an independent filter at each position x, resulting in a given phase and amplitude of the diffracted field along x, we could give an intuitive explanation of the various phenomena identified, based on Doppler effect, causality, and on the behaviour of the spectro-spatial RF filter.

The motivation of this study was to obtain a better comprehension of the spectrum analyzer, and in particular the influence of causality. The model developed in this thesis, more exhaustive than models previously proposed in the litterature, allows to obtain a physical understanding of the phenomena in play. When some conditions are met, which is the case in our experiment, the apparatus function of the rainbow spectrum analyzer can be described by an simple and intuitive expression.

An experimental validation is still necessary to confirm the models. Unfortunately, for technical reasons, this was not possible at the time this manuscript was written. This should be the object of further work on the topic, in order to pursue the study presented in this chapter and confirm the physical interpretation that is presented in this thesis.

Conclusion

During this PhD work, we have investigated the programming of RF processing functions in REIC, under the shape of spectro-spatial gratings. From an applicative point, we had two different objectives. The first one was to demonstrate the versatility of the spectro-spatial architectures for RF processing, beyond the historic rainbow spectrum analyzer, by studying novel functions. We chose to investigate the function of RF filter which is particularly relevant in our cases of use. The second objective was to continue the past studies on the rainbow spectrum analyzer, by improving its dynamic range and its spectral response, and further understand the underlying physical phenomenon.

We started with the study of the spectro-spatial RF filter. After a general overview of the photonic RF filters, we detailed the architecture of the spectro-spatial RF filter. We explained the experimental setup, and how frequency-selective spectro-spatial diffraction gratings are programmed in the absorption profile of the Tm^{3+}:YAG crystal. Then, we performed a parametrical study to optimize the amplitude response of the filter. In a first step, we realized an experimental study. We identified in particular the relation between programming delay and causality, ruling the overall shape of the filter. We showed the contribution of a well-adapted magnetic field on the diffraction efficiency, and consequently on the rejection of the filter, and we determined the influence of the noise of the lasers in the tails of the filter. In a second step, we developed an analytical model of the filter response. The model is based on the Optical Bloch Equations for the programming step, and on the light propagation equation for the interaction between the signal beam and the spectro-spatial grating. The model is in remarkably good agreement with the experiment. Using the model, we could understand conceptually the influence of causality, of the programming delay and the programming chirp, by introducing the impulse response of the filter. We finally studied the phase reponse of the filter. Using the model, we could determine the conditions where a linear phase response is achieved, and we discussed the Minimum Phase Response of the filter. As a conclusion, we have demonstrated a very high performance photonic RF filter, based on a spectro-spatial architecture inspired from the rainbow spectrum analyzer. The filter is frequency agile, with a tunable bandwidth from 50 MHz to 20 GHz. We achieved a rejection of

60 dB with a rejection of 45 dB at 50 MHz from the edge of the filter, at the state of the art of GHz-wide photonic RF filters shown in table I.1. These performances could be increased by reducing in particular the noise of the lasers. Another prospect is to include a downconversion stage allowing to shift the filtered signal to RF baseband, in order to address a high dynamic range ADC.

In a second step we focused on the rainbow spectrum analyzer, with a first objective of improving its dynamic range. Our starting point was the observation that, at large programming bandwidth, the diffraction efficiency is much lower than expected theoretically. We identified that this phenomenon was caused by the Instantaneous Spectral Diffusion. We showed that one solution to reduce this effect is to increase the spin lifetime, which implies to minimize the temperature elevation caused by the optical excitation inside the crystal. We performed SHB spectroscopy of the spin lifetime, in order to study the thermalization of the crystal under various experimental conditions. With a simple heat diffusion model, we could suggest solutions to decrease the temperature in the crystal. The first results presented in this chapter allow to pave the way for a more systematic and extensive study of the thermalization of REIC at cryogenic temperature under optical excitation.

We finally focused on the apparatus function of the rainbow spectrum analyzer. By exetdning the model of the spectro-spatial filter of the second chapter, we could develop a novel analytical model of the rainbow spectrum analyzer, more exhaustive than models previously reported in the litterature. This new model allowed to understanding more precisely the processes in play in the experiment. We determined that the movement of the programming beam results in a notable Doppler effect, causing frequency shifts along the beam. We saw that this effect could cause variations of the amplitude and the spatial frequency of the spectro-spatial grating, resulting in a broadened apparatus function. We could provide an intuitive description of the spectro-spatial grating, as a array of spectro-spatial filters. We finally applied the model to our experiment. We showed that, under certain conditions, the model can be greatly simplified and provide a very understandable description of the apparatus function.

As mentioned in the introductive chapter I, a long-term prospect of the RF filter and the spectrum analyzer is to cooperate to form an analog pre-processing unit for RF surveillance and intelligent digitization. In this PhD work, we have demonstrated the brick of RF filtering in an architecture compatible with the rainbow spectrum analyzer. The state-of-the-art performances reported in this work are highly adapted for RF processing, and would allow to grant the spectrum analyzer with a high quality filter with low additionnal size, weight, power consumption and cost. Combining the two functions would manifestly offer high capability for RF spectrum surveillance.

Besides, the thermal study reported in chapter III.A relates to a general prob-

lematic of REIC-based experiments. Indeed, many functions make use of the whole inhomogeneous linewidth of the REIC. In this case, all the rare-earth ions are potentially excited, leading to a heating of the crystal. For example in quantum memories architectures, programming atomic frequency combs on a large bandwidth is necessary to perform signal multiplexing. In this frame, controling the temperature of the crystal under optical excitation is a major concern in many REIC-based architectures.

Appendices

A.1 Power budget of the spectro-spatial RF filter

In this appendix, we derive the power transmission $P_{\text{out}}/P_{\text{in}}$ of the spectro-spatial RF filter inside the passing band. Figure 19 depicts a schematic description of the filter. In the following, $E_k(t)$ will denote the electric field at point k from figure 19. The signal laser is the optical input $E_a(t) = E_0 e^{i\omega t}$.

The voltage applied to the intensity modulator (MZM) has an RF part : $V_{RF}\sin(\omega_{RF}t)$, and a DC part : V_{bias}. We set V_{bias} such that even orders of modulation are suppressed by destructive intereference. After the MZM we get :

$$E_c(t) = -\frac{1}{2}\eta_{11}E_0 \sum_{n\in Z^*} J_n(\beta)e^{i(\omega+n\omega_{RF})t} \tag{18}$$

where J_n is the Bessel function of order n and $\beta = \pi V_{RF}/V_{\pi,RF}$ is the modulation index.

The purpose of the optical filter performed by the crystal is to select the first

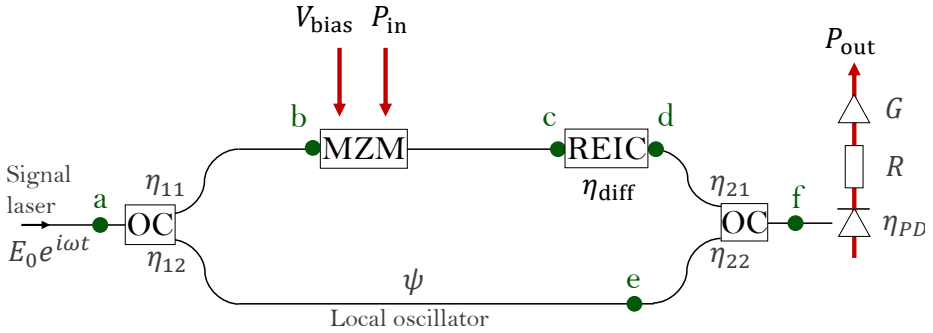

Figure 19: Schematics of the filter for power balance derivation of Appendix A.1 – Black line: optical path, Red line: electrical path, MZM: Intensity modulator, REIC: Rare-Earth Ions doped Crystal, OC: Optical Coupler with field coupling ratio noted above and below. ψ is the phase difference between the local oscillator (lower path) and the active path (upper path). R is the internal load of the photodiode of responsivity η_{PD} and G the electrical amplification gain. The oscillating part of the input tension $V(t)$ applied to the phase modulator is equivalent to an RF input power P_{in}.

harmonic of the modulation by diffraction. The losses induced by this process are described by the diffraction efficiency η_{diff}:

$$E_d(t) = -\frac{1}{2}\eta_{11}\eta_{\text{diff}}E_0 J_1(\beta)e^{i(\omega+\omega_{RF})t} \tag{19}$$

With ψ the phase difference between the local oscillator and the active path we find:

$$\begin{aligned} E_f(t) &= \eta_{22}E_e(t) + \eta_{21}E_d(t) \\ &= \eta_{22}\eta_{12}e^{i\psi}E_0e^{i\omega t} - \eta_{21}\frac{1}{2}\eta_{11}\eta_{\text{diff}}E_0J_1(\beta)e^{i(\omega+\omega_{RF})t} \end{aligned} \tag{20}$$

The oscillating part of the current produced by the photodiode under the electric field E_f reads:

$$\begin{aligned} I_{RF}(t) &= \eta_{PD} \times 2\,\text{Re}\left[\left(-\eta_{22}\frac{1}{2}\eta_{12}\eta_{\text{diff}}E_0J_1(\beta)e^{i(\omega+\omega_{RF})t}\right)\left(\eta_{21}\eta_{11}e^{i\psi}E_0e^{i\omega t}\right)^*\right] \\ &= -\eta_{11}\eta_{12}\eta_{21}\eta_{22}\ \eta_{PD}\eta_{\text{diff}}E_0^2J_1(\beta)\cos(\omega_{RF}t+\psi) \end{aligned} \tag{21}$$

The RF output power produced by $I_{RF}(t)$ over an internal charge R amplified with gain G reads:

$$\begin{aligned} P_{\text{out}} &= G\left\langle RI_{RF}(t)^2\right\rangle \\ &= \frac{GR}{2}\left(\eta_{11}\eta_{12}\eta_{21}\eta_{22}\ \eta_{PD}\eta_{\text{diff}}\right)^2E_0^4J_1(\beta)^2 \end{aligned} \tag{22}$$

With Z_{MZM} the input impedance of the phase modulator the RF input power reads:

$$\begin{aligned} P_{\text{in}} &= \frac{\left\langle\left(V_{RF}\sin(\omega_{RF}t)\right)^2\right\rangle}{Z_{\text{MZM}}} \\ &= \frac{V_{RF}^2}{2Z_{\text{MZM}}} = \frac{1}{2Z_{\text{MZM}}}\left(\frac{V_{\pi,RF}}{\pi}\right)^2\beta^2 \end{aligned} \tag{23}$$

Assuming that $\beta \ll \pi$ and with (23) we have:

$$J_1(\beta)^2 \simeq \left(\frac{\beta}{2}\right)^2 = \frac{P_{\text{in}}Z_{\text{MZM}}}{2}\left(\frac{\pi}{V_{\pi,RF}}\right)^2 \tag{24}$$

We replace the expression of $J_1(\beta)^2$ from (24) in (22) and noting that $E_0^2 \propto P_0$ we finally have:

$$\boxed{\frac{P_{\text{out}}}{P_{\text{in}}} \propto P_0^2\left(\frac{\pi}{V_{\pi,RF}}\right)^2 Z_{\text{MZM}}\eta_{\text{diff}}\mathcal{R}_L^2GR} \tag{25}$$

A.2 Field transmission of the spectro-spatial RF filter

For clarity, in appendix A.1 we omitted the frequency dependence of the diffraction efficiency of the crystal η_{diff} and did not consider the shape of the filter. The objective of this section is precisely to express this frequency dependence, and obtain the complete RF transfer function $H(\nu)$ of the filter. We first derive the optical transfer function $H_{opt}(\nu)$ of the optical filter, corresponding to the diffraction by the crystal. Here ν is the optical frequency. The diffraction efficiency is then given by:

$$\eta_{\text{diff}}(\nu) = |H_{opt}(\nu)|^2 \tag{26}$$

The derivation relies on light-matter interaction theory. It unfolds as follows: on the one hand the two programming beams - indexed with 1 for the first one and 2 for the delayed one - are repeatedly sent on the crystal, optically pumping the ions until the susceptibility of the crystal reaches a steady state. We then send the signal beam - indexed with 3 - which polarizes the crystal due to the crystal susceptibility. This produces the diffracted beam - indexed with 4 - according to the wave equation (the beams indexing corresponds to figure II.2). We derive the response of the crystal to an excitation by a monochromatic signal beam, without any assumption on the temporal shape of the programming beams. We describe the electromagnetic fields as plane waves.

Polarization

It was demonstrated in the PhD thesis [Lavielle, 2004] that, with the hypothesis of:

1. short excitations compared to the excited state lifetime
2. short programming repetition rate compared to the storage state lifetime
3. optically thin crystal,

the complex susceptibility of the crystal at steady state after several repetitions of the two programming beams reads:

$$\begin{aligned}\chi(\vec{r},t) =& \frac{2\pi\mu^2}{\hbar\varepsilon_0} e^{-\Gamma_h t} Y(t) \times \int_{-\infty}^{+\infty} \sin(2\pi\nu t) \\ & \left(1 - \frac{1}{\gamma T_P}\left(\left|\tilde{\Omega}_1 + \tilde{\Omega}_2\right|^2 \otimes \mathcal{L}_h\right)(\vec{r}, \nu - \nu_F)\right) \mathrm{d}\nu\end{aligned} \tag{27}$$

where $\otimes$ is the convolution product of variable ν, μ is the dipole moment of the optical transition, $\mathcal{L}_h$ is the lorentzian homogeneous lineshape of the optical transition of width Γ_h, $Y(t)$ is the Heaviside function, γ is the relaxation rate of the metastable state into the fundamental state, T_P is the programming repetition period and $\nu_F = \nu_1 = \nu_2$ is the center frequency of the programming beams 1 and 2.

Ω_j stands for the complex Rabi frequency of beam $j = 1; 2$. if the electric field reads $E_j(\vec{r}, t) = \mathcal{E}_j(\vec{r}, t)e^{i\vec{k}_j\cdot\vec{r}-2i\pi\nu_F t}$ then we have:

$$\Omega_j = \frac{\mu}{\hbar}\mathcal{E}_j(\vec{r}, t)e^{i\vec{k}_j\cdot\vec{r}} \tag{28}$$

The transverse spatial dimension of the beams is not relevant in the spectro-spatial RF filter architecture. We can consider infinitely wide beams, and write $E_1(\vec{r}, t) = A_1(t)e^{i\vec{k}_1\cdot\vec{r}-2i\pi\nu_F t}$. In this case $\mathcal{E}_1$ does not depend on $\vec{r}$, and $\mathcal{E}_1(\vec{r}, t) = A_1(t)$. Note that, on the contrary, the transverse dimension is crucial in the rainbow spectrum analyzer. The object of the last appendix A.3 will be to include the transverse spatial dimension in the derivation to describe the spectrum analyzer.

$\tilde{f}$ or $F[f]$ stands for the Fourier tranform of function f defined as:

$$\tilde{f}(\nu) = F[f](\nu) = \int_{-\infty}^{+\infty} f(t)e^{2i\pi\nu t}\mathrm{d}t \tag{29}$$

Equation 27 is obtained by a perturbative derivation of the optical Bloch equations. Refer to section 4.2.1 from [Lavielle, 2004] for the detailed calculus.

We develop $\left|\tilde{\Omega}_1 + \tilde{\Omega}_2\right|^2$ in 27 and we obtain three contributions in χ. One depends on $1 - \frac{1}{\gamma T_P}\left(\left|\tilde{\Omega}_1\right|^2 + \left|\tilde{\Omega}_2\right|^2\right) \otimes \mathcal{L}_h$, one on $\frac{1}{\gamma T_P}\left(\tilde{\Omega}_1^*\tilde{\Omega}_2\right) \otimes \mathcal{L}_h$ and one on $\frac{1}{\gamma T_P}\left(\tilde{\Omega}_1\tilde{\Omega}_2^*\right) \otimes \mathcal{L}_h$. With an identical reasoning than discussed around equation II.5 in section II.2, if we perform the derivation for all three contributions, we see that they respectively describe the orders of diffraction 0, +1 and −1 of the signal beam by the grating in the crystal. Similarly to equation II.5, we can only observe order +1 in practice, so we only consider the contribution depending on $\frac{1}{\gamma T_P}\left(\tilde{\Omega}_1^*\tilde{\Omega}_2\right) \otimes \mathcal{L}_h$:

$$\begin{aligned}\chi_{+1}(\vec{r}, t) = &-\frac{2\pi\mu^2}{\hbar\varepsilon_0\gamma T_P}e^{-\Gamma_h t}Y(t) \times \\ &\int_{-\infty}^{+\infty}\left[\left(\tilde{\Omega}_1^*\tilde{\Omega}_2\right) \otimes \mathcal{L}_h\right](\vec{r}, \nu - \nu_F)\sin(2\pi\nu t)\mathrm{d}\nu\end{aligned} \tag{30}$$

Let us derive the integral in equation 30, by developing $\sin(2\pi\nu t) = \frac{e^{2i\pi\nu t} - e^{-2i\pi\nu t}}{2i}$. Noting that $F^{-1}[\mathcal{L}_h](t) = e^{-\Gamma_h|t|}$ we find:

$$
\begin{aligned}
&\int_{-\infty}^{+\infty}\left[\left(\tilde{\Omega}_1^*\tilde{\Omega}_2\right)\otimes\mathcal{L}_h\right](\vec{r},\nu-\nu_F)\sin(2\pi\nu t)\mathrm{d}\nu\\
&\quad=\frac{1}{2i}\int_{-\infty}^{+\infty}\left[\left(\tilde{\Omega}_1^*\tilde{\Omega}_2\right)\otimes\mathcal{L}_h\right](\vec{r},\nu-\nu_F)e^{2i\pi\nu t}\\
&\qquad\qquad+\frac{1}{2i}\int_{-\infty}^{+\infty}\left[\left(\tilde{\Omega}_1^*\tilde{\Omega}_2\right)\otimes\mathcal{L}_h\right](\vec{r},\nu-\nu_F)e^{-2i\pi\nu t}\mathrm{d}\nu\\
&\quad=\frac{1}{2i}\int_{-\infty}^{+\infty}\left[\left(\tilde{\Omega}_1^*\tilde{\Omega}_2\right)\otimes\mathcal{L}_h\right](\vec{r},\nu)e^{2i\pi(\nu+\nu_F)t}\\
&\qquad\qquad+\frac{1}{2i}\int_{-\infty}^{+\infty}\left[\left(\tilde{\Omega}_1^*\tilde{\Omega}_2\right)\otimes\mathcal{L}_h\right](\vec{r},\nu)e^{-2i\pi(\nu+\nu_F)t}\mathrm{d}\nu\\
&\quad=\frac{1}{2i}F^{-1}\left[\left(\tilde{\Omega}_1^*\tilde{\Omega}_2\right)\otimes\mathcal{L}_h\right](\vec{r},-t)e^{2i\pi\nu_F t}+F^{-1}\left[\left(\tilde{\Omega}_1^*\tilde{\Omega}_2\right)\otimes\mathcal{L}_h\right](\vec{r},t)e^{-2i\pi\nu_F t}\\
&\quad=\frac{1}{2i}F^{-1}\left[\left(\tilde{\Omega}_1^*\tilde{\Omega}_2\right)\right](\vec{r},-t)e^{-\Gamma_h|t|}e^{2i\pi\nu_F t}+F^{-1}\left[\left(\tilde{\Omega}_1^*\tilde{\Omega}_2\right)\right](\vec{r},t)e^{-\Gamma_h|t|}e^{-2i\pi\nu_F t}
\end{aligned}
\tag{31}
$$

Injecting 31 in 30 we obtain:

$$
\begin{aligned}
\chi_{+1}(\vec{r},t)=&-\frac{2\pi\mu^2}{\hbar\varepsilon_0\gamma T_P}e^{-\Gamma_h t}Y(t)e^{-\Gamma_h|t|}\frac{1}{2i}\times\\
&\left(F^{-1}\left[\tilde{\Omega}_1^*\tilde{\Omega}_2\right](\vec{r},-t)e^{2i\pi\nu_F t}-F^{-1}\left[\tilde{\Omega}_1^*\tilde{\Omega}_2\right](\vec{r},t)e^{-2i\pi\nu_F t}\right)
\end{aligned}
\tag{32}
$$

The polarization produced by the susceptibility and the exciting signal beam E_3 is given by $\tilde{P}(\vec{r},\nu)=\varepsilon_0\tilde{E}_3(\vec{r},\nu)\tilde{\chi}_{+1}(\vec{r},\nu)$:

$$
\begin{aligned}
\tilde{P}(\vec{r},\nu)=&\tilde{E}_3(\nu)\frac{i\pi\mu^2}{\hbar\gamma T_P}F\Big[e^{-2\Gamma_h t}Y(t)\times\\
&\left(F^{-1}\left[\tilde{\Omega}_1^*\tilde{\Omega}_2\right](\vec{r},-t)e^{2i\pi\nu_F t}-F^{-1}\left[\tilde{\Omega}_1^*\tilde{\Omega}_2\right](\vec{r},t)e^{-2i\pi\nu_F t}\right)\Big](\nu)
\end{aligned}
\tag{33}
$$

$F\left[e^{-2\Gamma_h t}Y(t)F^{-1}\left[\tilde{\Omega}_1^*\tilde{\Omega}_2\right](\vec{r},-t)\right]$ is a function centered around $\nu=0$ as a product of functions centered around $\nu=0$, so $F\left[e^{-2\Gamma_h t}Y(t)F^{-1}\left[\tilde{\Omega}_1^*\tilde{\Omega}_2\right](\vec{r},-t)e^{2i\pi\nu_F t}\right]$ is centered around $\nu=-\nu_F<0$. Since $\tilde{E}_3$ is centered around $\nu=+\nu_3>0$, their domains are disjoints so the contribution of this term is null. We finally obtain, noting that $F\left[f(t)e^{-2i\pi\nu_F t}\right](\nu)=F\left[f\right](\nu-\nu_F)$:

$$
\begin{aligned}
\tilde{P}(\vec{r},\nu)&=\tilde{E}_3(\nu)\frac{\pi\mu^2}{i\hbar\gamma T_P}\times F\left[e^{-2\Gamma_h t}Y(t)F^{-1}\left[\tilde{\Omega}_1^*\tilde{\Omega}_2\right](\vec{r},t)e^{-2i\pi\nu_F t}\right](\nu)\\
&=\tilde{E}_3(\nu)\frac{\pi\mu^2}{i\hbar\gamma T_P}\times F\left[e^{-2\Gamma_h t}Y(t)F^{-1}\left[\tilde{\Omega}_1^*\tilde{\Omega}_2\right](\vec{r},t)\right](\nu-\nu_F)
\end{aligned}
\tag{34}
$$

We look for the filter response to a monochromatic excitation, so we consider $\tilde{E_3}(\vec{r},\nu) = A_3 e^{i\vec{k_3}\cdot\vec{r}}\delta_{\nu_3}(\nu)$. With the definition of Ω_j given in 28 we rewrite 34:

$$\tilde{P}(\vec{r},\nu) = A_3\delta_{\nu_3}(\nu)\frac{\pi\mu^4}{i\hbar^3\gamma T_P}\times F\left[e^{-2\Gamma_h t}Y(t)F^{-1}\left[\tilde{\mathcal{E}}_1^*\tilde{\mathcal{E}}_2\right](\vec{r},t)\right](\nu-\nu_F)e^{i(\vec{k_3}+\vec{k_2}-\vec{k_1})\cdot\vec{r}} \quad (35)$$

We have previoulsy defined $\mathcal{E}_j$ as $E_j(\vec{r},t) = \mathcal{E}_j(\vec{r},t)e^{i\vec{k_j}\cdot\vec{r}-2i\pi\nu_F t}$. As mentioned before, $E_1(\vec{r},t) = A_1(t)e^{i\vec{k_1}\cdot\vec{r}-2i\pi\nu_F t}$, so $\mathcal{E}_1(\vec{r},t) = A_1(t)$.

In our case beam 2 is identical to beam 1 but delayed and with a different angle of incidence on the crystal, so $E_2(\vec{r},t) = A_1(t-\tau)e^{i\vec{k_2}\cdot\vec{r}-2i\pi\nu_F(t-\tau)}$. We obtain $\mathcal{E}_2(\vec{r},t) = A_1(t-\tau)e^{2i\pi\nu_F\tau}$. Noting that $F\left[A_1(t-\tau)\right](\nu) = \tilde{A_1}(\nu)e^{2i\pi\nu\tau}$ we find:

$$\begin{aligned}\tilde{P}(\vec{r},\nu) &= A_3 e^{i\vec{k_3}\cdot\vec{r}}\delta_{\nu_3}(\nu)\frac{\pi\mu^4}{i\hbar^3\gamma T_P}\times \\ &\quad F\left[e^{-2\Gamma_h t}Y(t)F^{-1}\left[F\left[A_1(t)\right]^* F\left[A_1(t-\tau)e^{2i\pi\nu_F\tau}\right]\right](\vec{r},t)\right](\nu-\nu_F)e^{i(\vec{k_3}+\vec{k_2}-\vec{k_1})\cdot\vec{r}} \\ &= A_3\delta_{\nu_3}(\nu)\frac{\pi\mu^4}{i\hbar^3\gamma T_P}e^{2i\pi\nu_F\tau}F\left[e^{-2\Gamma_h t}Y(t)F^{-1}\left[\tilde{A}_1^*\tilde{A}_1 e^{2i\pi\nu\tau}\right](t)\right](\nu-\nu_F)e^{i(\vec{k_3}+\vec{k_2}-\vec{k_1})\cdot\vec{r}}\end{aligned} \quad (36)$$

We obtain:

$$\boxed{\tilde{P}(\vec{r},\nu) = A_3\delta_{\nu_3}(\nu)\frac{\pi\mu^4}{i\hbar^3\gamma T_P}e^{2i\pi\nu_F\tau}F\left[e^{-2\Gamma_h t}Y(t)F^{-1}\left[|\tilde{A}_1|^2 e^{2i\pi\nu\tau}\right](t)\right](\nu-\nu_F)e^{i(\vec{k_3}+\vec{k_2}-\vec{k_1})\cdot\vec{r}}} \quad (37)$$

Propagation of the signal beam

Now that we have written the polarization, we can derive the diffracted beam through the wave equation. Assuming that all beams share the same polarization and that the diffracted beam E_4 is a plane wave propagating along $z_4 = \vec{r}\cdot\vec{u_4}$ the frequency form of the wave equation reads :

$$\frac{\partial^2\tilde{E}_4}{\partial z_4^2}(z_4,\nu) + \left(\frac{2\pi\nu}{c}\right)^2\tilde{E}_4(z_4,\nu) = -\left(\frac{2\pi\nu}{c}\right)^2\frac{1}{\varepsilon_0}\tilde{P}(\vec{r}\cdot\vec{u_4},\nu) \quad (38)$$

We derive this differential equation analitically by rewriting it under the shape of a first order vectorial differential equation:

$$\frac{\partial}{\partial z_4}\begin{pmatrix}\tilde{E}_4\\ \frac{\partial\tilde{E}_4}{\partial z_4}\end{pmatrix}(z_4,\nu)=\underbrace{\begin{pmatrix}0 & 1\\ -\left(\frac{2\pi\nu}{c}\right)^2 & 0\end{pmatrix}}_{A}\begin{pmatrix}\tilde{E}_4\\ \frac{\partial\tilde{E}_4}{\partial z_4}\end{pmatrix}(z_4,\nu)+\begin{pmatrix}0\\ -\left(\frac{2\pi\nu}{c}\right)^2\frac{1}{\varepsilon_0}\tilde{P}(\vec{r}\cdot\vec{u_4},\nu)\end{pmatrix} \tag{39}$$

We can now solve 39 using the variation of constants method: a homogeneous solution of 39 is $z\to e^{Az}$, so we look for a general solution under the shape

$$\begin{pmatrix}\tilde{E}_4\\ \frac{\partial\tilde{E}_4}{\partial z_4}\end{pmatrix}(z_4,\nu)=e^{Az_4}U(z_4) \tag{40}$$

where U is a 2×1 matrix function. Injecting 40 in 39 we obtain

$$U(L)=\int_0^L e^{-Az}\begin{pmatrix}0\\ -\left(\frac{2\pi\nu}{c}\right)^2\frac{1}{\varepsilon_0}\tilde{P}(\vec{r}\cdot\vec{u_4},\nu)\end{pmatrix}\mathrm{d}z \tag{41}$$

We can derive the matrix exponential, noting I_2 the identity matrix:

$$e^{Az}=\sum_{n=0}^{+\infty}\frac{(Az)^n}{n!}=\sum_{n=0}^{+\infty}\frac{1}{(2n)!}(Az)^{2n}+\sum_{n=0}^{+\infty}\frac{1}{(2n+1)!}(Az)^{2n+1} \tag{42}$$

$$=\sum_{n=0}^{+\infty}\frac{1}{(2n)!}\left[-\left(\frac{2\pi\nu}{c}z\right)^2\right]^n I_2+\sum_{n+0}^{+\infty}\frac{1}{(2n+1)!}\left[-\left(\frac{2\pi\nu}{c}z\right)^2\right]^n A \tag{43}$$

$$=\cos\left(\frac{2\pi\nu}{c}z\right)I_2+\frac{c}{2\pi\nu}\sin\left(\frac{2\pi\nu}{c}z\right)A \tag{44}$$

We finally obtain from 40, 41 and 44:

$$\boxed{\tilde{E}_4(L,\nu)=-\frac{2\pi\nu}{c}\int_0^L\sin\left(\frac{2\pi\nu}{c}(L-z)\right)\frac{1}{\varepsilon_0}\tilde{P}(z\vec{u_4},\nu)\mathrm{d}z} \tag{45}$$

Filter transmission

Injecting 37 in 45 we find:

$$\begin{aligned}\tilde{E}_4(L,\nu)=A_3\delta_{\nu_3}(\nu)\frac{2i\pi^2\mu^4\nu_3}{c\hbar^3\varepsilon_0\gamma T_P}e^{2i\pi\nu_F\tau}\times\\ F\left[e^{-2\Gamma_h t}Y(t)F^{-1}\left[|\tilde{A}_1|^2e^{2i\pi\nu\tau}\right](t)\right](\nu_3-\nu_F)\times\\ \int_0^L\sin\left(\frac{2\pi\nu_3}{c}(L-z)\right)e^{i(\vec{k_3}+\vec{k_2}-\vec{k_1})\cdot z\vec{u_4}}\mathrm{d}z\end{aligned} \tag{46}$$

Now let us simplify the spatial integral of 46. The phase matching condition in

a three beams echo experiment like ours implies that $\vec{k_4} = \vec{k_3} + \vec{k_2} - \vec{k_1}$ and that $\vec{k_4} = \frac{2\pi\nu_3}{c}\vec{u_4}$, which gives:

$$\begin{aligned}\int_0^L \sin\left(\frac{2\pi\nu_3}{c}(L-z)\right) e^{i(\vec{k_3}+\vec{k_2}-\vec{k_1})\cdot z\vec{u_4}}\mathrm{d}z \\ = \frac{1}{2i}\int_0^L \left[e^{\frac{2i\pi\nu_3}{c}(L-z)} - e^{-\frac{2i\pi\nu_3}{c}(L-z)}\right] e^{\frac{2i\pi\nu_3}{c}z}\mathrm{d}z \\ = \frac{1}{2i}\int_0^L e^{\frac{2i\pi\nu_3}{c}L} - e^{\frac{2i\pi\nu_3}{c}(L-2z)}\mathrm{d}z \end{aligned} \tag{47}$$

We neglect the rapidly oscillating $e^{\frac{2i\pi\nu_3}{c}(L-2z)}$ part and obtain:

$$\int_0^L \sin\left(\frac{2\pi\nu_3}{c}(L-z)\right) e^{i(\vec{k_3}+\vec{k_2}-\vec{k_1})\cdot z\vec{u_4}}\mathrm{d}z = \frac{L}{2i}e^{\frac{2i\pi\nu_3}{c}L} \tag{48}$$

Injecting 48 in 46 we can write the optical transfer function defined as $H_{\mathrm{opt}}(\nu_3) = \frac{\tilde{A_4}(L,\nu_3)}{A_3} = \frac{\tilde{E_4}(L,\nu_3)e^{-\frac{2i\pi\nu_3}{c}L}}{A_3}$:

$$\begin{aligned}H_{\mathrm{opt}}(\nu) =& \frac{\pi^2\mu^4\nu L}{c\hbar^3\varepsilon_0\gamma T_P}e^{2i\pi\nu_F\tau}\times \\ & F\left[e^{-2\Gamma_h t}Y(t)F^{-1}\left[|\tilde{A_1}|^2 e^{2i\pi\nu\tau}\right](t)\right](\nu-\nu_F)\end{aligned} \tag{49}$$

Note that, in particular due to the hypothesis of optically thin crystal, the amplitude of $H_{\mathrm{opt}}(\nu)$ is largely misestimated by this derivation. However, as demonstrated in section II.4, the spectral shape is very accurate. One should retain the following expression:

$$H_{\mathrm{opt}}(\nu) \propto F\left[e^{-2\Gamma_h t}Y(t)F^{-1}\left[|\tilde{A_1}|^2 e^{2i\pi\nu\tau}\right](t)\right](\nu-\nu_F) \tag{50}$$

Note that we also discarded ν in the multiplying prefactor. Indeed, we study the behaviour over a range of a few GHz around $\nu_F > 100$ THz, so ν is almost constant to ν_F. The variable of interest is actually the difference $\nu - \nu_F$, as it appears in the 50.

With $F[f \times g] = F[f] \otimes F[g]$ we can rewrite 50, obtaining two equivalent formulations:

$$\boxed{H_{\mathrm{opt}}(\nu) \propto F\left[e^{-2\Gamma_h t}Y(t)F^{-1}\left[|\tilde{A_1}|^2\right](t-\tau)\right](\nu-\nu_F).} \tag{51}$$

$$\boxed{H_{\mathrm{opt}}(\nu) \propto \left[\left(|\tilde{A_1}|^2 e^{2i\pi\nu\tau}\right) \otimes \mathcal{L}_h \otimes \mathcal{L}_h \otimes \tilde{Y}\right](\nu-\nu_F)} \tag{52}$$

We obtain the RF transfer function by downconverting H_{opt} with the local oscillator frequency ν_0. Here $\nu_0 = \nu_3$. We finally find the RF transfer function $H(\nu)$ of the spectro-spatial filter, with $|H(\nu)|^2 = T(\nu) = P_{\text{out}}(\nu)/P_{\text{in}}$:

$$\boxed{H(\nu) \propto F\left[e^{-2\Gamma_h t} Y(t) F^{-1}\left[|\tilde{A}_1|^2\right](t-\tau)\right](\nu - (\nu_F - \nu_0))} \tag{53}$$

$$\boxed{H(\nu) \propto \left[\left(|\tilde{A}_1|^2 e^{2i\pi\nu\tau}\right) \otimes \mathcal{L}_h \otimes \mathcal{L}_h \otimes \tilde{Y}\right](\nu - (\nu_F - \nu_0))} \tag{54}$$

A.3 Apparatus function of the rainbow spectrum analyzer

In this section we will derive the apparatus function of the rainbow spectrum analyzer. In the previous appendix we have derived the frequency dependence of the diffracted field, which provides the filter response. The spectrum analyzer configuration is similar to the RF filter. The only difference is that the angle of incidence of one programming beam varies in time: $\vec{k}_2$ becomes $\vec{k}_2(t)$. This way, we can diffract each frequency in a different direction, creating the spectrum analysis function.

The derivation presented here is an extension to appendix A.2, where we add the transvers spatial dependence along x. The vertical component y is not relevant here. We first derive the diffracted field in close field, right at the output of the crystal, as a function of frequency and position. We can then obtain the diffracted field in far field, on the camera, as a function of frequency and angle.

We derive a complete formula, without any strong hypothesis, providing the apparatus function of the spectrum analyzer, that is to say the shape of the beam acquired by the camera for a monochromtaic input (signal beam). This function is crucial to characterize any system, and provides in particular its resolution.

Programming beams E_1 and E_2

The notations are identical to previous appendix A.2. The geometry of the beams is depicted in figure 20.

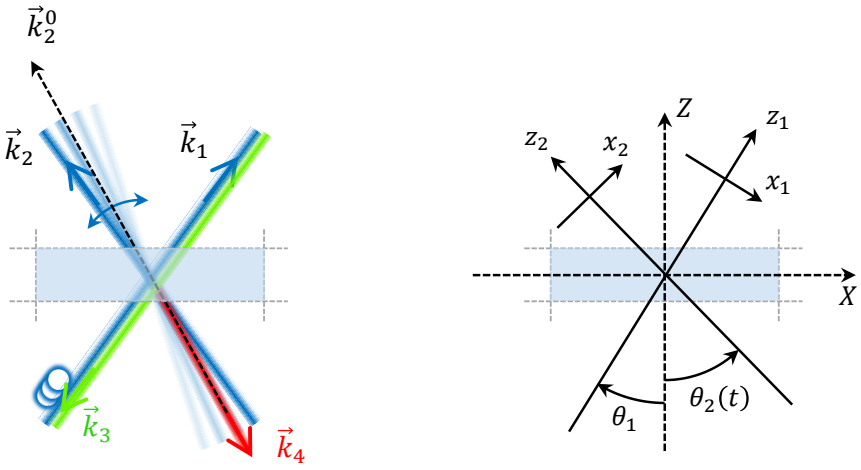

Figure 20: Left – Geometry of the crystal and the beams. $\vec{k}_2^0$ is $\vec{k}_2(t)$ at the precise intant where the frequency of the programming chirp matches the signal beam frequency ν_0. In other words, $\vec{k}_2^0$ corresponds to the direction of diffraction. Right – The frame (X,Z) is associated with the crystal, frame 1 with E_1 and E_3 and frame 2 with E_2.

Contrarily to the previous section, we now consider the spatial shape of the beams.

As a plane wave, we can write $E_1(\vec{r},t) = \mathcal{E}_1(\vec{r},t)e^{2i\pi\nu_P t - i\vec{k}_1\cdot\vec{r}} = G(x_1)A_1(t)e^{2i\pi\nu_P t - i\vec{k}_1\cdot\vec{r}}$. G describes the spatial shape of the beams. G remains very general in the present derivation, although in our experiment the beams are gaussian. For simplicity, we consider that E_1, E_2 and E_3 have the same spatial shape G.

A_1 contains the frequency chirp, and possibly laser noise such as intensity noise or phase noise. ν_P is the center frequency of the programming chirp.

In the spectrum analyzer setup, contrarily to the RF filter, E_3 propagates in the opposite direction than E_1. This is a counterpropagative configuration. Copropagative and counterpropagative situations provide rigorously the same results, the choice is only given by experimental considerations.

The model is conceptually unchanged, except that $\vec{k}_3 = -\vec{k}_1$ instead of $\vec{k}_3 = +\vec{k}_1$. Considering the discussion around equation II.5 or figure II.7, we see that in this case, the diffracted beam can only respect both the phase matching condition and causality if beam 1 is delayed, and in that case $\vec{k}_4 = \vec{k}_3 - (\vec{k}_2 - \vec{k}_1)$.

In a nutshell, to adapt the description from appendix A.2 to the counterpropagative configuration, we change:

- $\vec{k}_3$ in $-\vec{k}_3$,
- τ in $-\tau$, thus keeping $\tau > 0$,
- $\vec{k}_4 = \vec{k}_3 + (\vec{k}_2 - \vec{k}_1)$ in $\vec{k}_4 = \vec{k}_3 - (\vec{k}_2 - \vec{k}_1)$.

With τ changed in $-\tau$, we now have $E_2(\vec{r},t) = G(x_2)A_1(t+\tau)e^{2i\pi\nu_P(t+\tau) - i\vec{k}_2(t)\cdot\vec{r}}$.

A crucial point in this derivation is the fact that, although we program different diffraction gratings for a whole frequency band, the signal beam is monochromatic at ν_0. So it is diffracted mainly in only one direction, given by the grating programmed for frequency ν_0. We note $\vec{k}_2^0$ the wavector of beam 2 at the precise intant where the programming chirp frequency equals ν_0, i.e. the instant where the grating at frequency ν_0 is written. The signal beam is then diffracted mainly in direction $\vec{k}_3 - (\vec{k}_2^0 - \vec{k}_1) = -\vec{k}_2^0 := \vec{k}_4$.

As a consequence, we can derive E_4 with a perturbative approach around $\vec{k}_4 = -\vec{k}_2^0$. We note $\theta_2(t)$ the angle between $\vec{k}_2(t)$ and the frame of the crystal (X,Z). Since we only consider the behaviour around $\vec{k}_2^0$, we write $\theta_2(t) = \theta_2^0 - \delta\theta_2(t)$, where θ_2^0 is associated with $\vec{k}_2^0$, and $\delta\theta_2(t) \ll 1$. With the change of frame depicted in figure 21,

we find at first order in $\delta\theta_2$:

$$\begin{aligned}
\vec{k_2}(t) &= k_2\hat{z_2} = k_2\cos(\theta_2)\hat{Z} - k_2\sin(\theta_2)\hat{X} && (55)\\
&= k_2\cos\left(\theta_2^0 - \delta\theta_2\right)\hat{Z} - k_2\sin\left(\theta_2^0 - \delta\theta_2\right)\hat{X} && (56)\\
&= k_2\cos\left(\theta_2^0\right)\cos(\delta\theta_2)\hat{Z} + k_2\sin\left(\theta_2^0\right)\sin(\delta\theta_2)\hat{Z}\\
&\qquad + k_2\cos\left(\theta_2^0\right)\sin(\delta\theta_2)\hat{X} - k_2\sin\left(\theta_2^0\right)\cos(\delta\theta_2)\hat{X} && (57)\\
&= k_2\cos\left(\theta_2^0\right)\hat{Z} + k_2\sin\left(\theta_2^0\right)\delta\theta_2\hat{Z} + k_2\cos\left(\theta_2^0\right)\delta\theta_2\hat{X} - k_2\sin\left(\theta_2^0\right)\hat{X} && (58)\\
&= k_2\left[\cos\left(\theta_2^0\right)\hat{Z} - \sin\left(\theta_2^0\right)\hat{X}\right] + k_2\delta\theta_2\left[\left(\sin\left(\theta_2^0\right)\hat{Z} + \cos\left(\theta_2^0\right)\hat{X}\right]\right. && (59)\\
&= \vec{k_2^0} + k_2\delta\theta_2\hat{x_2^0} && (60)
\end{aligned}$$

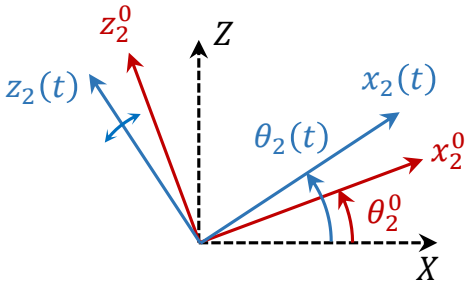

Figure 21: Change of frame between (X, Y), (x_2^0, z_2^0) and (x_2, z_2).

We define $\mathcal{E}_2 = E_2/e^{2i\pi\nu_P t - i\vec{k_2^0}\cdot\vec{r}}$, similarly to $\mathcal{E}_1 = E_1/e^{2i\pi\nu_P t - i\vec{k}_1\cdot\vec{r}}$. Noting that $\hat{x_2^0} = \hat{x_4}$ we finally obtain:

$$\boxed{\begin{cases} \mathcal{E}_1(\vec{r},t) = G(x_1)A_1(t) \\ \mathcal{E}_2(\vec{r},t) = G(x_2)A_1(t+\tau)e^{-ik_2\delta\theta_2(t)x_4}e^{2i\pi\nu_P\tau} \end{cases}} \qquad (61)$$

Polarization

The derivation of the polarization is virtually identical to the derivation performed in appendix A.2, with the only difference of the counterpropagative configuration mentioned above. We adapt equation 35 to this situation, so $\vec{k}_3 + (\vec{k}_2 - \vec{k}_1)$ becomes $\vec{k}_3 - (\vec{k}_2 - \vec{k}_1) = -\vec{k}_4$. We now consider the spatial shape of E_3, so A_3 becomes $A_3 G(x_3)$. We obtain:

$$\tilde{P}(\vec{r},\nu) \propto G(x_3)\delta_{\nu_3}(\nu)F\left[e^{-2\Gamma t}Y(t)F^{-1}\left[\tilde{\mathcal{E}}_1^*\tilde{\mathcal{E}}_2\right]\right](\vec{r},\nu-\nu_P)e^{-i\vec{k}_4\cdot\vec{r}} \qquad (62)$$

Let us rewrite $\mathcal{E}_2$. We consider that the angle θ_2 is swept linearly, so $\delta\theta_2(t) = v_\theta t$.

We find:

$$\tilde{\mathcal{E}}_2(\vec{r},\nu) = G(x_2)F\left[A_1(t+\tau)e^{-ik_2 v_\theta t x_4}\right](\nu) \tag{63}$$
$$= G(x_2)F\left[A_1(t+\tau)\right](\nu - v_\theta x_4/\lambda) \tag{64}$$
$$= G(x_2)\tilde{A}_1(\nu - v_\theta x_4/\lambda)e^{2i\pi(\nu - v_\theta x_4/\lambda)\tau} \tag{65}$$

Injecting equations 61 and 65 in equation62, we have:

$$\tilde{P}(\vec{r},\nu) \propto G(x_3)\delta_{\nu_3}(\nu)\times$$
$$F\left[e^{-2\Gamma t}Y(t)F^{-1}\left[G(x_1)\tilde{A}_1^*(\nu)G(x_2)\tilde{A}_1(\nu - v_\theta x_4/\lambda)e^{2i\pi(\nu - v_\theta x_4/\lambda)\tau}\right](t)\right](\nu - \nu_P)e^{ik_4 z_4} \tag{66}$$

We neglect the size difference of the three beams in the crystal due the different incidence angle, so that $G(x_1) \simeq G(x_2(t)) \simeq G(x_4)$. We finally obtain:

$$\boxed{\tilde{P}(\vec{r},\nu) \propto G(x_4)^3\delta_{\nu_3}(\nu)F\left[e^{-2\Gamma t}Y(t)F^{-1}\left[\tilde{A}_1^*(\nu)\tilde{A}_1(\nu - v_\theta x_4/\lambda)\right](t-\tau)\right](\nu - \nu_P)e^{ik_4 z_4}e^{2i\pi\tau v_\theta x_4/\lambda}} \tag{67}$$

Propagation of the signal beam

Let us isolate the rapid spatial exponential in E_4, by writing $E_4(\vec{r},t) = \mathcal{A}_4(\vec{r},t)e^{ik_4 z_4}$. Similarly to 38, except that we now have to take into account two space variables, the wave equation reads in its frequency form:

$$\Delta\tilde{E}_4(\vec{r},\nu) + \left(\frac{2\pi\nu}{c}\right)^2\tilde{E}_4(\vec{r},\nu) = -\left(\frac{2\pi\nu}{c}\right)^2\frac{1}{\varepsilon_0}\tilde{P}(\vec{r},\nu) \tag{68}$$

We develop the left-hand term:

$$\Delta\tilde{E}_4(\vec{r},\nu) + \left(\frac{2\pi\nu}{c}\right)^2\tilde{E}_4(\vec{r},\nu) = \frac{\partial^2\tilde{E}_4}{\partial x_4^2}(\vec{r},\nu) + \frac{\partial^2\tilde{E}_4}{\partial z_4^2}(\vec{r},\nu) + \left(\frac{2\pi\nu}{c}\right)^2\tilde{E}_4(\vec{r},\nu) \tag{69}$$
$$= \left[\frac{\partial^2\tilde{\mathcal{A}}_4}{\partial x_4^2}(\vec{r},\nu) + \frac{\partial^2\tilde{\mathcal{A}}_4}{\partial z_4^2}(\vec{r},\nu) + ik_4\frac{\partial\tilde{\mathcal{A}}_4}{\partial z_4}(\vec{r},\nu) - k_4^2\tilde{\mathcal{A}}_4(\vec{r},\nu) + \left(\frac{2\pi\nu}{c}\right)^2\tilde{\mathcal{A}}_4(\vec{r},\nu)\right]e^{ik_4 z_4} \tag{70}$$

We know that diffraction is a linear process in frequency. We derive here the response to a monochromatic input at frequency ν_3, so we will actually only consider $\tilde{E}_4(\nu_3)$. $\tilde{E}_4$ is zero at any other frequency annyway, as imposed by the δ_{ν_3} function in 67. Besides, according to the phase matching condition, $k_4 = k_3 = 2\pi\nu_3/c$. So the

terms 4 and 5 from equation 70 cancel out, and we have:

$$\Delta\tilde{E}_4(\vec{r},\nu_3)+\left(\frac{2\pi\nu_3}{c}\right)^2\tilde{E}_4(\vec{r},\nu_3)=\left[\frac{\partial^2\tilde{\mathcal{A}}_4}{\partial x_4^2}(\vec{r},\nu_3)+\frac{\partial^2\tilde{\mathcal{A}}_4}{\partial z_4^2}(\vec{r},\nu_3)+ik_4\frac{\partial\tilde{\mathcal{A}}_4}{\partial z_4}(\vec{r},\nu_3)\right]e^{ik_4z_4} \tag{71}$$

We can estimate the order of magnitude of the three remaining terms. The characteristic dimension of the beam along the tranverse axis is the width of the beam, typically $\Delta x \sim 1$ mm. The characteristic dimension along the propagation axis is typically the length of the crystal $\Delta z \sim 1$ mm. With $k_4 = 2\pi\nu_3/c \sim 10^7$ m^{-1}, we obtain:

$$\begin{cases} k_4\frac{\partial\tilde{A}_4}{\partial z_4} \sim \frac{k_4}{\Delta z}\tilde{\mathcal{A}}_4 \sim 10^{10}\tilde{\mathcal{A}}_4 \\ \frac{\partial^2\tilde{A}_4}{\partial x_4^2} \sim \frac{1}{\Delta x^2}\tilde{\mathcal{A}}_4 \sim 10^{6}\tilde{\mathcal{A}}_4 \\ \frac{\partial^2\tilde{A}_4}{\partial z_4^2} \sim \frac{1}{\Delta z^2}\tilde{\mathcal{A}}_4 \sim 10^{6}\tilde{\mathcal{A}}_4 \end{cases} \tag{72}$$

We see that we can neglect the second order derivatives, which are 4 orders of magnitude below the first order derivative, i.e. 80 dB in power. Neglecting these terms in 71, and injecting in 68, we finally obtain:

$$\boxed{ik_4\frac{\partial\tilde{\mathcal{A}}_4}{\partial z_4}(\vec{r},\nu_3)=-\left(\frac{2\pi\nu_3}{c}\right)^2\frac{1}{\varepsilon_0}\tilde{P}(\vec{r},\nu_3)e^{-ik_4z_4}} \tag{73}$$

Close field and far field diffracted field

From 68 and 73, we see that $\frac{\partial\tilde{\mathcal{A}}_4}{\partial z_4}$ does not depend on z_4. Similarly to equation 50 in the previous appendix, we admit that the amplitude of the derived formula is largely misestimated due to the initial hypothesis, so that we discard the multiplying prefactors, to retain only the dependence in ν_3 and x_4.

The diffracted field in close field, right at the output of the crystam, then reads:

$$\boxed{\tilde{\mathcal{A}}_4(x_4,z_4=d,\nu_3)\propto G(x_4)^3F\left[e^{-2\Gamma t}Y(t)F^{-1}\left[\tilde{A}_1^*(\nu)\tilde{A}_1(\nu-v_\theta x_4/\lambda)\right](t-\tau)\right](\nu_3-\nu_F)e^{2i\pi\tau v_\theta x_4/\lambda}} \tag{74}$$

The diffracted field, that we can acquire on a camera, is in far field. It is given by the spatial Fourier transform of the close field, defined as:

$$F_x[f](\theta)=\int_{-\infty}^{+\infty}f(x)e^{2i\pi\theta x/\lambda}\mathrm{d}x \tag{75}$$

We finally obtain, writing x for x_4 and ν for ν_3 for simplicity:

$$\boxed{\tilde{\mathcal{A}}_4(\theta,\nu) \propto F_x\left[G(x)^3 F_t\left[e^{-2\Gamma t}Y(t)F_t^{-1}\left[\tilde{A}_1^*(\nu)\tilde{A}_1(\nu-v_\theta x/\lambda)\right](t-\tau)\right](\nu-\nu_F)\right](\theta-v_\theta\tau)} \tag{76}$$

Similary to the previous appendix A.2, we can express this formula with convolution products, which provide a more intuitive formulation. We note $\otimes_\theta$, respectively $\otimes_\nu$, the convultion product of variable θ, respectively ν. We can rewrite 76 as:

$$\tilde{\mathcal{A}}_4(\theta+v_\theta\tau,\nu+\nu_F) \propto \tilde{G}\otimes_\theta \tilde{G}\otimes_\theta \tilde{G}\otimes_\theta \tilde{K}(\theta,\nu) \tag{77}$$

Equation 77 shows that the diffracted field in far field is nothing more than the convolution of the spatial shape of the three incoming beams (the two programming beams and the signal beam), convoluted with a function K. This function describes the coupling between space and frequency, caused by the simultaneous sweeps in angle and frequency of programming beam 2. It is itself given by:

$$K(x,\nu) = \mathcal{L}_h \otimes_\nu \mathcal{L}_h \otimes_\nu \tilde{Y} \otimes_\nu \left[\tilde{A}_1^*(\nu)\tilde{A}_1(\nu-v_\theta x/\lambda)e^{2i\pi(\nu-v_\theta x/\lambda)\tau}\right] \tag{78}$$

We find again the two lorentzian function of the atomic response, one for the response to programming and one for readout, convoluted by the Heaviside function imposing causality. The last term is the one effectively describing the space-frequency coupling, through the mixed variable $\nu - v_\theta x/\lambda$. It accounts in particular for the modification of the programming excitation due to the Doppler effect in the moving programming beam. See section III.B for more details.

A.4 Derivation of K for an infinite chirp

In this appendix, we derive the function K in the case where the programming chirp can be considered infinitely long, written simply $A_1(t) = e^{i\pi r t^2}$ without gating function. This is equivalent to neglect the fine effects of causality, as the cardinal sine impulse response described in figure II.22 becomes infinitely narrow, and casusality becomes a discontinuous 0-1 phenomenon.

To simplify the derivation, we also note that, similarly to the RF filter in equation II.8, the homogeneous linewidth of 10 kHz can be neglected as it is much narrower than any other spectral feature. This corresponds to neglect $\mathcal{L}_h$ and $e^{-\Gamma t}$ in the expressions. In this case, the function K defined in equation III.B.3 becomes:

$$K(x,\nu) = F_t\left[Y(t)F_t^{-1}\left[\tilde{A}_1^*(\nu)\tilde{A}_1(\nu - v_\theta x/\lambda)\right](t-\tau)\right](\nu) \tag{79}$$

The Fourier transform of $A_1(t)$ is $\tilde{A}_1(\nu) \propto e^{-\frac{i\pi\nu^2}{r}}$. We obtain:

$$\tilde{A}_1^*(\nu)\tilde{A}_1(\nu - v_\theta x/\lambda) \propto e^{\frac{i\pi\nu^2}{r}} e^{-\frac{i\pi(\nu - v_\theta x/\lambda)^2}{r}} \tag{80}$$

$$= e^{2i\pi\nu\frac{v_\theta x}{\lambda r}} e^{-\frac{i\pi}{r}(v_\theta x/\lambda)^2} \tag{81}$$

With $r = (20\text{ GHz})/(2\text{ ms})$, $v_\theta = (320\text{ mrad})/(2\text{ ms})$, $r < 2.5$ mm and $\lambda = 793$ nm, we find that $\frac{\pi}{r}(v_\theta x/\lambda)^2 < 0.2$. So $e^{-\frac{i\pi}{r}(v_\theta x/\lambda)^2}$ can be neglected and we find, noting δ_0 the Dirac function:

$$F_t^{-1}\left[\tilde{A}_1^*(\nu)\tilde{A}_1(\nu - v_\theta x/\lambda)\right](t) \propto \int e^{2i\pi\nu\frac{v_\theta x}{\lambda r}} e^{-2i\pi\nu t}\mathrm{d}t \propto \delta_0\left(t - \frac{v_\theta x}{\lambda r}\right) \tag{82}$$

Then we obtain:

$$K(x,\nu) \propto F_t\left[Y(t)\delta_0\left(t - \tau - \frac{v_\theta x}{\lambda r}\right)\right](\nu) \tag{83}$$

We can distinguish two cases, depending on the position x:

- If $\tau + \frac{v_\theta x}{\lambda r} < 0$, then $K(x,\nu) \propto F_t[0](\nu) = 0$.
- If $\tau + \frac{v_\theta x}{\lambda r} \geq 0$, then $K(x,\nu) \propto F_t\left[\delta_0\left(t - \tau - \frac{v_\theta x}{\lambda r}\right)\right](\nu) = e^{-2i\pi\nu(\tau + \frac{v_\theta x}{\lambda r})}$.

So we can finally write:

$$\boxed{K(x,\nu) \propto e^{-2i\pi\nu(\tau + \frac{v_\theta x}{\lambda r})} Y\left(\tau + \frac{v_\theta x}{\lambda r}\right)} \tag{84}$$

A.5 Interpretation of the apparatus function from [Lorgeré et al., 2002]

In the litterature, the only analytical expression of apparatus function of the rainbow spectrum analyzer wich includes the dependance of the programming delay is found in [Lorgeré et al., 2002]. The objective of this appendix is to rewrite the formula presented in this paper in order to interpret it in terms of grating in close field. This will allow to compare it to the more detailed model presented in the chapter III.B of this thesis. The comparison is presented in section III.B.4.

First, we simplify the apparatus function claimed in [Lorgeré et al., 2002], which reads as follows. We remind that n is the gaussian function related to the gaussian shape of the beams.

$$F(\nu_0,\nu) \propto \int_{-\infty}^{+\infty} \mathrm{d}\nu' \int_0^{+\infty} \mathrm{d}\tau \left[n(\nu'-\nu) e^{2i\pi t_{12}(\nu'-\nu)} \otimes L(\nu'-\nu) \right] e^{2i\pi\tau(\nu'-\nu_0)-\Gamma_h\tau} \quad (85)$$

Let us rewrite this expresssion. Similarly to the RF filter in equation II.8, in our case the homogeneous linewidth of 10 kHz can be neglected as it is much narrower than any other spectral feature:

$$F(\nu_0,\nu) \propto \int_{-\infty}^{+\infty} \mathrm{d}\nu' \int_0^{+\infty} \mathrm{d}\tau \; n(\nu'-\nu) e^{2i\pi t_{12}(\nu'-\nu)} e^{2i\pi\tau(\nu'-\nu_0)} \quad (86)$$

With the change of variable $\nu'' = \nu' - \nu$, we obtain:

$$F(\nu_0,\nu) \propto \int_{-\infty}^{+\infty} \mathrm{d}\nu'' \int_0^{+\infty} \mathrm{d}\tau \; n(\nu'') e^{2i\pi t_{12}\nu''} e^{2i\pi\tau(\nu''+\nu-\nu_0)} \quad (87)$$

$$\propto \int_0^{+\infty} \mathrm{d}\tau \left[\int_{-\infty}^{+\infty} \mathrm{d}\nu'' \; n(\nu'') e^{2i\pi(\tau+t_{12})\nu''} \right] e^{2i\pi\tau(\nu-\nu_0)} \quad (88)$$

$$\propto \int_0^{+\infty} \tilde{n}(\tau+t_{12}) e^{2i\pi\tau(\nu-\nu_0)} \mathrm{d}\tau \quad (89)$$

With the change of variable $\tau' = \tau + t_{12}$, we find:

$$\boxed{F(\nu_0,\nu) \propto \int_{t_{12}}^{+\infty} \tilde{n}(\tau') e^{2i\pi\tau'(\nu-\nu_0)} \mathrm{d}\tau' \; e^{-2i\pi t_{12}(\nu-\nu_0)}} \quad (90)$$

This results in a simple expression of the apparatus function:

$$\boxed{\boxed{\mathcal{S}(\nu_0,\nu) \propto \left| \int_{t_{12}}^{+\infty} \tilde{n}(\tau') e^{2i\pi\tau'(\nu-\nu_0)} \mathrm{d}\tau' \right|^2}} \quad (91)$$

Although the notations are different, we see that equation 91 is similar to equation III.B.17: under hypothesis corresponding to our experimental conditions, the two models are in agreement.

The correspondance between the two models allows to interpret [Lorgeré et al., 2002] in terms of near field. Indeed, we recognize that τ corresponds to the effective delay associated to each position x by Doppler effect, as described in section III.B.3.1 where we noted it τ_{eff}. The relation reads $\tau = \frac{x}{\lambda}\frac{v_\theta}{r} = \frac{x}{\lambda}\frac{\Delta\theta}{\Delta\nu}$.

For clarity, let us change the notations to the notations used in the chapter III.B:

- ν_0 is defined as the frequency of the input signal. In our notation, this corresponds to $-\nu$. The $-$ sign stands for different Fourier transforms definition.
- ν is defined as the frequency observed on the camera. In our notation, this corresponds to $-\nu_\theta = -\frac{\Delta\nu}{\Delta\theta}\theta$.
- The programming delay t_{12} corresponds in our notation to $-\tau$.

With the change of variable $\tau' = \frac{x}{\lambda}\frac{\Delta\theta}{\Delta\nu}$ in equation 89, we obtain:

$$F(\nu,\nu_\theta) \propto \int_0^{+\infty} \tilde{n}\left(\frac{x}{\lambda}\frac{\Delta\theta}{\Delta\nu} - \tau\right) e^{-2i\pi\frac{x}{\lambda}\frac{\Delta\theta}{\Delta\nu}(\nu_\theta-\nu)}\mathrm{d}x \tag{92}$$

$$\propto \int_{-\infty}^{+\infty} Y(x)G'(x-x_\tau)e^{-2i\pi\frac{x}{\lambda}\left(\theta-\frac{\Delta\theta}{\Delta\nu}\nu\right)}\mathrm{d}x \tag{93}$$

where we noted the spatial gaussian function $G'(x) = \tilde{n}(\frac{x}{\lambda}\frac{\Delta\theta}{\Delta\nu})$ and $x_\tau = \lambda\tau\frac{\Delta\nu}{\Delta\theta}$. Y represents the Heaviside function.

By definition of the apparatus function, this expression is proportional to the diffracted field in far field. We obtain the field in near field by inverse spatial Fourier transform:

$$F_x^{-1}[F](\nu,X) = \int_{-\infty}^{+\infty} F(\nu,\theta)e^{2i\pi\frac{X}{\lambda}\theta}\mathrm{d}\theta \tag{94}$$

$$\propto \int_{-\infty}^{+\infty}\int_{-\infty}^{+\infty} Y(x)G'(x-x_\tau)e^{-2i\pi\frac{x}{\lambda}\left(\theta-\frac{\Delta\theta}{\Delta\nu}\nu\right)}\mathrm{d}x\; e^{2i\pi\frac{X}{\lambda}\theta}\mathrm{d}\theta \tag{95}$$

$$\propto \int_{-\infty}^{+\infty} Y(x)G'(x-x_\tau)\left[\int_{-\infty}^{+\infty} e^{-2i\pi\frac{x-X}{\lambda}\theta}\mathrm{d}\theta\right] e^{2i\pi\frac{x}{\lambda}\frac{\Delta\theta}{\Delta\nu}\nu}\mathrm{d}x \tag{96}$$

$$\propto \int_{-\infty}^{+\infty} Y(x)G'(x-x_\tau)\delta_0(x-X)e^{2i\pi\frac{x}{\lambda}\frac{\Delta\theta}{\Delta\nu}\nu}\mathrm{d}x \tag{97}$$

$$\propto Y(X)G'(X-x_\tau)e^{2i\pi\frac{X}{\lambda}\frac{\Delta\theta}{\Delta\nu}\nu} \tag{98}$$

We see that in the model presented in [Lorgeré et al., 2002], the diffracted field in the crystal is an oscillating function contained in a truncated gaussian envelope. The place of the truncature can be moved by increasing the programming delay. The wings of the apparatus function appearing at short delay, called in the paper non-resonant dispersive grating component, are actually the result of the truncature of the gaussian profile in near field.

Bibliography

[Abragam and Bleaney, 2012] Abragam, A. and Bleaney, B. (2012). *Electron paramagnetic resonance of transition ions*. Oxford University Press.

[Afzelius et al., 2009] Afzelius, M., Simon, C., De Riedmatten, H., and Gisin, N. (2009). Multimode quantum memory based on atomic frequency combs. *Physical Review A*, 79(5):052329.

[Attal, 2017] Attal, Y. (2017). *Processeurs atomiques utilisant la propriété de creusement spectral: modélisation et application à l'analyse spectrale radiofréquence large bande sur porteuse optique*. PhD thesis, Paris Saclay.

[Attal et al., 2016] Attal, Y., Berger, P., Dolfi, D., Morvan, L., Louchet-Chauvet, A., and Chanelière, T. (2016). Estimation of the dynamic range of the rainbow RF spectrum analyzer. In *2016 IEEE International Topical Meeting on Microwave Photonics (MWP)*, pages 110–113. IEEE.

[Basiev et al., 1996] Basiev, T., Orlovskii, Y. V., Pukhov, K., Sigachev, V., Doroshenko, M., and Vorob'Ev, I. (1996). Multiphonon relaxation rates measurements and theoretical calculations in the frame of non-linear and non-coulomb model of a rare-earth ion-ligand interaction. *Journal of luminescence*, 68(5):241–253.

[Benbachir et al., 1985] Benbachir, K., Mazuer, J., and Senateur, J. (1985). Low temperature thermal conductivity of pure and doped single crystals of semiconducting sms. *Solid state communications*, 54(11):965–968.

[Berger et al., 2016] Berger, P., Attal, Y., Schwarz, M., Molin, S., Louchet-Chauvet, A., Chanelière, T., Le Gouët, J.-L., Dolfi, D., and Morvan, L. (2016). RF spectrum analyzer for pulsed signals: ultra-wide instantaneous bandwidth, high sensitivity, and high time-resolution. *Journal of Lightwave Technology*, 34(20):4658–4663.

[Berger et al., 2014] Berger, P., Schwarz, M., Molin, S., Dolfi, D., Morvan, L., Louchet-Chauvet, A., Chanelière, T., and Le Gouët, J.-L. (2014). 20 GHz instantaneous bandwidth RF spectrum analyzer with high time-resolution. In *Microwave*

Photonics (MWP) and the 2014 9th Asia-Pacific Microwave Photonics Conference (APMP) 2014 International Topical Meeting on, pages 331–334. IEEE.

[Caird et al., 1975] Caird, J., DeShazer, L., and Nella, J. (1975). Characteristics of room-temperature 2.3-μm laser emission from Tm^{3+} in YAG and $YAlO_3$. *IEEE Journal of Quantum Electronics*, 11(11):874–881.

[Coppinger et al., 1996] Coppinger, F., Yegnanarayanan, S., Trinh, P., Jalali, B., and Newberg, I. (1996). Nonrecursive tunable photonic filter using wavelength-selective true time delay. *IEEE Photonics Technology Letters*, 8(9):1214–1216.

[Crozatier et al., 2004] Crozatier, V., Lavielle, V., Bretenaker, F., Le Gouët, J.-L., and Lorgeré, I. (2004). High-resolution radio frequency spectral analysis with photon echo chirp transform in an Er:YSO crystal. *IEEE journal of quantum electronics*, 40(10):1450–1457.

[Dajczgewand et al., 2015] Dajczgewand, J., Ahlefeldt, R., Böttger, T., Louchet-Chauvet, A., Le Gouët, J.-L., and Chaneliere, T. (2015). Optical memory bandwidth and multiplexing capacity in the erbium telecommunication window. *New Journal of Physics*, 17(2):023031.

[Deevi and Rao, 2017] Deevi, B. N. and Rao, N. B. (2017). Miniature on-chip band pass filter for RF applications. *Microsystem Technologies*, 23(3):633–638.

[Dieke, 1968] Dieke, G. H. (1968). *Spectra and Energy Levels of Rare Earth Ions in Crystals.* Interscience Publisher, New York.

[Dolfi et al., 1991] Dolfi, D., Michel-Gabriel, F., Bann, S., and Huignard, J.-P. (1991). Two-dimensional optical architecture for time-delay beam forming in a phased-array antenna. *Optics Letters*, 16(4):255–257.

[Fedder and Mukherjee, 2005] Fedder, G. K. and Mukherjee, T. (2005). Tunable RF and analog circuits using on-chip MEMS passive components. In *ISSCC. 2005 IEEE International Digest of Technical Papers. Solid-State Circuits Conference, 2005.*, pages 390–391. IEEE.

[Galaup et al., 1998] Galaup, J.-P., Grelet, Fand Le Gouët, J.-L., Dolfi, D., and Huignard, J.-P. (1998). Analyseur de spectre de fréquence. Patent FR9802626.

[Ghelfi et al., 2019] Ghelfi, P., Scotti, F., Onori, D., and Bogoni, A. (2019). Photonics for ultrawideband RF spectral analysis in electronic warfare applications. *IEEE Journal of Selected Topics in Quantum Electronics*, 25(4):1–9.

[Gruber et al., 1989] Gruber, J. B., Hills, M. E., Macfarlane, R. M., Morrison, C. A., Turner, G. A., Quarles, G. J., Kintz, G. J., and Esterowitz, L. (1989). Spectra and energy levels of Tm^{3+}:$Y_3Al_5O_{12}$. *Physical Review B*, 40(14):9464.

[Gupta et al., 2007] Gupta, D., Filippov, T. V., Kirichenko, A. F., Kirichenko, D. E., Vernik, I. V., Sahu, A., Sarwana, S., Shevchenko, P., Talalaevskii, A., and Mukhanov, O. A. (2007). Digital channelizing radio frequency receiver. *IEEE Transactions on applied superconductivity*, 17(2):430–437.

[Gurevich et al., 2004] Gurevich, B. S., Andreyev, S. V., Belyaev, A. V., Akimjanova, C., and Sagymbaeva, K. (2004). RF signal analysis using combined acousto-optical correlator and spectrum analyzer. In *Sixth International Conference on Correlation Optics*, volume 5477, pages 330–334. SPIE.

[Guzzon et al., 2010] Guzzon, R. S., Norberg, E. J., Parker, J. S., Johansson, L. A., and Coldren, L. A. (2010). Monolithically integrated programmable photonic microwave filter with tunable inter-ring coupling. In *2010 IEEE International Topical Meeting on Microwave Photonics*, pages 23–26. IEEE.

[Haynes et al., 2016] Haynes, W. M., Lide, D. R., and Bruno, T. J. (2016). *CRC handbook of chemistry and physics*. CRC press.

[Hogan et al., 2019] Hogan, J., Babbitt, W. R., Benko, C., Bekker, S., Stiffler, C., Winn, K., Price, R., and Merkel, K. (2019). Assured capture of transient RF events across extremely wide bandwidths. In *2019 IEEE Research and Applications of Photonics in Defense Conference (RAPID)*, pages 1–4. IEEE.

[Huang et al., 1989] Huang, J., Zhang, J., Lezama, A., and Mossberg, T. (1989). Excess dephasing in photon-echo experiments arising from excitation-induced electronic level shifts. *Physical review letters*, 63(1):78.

[Jeong and Park, 2015] Jeong, S. and Park, C. (2015). Thermal contact problems at cryogenic temperature. *Progress in Superconductivity and Cryogenics*, 17(4):1–7.

[Jonsson, 2012] Jonsson, B. E. (2012). ADC performance evolution: Sampling rate and resolution. *Converter Passion*, pages 08–16.

[Kervella et al., 2014] Kervella, G., Maxin, J., Faugeron, M., Berger, P., Lanctuit, H., Pillet, G., Morvan, L., van Dijk, F., and Dolfi, D. (2014). Laser sources for microwave to millimeter-wave applications. *Photonics Research*, 2(4):B70–B79.

[King et al., 2021] King, D. J., Emara, M. K., and Gupta, S. (2021). Millimeter-wave integrated side-fire leaky-wave antenna and its application as a spectrum analyzer. *IEEE Transactions on Antennas and Propagation*, 69(9):5401–5412.

[Kinos et al., 2021] Kinos, A., Hunger, D., Kolesov, R., Mølmer, K., de Riedmatten, H., Goldner, P., Tallaire, A., Morvan, L., Berger, P., Welinski, S., et al. (2021). Roadmap for rare-earth quantum computing. *arXiv preprint arXiv:2103.15743*.

[Kinos et al., 2016] Kinos, A., Li, Q., Rippe, L., and Kröll, S. (2016). Development and characterization of high suppression and high étendue narrowband spectral filters. *Applied optics*, 55(36):10442–10448.

[Kop et al., 1997] Kop, R. H., De Vries, P., Sprik, R., and Lagendijk, A. (1997). Kramers-kronig relations for an interferometer. *Optics communications*, 138(1-3):118–126.

[Korablev et al., 2018] Korablev, O. I., Belyaev, D. A., Dobrolenskiy, Y. S., Trokhimovskiy, A. Y., and Kalinnikov, Y. K. (2018). Acousto-optic tunable filter spectrometers in space missions. *Applied Optics*, 57(10):C103–C119.

[Lavielle, 2004] Lavielle, V. (2004). *Processus atomiques cohérents appliqués à l'analyse spectrale très large bande de signaux radio fréquence.* PhD thesis, Universite Paris Sud-Paris XI.

[Le Gouët et al., 2007] Le Gouët, J.-L., Bretenaker, F., and Lorgeré, I. (2007). Atomic processing of optically carried RF signals. *Advances In Atomic, Molecular, and Optical Physics*, 54:549–613.

[Lenz et al., 1998] Lenz, G., Eggleton, B., Giles, C., Madsen, C., and Slusher, R. (1998). Dispersive properties of optical filters for WDM systems. *IEEE journal of quantum electronics*, 34(8):1390–1402.

[Li et al., 2017] Li, P., Zou, X., Pan, W., Yan, L., and Pan, S. (2017). Tunable photonic radio-frequency filter with a record high out-of-band rejection. *IEEE Transactions on Microwave Theory and Techniques*, 65(11):4502–4512.

[Lin et al., 1995] Lin, H., Wang, T., Wilson, G., and Mossberg, T. (1995). Experimental demonstration of swept-carrier time-domain optical memory. *Optics letters*, 20(1):91–93.

[Linget et al., 2015] Linget, H., Chanelière, T., Le Gouët, J.-L., Berger, P., Morvan, L., and Louchet-Chauvet, A. (2015). Interlaced spin grating for optical wave filtering. *Physical Review A*, 91(2):023804.

[Linget et al., 2013] Linget, H., Morvan, L., Le Gouët, J.-L., and Louchet-Chauvet, A. (2013). Time reversal of optically carried radiofrequency signals in the microsecond range. *Optics Letters*, 38(5):643–645.

[Liu et al., 1987] Liu, G., Joubert, M., Cone, R., and Jacquier, B. (1987). Photon echo relaxation and hole burning in Tb^{3+}:$LiYF_4$ and $LiTbF_4$. *Journal of Luminescence*, 38(1-6):34–36.

[Liu et al., 2011] Liu, X., Wang, X., Ke, W., Tao, W., Zhao, X., and Sun, X. (2011). Thermal conductivity of pure and Zn-doped $LiCu_20_2$ single crystals. *Physical Review B*, 83(14):144408.

[Lorgeré et al., 2002] Lorgeré, I., Menager, L., Lavielle, V., Le Gouët, J.-L., Dolfi, D., Tonda, S., and Huignard, J.-P. (2002). Demonstration of a radio-frequency spectrum analyser based on spectral hole burning. *journal of modern optics*, 49(14-15):2459–2475.

[Lorgeré et al., 2001] Lorgeré, I., Ménager, L., and Le Gouet, J.-L. (2001). Radio frequency spectrum analyzer based on spectral hole burning. In *Technical Digest. Summaries of papers presented at the Conference on Lasers and Electro-Optics. Postconference Technical Digest (IEEE Cat. No. 01CH37170)*, pages 370–371. IEEE.

[Louchet, 2008] Louchet, A. (2008). *Manipulation optique d'une cohérence de spin nucléaire dans l'ion thulium en matrice cristalline*. PhD thesis, Université Paris Sud-Paris XI.

[Louchet-Chauvet, 2018] Louchet-Chauvet, A. (2018). Analog time-reversal of optically-carried RF signals with a rare earth ion-doped processor with broadband potential. In *2018 International Topical Meeting on Microwave Photonics (MWP)*, pages 1–4. IEEE.

[Louchet-Chauvet, 2019] Louchet-Chauvet, A. (2019). Processeurs atomiques pour le traitement de signaux optiques et radio-fréquence.

[Madsen and Zhao, 1999] Madsen, C. K. and Zhao, J. H. (1999). *Optical filter design and analysis*. Wiley New York.

[Magaletti et al., 2022] Magaletti, S., Mayer, L., Roch, J.-F., and Debuisschert, T. (2022). A quantum radio frequency signal analyzer based on nitrogen vacancy centers in diamond. *Communications Engineering*, 1(1):1–8.

[Matsko et al., 2012] Matsko, A., Liang, W., Savchenkov, A., Ilchenko, V., Seidel, D., and Maleki, L. (2012). Multi-octave tunable agile RF photonic filters. In *2012 IEEE International Topical Meeting on Microwave Photonics*, pages 6–9. IEEE.

[Ménager, 2000] Ménager, L. (2000). *Traitement optique de signaux radio-fréquence par holographie spatio-temporelle*. PhD thesis, Paris 11.

[Ménager et al., 2001] Ménager, L., Lorgeré, I., Le Gouët, J.-L., Dolfi, D., and Huignard, J.-P. (2001). Demonstration of a radio-frequency spectrum analyzer based on spectral hole burning. *Optics Letters*, 26(16):1245–1247.

[Merkel and Babbitt, 1996] Merkel, K. and Babbitt, W. (1996). Optical coherent-transient true-time-delay regenerator. *Optics letters*, 21(15):1102–1104.

[Merkel et al., 2014] Merkel, K. D., Bekker, S. H., Traxinger, A. S., Stiffler, C. R., Woidtke, A. J., Chase, M. D., Babbitt, W. R., Barber, Z. W., and Harrington, C. H. (2014). 20 GHz instantaneous bandwidth RF spectrum analyzer measurements with high sensitivity and spur free dynamic range. In *Proceedings of the GOMAC2014 Conference, Charleston, SC*.

[Mossberg, 1982] Mossberg, T. W. (1982). Time-domain frequency-selective optical data storage. *Optics letters*, 7(2):77–79.

[Mukhanov et al., 2004] Mukhanov, O. A., Gupta, D., Kadin, A. M., and Semenov, V. K. (2004). Superconductor analog-to-digital converters. *Proceedings of the IEEE*, 92(10):1564–1584.

[Ng et al., 1991] Ng, W., Walston, A. A., Tangonan, G. L., Lee, J. J., Newberg, I. L., and Bernstein, N. (1991). The first demonstration of an optically steered microwave phased array antenna using true-time-delay. *Journal of Lightwave Technology*, 9(9):1124–1131.

[Norberg et al., 2011] Norberg, E. J., Guzzon, R. S., Parker, J. S., Johansson, L. A., and Coldren, L. A. (2011). Programmable photonic microwave filters monolithically integrated in InP–InGaAsP. *Journal of Lightwave Technology*, 29(11):1611–1619.

[Peijzel et al., 2005] Peijzel, P. S., Meijerink, A., Wegh, R., Reid, M., and Burdick, G. W. (2005). A complete $4f^n$ energy level diagram for all trivalent lanthanide ions. *Journal of solid state chemistry*, 178(2):448–453.

[Preussler et al., 2016] Preussler, S., Zadok, A., Stern, Y., and Schneider, T. (2016). Microwave-photonic filters. In *2016 German Microwave Conference (GeMiC)*, pages 61–64. IEEE.

[Reibel et al., 2004] Reibel, R., Barber, Z., Fischer, J., Tian, M., and Babbitt, W. (2004). Broadband demonstrations of true-time delay using linear sideband chirped programming and optical coherent transients. *Journal of luminescence*, 107(1-4):103–113.

[Reibel et al., 2002] Reibel, R., Barber, Z., Tian, M., and Babbitt, W. (2002). Temporally overlapped linear frequency-chirped pulse programming for true-time-delay applications. *Optics letters*, 27(7):494–496.

[Sangouard et al., 2008] Sangouard, N., Simon, C., Zhao, B., Chen, Y.-A., De Riedmatten, H., Pan, J.-W., and Gisin, N. (2008). Robust and efficient quantum repeaters with atomic ensembles and linear optics. *Physical Review A*, 77(6):062301.

[Savchenkov et al., 2009] Savchenkov, A. A., Liang, W., Ilchenko, V. S., Matsko, A. B., Seidel, D., and Maleki, L. (2009). RF photonic signal processing components: From high order tunable filters to high stability tunable oscillators. In *2009 IEEE Radar Conference*, pages 1–6. IEEE.

[Schlottau and Wagner, 2004] Schlottau, F. and Wagner, K. H. (2004). Demonstration of a continuous scanner and time-integrating correlator using spatial–spectral holography. *Journal of luminescence*, 107(1-4):90–102.

[Shekar et al., 2021] Shekar, P., Latha, D. M., Kumari, K., and Pisipati, V. (2021). Optimal parameters for fiber bragg gratings for sensing applications: a spectral study. *SN Applied Sciences*, 3(6):1–12.

[Shen and Kachru, 1997] Shen, X. and Kachru, R. (1997). High-speed holographic recording of 500 images in a rare earth doped solid. *Journal of alloys and compounds*, 250(1-2):435–438.

[Slack and Oliver, 1971] Slack, G. A. and Oliver, D. (1971). Thermal conductivity of garnets and phonon scattering by rare-earth ions. *Physical Review B*, 4(2):592.

[Tariq and Asif, 2016] Tariq, A. and Asif, M. (2016). Experimental investigation of thermal contact conductance for nominally flat metallic contact. *Heat and Mass Transfer*, 52(2):291–307.

[Taylor and Hessler, 1974] Taylor, D. and Hessler, J. (1974). Photon echo decay in ruby: electric dipole interactions and instantaneous diffusion. *Physics Letters A*, 50(3):205–207.

[Thiel et al., 2011] Thiel, C., Böttger, T., and Cone, R. (2011). Rare-earth-doped materials for applications in quantum information storage and signal processing. *Journal of luminescence*, 131(3):353–361.

[Thiel et al., 2014a] Thiel, C., Macfarlane, R., Sun, Y., Böttger, T., Sinclair, N., Tittel, W., and Cone, R. (2014a). Measuring and analyzing excitation-induced decoherence in rare-earth-doped optical materials. *Laser Physics*, 24(10):106002.

[Thiel et al., 2014b] Thiel, C. W., Cone, R. L., and Böttger, T. (2014b). Laser linewidth narrowing using transient spectral hole burning. *Journal of luminescence*, 152:84–87.

[Tian et al., 2001] Tian, M., Reibel, R., and Babbitt, W. R. (2001). Demonstration of optical coherent transient true-time delay at 4 Gbits/s. *Optics Letters*, 26(15):1143–1145.

[Tittel et al., 2010] Tittel, W., Afzelius, M., Chaneliere, T., Cone, R. L., Kröll, S., Moiseev, S. A., and Sellars, M. (2010). Photon-echo quantum memory in solid state systems. *Laser & Photonics Reviews*, 4(2):244–267.

[Tkach and Chraplyvy, 1986] Tkach, R. and Chraplyvy, A. (1986). Phase noise and linewidth in an InGaAsP DFB laser. *Journal of Lightwave Technology*, 4(11):1711–1716.

[Toughlian et al., 1994] Toughlian, E. N., Zamuda, H., and Carter, C. A. (1994). True-time-delay transmit/receive optical beam-forming system for phased arrays and other signal processing applications. In *Optoelectronic Signal Processing for Phased-Array Antennas IV*, volume 2155, pages 181–191. SPIE.

[Veissier et al., 2016] Veissier, L., Thiel, C. W., Lutz, T., Barclay, P. E., Tittel, W., and Cone, R. L. (2016). Quadratic zeeman effect and spin-lattice relaxation of Tm^{3+}:YAG at high magnetic fields. *Physical Review B*, 94(20):205133.

[Walden, 1994] Walden, R. H. (1994). Analog-to-digital converter technology comparison. In *Proceedings of 1994 IEEE GaAs IC Symposium*, pages 217–219. IEEE.

[Wickham et al., 1995] Wickham, M. G., Dozal, L. A., Lembo, L. J., and Brock, J. C. (1995). Fiber optic bragg grating true-time-delay generator for broadband RF applications. In *Optical Technology for Microwave Applications VII*, volume 2560, pages 148–157. SPIE.

[Xue et al., 2008] Xue, W., Sales, S., Mork, J., and Capmany, J. (2008). Widely tunable microwave photonic notch filter based on slow and fast light effects. *IEEE Photonics Technology Letters*, 21(3):167–169.

[Yao and Capmany, 2022] Yao, J. and Capmany, J. (2022). Microwave photonics. *Science China*.

RÉSUMÉ

Les propriétés de creusement de trou spectral, que l'on trouve à température cryogénique dans certains cristaux dopés aux ions de terres rares, offrent des possibilités prometteuses pour le traitement de signaux radiofréquence large bande. En effet ces propriétés permettent de programmer des fonctions de traitement radiofréquence dans le spectre d'absorption du cristal. Partant des premières démonstrations hors laboratoire d'un analyseur de spectre large bande reposant sur un cristal de Tm^{3+}:YAG, l'objectif de ce travail de thèse est double: d'une part démontrer la versatilité de l'architecture utilisée en développant de nouvelles fonctions de traitement radiofréquence, et plus spécifiquement la fonction de filtrage, et d'autre part améliorer les performances de l'analyseur de spectre.
Nous commençons par l'étude de la fonction de filtrage radiofréquence. Nous démontrons la première réalisation de la fonction de filtrage dans des cristaux dopés aux terre rares. Cette démonstration s'appuie sur l'architecture "arc-en-ciel" dans un cristal de Tm3+:YAG. Nous présentons une étude paramétrique afin d'optimiser les performances du filtre. Nous développons ensuite un modèle analytique décrivant la réponse du filtre en amplitude et en phase. Après optimisation du filtre, nous obtenons une réjection de 60 dB, avec une réjection de 45 dB à 50 MHz du bord du filtre, à l'état de l'art des filtres photoniques GHz.
Dans un second temps, nous nous intéressons au montage historique de l'analyseur de spectre large bande. Le premier axe d'étude est dédié à la baisse de dynamique observée expérimentalement lorsque la bande d'analyse augmente. Nous identifions que cette baisse est liée à une élévation de température dans le cristal due aux excitations optiques. Nous nous attachons à mesurer le profil de température à l'intérieur du cristal par spectroscopie SHB, dans l'objectif de déterminer une configuration expérimentale favorable à une meilleure thermalisation du cristal. Dans le second axe d'étude dédié à l'analyseur spectral, nous nous intéressons à sa réponse fréquentielle. Nous étendons notre modèle de filtre radiofréquence pour l'adapter à cette configuration. Nous utilisons ce modèle pour comprendre les phénomènes pouvant mener un élargissement de la réponse de l'analyseur. Finalement nous appliquons notre modèle aux paramètres expérimentaux pour quantifier l'impact de ces phénomènes en pratique.

MOTS CLÉS

Traitement de signal, Optique radiofréquence, Cristaux dopés aux terres rares, Creusement de trou spectral

ABSTRACT

The property of Spectral Hole Burning, available in rare-earth ions-doped crystals at cryogenic temperature, offers promising opportunities for wideband radiofrequency signal processing. Indeed, this property allows to program radiofrequency processing functions in the absorption profile of the crystal. Starting from first out-of-lab demonstrations of wideband spectrum analysis using a Tm^{3+}:YAG crystal, the objective of this PhD work is double: first, demonstrate the versatility of the architecture by developing new radiofrequency processing functions, more specifically the function of filtering, and second to improve the performances of the spectrum analyzer.
We start with the study of radiofrequency filtering. We report the first demonstration of a radiofrequency filter using rare-earth ions-doped crystals. This demonstration relies on a spectro-spatial architecture in a crystal of Tm^{3+}:YAG. We present a parametrical study, aiming to optimze the performances of the filter. We develop an analytical model describing the response of the filter in amplitude and in phase. After optimizing the filter shape, we obtain a rejection of 60 dB, with a rejection of 45 dB at 50 MHz from the edge of the filter, at the state of the art of GHz-wide photonic RF filters.
In a second part, we focus on the historical setup of wideband spectrum analysis. The first area of study is dedicated to the limited dynamic range observed experimentally when the analysis bandwidth is large. We identify that this diminution is related to a temperature elevation in the crystal caused by the optical excitations. We measure the temperature profile inside the crystal by SHB spectroscopy, with the objective to determine an experimental configuration beneficial for a better thermalization of the crystal. In the second area of study dedicated to the spectrum analyzer, we focus on its frequency response. We extend our model of radiofrequency filter to adapt it to this confguration. Using this model, we investigate the phenomenon possibly causing a broadening of the frequency response. Finally, we apply our model with the experimental parameters to quantify the impact of these phenomenon in practice.

KEYWORDS

Signal processing, Microwave photonics, Rare-earth ions-doped crystals, Spectral Hole Burning